Equilibrium and Non-Equilibrium Phenomena in Two- and Three-Dimensional Correlated Systems

by

Michael J. Young

Bachelor of Science, College of Engineering,
The University of California, Berkeley (June 1989)

Submitted to the Department of Physics
in partial fulfillment of the requirements for the degree of

Doctor of Philosophy

at the

MASSACHUSETTS INSTITUTE OF TECHNOLOGY

June 1996

Author .....
Department of Physics
May 16, 1996

Certified by .....
Robert J. Birgeneau
Dean of Science and Cecil and Ida Green Professor of Physics
Thesis Supervisor

Accepted by .....
George F. Koster
Chairman, Departmental Committee on Graduate Students

Equilibrium and Non-Equilibrium Phenomena in Two- and Three-Dimensional Correlated Systems

by

Michael J. Young

Submitted to the Department of Physics
on May 16, 1996, in partial fulfillment of the
requirements for the degree of
Doctor of Philosophy

Abstract

Ultra-high vacuum (UHV) x-ray diffraction studies have been conducted on adsorbate-free silicon surfaces miscut from (111) up to 8° toward $\langle 11\bar{2} \rangle$ revealing dynamical changes in the surface morphology which are reversible and can be controlled by the direction of current flow through the crystal. These studies cover the temperature range 1200 K to 1525 K with direct current flowing parallel and anti-parallel to the $(11\bar{2})$ direction, i.e. normal to the average step flow direction. The surface morphology changes which characterize this dynamical phenomenon occur on mesoscopic length-scales and exhibit time-dependence which is ascertained directly from the x-ray experiments. The time-evolution of the surface morphology is obtained on quenching and on current reversal. The high-temperature step order-disorder transitions are found to be independent of the step spacing within the resolution of the experiment. These measurements suggest that recent theoretical models for the step behavior on vicinal surfaces incorrectly account for the stability conditions in the vicinity of these surface phase transitions.

High-resolution x-ray scattering investigations of the Nematic (N) –Smectic-A_1(Sm-A_1) transition are presented for two materials with large nematic ranges: the pure compound octyloxyphenyl-nitrobenzoyloxy benzoate (DB_8ONO_2), and the binary mixture pentylphenylcyanobenzolyoxy benzoate (DB_5CN)+ cyanobenzoyloxypentyl-stilbene (49.5 mole %C_5 stilbene). The critical behavior of the longitudinal and transverse correlation lengths $\xi_{\|}$ and $\xi_{\perp}$ and smectic susceptibility σ are determined for DB_8ONO_2 and DB_5CN+C_5 stilbene and analyzed with asymptotic (pure power-law) and pre-asymptotic forms. A conventional analysis of the x-ray data yielded critical exponents γ and $\nu_{\|}$ close to the 3D-XY values for both samples, albeit with a correlation length anisotropy ($\nu_{\perp} < \nu_{\|}$) and a violation of anisotropic hyperscaling is observed. First-order corrections-to-scaling terms, previously known to be important for describing C_p, are shown to be consistent in describing the *correlation volume* $\xi_{\|}\xi_{\perp}^2$ and the smectic susceptibility σ obtained from the x-ray data. The development of in-plane smectic modulations is also investigated for DB_5CN+C_5 stilbene.

A high-resolution x-ray scattering study has been made of the first- and second-

harmonic of the order parameter near the nematic(N) to smectic-A_2 (bilayer smectic) transition in the liquid crystal material 4′-n-heptyloxycarbonyl-phenyl-4′-(4″-cyanobenzoyloxy) benzoate (7APCBB). The critical behavior of the smectic susceptibility, and correlation lengths for both the fundamental and second harmonic are determined. A new theory for the scaling behavior of quartic correlations predicts that the structure factor $S_n(\mathbf{q}) = \langle \psi_n(\mathbf{q}) \psi_n^*(\mathbf{q}) \rangle$ associated with fluctuations in the n'th harmonic density wave order parameter ψ_n of a uniaxial system depends on both its bare $\mathbf{q}$-dependence, and by the coupling $Re(\psi_n^* \psi_1^n)$. The latter involves quartic correlations in the secondary order parameter ψ_1^n, characterized by a correlation length $\xi_n = \xi_{n0}[(T - T_c)/T_c]^{-\nu}$, with *the same* XY model exponent ν for all n, and decaying as $q^{-(2-\eta_n)}$ for large q. The correlation lengths associated with the higher harmonics are related to the fundamental by universal ratios X_n which were calculated in the theory. Consistency between the experimental data and these new theoretical developments is shown for the second harmonic (n=2), thus providing the only evidence to date for 3D-XY-like criticality in the disordered phase of a multi-component order parameter system.

Thesis Supervisor: Robert J. Birgeneau
Title: Dean of Science and Cecil and Ida Green Professor of Physics

Acknowledgments

This thesis in many ways (if not by its contents, by its timing) marks the closure of the longest chapter in my college education, full of many fond memories, and life enriching experiences. Despite my tendency to go against the grain of tradition, it is a pleasure to be able to send the traditional "distended" acknowledgements to the many people who have either directly or indirectly contributed to the work presented in this thesis.

Firstly, I would like to thank my research advisor, Bob Birgeneau. In many ways Bob is inimitable: he is enthusiastic, adamantly consistent, and deeply loves research. Bob managed to structure our group in a way that exacted a great deal of individual effort and self-confidence. This is the aspect of my experience in his research group which had the greatest impact on me. He also taught me many important things about the communication of ideas, especially with regard to scientific work. I was particularly impressed by his ability to quickly formulate a thought and then articulate it using a minimal set of carefully chosen words, with his countenance and gestures supplying an almost trademark emphasis – and he was always very dynamic and motivated.

I would like to take the opportunity to give special thanks to both Profs. John Allen (director of the Research Laboratory of Electronics) and Bob Birgeneau for their unsolicited choice to nominate me for the J.S.E.P. fellowship award which covered nearly half of the stipend I received while a graduate student.

I would also like to thank Prof. Carl Garland for collaborating with us on the liquid crystal experiments which comprise a good portion of this thesis. He led many fruitful discussions throughout our experiments, and taught me an enormous amount about liquid crystal phase transitions (and life) in the process.

Deepest thanks are also due Dr. George Nounesis who was a powerful mentor for me, and a great friend. It was also a pleasure to collaborate with Dr. Lei Wu and Yongmei Shao on a number of liquid crystal experiments. The energy and enthusiasm they brought into their work is something I will always remember.

I greatly appreciate the endless help I received from Young-June Kim on the Si(111) and Ge(111) synchrotron experiments. I also would like to thank Qiang Feng and Young Sang Lee who helped me in my time of need during the penultimate stage of my thesis experiments, and Barry Wells for providing me with a wealth of advice on conducting proper experiments. I would like to thank Monte Ramstad for his valuable advice on the direction of the semiconductor surface project, and beyond.

Some of my most enjoyable hours in the lab were those spent working with Bill Nuttall, Kevin Fahey, and Do-Young Noh. Their patience, unceasing optimism, and sense of humor made life in "the trenches" of BNL enjoyable. I benefited immensely throughout my surface experiments from the help and expertise of Mirang Yoon and Seungheon Song.

I am extremely pleased to have had Professors Toyoishi Tanaka and Alan Guth as my thesis readers and teachers. Over the last few years I have enjoyed working with and knowing many people at the professional and personal level: these include Dr. Jean Jordan-Sweet, René Holaday, Alan Mak, John Hill, Bernhard Keimer, Brian McClain, Libby Shaw, Bruce Carvalho, Nihat Berker, Laurence Navailles, Amnon Aharony, Ken Blum, Elizabeth Muylaert, and Helena Bazile. I have also benefited tremendously from the help of computer gurus James Njeru and Gerry Swislow who manage to bail me out of countless computer problems.

It is a great pleasure for me to thank Mike Titko, Roland Netz, Cláudio Chamon, Marcos Gurgel Fernandes, Bill Hoston, Tomaz Catunda, and Marisa Mendonça Netto for their friendship over the years. Of course, all of my many brothers remained highly unconventional sources of encouragement and entertainment throughout my time in college: not a single Grand Panjandrum in sight.

Heart-felt thanks go to the other members of the "team": Barry Wells, Joan Harris, Young-June Kim, Young Lee , Qiang Feng, Martin Greven, Patrick Mang, Rebecca Christianson, Sungil Park, Yujie Wang, and Michelle Girven. Each one of you rank among the most exceptionally talented and gifted people I know. I wish you all continued success in your pursuits.

I cannot forget to acknowledge the advice I received from my friend Scott Hughes

and his father Richard who convinced me that there is value in education. Without their advice and encouragement I would have never even considered going to college.

My graduate research would not have been possible without the generosity and support of the staff at the Center for Materials Science and Engineering: especially Virginia Esau, Susan Rosevear, Ron Hasseltine, Amanda Tat, and Karen Fosher. I don't know what I would have done if it hadn't been for all of the left-over food they managed to dish out after seminars. I would like to acknowledge the receipt of financial support from the following sources, in chronological order: the MIT Physics Department, the Center for Materials Science and Engineering, the Joint Services Electronics Program.

To ennoble our emotions, to decorate and enrich our life, to proportionate to us joy and feeling, is the mission of art.

– Mokiti Okada

Contents

List of Figures

List of Tables

Chapter 1

Phase Transitions in Correlated Systems

...The human heart does its work on earth, and that moves the great deep. What is that incomprehensible meeting of material sublimation and moral sublimation in the atom, indivisible if looked at from life, incorruptible if looked at from death? ...No dimension, no extent, nor height, nor width, nor thickness, independent of every possible measure, and yet, everything in this nothing! For algebra, the geometrical point. For philosophy, a soul. As a geometrical point, the basis of science; as a soul, the basis of faith. Such is the atom.

From the essay "The Souls", by Victor Hugo.

Many of the concepts encountered in the study of phase transitions in materials can be formulated without an explicit reference to atomic structure, or even to the details of the interactions between atoms, beyond knowing their range of interaction. Although the atom is far from the geometrical point Hugo describes, it often suffices to know only a minimal set of information about its electronic state to be able to arrive at an understanding of many properties of real materials. The subject of this thesis concerns phase transitions in condensed matter systems and the subsequent physical behavior resulting from changing thermodynamic properties of materials. Studies of phases and phase transitions encompass a vast assortment of research. It is therefore useful to define some of basic concepts, particularly with respect to why phase transitions are interesting to study, and what thermodynamic properties are essential in order to

elucidate the physical behavior in the vicinity of a phase transition.

One of the most common ways phase transitions enter into everyday experience is through the temperature scale; the familiar ones being the Kelvin, Fahrenheit, Celsius, or even (sic) Rankine scales. The standard for temperature seems so trivial and commonplace today, one can easily forget its importance. The Celsius scale was at one time defined by two fixed temperatures, the ice point and the steam point for H_20 at 1 atmosphere of pressure. More recently it has been based on the triple point where water coexists with ice and water vapor. The Fahrenheit scale, which the United States embraces to this day, emerged from an almost bizarre choice of two unrelated temperature "standards" set by Gabriel Fahrenheit (1686-1736): these were the average temperature of the human body, which he defined arbitrarily to be 96°F, and the ice point of a water and salt mixture in equilibrium with a salt solution, defining 0°F. Using these two "fixed" temperatures, the ice point of pure water at 1 atmosphere is at 32°F and the boiling point is at 212°F. The funniest part of this anecdote is that, given this temperature scale, the average temperature of the human body is actually 98.6°F, not 96°F (right?). One can certainly criticize Fahrenheit's choice of standards; he evidently thought that these two temperatures could be conveniently reproduced. Fahrenheit's logic was no more unusual then that used in defining the foot or the pound.

It is very common to define scientific concepts by resorting to simple physical descriptions based on macroscopic properties of a system. In fact, the physical concepts which are the building blocks of classical thermodynamics essentially define a science of work and heat, without any reference to the atomistic nature of matter. One could easily develop the concept of the solid phase, without assuming anything about the particulate nature of matter, simply by measuring the finite shear forces that can be transmitted into the bulk of a solid across its surface. Likewise, one could use a bunsen burner to melt their favorite solid, measure the vanishing shear restoring force (or the finite viscosity) and arrive at a consistent definition of the fluid phase. With these two simple observations of the solid and its melt, one would probably define a fluid as something which does not restore shear forces, and a solid as something

which can restore a shear force (ignoring the possibility of the glass phase). This latter definition for a solid clearly circumvents a knowledge of crystalline order and, in fact, one would need to invent slightly more sophisticated ways to uncover the nature of crystalline solids to be able to think properly about their electronic or magnetic properties. The distinction between crystalline solids, amorphous solids, fluids (and glasses) would need to be made unambiguously. This task is obviously difficult to achieve without microscopic probes.

A phase of matter which has become of substantial technological importance over the last two decades is the so-called liquid crystalline phase which one encounters in display technology (LCD's), and in many electronic devices. Liquid crystalline phases are elaborate phases of matter occurring in some systems of organic molecules, and have properties intermediate between those of normal liquid and crystal phase. Generally, the shape of the molecules in liquid crystalline materials is fundamental in determining the types of phases that can exist in these systems. It is interesting to note that the existence of liquid crystalline materials has been known for more than a century, and are important in biological systems. The lipid bilayer which surrounds cells is an example of a material in a liquid crystal phase and the resulting properties of this bilayer structure are essential to proper cell function. Liquid crystal phase transitions are directly related to a number of diseases such as arteriosclerosis and sickle cell anemia.

One might think that an explanation of the intricate physical properties occurring in liquid crystal materials would require a detailed understanding of their molecular structure. However, one can infer a great deal of information about some liquid crystal phases by simple inspection: for example, the visibly turbid appearance of the nematic phase found in many of liquid crystal materials is the result of an orientational ordering of the molecules in a fluid phase [1]. One could gather more information of this orientationally ordered phase by exploiting the vector nature of electromagnetic radiation, and pass some light through linear polarizers: polarized light, when illuminating a liquid crystal material, will be preferentially scattered depending on the anisotropic dielectric properties of the material. This optical behavior

is common to liquid crystals and is the basis for LCD's. Response functions associated with the dielectric properties of these materials have macroscopic meaning, as do those associated with its anisotropic elastic properties. These anisotropies have a microscopic origin directly related to the anisotropic *geometry* of the molecules. The nematic phase is a *fluid* phase in that it cannot restore a shear distortion, but a finite torque can be transmitted across the surface of a nematic into the bulk due to its molecular anisotropy: once again, macroscopic phenomena can open up vistas to the microscopic world.

Equilibrium and Non-Equilibrium Systems

A number of phases of matter have now been introduced with a phase transition being the result of some change in the thermodynamic properties of the system. A tractable theoretical description of thermodynamic and mechanical properties such as volume, temperature, viscosity, thermal expansion, or surface tension, generally requires that the system be at its equilibrium state. A phase diagram describes a space of equilibrium states of a material which are uniquely characterized by thermodynamic variables (ie. P, T, or V). The condition of equilibrium typically implies that these states do not depend on time, and thermodynamic "changes" in the system do not depend on the "path" in the space of thermodynamic potentials. This latter condition is equivalent to the statement that hysterisis is not relevant. The time dependence aspect of this description can be quite complicated. It suffices to define the difference between equilibrium and non-equilibrium processes in terms of reversible and irreversible changes in a system. The equiliubrium development of a system can occur reversibly when the system undergoes infinitessimal thermodynamic changes between equilbrium states of the system. Non-equilibrium changes happen irreversibly.

Early theoretical attempts applied classical thermodynamics to explain phase transition behavior and were remarkably successful for some systems. For example, the liquid-gas transition which is at the core of the steam engine can be understood to some degree by the Gibbs formalism which is based on the existence of an equation

of state; that is, a function relating the pressure, temperature, volume, in the *equilibrium* phases of the system. Of course, the expansion of the vapor and subsequent flow of the working fluid in an engine is far from equilibrium. Regardless, many problems can be satisfactorily understood within the context of equilibrium physics, without resorting to any of the details of the atomic structure or interactions between the constituents of the system.

In the language of modern condensed matter physics, one can talk about an equilibrium phase transition in a condensed system from a high temperature phase to a low temperature phase in terms of the behavior of an *order parameter* on altering the system thermodynamically. The concept of an order parameter is more than just simple extension of the ideas described above. Namely, one defines an order parameter as a physical observable (eg. magnetization, staggered magnetization, mass density, polarization) which is non-zero in the low temperature (ordered) phase, and zero in the disordered phase. The physical behavior occurring in the vicinity a phase transition can be discussed almost solely in terms of this order parameter and its conjugate field (eg. magnetic field, pressure) which depends on the nature of the problem.

The order parameter is typically selected phenomenologically and it therefore helps to have some intuition about the physics of the system. Naturally, there are systems where the choice of the order parameter is not obvious. In some instances it is questioned whether a order parameter needs to exist in the traditional sense (for example, in spin glasses, or in a Kosterlitz-Thouless surface phase transition) [3, 5]. It is often useful to choose a *local* order parameter defined as the average value of the observable at a specific point in space. Compare this with a *global* order parameter which is simply the value of a macroscopic observable averaged over the whole system. As an example, one can look at the liquid-gas transition mentioned above. The order parameter in this case is defined as the difference in the densities between the liquid and the gas, $\rho_{liquid} - \rho_{gas}$. In the lower temperature phase the liquid and gas coexist, therefore the difference in densities is non-zero. In the higher temperature gas phase, the liquid density and gas density are indistinguishable and the order parameter is zero. An order parameter need not be unique in any one system since any power of

the order parameter will function equally well.

The occurrence of a phase transition in a condensed system is usually governed either by interatomic (or intermolecular) interactions, or statistics, or both. An example of a case where a system can condense to a particular phase simply due to the statistical nature of its constituents is manifested in Bose-Einstein condensation. This was elegantly demonstrated in experiments by Anderson and co-workers in 1995 [2] in a system of dilute atomic rubidium-87 vapor near a T_c of 170 nanokelvin. Numerous examples can be found of systems exhibiting phase transitions due to the presence of interatomic interactions. For example, in most liquid crystal systems, the dominant physical processes are entropic in nature; steric forces arise due to a reduced volume accessible to the molecules.

One of the triumphs of modern critical phenomena theory was uncovering the role of symmetries and geometry in determining the types of phases which materials can possess without considering the details of the interactions between the constituents. In fact, many condensed matter systems have phase transitions which can ultimately be understood by knowing the symmetry of the order parameter, spatial dimensionality of the system, and the *range* of the interactions. Ultimately, fluctuations in the order parameter of a system give rise to singular behavior in thermodynamic quantities (eg. susceptibilities, heat capacity) and this is at the heart of the theoretical and experimental challenges to delineate the nature of equilibrium phase transitions. One of the challenges for the experimentalist is to identify and understand model systems with which to test critical phenomena theory.

Dynamical phenomena present a far more difficult challenge due to their inherently complex nature. The evolution of growth patterns and hydrodynamic patterns was shown analytically by the well-known KPZ model for dynamical scaling at growing interfaces [4]. Studies of the time development of semiconductor surface structure present one realization of a system with potential to test dynamical growth theory. The homoepitaxial growth at semiconductor interfaces would be an interesting problem to study. Clean surfaces which terminate to vacuum also possess a rich variety of dynamical behavior and form the basis of the surface studies described in this

thesis. This nascent experimental progress on studies of non-equilibrium phenomena in two-dimensional systems is expected to provide an ideal testing ground for some of the more recent theoretical models.

Outline

This thesis consists of experimental studies of phase transformations occurring in two classes of condensed matter systems. The ordering and disordering of steps on silicon surfaces and the onset of smectic mass density waves in bulk nematic liquid crystals are model phenomena exhibited by highly correlated condensed matter systems. The thermodynamic behavior of steps on silicon surfaces is evinced in the non-equilibrium, electromigration-driven faceting which occurs under sublimation and it is described by two-dimensional step-step correlations. Moreover, thermotropic, polar, smectic liquid crystals exhibit a wide variety of polymorphic phases characterized by differing uniaxial molecular arrangements described in three-dimensions by mass density waves with different periodicities. The main thrust of the x-ray diffraction studies concerns the equilibrium and non-equilibrium behavior of steps on vicinal silicon surfaces with large surface miscut orientations, and also the study of critical fluctuations near the nematic to monolayer smectic-A and nematic to bilayer smectic-A phase transitions in bulk nematic liquid crystals. The development of in-plane smectic modulations is also investigated for one binary mixture of polar liquid crystalline compounds. These systems, although disparate in their nature, provide excellent examples with which to test current phase transition theories and identify new experimental and theoretical challenges which might be undertaken.

Adsorbate-free silicon surfaces intentionally miscut close to the (111) high symmetry facet, are the main focus of the ultra-high vacuum (UHV) x-ray surface diffraction studies. Under the appropriate thermodynamic conditions, these *vicinal* surfaces will possess monoatomic steps when miscut toward $\langle 11\bar{2} \rangle$. A variety of interesting physics are exhibited on these stepped surfaces, perhaps the most exotic example being the electromigration current-induced morphological instability, which occurs when one joule-heats an optically flat piece of silicon to high temperatures. Specifically, x-ray

diffraction was used to study surface faceting on 3° miscut Si (111) samples in the temperature range 1175K to 1525K with direct current flowing anti-parallel to the $(11\bar{2})$ direction (step-up direction), i.e. normal to the mean step flow. Above 1523K at this current direction the surface structure consists of an *ordered array* of steps which exhibits a peculiar non-equilibrium behavior. At positive current between approximately 1175K and 1525K step-step correlations increase, but are accompanied by a transverse step wandering. Above 1525K, the surface develops an intricate faceted structure which has not been well-understood. The preliminary studies of these high-temperature transformations provided an indication of partially reversible phase behavior, and it was suggested that the governing mechanism involves the combined effects of thermal diffusion, sublimation, step kinetics, and electromigration. In order to fully test these hypotheses, x-ray studies were conducted of the time-dependence of these surfaces as well as the resulting steady-state surface structures.

In Chapter 2, an overview of the vicinal Si(111) surface is presented along with a description of some of the thermally-induced phase transformations which have been observed in this system. The concept of a current-induced phase transformation is introduced and explained in terms of the phenomenon of electromigration. Surface x-ray diffraction studies under ultra-high vacuum (UHV) conditions were conducted to elucidate the *in-situ* behavior of vicinal Si(111) under the action of electromigration. These experiments are presented along with a discussion of *ex-situ* Atomic Force Microscopy (AFM) and optical microscopy studies of quenched Si(111) samples which had been under the influence of electromigration at high temperatures. Studies of the behavior of steps under direct-current heating are presented which address recent models attempting to describe the morphological instability of crystal surfaces induced by an applied electric field. An account of the high-temperature step kinetics had been previously attempted with a one-dimensional continuum model which treats the interaction of the steps with a smoothly varying adatom density. Many of the recent models fail to account for sublimation which, according to our experimental results, will lead to substantial deviations from the predictions of one-dimensional analysis. These experiments confirm some of our original proposals which were based

on cursory diffraction and imaging data [20]. The results from these studies also identify inconsistencies in some of the continuum models which have been proposed recently to explain the temperature and current-direction dependence of these surface phase transitions.

The x-ray diffraction studies presented in Chapter 3 address fundamental questions regarding the critical behavior near the nematic(N)-smectic-A_1 (monolayer SmA) in liquid crystals. Among these questions is the well-known complication that the three dimensional (3D) XY critical behavior predicted by theory for the N-SmA_1 transition is affected by the proximity of the phase transition to a tricritical point. Systems with large nematic temperature ranges are expected to exhibit nearly ideal 3D-XY-like behavior. A high-resolution x-ray scattering investigation is presented for the N-SmA_1 transition in two materials (DB_8ONO_2 and DB_5CN+C_5 stilbene) which have large nematic ranges. These x-ray data are presented in the context of the asymptotic (pure power-law) theory and a pre-asymptotic theory. The results of this analysis underline the importance of corrections-to-scaling in describing the critical divergences in the correlated volume and smectic susceptibility. These results are shown to be consistent with those from heat capacity studies on these same materials.

In chapter 4, results are presented from high-resolution x-ray scattering studies of the first- and second-harmonic of the order parameter near the nematic to bilayer smectic-A_2 transition in the polar liquid crystal material 7APCBB. Previous heat-capacity measurements on this same compound determined that this phase transition belonged to the 3D-XY universality class, and this motivated the x-ray studies. From the x-ray scattering data it was determined that the predictions of 3D-XY multicritical scaling theory are in good agreement with the critical exponents for the smectic susceptibility, and correlation lengths for the fundamental, as well as the smectic susceptibility for the second harmonic. However, applying a conventional analysis for the x-ray scattering at the second-harmonic yielded results in clear disagreement with the theory. Specifically, the correlation lengths for the second harmonic were found to differ both in magnitude and in there critical behavior from the correlation lengths describing the first harmonic. This experimental finding induced a re-examination of

the theory which made a striking prediction: namely, the critical fluctuations associated with the second harmonic ψ_2 (and all higher harmonics ψ_n) involve couplings of the form $\psi_1^n \psi_n^*$. This theoretical prediction led to the result that correlation lengths should diverge with the same 3D-XY model critical exponent, ν_{XY}. The x-ray data are found to be consistent with the theoretical predictions including the ratio of the correlation lengths $\sqrt{X_2} = \xi_2/\xi_1 = 0.02$, calculated to second order in an ϵ-expansion. The new theoretical developments provide a consistent explanation of our experimental results for the structure factor describing the second harmonic, $S_2(\mathbf{q})$.

In Chapter 5, experimental results are presented from an x-ray diffraction study of the binary liquid crystal mixture DB_5CN + C_5 stilbene which has a sequence of smectic phases on cooling below the N–Sm-A_1 transition distinguished primarily by the arrangements of dipolar molecules within the smectic layers. The behavior of the smectic-A fluid antiphase (Sm-$\tilde{A}$) ordering and the evolution of the system to Sm-A_2 order via a two-phase coexistence region are described in detail. These results are contrary to those of previous studies which reported the existence of a new phase separating the Sm-A_2 phase from the fluid antiphase Sm-$\tilde{A}$. This x-ray diffraction study is presented as a compliment to the study of the N-Sm-A_1 critical behavior on the same compound.

Bibliography

[1] J. D. Litster and R. J. Birgeneau, Phys. Today **35**, No. 5, 261 (1982).

[2] M. H. Anderson, J. R. Ensher, M. R. Matthews, C. E. Wieman, E. A. Cornell, Science, **269**, 5221, p. 198-201.

[3] Kerson Huang, *Statistical Mechanics*, Second Edition (John Wiley & Sons, New York, 1987).

[4] Mehran Kardar, Giorgio Parisi, and Yi-Cheng Zhang, Phys. Rev. Lett. **56**, p. 889 (1986).

[5] John W. Negele and Henri Orland, *Quantum Many-Particle Systems*, (Addison Wesley, Redwood City, California, 1988).

Chapter 2

The Electromigration-driven Behavior of Steps on Vicinal Si(111)

2.1 Introduction

Where do atoms reside on a surface? This is a question that has become markedly important as advancements in fabrication technology yield increasingly smaller electronic devices. Techniques such as molecular beam epitaxy (MBE) have made possible unprecedented control over fabrication processes, and allow one to create intricate multi-layer semiconductor devices. Sub-micron control during such fabrication processes clearly requires knowledge of the details of both the bulk structure and the surface structure of materials. There are many issues of technological importance which hinge upon a detailed understanding of *dynamical* changes as well, particularly in the morphology of surfaces. The deposition of one electronic material on another, as in thin film growth, is typically accompanied by step flow and other surface kinetic phenomena which will ultimately determine the quality and stability of the growth process [1, 2]. The manner by which a surface structure arrives at equilibrium can be understood through step motion and step kinetics. In general, a microscopic descrip-

tion of static or dynamic surface processes requires a knowledge of the behavior of the surface defects; an example of surface defects accessible to surface probes would include atomic height steps. Dynamical phenomena such as catalysis also depend strongly on the behavior of steps and other surface defects. Of course, one would expect the microscopic behavior of steps to play a fundamental role in evaporation processes as well. In this chapter, an investigation is presented of some interesting novel behavior occurring on stepped silicon surfaces. It is shown that cooperative behavior involving the agglomeration and arrangement of steps can lead to dramatic time-dependent changes in the surface structure on mesoscopic (nanometer to micron) length-scales. Further, these surface transformations are observed to result from competing interactions under non-equilibrium conditions, yet are surprisingly reversible.

Silicon surfaces are known to exhibit a rich assortment of surface structural transformations, such as reconstructions, which can be induced thermodynamically or by introducing impurities. In recent years, the development of surface-sensitive techniques such as x-ray diffraction has made it possible to probe the structure of these surfaces at the microscopic level, as well as examine the dynamical changes in their morphology. Morphology changes occurring on stepped semiconductor surfaces such as vicinal Si(111) have received attention not only because to their obvious practical importance, but also because of the variety of fundamental physics which is involved in understanding these processes. In particular, the mechanical and electronic properties of silicon make it an ideal system in which to investigate adatom interactions and their role in determining the equilibrium and non-equilibrium changes in the surface morphology.

The System: Vicinal Si(111)

The ideally terminated flat Si(111) surface has a three-fold ($3m$) symmetry. The two uppermost sub-lattices of this surface are depicted in Figure 2-1 where arrows are drawn to indicate three symmetry equivalent directions $[11\bar{2}]$, $[1\bar{2}1]$, and $[\bar{2}11]$. The surface of the model system, vicinal Si(111), is created by truncating a Si(111) crystal and polishing it such that the surface normal ($\hat{n}$) makes a small angle with (111) toward one of these three-fold symmetric directions. The term vicinal refers to surfaces oriented close to (or in the vicinity of) a low-index facet. Truncating a Si(111) crystal toward the direction $[11\bar{2}]$ will result in the breaking of single bonds joining atoms in the second layer to their nearest neighbors in the third layer. This is shown schematically in Figure. 2-2. In this example, a vicinal surface is revealed having steps which define the linear boundary marking a jump from atoms in the second layer (on one side of the step) to atoms in the third layer on the other side of the step. An isolated bilayer step of height d is depicted in Fig. 2-2. Vicinal surfaces possessing multi-height steps are allowed, but typically cost a large energy to create [27].

Equilibrium Step Behavior and Faceting

The vicinal Si(111) surface is known to undergo an equilibrium phase separation to a "hill and valley" structure, such as that depicted in Fig. 2-3(b), with large faceted regions separated by step bunches. Generally, a surface will be unstable to faceting if the surface tension is decreased by the formation of faceted and stepped regions. An understanding of this equilibrium phenomena on stepped surfaces can be made within the context of the Gibbs Free-energy formalism as was elegantly demonstrated in ref. [17]. This classical thermodynamic description of the surface phase behavior treats both the temperature and the *surface orientation* as parameters in the surface free energy. The latter quantity can be mapped directly onto the step density and is thus analogous to the particle concentration which parameterizes the phase separation occurring in the familiar liquid-gas phase coexistence. The two-phase region (facets

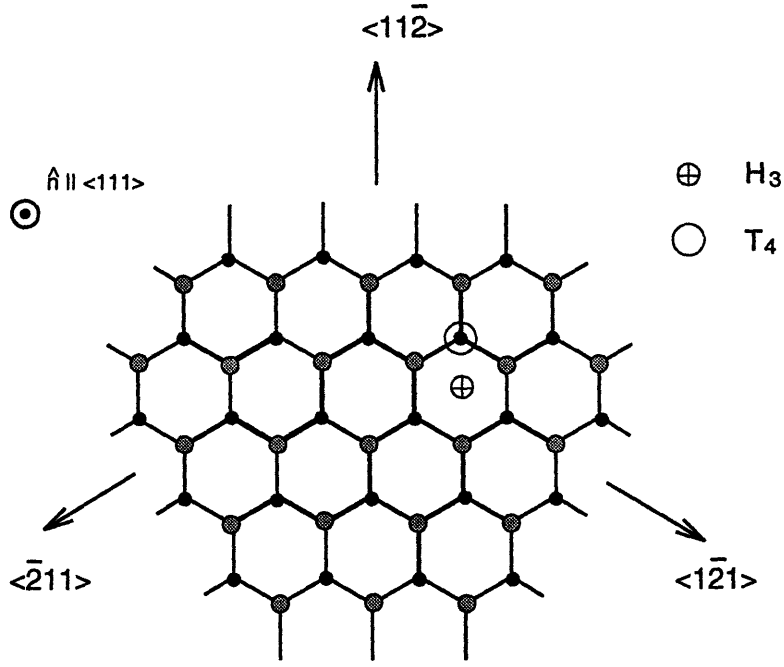

Figure 2-1: Surface structure of the ideally terminated flat Si(111) surface showing the two uppermost sub-lattices. The <111> surface normal is marked by the vector pointing out of the page. Three vectors indicate the $3m$ rotation symmetry of this surface.

+ steps) is also analogous to that observed in many other condensed systems (eg. in binary solutions).

It is useful to discuss the equilibrium behavior of steps by first considering the relationship between a given step distribution and the orientation of the surface. A surface with a small misorientation from a low-index facet has a *surface* free energy density of the form,

$$\phi(\alpha, T) = \phi_0(T) + \frac{\eta(T)}{h}|tan(\alpha)| + \frac{B(T)}{a_{\|}h^3}|tan(\alpha)|^3 . \tag{2.1}$$

This can be expressed in terms of the inter-step spacing $l = tan(\alpha)/h$. The surface free energy of the low-index terrace is $\phi_0(T)$. The two terms in this expression which depend on the orientation angle, α, originate from the free energy associated with the creation of a single step, and the effective entropic interaction between steps, respectively. The latter term arises because there is an energy cost for step crossings which is proportional to $k_BT/\Gamma l^3$, ie. the number density of step crossings. This expression

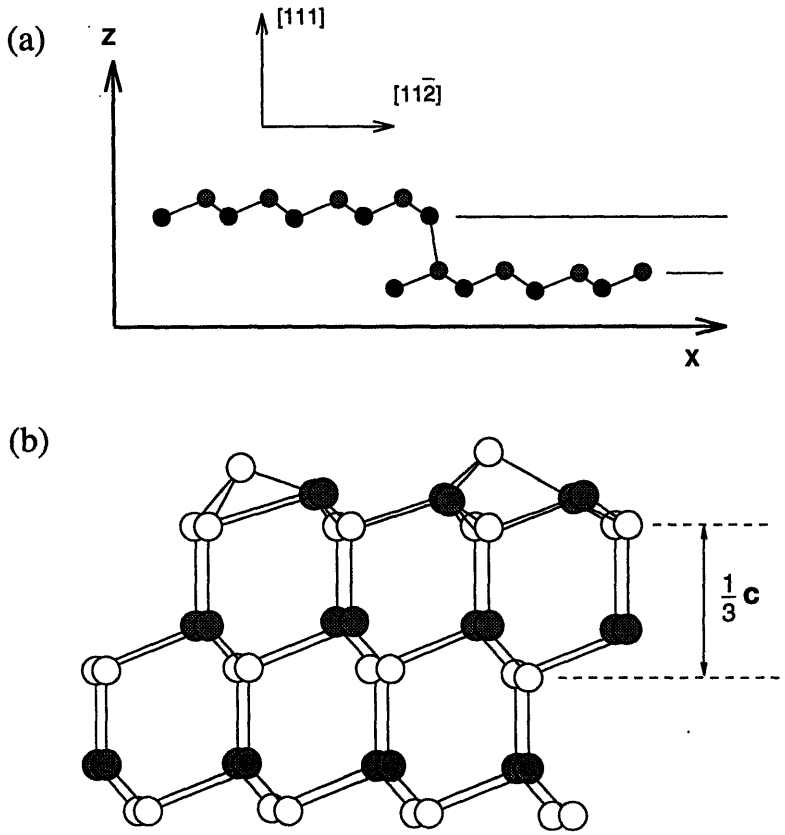

Figure 2-2: Si(111) cross-sections revealing (a) a single <11$\bar{2}$> step on the Si(111) surface showing that the stepped Si(111) surface has three sublattices, and (b) the 1×1 Si(111) surface showing the adatoms at T_4 and H_3 sites [S. Kodiyalam, et al.].

assumes that step kinks do not have overhangs, and that thermal meandering of steps is governed by fluctuations which are inversely proportional to the line tension, and directly proportional to $\sqrt{\Delta y}$, where Δy is the step length, as per the usual thermal wandering of an array of lines in two-dimensions.

It is known that an equilibrium surface phase transition occurs for Si(111) on cooling below about 1140 K at the 1×1→7×7 reconstruction transition. This phase transition, characterized by the rearrangement of the atoms in the upper bilayer, is driven by the elimination of dangling bonds at the surface which lowers the surface free-energy. It is worth noting that the symmetry change on going from a 1×1 structure to a 7×7 structure involves a discontinuous change in the symmetry of the surface and is thus strongly first-order.

The driving mechanism for a *faceting* transition at $\sim$ 1140 K on vicinal Si(111)

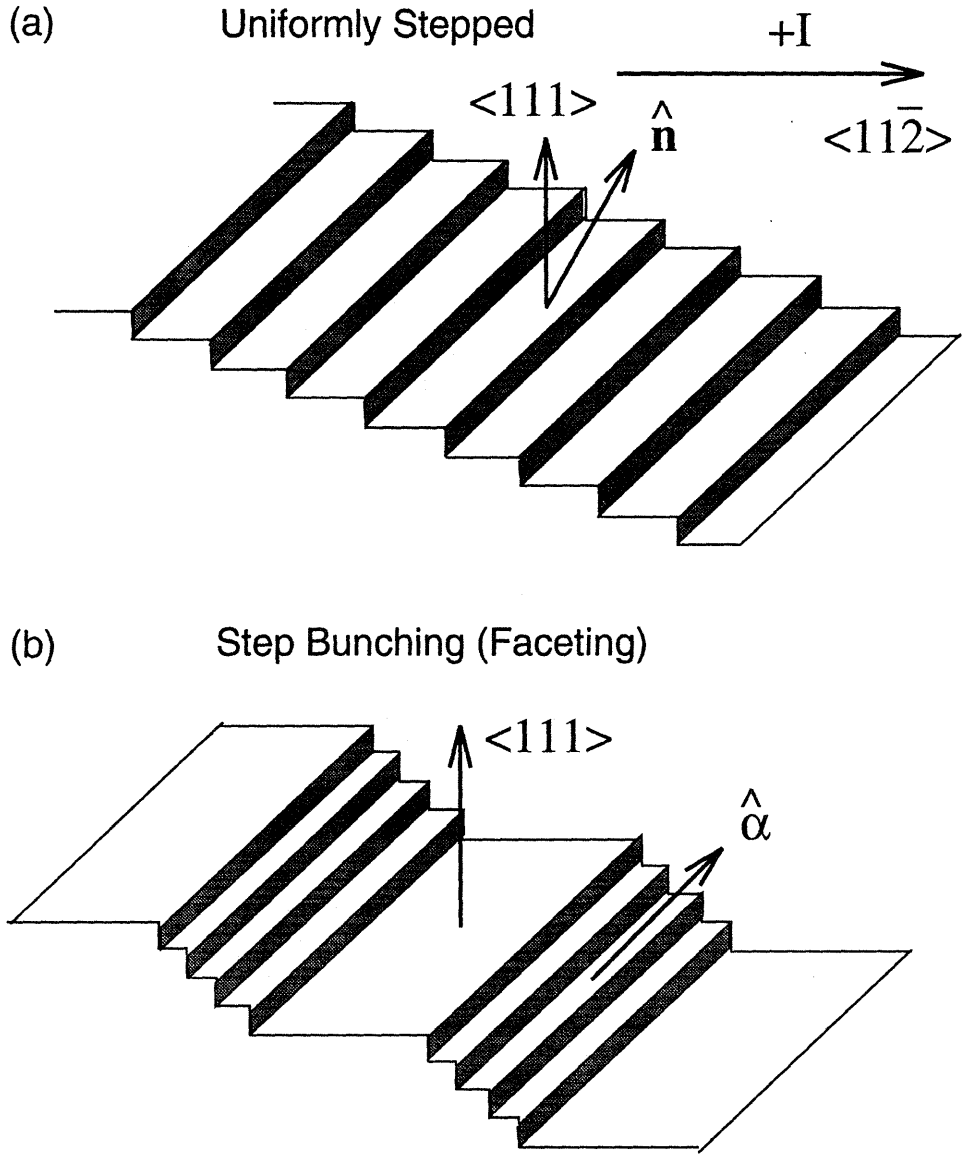

Figure 2-3: A schematic of (a) a uniformly stepped surface, and (b) a step bunched (or faceted) surface. Positive current flows in the step-down <11$\bar{2}$> direction, as indicated by the arrow in (a). A uniformly stepped Si(111) surface will have steps distributed according to the macroscopic miscut (defined by $\hat{n}$), and separated by 1×1 terraces. The angle $\hat{\alpha}$ will be a function of the step density within the bunched regions (step bands).

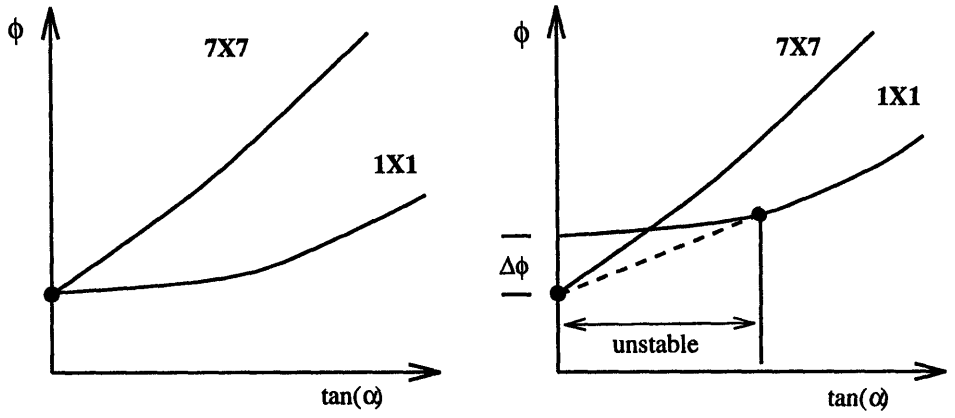

Figure 2-4: Surface free-energy density as a function of surface misorientation for the 7×7 reconstruction on Si(111).

arises due to a lowering of the surface free-energy associated with the 7×7 reconstruction compared to that associated with the 1×1 (unreconstructed) surface. Due to surface energetics, steps are forces away from the 7×7 reconstructed regions resulting in a step disordering. Hence, this surface phase transition is sometimes referred to as a *step bunching* transition, as the development of faceted regions on vicinal surfaces must be accompanied by step rearrangements or agglomeration with an increasing step density.

Figure 2-4 illustrates possible free energy curves as a function of miscut for one misorientation direction; for convenience assume this direction is along $<11\bar{2}>$. One can understand the orientational phase separation by the following thermodynamic argument (analogous to the Gibb's argument for a normal two phase system) [17]. Imagine that each surface structure is described by a distinct continuous free energy, parameterized by the surface orientation according to the free energy of Eq. 2.1. Also, assume that one of these phases (call it the low-T phase) is stable at sufficiently low temperature. At the phase transition temperature T_c, there is a two-phase coexistence defined by the intersection of these two curves, as in Fig. 2-4(a). Since these surfaces are of different symmetry and structure, the step energies and the energies required to form step kinks on these surfaces will be different. Therefore, lowering the temperature will lead to a lowering of one free energy curve relative to the other.

Figure 2-4(b) shows the result of lowering the temperature in the case that the low-T phase has the 7×7 reconstruction. One sees that a phase separation must occur below T_c with regions of two distinct orientations: flat regions ($\alpha = 0$) which are reconstructed, and stepped regions with orientation α_0 which are unreconstructed.

This phase separation can also be described in terms of step energetics. Calculations have shown that the energy of a straight step on a surface with a 7×7 symmetry is higher than that for an equivalent straight step on an unreconstructed surface [21]. Therefore, below temperatures where the 7×7 reconstruction is allowed, it is energetically favorable for this Si(111) surface to separate into regions of high and low step density; ie. the steps are pushed away from the reconstructed regions and tend to bunch onto the unreconstructed 1×1 regions of the surface. Surface *faceting* is characterized precisely by such changes in the step arrangements and this leads to dramatic changes in the morphology with temperature. Faceted Si(111) consists of large 7×7 reconstructed terraces separated by unreconstructed step bunches (or step bands). The symmetry of the surface causes the steps to move predominately in the direction of the miscut $[11\bar{2}]$, although even a uniformly stepped surface will exhibit thermal meandering of the steps. The surface morphology, dictated by the motion of steps, changes continuously on cooling below the 1×1→7×7 reconstruction transition temperature, and these changes correspond at the microscopic level to the step regions becoming more densely packed.

Electromigration

The relatively low temperatures at which the above equilibrium morphology changes occur have made these systems readily accessible to a number of experimental surface probes. Extensive studies of equilibrium faceting and step behavior have already been conducted with electron and x-ray diffraction, and with direct imaging techniques such as scanning tunneling microscopy (STM) and atomic force microscopy (AFM). Vicinal Si(111) is one of many systems exhibiting a rich assortment of morphological changes which depend not only on the temperature, but also on the manner by which the sample is heated. Specifically, an elaborate array of surface structures are known to

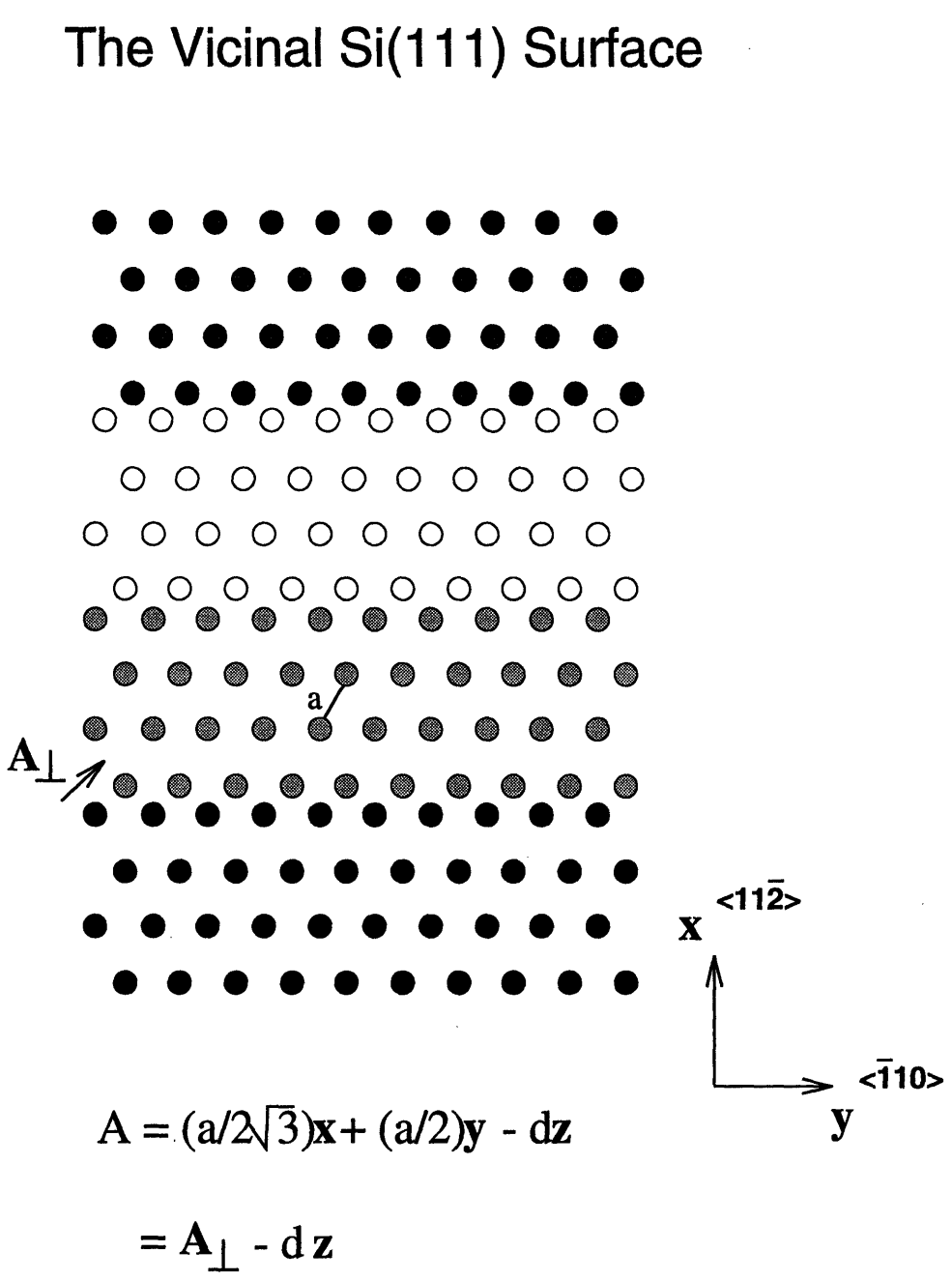

Figure 2-5: Schematic drawing of the uppermost layer of a vicinal Si(111) surface revealing (11$\bar{2}$) steps

appear simply by flowing a direct current through the sample in a particular direction relative to the step flow. The first studies of these high temperature structural changes on Si(111) and Si(001) [3, 7, 4] provided evidence that this apparently non-equilibrium phenomenon was due to *electromigration* processes.

Electromigration is the motion of atoms through a solid due to an externally applied electric field. One of the first observations of this effect was made by Haeffner in 1953 who used a constant current to separate isotopes of mercury ions in solution [24]. Such atomic motion can also occur at the metal or semiconductor interfaces and surfaces in electronic devices (which operate in the presence of electric fields) and thus is of obvious technological importance. The experiments in this thesis focus exclusively on the electromigration-induced morphology changes occurring at the surface of vicinally polished, clean single crystals of Si(111). Electromigration arises since the samples are heated resistively with a D.C. current flowing through the bulk. The resultant *static* electric field at the surface acts as the driving force for surface ordering. Preliminary work on quenched samples revealed that these semiconductor surfaces possess a particularly elegant manifestation of electromigration yielding a complex variety of faceted surface morphologies which are essentially reversible, both thermodynamically and on changing the direction of current flow through the crystal.

A Current direction versus Temperature phase diagram for Si(111) vicinally cut toward $<11\bar{2}>$ is shown in Fig. 2-6. These surface phases can be described as follows. Below the 7×7–1×1 reconstruction transition, one observes a surface phase separation independent of current direction. This two-phase region consists of large 7×7 terraces separated by step bands. The flat terraces have a surface normal ($\hat{n}$) along (111) while the bunched step regions have a local surface normal which is larger than the macroscopic miscut. In equilibrium, the relative size of the flat regions compared with the step regions is then determined by the macroscopic miscut. This is illustrated in the schematic of fig. 2-3(b). In this diagram, positive current (+I) is defined as current flowing toward $<11\bar{2}>$, ie. in the direction of step flow. The positive current direction is sometimes referred to as the step-down direction. The crystallographic direction transverse to the miscut is the $<\bar{1}10>$ direction. Experimentally it was

found that the phase separation at positive current is accompanied by a transverse instability due to a meandering of the steps within the step bands [23]. The small dependence of the reconstruction transition temperature on sample miscut is not represented in this phase diagram.

Above the reconstruction transition temperature at T$\sim$ 1140 K and at negative current ($-$I in the diagram) there is a transition to a single-phase uniformly stepped region which persists up to T$\sim$ 1370 K. This single-phase surface has steps separated by disordered 1$\times$1 terraces, typically a few hundred angstroms across. Therefore, the integer order peak at (1,0) will not be present when scattering x-rays from the single-phase stepped surface structure. At positive current between these same temperatures the steady-state surface structure consists of unreconstructed 1$\times$1 facets, also with a transverse step meandering. The phase behavior on reversing the current direction in this temperature regime is driven by electromigration. Note, these low temperature phases exhibit very slow dynamics and are not part of the major thrust of this thesis.

Above T$\sim$ 1370 K and at negative current the steps tend to bunch into disordered stepped bands, allowing the slow formation of large 1$\times$1 facets. At this same temperature and positive current these step bunches slowly reorganize as the facets decrease in extent, the eventual surface structure consists predominately of distributed steps with a large transverse step meadering. The transverse step modes will ultimately lead to a dramatic transverse modulation of the order of several microns depending on the size of the miscut. Heating through this faceted regime at negative current one will encounter a transition at T$\sim$ 1525 K. In this case the steps redistribute themselves uniformly and with no significant transverse wandering. At positive current above T$\sim$ 1525 K the surface develops facets with disordered step bands, although the excessive sublimation rates at these temperatures will prohibit well-ordered facets after long times. This electromigration- or current-driven faceting shares many of the same characteristics with the reconstruction-driven faceting, however, it is obviously governed by fundamentally different physics which can lead to dramatic dynamical changes.

In the simplest microscopic picture, the phenomenon of electromigration of atoms

on the surface of a metal or a semiconductor involves a competition between the direct force on the adatoms due to the electric field, and the force due to the scattering of electrons with the adatoms. The *wind force* due to electron scattering is always in the direction opposite to the electric field while the direction of the *direct force* on an adatom will depend on its effective valence; the effective valence can take either sign depending on which interaction is dominant. An effective valence of positive sign occurs when the direct force is dominant, a negative valence Of course, the competition between the wind force and the direct force will have a varying degree of importance depending on the local electronic and thermal environment. For example, a surface pre-melting can lead to an enhanced electron density at the surface which will increase the effect of the wind force on the adatoms.

Ultra-high vacuum (UHV) surface x-ray diffraction experiments were conducted to study the effect a direct current has on the arrangement of steps at a Si(111) crystal surface miscut toward $<11\bar{2}>$ by up to 8°. These studies revealed spectacular dynamical changes in the surface morphology which are reversible and can be controlled by the direction of current flow through the crystal. The current direction- and time-dependent morphology changes in question were found to result from an intricate set of competing interactions, electromigration being a central component, and actually occur at sublimating temperatures. Moreover, the time-scales involved in many of these surface transformations are readily accessible in the x-ray diffraction experiments. The surface morphology changes which characterize this dynamical phenomenon occur on mesoscopic length-scales and exhibit time-dependence which is ascertained directly from the surface diffraction experiments. *Ex-situ* atomic force microscopy experiments were also conducted on quenched samples following each experiment to compliment the x-ray studies. Direct imaging proved useful in determining large-scale structure which in some cases occurred at distance scales exceeding the resolution of the x-ray experiments.

Surface Morphologies as a Function of Temperature and Current Direction

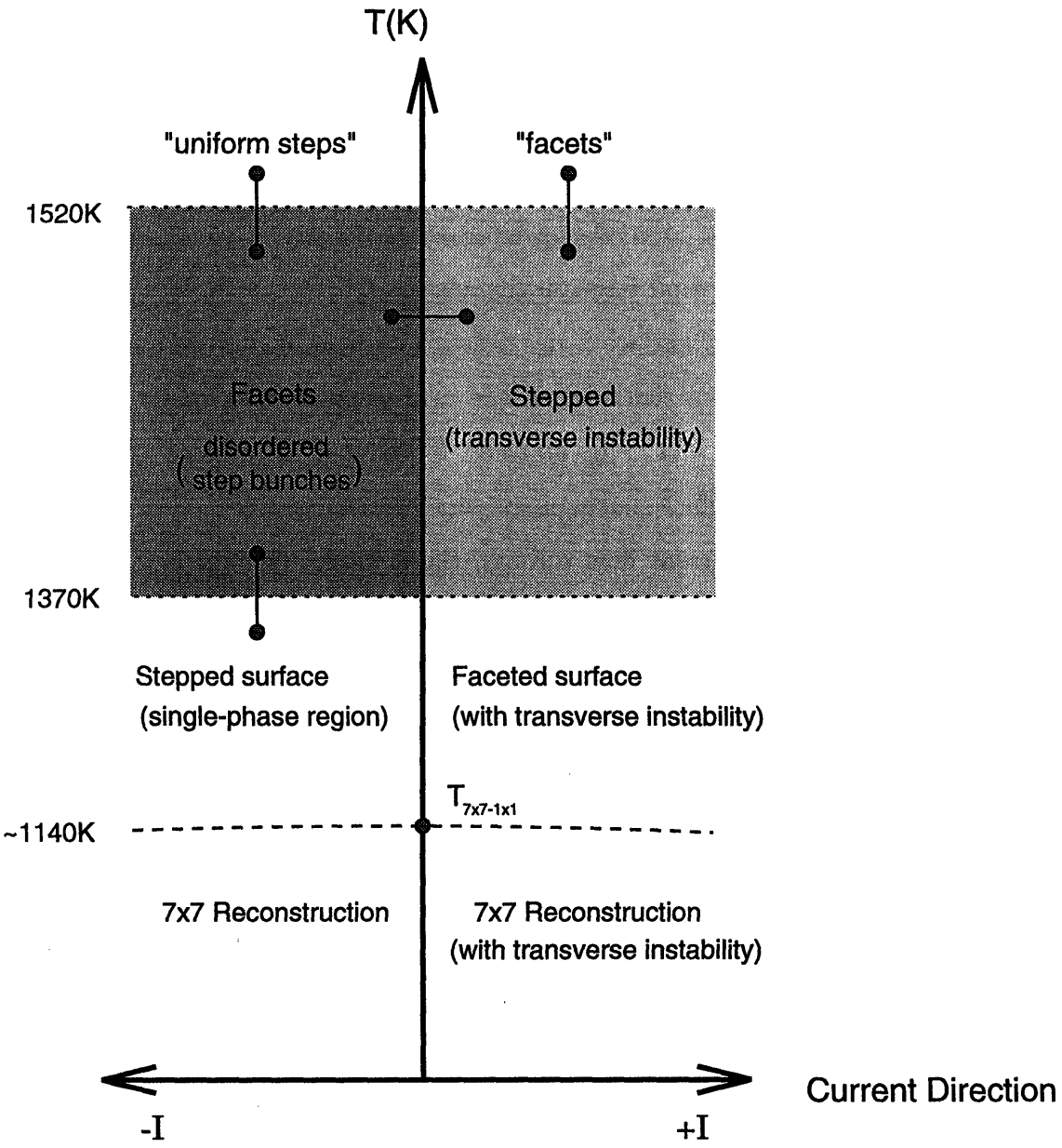

Figure 2-6: Current-direction vs. Temperature phase diagram for vicinal Si(111) miscut toward [11$\bar{2}$] indicating some of the regimes where electromigration-driven surface morphologies exist, and the region where reconstruction-driven step bunching is observed. The dashed line indicates the $T_{7\times7-1\times1}$ reconstruction temperature which is weakly dependent on the magnitude of the miscut. Bars indicate regions studies with x-ray diffraction.

Comment

The phase transition concepts discussed above apply only to those systems which are either at equilibrium or in some meta-stable state. The electromigration-driven surface structural changes occur under non-equilibrium conditions, and thus the classical thermodynamic formalism [17] is most likely inappropriate for describing these types of phase transformations. Moreover, the order–disorder phenomena covered in this chapter involve the sublimation of atoms from the surface and the diffusion of adatoms under the action of an applied electric field, greatly complicating theoretical analysis.

A variety of models have been proposed to approximate the behavior of steps and the subsequent morphological transformations that are governed by the step dynamics [30, 31]. In the final section of this chapter, some theoretical approaches to understanding the static (or steady-state) behavior of steps on the vicinal Si(111) are addressed. A phenomenological model is examined which treats the interaction of adatoms with a smoothly varying continuous step density, electromigration being introduced as a static driving force via the applied electric field. This continuum model provides a qualitative description of the step behavior by way of a non-linear diffusion equation. A comparison of the results of this continuum theory to the experimental results on quenched Si(111) samples is presented. In addition, a discussion is made of a microscopic theory [8] which makes a local density functional approximation in order to calculate the effect an applied electric field has on adatoms for the Si(111) surface. In particular, this model provides an explanation of the bias in adatom diffusion due to the applied field, and reveals a crossover at two temperatures on heating *above* the 7×7–1×1 reconstruction temperature each one marking a change in the surface kinetics. These temperatures are identified with the faceting transition temperatures observed in experiment.

2.2 Current-Driven Step Behavior on Si(111)

The remainder of this chapter will address current-driven (ie. electromigration-driven) phenomena on vicinal Si(111). X-ray diffraction and direct imaging studies of Si(111) samples miscut up to 8° are presented below. These include ex-situ microscopy studies on quenched samples conducted after each x-ray experiment in addition to ex-situ studies conducted independent from the x-ray experiments. A discussion of recent theoretical models will be given in Sec. 2.3 and compared with the results from the surface x-ray diffraction and microscopy experiments on Si(111) vicinally cut toward the $[11\bar{2}]$ direction.

2.2.1 Surface X-ray Diffraction Studies

Results are presented from synchrotron x-ray diffraction studies of n-type (phosphorus doped) silicon wafers miscut from the (111) high-symmetry direction toward $[11\bar{2}]$ by 8°. These samples had miscut errors of $\pm 0.25°$ in the direction of $[11\bar{2}]$ and had azimuthal errors of less than 0.5°. The x-ray experiment employed a five-circle diffractometer, shown in fig. 2-7, coupled via rotating teflon seals to an ion-pumped UHV chamber with typical base pressures of $1.5 - 4.0 \times 10^{-10}$ torr [15]. The samples were resistively heated by passing a direct current through the bulk of the crystal. This was achieved with electrical contacts made from layers of thin silicon wafers sandwiched between flexible molybdenum foil clips which were electrically isolated from the molybdenum and stainless steel sample mount. A 2 kW DC power supply could provide up to 14 Amps direct current to the sample (at $\sim$10 V). The sample temperature was then controlled by adjusting the current. The resistivity of the silicon wafers are on the order of 1Ω at 1000 K. The temperature of the sample was monitored with an optical pyrometer which was focused to a spot diameter of approximately 3mm at the sample center. All of the optical pyrometer temperature measurements were corrected for the emissivity of silicon. The relative temperature measurement and control stability has an estimated precision of 1 K and an accuracy in the absolute temperature determination of 40 K calibrated against the temperature

dependence of the bulk lattice constants.

The x-ray experiments were performed on the X20A and X20C bending magnet beamlines at the National Synchrotron Light Source (NSLS) and Brookhaven National Laboratory. At both beamlines the synchrotron "white" beam was focused with a grazing incidence mirror and then monochromated with double bounce Si(111) monochromator crystals. The resultant monochromatic x-rays had a wavelength of 1.54Å. The size of the beam incident on the sample was set by horizontal and vertical slits, the former of which define the broad out-of-plane resolution. The in-plane resolution profile is determined by the convolution of the incoming and outgoing beam divergences and the Darwin widths of the monochromator crystals, with an additional contribution due to the focusing of the grazing-incidence mirror. A vertical scattering geometry was used to exploit the naturally high-resolution of the synchrotron radiation.

A *cubic* coordinate system was chosen such that the bulk forbidden surface peak at $<\frac{2}{3}\frac{2}{3}\frac{4}{3}>$ was centered at (1,0,L). In surface diffraction, the scattering varies only slowly with the out-of-plane coordinate L. Thus, one typically refers to surface peaks in units (H,K) where a small L is chosen depending on the grazing incidence scattering geometry. Figure 2-8 illustrates a typical grazing-incidence scattering configuration but with the sample rotated into the horizontal plane for clarity. The incoming and outgoing wavevectors $\mathbf{k}_i$ and $\mathbf{k}_f$ are shown with their corresponding incident and exit angles, α and β, respectively. In this scattering geometry, the momentum transfer has a small component $\mathbf{q}_z$ perpendicular to the plane and an in-plane longitudinal component $\mathbf{q}_{\|}$; the relative magnitudes of these vectors are exaggerated in the figure. The vector **I** indicates the direction of current flow through the sample, which is chosen to be along $<11\bar{2}>$ in this experiment.

At the (1,0) surface peak in this experiment, the incident x-rays made an angle of 0.27° with the sample surface. The reciprocal lattice for a uniformly stepped vicinal Si(111) surface is shown in fig. 2-9 showing the crystal truncation rods (CTR's) passing through bulk peaks. This figure is based on the calculations of Appendix A. The arrow in the figure indicates the in-plane location of the (1,0) surface peak. Scatter-

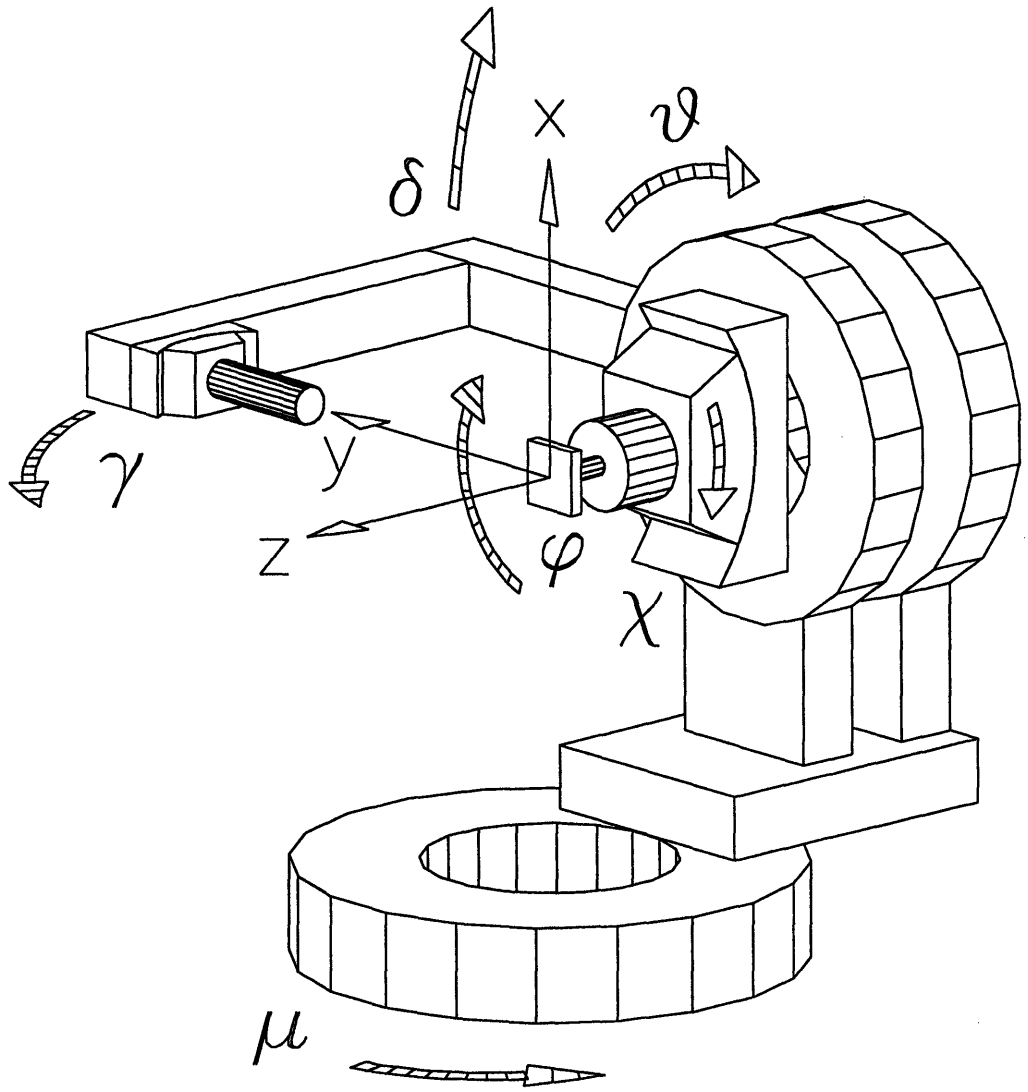

Figure 2-7: Diagram of spectrometer configuration for a 6-circle diffractometer [15]. The surface diffraction experiments for this thesis were conducted using a four-circle mode by fixing μ and γ. The remaining rotational degrees of freedom (δ, θ, ϕ, andχ) are indicated by the arrows. [Figure courtesy of Dr. D. Abernathy].

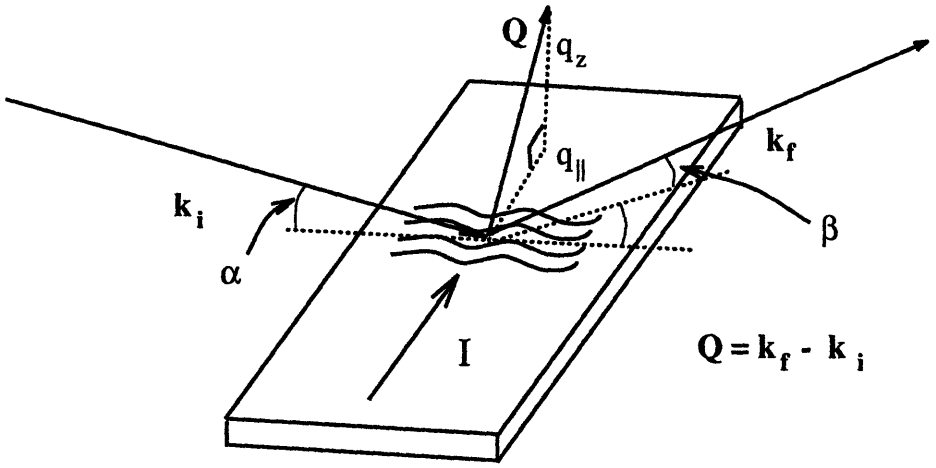

Figure 2-8: Grazing Incidence Diffraction Geometry. The momentum transfer to the sample, $\mathbf{Q}=\mathbf{k}_f-\mathbf{k}_i$, has components parallel ($q_{\|}$) and perpendicular (q_z) to the sample surface. α and β are the incident and exit angles measured with respect to the plane of the sample. A heating current I flows through the sample in the direction $<11\bar{2}>$ (this is indicated by an arrow in the sample plane).

ing from the flat unreconstructed Si(111) surface, or equivalently flat (111) terrace regions, will by centered precisely at (1,0,L). Coexistence of stepped regions with flat (111) terraces will lead to scattering at both the integer order (1,0) position and at incommensurate positions, (1-h,0), depending on the step density. The symmetry of the 7×7 reconstructed surface is readily observed from CTR's passing through ($\frac{m}{7}$,0), for integer m. The ($\frac{6}{7}$,0) peak can be seen in Fig. 2-10 and vanishes at about 874°C (1147 K) which marks the 1×1→7×7 reconstruction transition temperature.

The instrumental resolution function was constructed from $Q_{\|}$ (longitudinal), θ (transverse) and δ scans through the bulk $<22\bar{4}>$ peak. Since the cross-section of the ellipse was almost perfectly Gaussian in both longitudinal and transverse directions, the resolution scans were simultaneously fit to a two-dimensional Gaussian ellipse with a fixed major axis angle of 43.62° with respect to the longitudinal direction $<11\bar{2}>$. The final resolution shape was then calculated for the (1,0) peak using the relations stated in the Appendix. The resolution approximation yielded results consistent with an independent estimation of the resolution widths which were extracted from fitting the sharpest (1,0) peak measured in the 7×7–1×1 phase to a two-dimensional Gaussian shape. Facet widths in the two-phase region typically

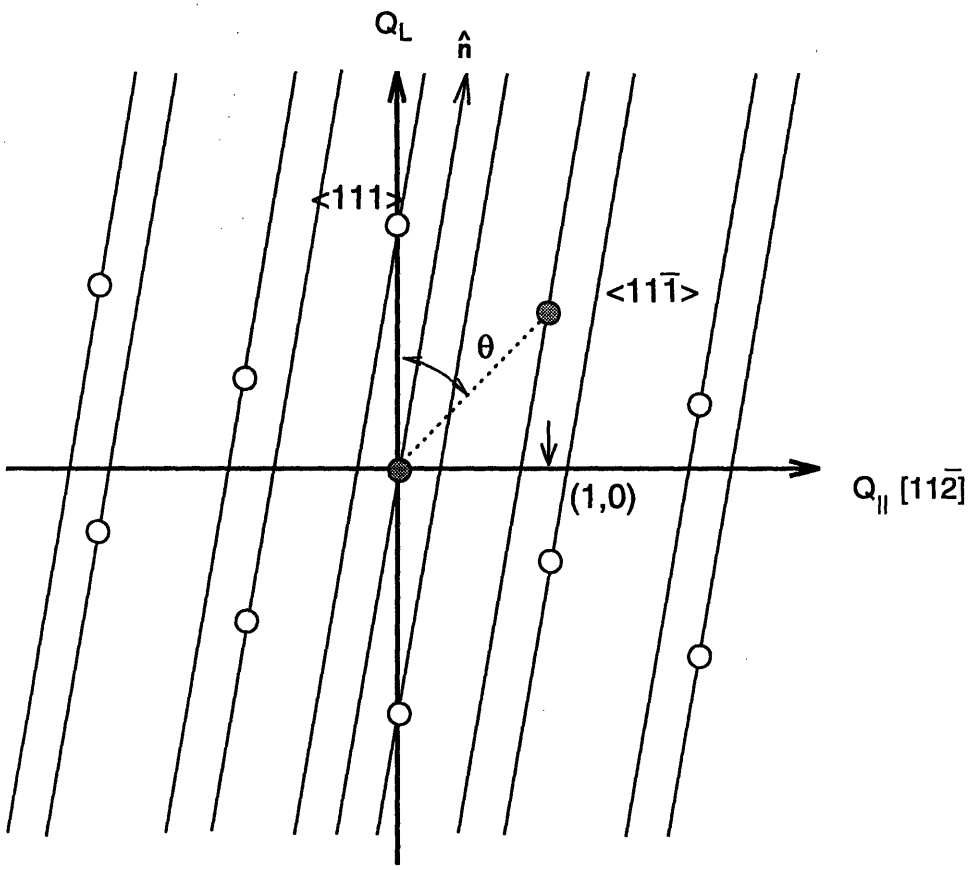

Figure 2-9: Reciprocal lattice for a vicinal surface revealing tilted truncation rods (CTR's). Scattering originating from the CTR passing through the bulk peak $(1,1,\bar{1})$ was studied in this experiment (Note: The angle θ between $(11\bar{1})$ and (111) is actually 19.47°. The scale is exaggerated here for clarity. The arrow indicates the location of the integer order in-plane (L=0) surface peak expressed in the cubic coordinates $(1,0)$. Only CTR's originating from bulk peaks close to the origin are shown.

exceeded 0.5μ longitudinally and 2μ transversely. The elongated shape of the resolution ellipse introduced systematically high scattering in the tails of the sharpest scattering peaks measured in the course of the experiment. This effect leads to the slight deviations occurring in the fits to the nearly resolution limited data. This had a negligible effect on the scattering at the step peak position due to its substantially broader width.

The final calculated resolution used in studying the (1,0) surface peak for the 8° miscut samples was well-approximated by a Gaussian ellipse with a major axis tilted by 14.89° away from the $<11\bar{2}>$ direction. The major axis had a width of 0.007 $\AA^{-1}$ Gaussian half-width half-maximum (HWHM), while the minor axis had a width of roughly $2.2 \times 10^{-4}\AA^{-1}$ HWHM. For the scattering geometry chosen, the resolution was 8.9×10^{-4} $\AA^{-1}$ HWHM along $<11\bar{2}>$ ($Q_{\|}$) and 2.4×10^{-4} $\AA^{-1}$ HWHM in the transverse ($Q_{\perp}$) direction. These correspond to the longitudinal and transverse resolutions, respectively. A broad out-of-plane resolution was chosen by opening the horizontal slits in front of the detector, thus integrating over the crystal truncation rod (CTR). This is optimal for in-plane surface diffraction since the weak signal is slowly varying along the CTR.

Sample Preparation

The miscut Si(111) samples used in the ultra-high vacuum (UHV) x-ray diffraction experiments were 0.016" wafers, polished on both sides and cut with either a diamond scribe or a diamond wheel saw to dimensions roughly 0.3"×1.25". The cutting process cannot be performed in a clean-room, therefore extensive cleaning is necessary to remove impurities prior to mounting the sample in the UHV chamber. Through trial and error it was found that standard RCA-cleaning followed by several cycles of washes, first with trichloroethylene, then acetone and methanol, were satisfactory in achieving adequate cleanliness for the UHV experiments. This cleaning process is performed in atmosphere resulting in a native oxide on the sample surface. However, this oxide is a benign impurity which, in fact, serves to protect the surface from reactive contaminates which might come into contact with the sample before transferring

it to the UHV chamber. Moreover, it is known that with sufficient care, heating Si wafers under UHV conditions to high-temperatures can be extremely effective for removing impurities (including carbon) from the surface [43]. This flash-cleaning (or rapid thermal annealing) procedure involves rapidly heating the sample to 1530 K and annealing for approximately 1 minute, and then cooling the sample to between 1150 K and 1175 K where it is annealed for 30–60 minutes. The flash-cleaning temperature at 1530 K was chosen for convenience since it is slightly higher than the highest reported faceting transition at negative current. During the course of the experiment the sample went through several flash-cleaning cycles. The Si(111) sample was determined to be satisfactorily cleaned when it yielded a well-ordered 7×7 reconstructed phase and subsequently showed well-behaved changes in step density below the 7×7–1×1 transition. (see figure 2-10). It has been previously demonstrated that impurity pinning of steps has a clear signature in the broadening of the x-ray scattering profile at the step peak and in the anomalous temperature dependence of the longitudinal step peak position [23]. This will be discussed below in more detail.

Preliminary Studies

Immediately after the cleaning process, the samples were transferred in atmosphere to the vacuum chamber which was then pumped down to 1×10^{-7} torr by a turbo-molecular pump and an ion-pump. The vacuum system was then baked for 12–18 hours. After reaching UHV conditions the sample underwent a preliminary flash-cleaning cycle. This cleaning technique was employed at the start of each experiment. [Note: The terms flashing, flash-cleaning, and flash-heating will be used interchangeably in this section. Flashing at negative current above 1525 K is also routinely employed to induce unfaceting, ie. step *debunching*, which will be described in detail later]. During the initial flash-cleaning, the pressure in the UHV chamber typically rose to about 2×10^{-8} torr, due to out-gassing from the molybdenum and stainless steel sample mount, and finally recovered to a steady-state pressure of $0.4 - 2 \times 10^{-9}$ torr depending on the annealing temperature. Subsequent *flashing* usually resulted in pressures stabilizing at $\sim 2 \times 10^{-9}$ torr at the final annealing temperature. This

cleaning procedure was repeated several times throughout the course of the experiment.

Prior to studying the high-temperature step behavior, the cleanliness of the surface had to be established. Based on previous studies and reports from other experiments on these systems [13, 19, 20], it is believe that the surface cleanliness can be inferred from the shape of the step peak in the single-phase region *and* the existence of a well-defined 7×7–1×1 reconstructed surface (with reversible changes in the step density on cycling in temperature through the two-phase region). Further evidence for the absence of significant impurity concentrations was found by examining the well-ordered step phase which persists up to temperatures well-above the 7×7–1×1 reconstruction transition (as shown in Fig. 2-11). As outlined in the results section, it is concluded that step pinning due to surface impurities was insignificant during all of the measurements in both the low- and high-temperature regions of the phase diagram. It is important to note that the high-temperature data were taken only after a successful preliminary study of the 7×7–1×1 reconstruction region was conducted. This precluded a rapid completion of the studies of the high-temperature phases. However, no adverse effects on the *reversible* surface morphology changes resulted from this, despite the long time-periods (ie. several days) involved in each experiment.

Maintaining these thin silicon samples at high-temperatures (on the order of 1500 K) for excessive time periods can actually lead to a macroscopic change in the thickness of the wafer, sometimes producing temperature gradients across the full length of the sample as large as 50 K. Hence, the high-temperature measurements were performed by carefully taking this time limitation into account. There is substantial heat loss at the sample contacts, resulting in an approximately linear gradient across the illuminated area of the sample which was estimated to be about 2 K for a sample temperature of 1200 K, and 1 K up to a sample temperature of 1480 K. The complications due to these small gradients were included systematically in the data analysis.

Low-Temperature Surface Behavior

The x-ray scattering study of the 7×7–1×1 reconstruction began with a sample miscut by 8° toward <11$\bar{2}$> which was flash-cleaned at negative current to 1524 K for 50 seconds. The initial surface state was determined after quenching to the single-phase region at 1147 K and annealing for 30 minutes. This yielded a stepped surface with a longitudinal step-step correlation length ($\xi_{\|}$) of 1100$\mathring{A}$ and a transverse step-step correlation length ($\xi_{\perp}$) of 4900$\mathring{A}$ determined from the half-widths at half-maximum of the fits of the scattering to a two-dimensional Gaussian convoluted with the Gaussian resolution function. The sample was then cooled to 1083 K (approximately 60 K below the reconstruction transition temperature $T_{7\times7-1\times1}$) where a cooling study of the two-phase region ensued. Figure 2-10 shows the scattering distribution on cooling through this two-phase region down to 961 K ($\sim$ 186 K below $T_{7\times7-1\times1}$) indicating a smoothly varying change in the position of the step peak as the step density increases, accompanied by a broadening in the peak width. At 961 K $\xi_{\|}$ is 135$\mathring{A}$; roughly a factor of 3 smaller than in the single-phase region. The local orientation (α) which the stepped regions make with respect to the (111) terraces can be inferred from the longitudinal separation of the step peak and (1,0) peak. This can be understood from the reciprocal lattice diagram of Figure 2-9.

The x-ray data in Fig. 2-10 were taken while heating this sample through the 7×7 reconstruction phase up to just above the 7×7–1×1 transition temperature which was estimated to occur at approximately 1147 K. Just below this transition temperature, at 1140 K, the (1,0) facet peak had a nearly resolution limited longitudinal width of $5.7 \times 10^{-4}\mathring{A}^{-1}$ (Gaussian HWHM) and a resolution limited transverse width; these correspond to facet sizes extending roughly 5500$\mathring{A}$ longitudinally and exceeding 2μ transversely. At this temperature the step peak was quite broad, having a a longitudinal correlation length $\xi_{\|}$ of 150$\mathring{A}$, and a transverse correlation length $\xi_{\perp}$ of 920$\mathring{A}$. Note the seven-fold decrease in the transverse step-step correlation length and the five-fold decrease in the longitudinal length compared with the lengths measured (after the initial flash) in the uniformly stepped phase which is only 7 K higher in temperature.

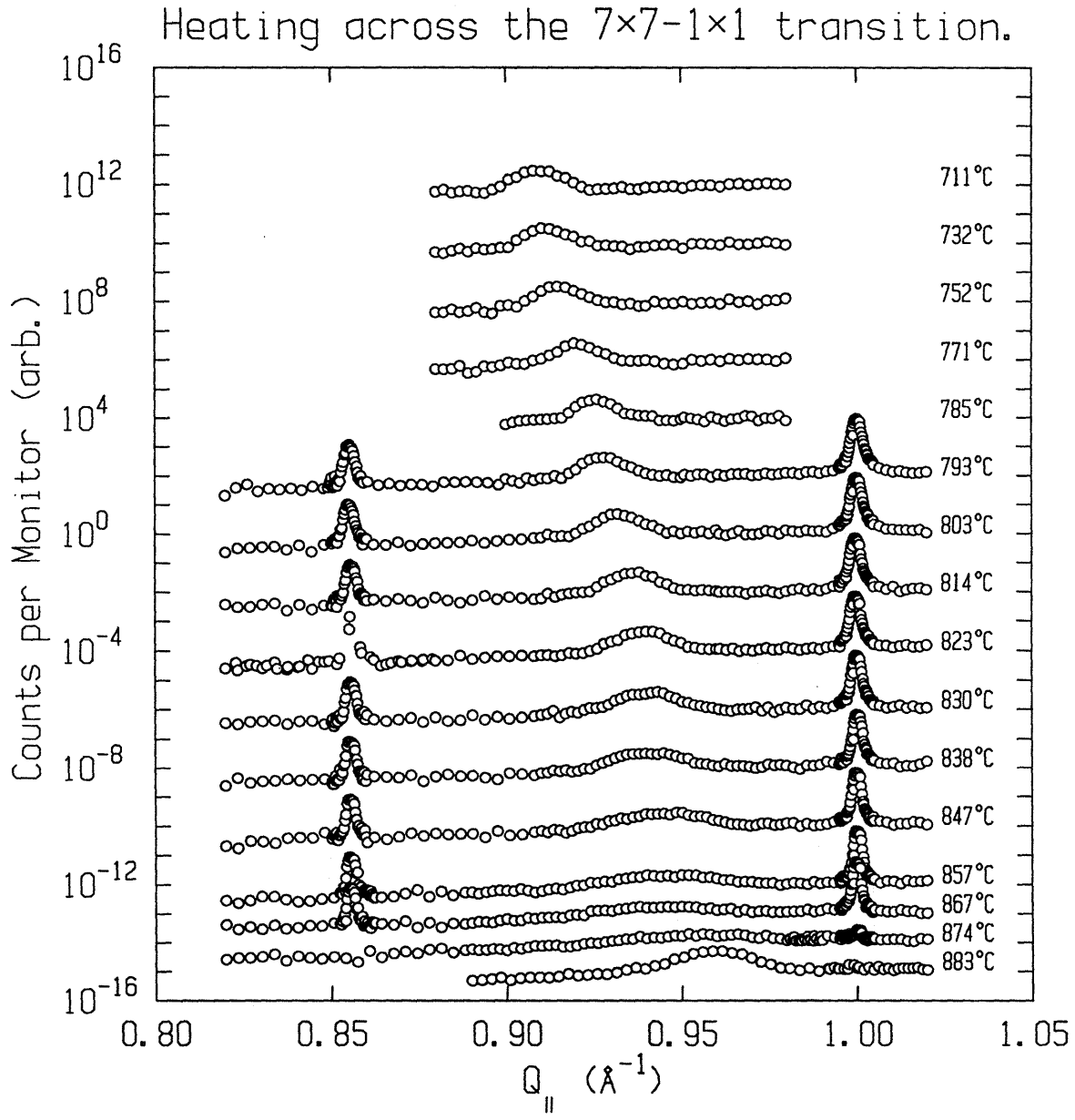

Figure 2-10: Heating across the 7×7-1×1 reconstruction transition (T_c = 874°) at negative current.

The loss of 7×7 order on crossing the 7×7–1×1 reconstruction transition is marked by the disappearance of both (1,0) and non-integer order (6/7,0) peaks indicated in Fig. 2-10. The resulting uniformly stepped surface morphology as measured at 1156 K is characterized by a step peak having a longitudinal correlation length ($\xi_{||}$) of approximately 280$\mathring{A}$, which is small compared to the width of the step peak in this phase prior to cycling through the reconstruction region. This broadening of the step peak is consistent with earlier observations [26, 18] which revealed that slow kinetics, which can broaden the step peak, occur at temperatures lying within the meta-stable region separating the spinodal T_s from $T_{7\times7-1\times1}$. This difference between T_s and $T_{7\times7-1\times1}$ is approximately 2 K for a Si(111) sample miscut by 8° toward <11$\bar{2}$> as determined from STM imaging experiments [26]. The details of the meta-stable region of the phase diagram will not be discussed in this work as extensive studies by our group and others [28, 23] have already been presented.

In order to test the hypothesis that the step peak broadening is not induced by impurity pinning, the 7×7–1×1 transition study was repeated on this sample using the same systematic procedure described above. This sample was flash-cleaned again for 1 minute at 1525 K before quenching to 1147 K (just above the 7×7–1×1 transition temperature) where it was then annealed for about 30 minutes. The step-step correlation lengths at 1147 K (after annealing) were 1040$\mathring{A}$ longitudinally and 4300$\mathring{A}$ transversely. Thus, the peak widths and peak amplitudes were comparable to those measured at the beginning of this study. The total integrated intensity of the step peak was actually 18% larger than that in the previous measurements at 1147 K, indicating that step ordering occurred over a larger area of the sample. A study of both the (1,0) and step peaks was conducted on cooling through the two-phase region immediately following the anneal. The step-step correlation lengths were observed to broaden longitudinally from $\xi_{||} = 350\mathring{A}$ at 1095 K, to $\xi_{||} = 450\mathring{A}$ at 1063 K. Throughout this cooling run the transverse widths ($\xi_{\perp}$) remained at an essentially constant value of 2450$\mathring{A}$. The (1,0) facet peak widths yielded terrace sizes of approximately 3200$\mathring{A}$ longitudinally and 12000$\mathring{A}$ transversely at 1095 K, and 4300$\mathring{A}$ longitudinally and 17000$\mathring{A}$ transversely at 1063 K. Further measurements of

the step peak widths were made at 1150 K (ie. above $T_{7\times7-1\times1}$) which revealed step-step correlations in agreement with the values measured in the previous run. These widths did not exhibit any detectable dependence on the direction of the current flow through the sample with respect to the $<11\bar{2}>$ direction. The reproducibility in the step behavior observed from these data provides strong evidence that impurities played a negligible role in these surface morphology changes.

High-Temperature Studies

Following the low temperature study of the 7×7–1×1 reconstruction region, this sample was heated through the single-phase (stepped) region at negative current up to $\sim$ 1380 K where the surface morphology becomes unstable with respect to step bunching. Data showing the vanishing of the single-phase region for an 8° miscut Si(111) sample are presented in Figs. 2-11 and 2-12 indicating a transition at $\sim$ 1376 K which is fairly sharp in temperature.

The Single-phase Stepped Surface

Consider an array of steps with coordinates x and y normal and parallel to the steps, respectively, with their corresponding short-range correlation lengths ξ_x and ξ_y. Within a uniformly stepped surface phase in thermal equilibrium, step-step interactions result in an algebraically decaying correlation function. The correlation function is given by

$$C_{\mathbf{Q}-\mathbf{G}}(\rho_{\|}) \approx \left\{\left(\frac{x}{\xi_x}\right)^2 + \left(\frac{y}{\xi_y}\right)^2\right\}^{-\frac{\eta(\mathbf{Q}-\mathbf{G})}{2}} , \tag{2.2}$$

where

$$\eta_{(\mathbf{Q}-\mathbf{G})} = \frac{k_B T[(\mathbf{Q}-\mathbf{G})\cdot\hat{\mathbf{n}}]^2 \sin^2\alpha}{2\pi\sqrt{K_x K_y}} , \tag{2.3}$$

and K_x and K_y are the elastic constants along x and y step directions and α is the miscut angle. Surface x-ray diffraction from a uniformly stepped surface at thermal equilibrium can be described by the following two-dimensional structure factor [12]:

$$S(\mathbf{q}) = \frac{I_0(\eta_\mathbf{q})}{(q_x^2\xi_x^2 + q_y^2\xi_y^2)^{\frac{(2-\eta_\mathbf{q})}{2}}} \ , \tag{2.4}$$

where

$$\eta_\mathbf{q} = \frac{k_B T[(\mathbf{Q}-\mathbf{G})\cdot\hat{\mathbf{n}}]^2 l^2 \sin^2\alpha}{2\pi^2\sqrt{k_B^2T^2 + C_0}} \ . \tag{2.5}$$

In writing Eq. 2.5, a free energy density of the form in Eq. 2.1 was assumed. Thus, the elastic constants are $K_x \sim \Gamma/l$, and $K_y = l^2\frac{d^2f}{dl^2} = 12k_BT/\Gamma l$, and l is the inter-step spacing. The product $(l \times \sin\alpha)^2 = h$ is simply the height change of a single step in the [111] direction. The constant C_0 allows for the possibility of temperature-independent contributions to the entropic interactions such as elastic strain and dipole-induced step-step interactions [14] and is proportional to $12\Gamma/\pi^2$. Shulz showed that in the absence of this latter term, this array of steps in two-dimensions behaves like a system of fermions in 1+1-dimensions [44]. According to the theory, when $C_0 = 0$ the temperature dependence of η drops out completely. A theoretical value of $\eta = 2/9$ is expected for the step peak closest to (1,0). The dependence on $[(\mathbf{Q}-\mathbf{G})\cdot\hat{\mathbf{n}}]^2$ in the definition of η shows that this exponent will be larger for surface step peaks associated with truncation rods originating further from the L=0 plane.

Provided kinetic effects do not significantly alter the diffusion of adatoms [18], this expression should be valid above the 7×7–1×1 reconstruction transition and, as will be clear from the following results, just below T$\sim$ 1380 K where the electromigration force drives a step bunching transition. Of course, for temperatures within the step bunched region of the phase diagram of Fig. 2-6 the structure factor should experience a marked deviation from the form in Eq. 2.4

The x-ray scattering data obtained in the single-phase stepped region at negative current showed substantial deviations from the form of Eq. 2.4. Therefore, an empirical form for the structure factor was used:

$$S(\mathbf{q}) \sim \frac{I_0(T)}{[1+\xi_x^2(q_x-q_{x0})^2+\xi_y^2 q_y^2]^{\eta_{\mathbf{q}}(T)}} \tag{2.6}$$

where $\eta_{\mathbf{q}}$ is weakly temperature dependent. Under the step flow conditions expected at these temperatures, step-step interactions result in a divergent correlation function $C(\mathbf{r})$ which can be deduced directly from the Fourier transform of the structure factor Eq. 2.6. One can therefore write,

$$\begin{aligned} C(\mathbf{r}) &\sim I_0(T)\int d\mathbf{q}\frac{e^{-i\mathbf{q}\cdot\mathbf{r}}}{(1+\xi_x^2 q_x^2+\xi_y^2 q_y^2)^{\eta}} \\ &= I_0(T)\int d^2q\frac{\exp(-iqr\cos\theta)}{[1+(\xi_x q_x)^2+(\xi_y q_y)^2]^{\eta}}\,. \end{aligned} \tag{2.7}$$

This integral can be evaluated by considering two limiting cases: $\mathbf{q} \gg 1/\xi$, and $\mathbf{q} < 1/\xi$, where ξ represents a characteristic correlation length. In the first limiting case the integral of Eq. 2.8 can be evaluated by power counting, giving $C(\mathbf{r}) \sim |\mathbf{r}|^{2(1-\eta)}$, for $\eta \neq 1$. In the second limiting case, one expects the usual exponentially decaying correlations, $C(\mathbf{r}) \sim \exp(-|\mathbf{r}|/\xi)$. Therefore, the form of the correlation function for all length-scales should be,

$$C(\mathbf{r}) \sim \frac{e^{-(x^2/\xi_x^2+y^2/\xi_y^2)^{1/2}}}{(x^2/\xi_x^2+y^2/\xi_y^2)^{2(\eta-1)}}\,. \tag{2.8}$$

In applying the power counting argument, it is assumed that the result obtained using $\xi_x = \xi_y \equiv \xi$ can be extended to the anisotropic case. Furthermore, this form for the correlation function is expected to apply only when the ratio ξ_y/ξ_x is a constant, which is a good approximation across most of the range of temperature as is shown by the data in the bottom panel of Fig. 2-14. Of course, the correlation function of Eq. 2.8 deviates from the usual pure algebraic decay of step-step correlations. This is probably associated with changes in the kinetic behavior of these steps under the

action of the applied static electric field, consistent with previously reported results on smaller miscut samples [18]. In fact, it is known that electromigration is relevant even for these lower temperature phases and will actually lead to step bunching below 1370 K (the unreconstructed region) for *positive* current [23]. However, the effect this might have on the form of the structure factor has not been calculated as yet.

The structure factor given by Eq. 2.6 was found to accurately describe all of the data for the step peak in the single-phase region below 1380 K. Best-fits of the scans at the step peak were obtained using Eq. 2.6 convoluted with the Gaussian instrumental resolution. A gradual variation of η between 1.5 and 1.8 was observed across the full range of temperatures in the single-phase region. Fits obtained by allowing η to vary were of reasonable quality, however, fairly large statistical deviations in the value η were observed resulting in poorer agreement in the tails of the peaks.

The results from these fits with η(T) fixed at its mean value of 1.75 are shown in Figs. 2-13 and 2-14. The vanishing of the step peak and the concomitant appearance of the integer order facet peak at (1,0) is the signature of the step bunching surface phase transition. This same transition has been observed independently by both diffraction and imaging techniques [3, 5, 7], but on Si(111) samples of different surface misorientations. Interestingly, the transition temperature at T$\sim$ 1376 K estimated in the present experiment agrees with results reported for other samples, indicating that the average step spacing, or equivalently the magnitude of the miscut angle, apparently does not affect the phase transition temperature. It had been argued by Stoyanov that this transition is determined by the condition that the magnitude of the *temperature-dependent* diffusion length becomes less than the average terrace width (about 100-300 Å). The fact that the miscut angle does not seem to affect this transition temperature suggests that Stoyanov's argument is not correct. This will be discussed further in Sec. 2.3 where it is argued that the mechanism proposed by Stoyanov is most likely insufficient to determine the transition at 1376 K.

One caveat should be noted: namely, a precise determination of this transition temperature was complicated by very slow dynamics which could not be readily separated from the temperature dependence of the surface structure. However, from

the faceting observed in the quenching studies which follow, it is clear that the surface phase transition must occur below 1376 K. The data shown from the heating sequence of Figs. 2-11 and 2-12 indicate an *upper bound* on the transition at 1376 K. The dynamical behavior observed at these temperatures motivated an extended series of studies in order to extract information on the time-evolution of the surface morphology, in addition to determining length-scales for the steady-state structures. It will be shown in the following sections that high-temperature faceting (and therefore step bunching) possesses characteristics which are markedly different from those observed in the low-temperature, reconstruction-driven faceting regime. The physics underlying these differences is presented in the discussion sections.

Dynamics at High-Temperature

The studies of dynamical changes in the surface morphology at high-temperatures are separated into two categories: time-dependence after quenching, and time-dependence after current reversal. In both cases the goal was to ascertain the manner by which the surface morphology evolves toward steady-state after changing one of the external thermodynamic parameters (in this case the temperature, or the direction of the applied electric field). A determination is made of the characteristic lengths describing the step-step correlations and the surface-averaged facet size, in addition to the time constants involved in transforming the surface morphology (at fixed temperature) by reversing the current direction and on quenching from high temperature. The effects of hysterisis and reversibility are also addressed.

Protocol for the Time-dependent Surface Studies

Initial measurements in the high-temperature regime (between 1375 K and 1525 K) were conducted at the (1,0) facet peak to determine the time and temperature dependence of both the scattering intensity (at fixed momentum transfer) and the peak position. The first set of x-ray data were taken by simply counting the scattered intensity at the (1,0) peak position to measure the rate of decay of the peak signal.

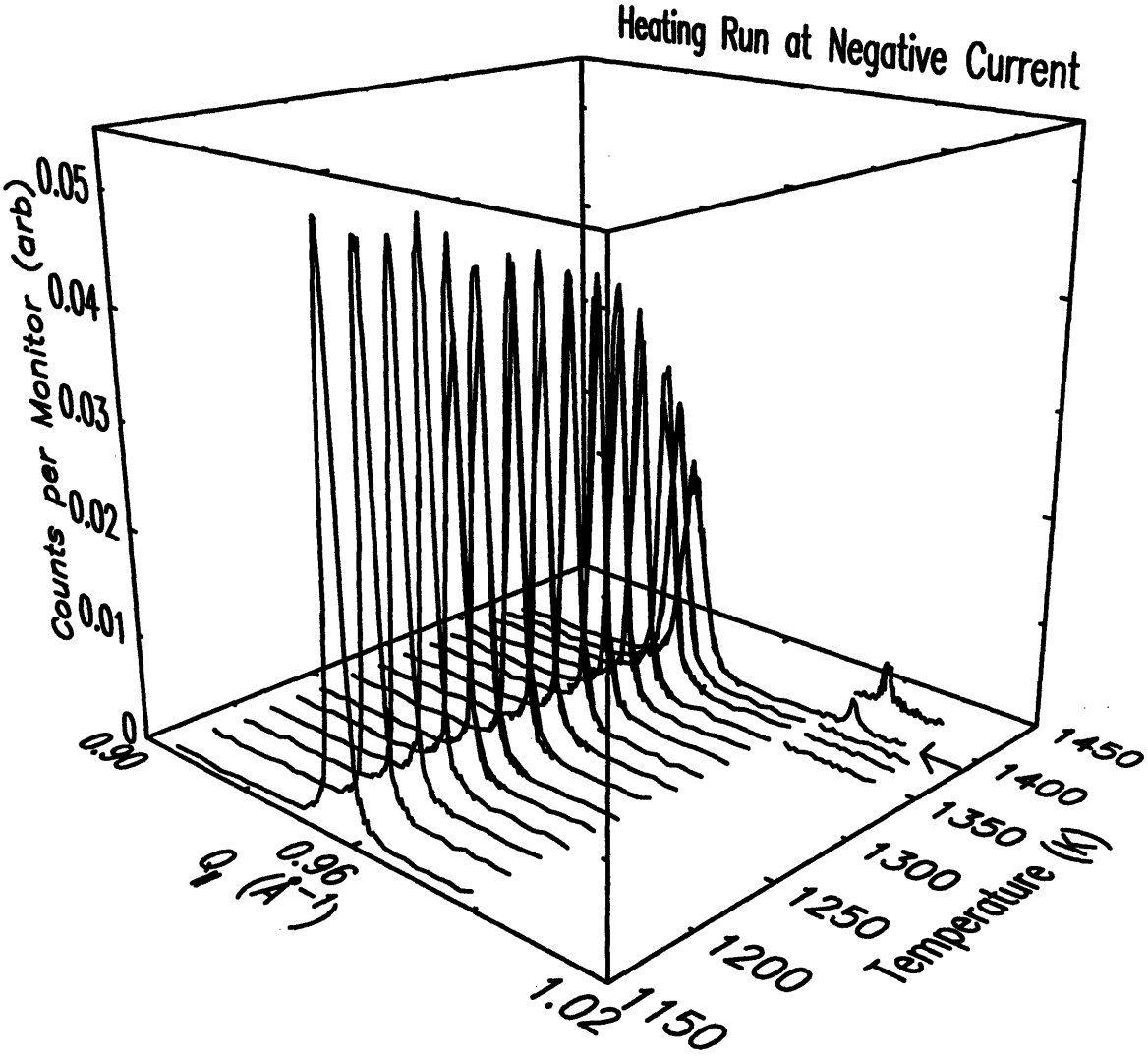

Figure 2-11: Longitudinal scans at the step peak on heating through single-phase stepped region at negative current. At approximately 1370 K there is an onset of step bunching marked by a broadening of the step peak and the appearance of weak scatter at the integer order (1,0) peak position. Background measurements from θ scans around the (1,0) position are shown for three temperatures indicating no substantial scattering below 1370 K.

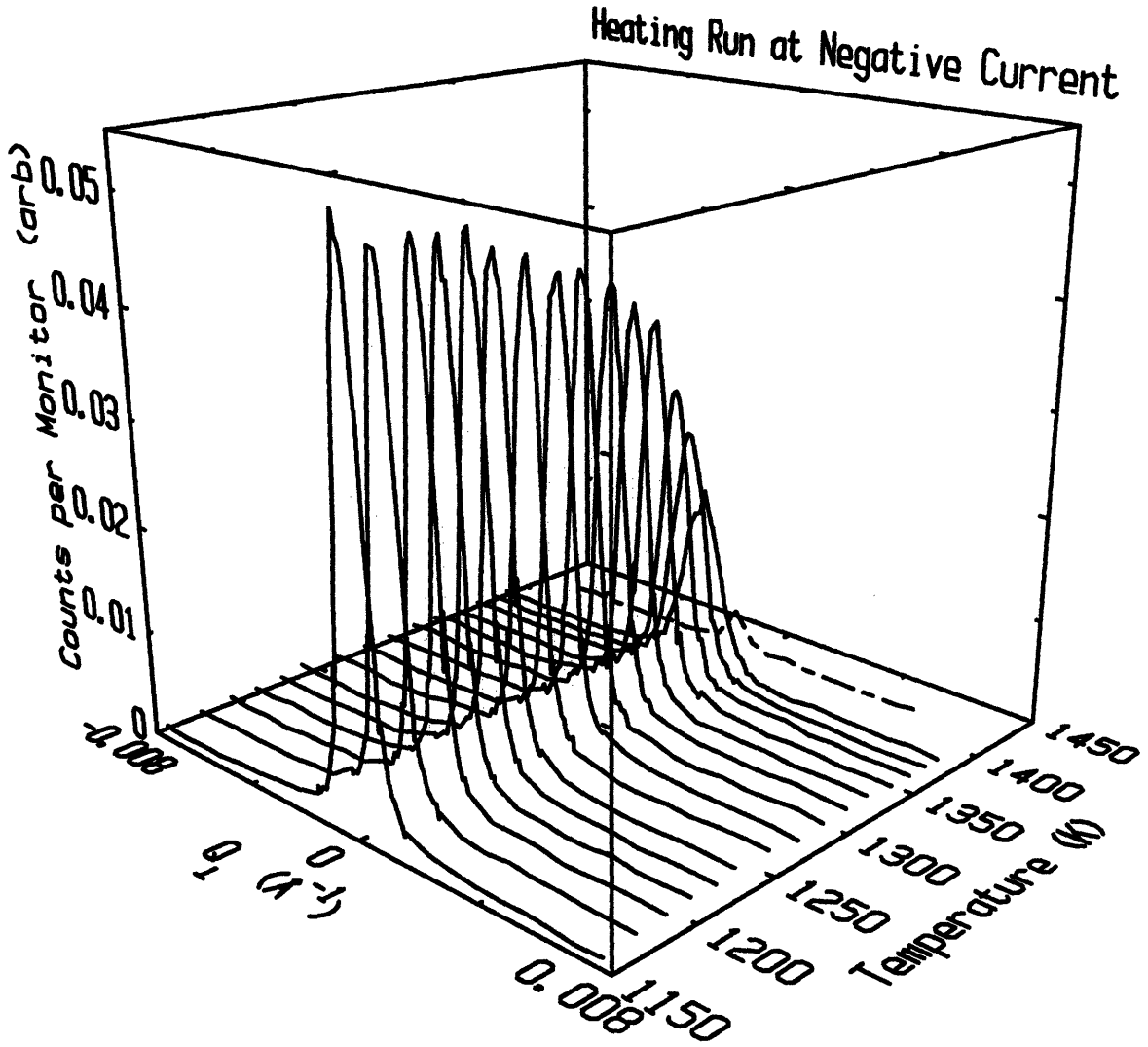

Figure 2-12: Transverse scans at the step peak position on heating through the single-phase stepped region at negative current. A tranverse broadening is observed at a temperature which roughly coincides with the onset of the integer order (1,0) peak. Dashed line at 1406 K shows scattering at the (1,0) peak from a θ scan for comparison with the step peak.

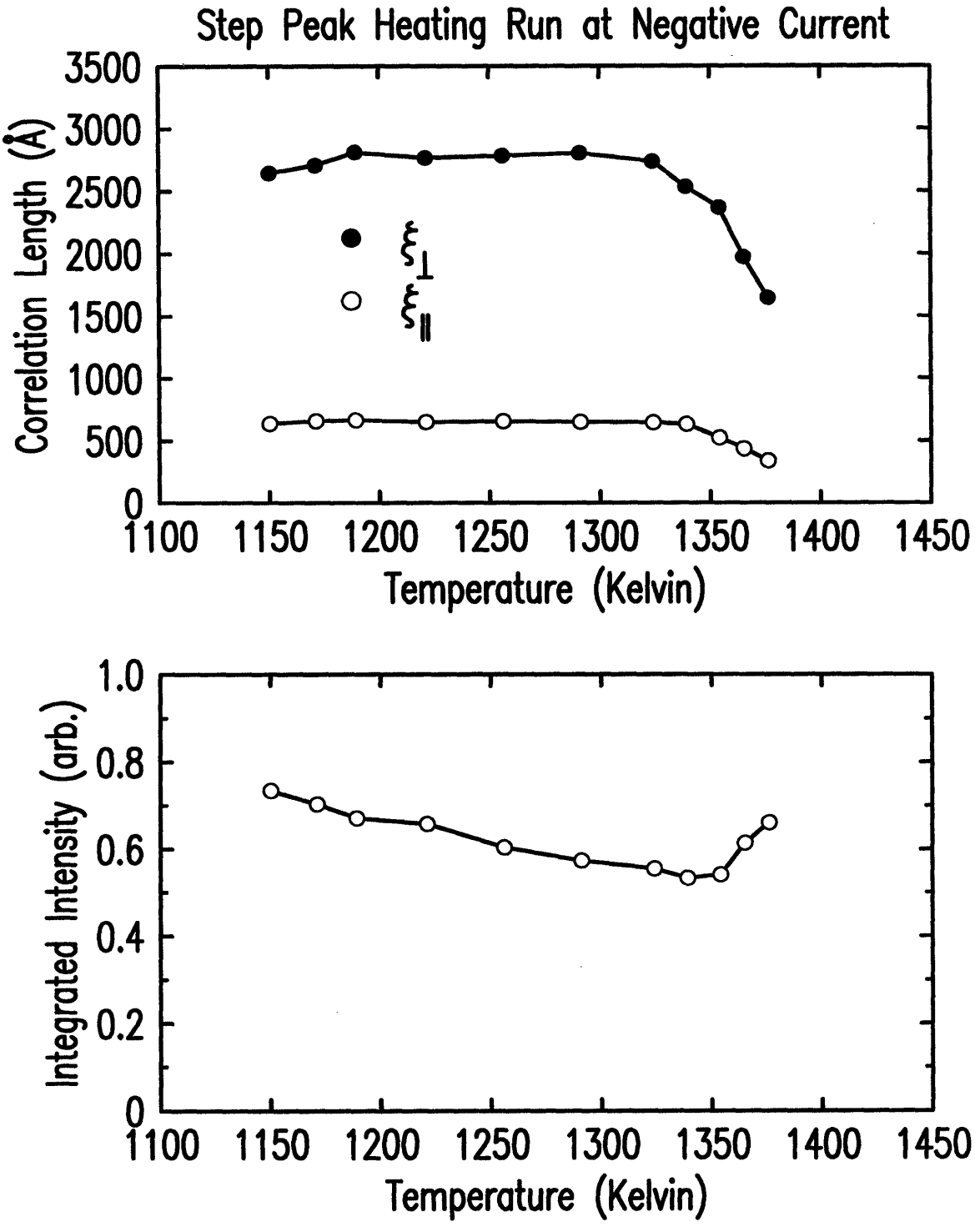

Figure 2-13: Results from the heating run through the single-phase stepped region at negative current. Longitudinal and transverse step-step correlation lengths are determined from fits of the scattering to a Lorentzian to a power. Solid lines are guides for the eye.

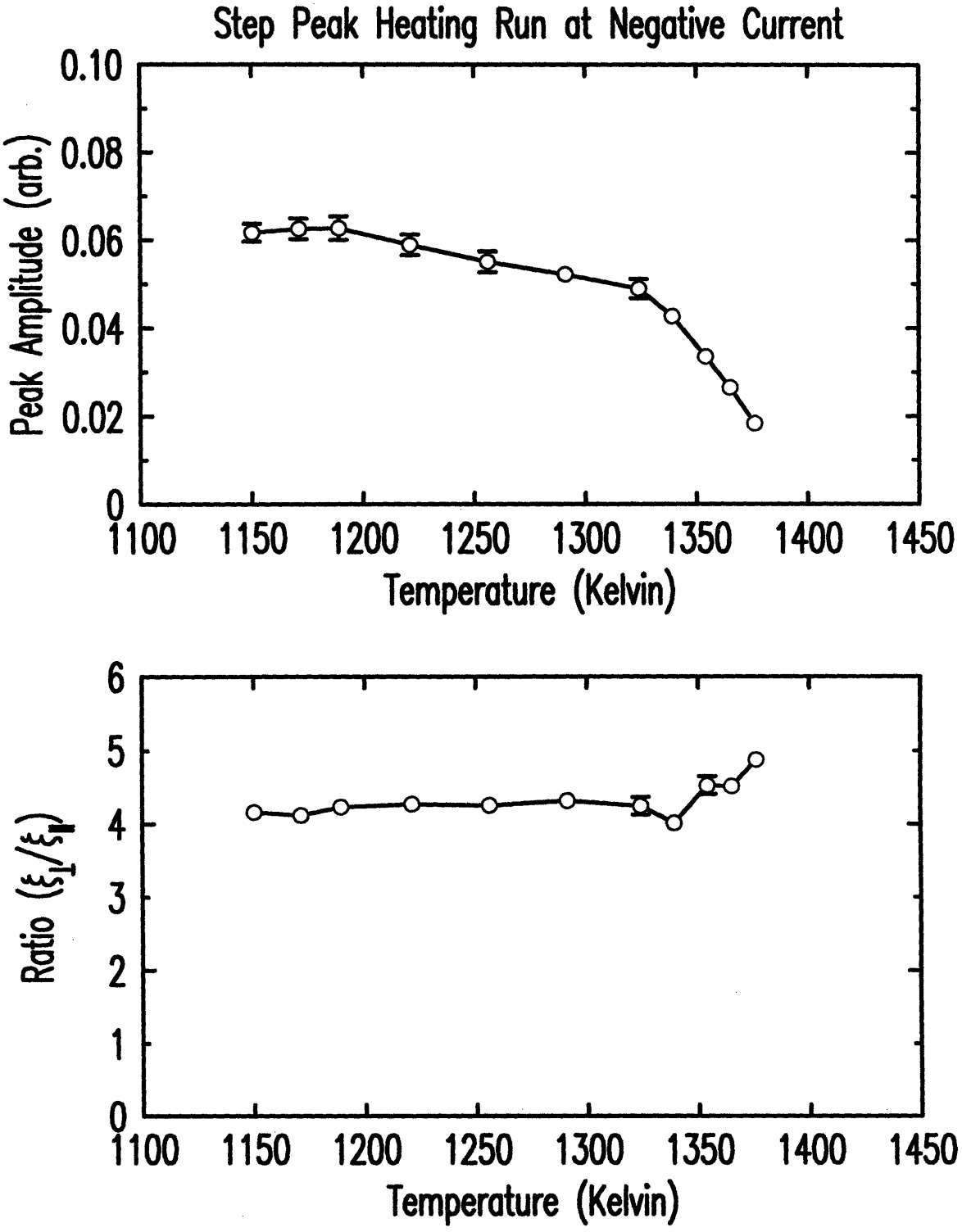

Figure 2-14: Results from the heating run through single-phase stepped region at negative current showing the scattering amplitude and the ratio of the step-step correlation lengths ($\xi_\perp/\xi_\parallel$). The peak intensity is significantly above the background for the highest temperature point shown. Solid lines are guides for the eye.

This information is necessary in order to obtain **q**-dependent data with satisfactory statistics. Assessing information of time-dependence in a conventional scattering experiment can be a formidable task due to the limitations imposed by the finite time require to move the spectrometer motors. However, by a careful estimation it is possible to choose the counting time per point ($q_{\parallel}$,$q_{\perp}$) which will yield scattering profiles which are undistorted by the time-dependence. It is also essential to account for the systematic error due to the evolution of the peak lineshapes which is generally largest in the tails of the peak. Nontheless, the critical information of interest regards the characteristic lengths of the facets and the step-step correlation lengths which can be easily measured from the HWHM of the peaks. The latter quantities can be difficult to interpret in this system as is clear from examining the large wavelength surface undulations seen in the real-space images of these samples. This dilemma will be covered in the section 2.3. To date, the structure factor for these phases has not been calculated. This will be discussed in detail later.

Figure 2-15 shows the initially stepped surface state at 1419 K (+10.4 Amps). The x-ray scattering lineshape was characterized by a Lorentzian to a power η convoluted with the Gaussian resolution. The resolution shape is shown by the dashed line in Fig. 2-15 for comparison. The surface was thrown out of steady-state upon current flipping at which point it relaxed slowly to a new steady-state faceted configuration, shown in the bottom panel of Fig. 2-15. The facet peak became resolution limited transversely and longitudinally after 100 minutes. A high-current relay with a switching time of less than 0.1 seconds was used to control the current direction. No substantial temperature change was observed after changing the current direction. The initial time (t_0) was taken to be the time of the first temperature measurement after switching the current. Approximately 6–8 seconds elapsed between current reversal and setting t_0 due to the long data transfer time from the optical pyrometer (via a standard serial connector port) which was used to make the temperature measurement. However this error in t_0 was small compared to the total elapsed time (15–200 minutes) involved in each time-dependence run. Subsequent time measurements (measured with respect to t_0) were taken to be the elapsed time at the peak

maximum in each x-ray **q**-scan. The slow spectrometer motors added a systematic time delay between consecutive scans which could not be reduced. The average time of a single scan (including the time required to move the spectrometer motors) was 4.5 minutes at -8.6 Amps, and could be controlled by adjusting the monitor counting time. This insured that both the incident beam intensity and scan rate were constant, thus eliminating possible unsystematic distortions in the shape of the scattering peaks due to the time dependence of the peak widths and peak intensity. Our highest temperature measurements (above 1473 K) were limited predominately by the more rapid changes in the scattering profile, and thus were not included in the lineshape analysis.

In order to determine the time-dependence of the characteristic widths and peak intensities from the scattering distribution at the (1,0) and step peak positions, it was necessary to make some simple approximations. The rapid time dependence observed for most of the range of temperature prevented a full two-dimensional deconvolution of the scattering profile (as had been performed for the lower temperature scattering data discussed above). This limitation can be understood by examining the raw data which show that the peak intensities between consecutive transverse and longitudinal scans evolve non-linearly for most of the temperatures studied. The precise time-dependence of the scattering profiles as an explicit function of time and temperature is not known, thus preventing a simple interpolation of either the peak intensities or the peak widths between two consecutive longitudinal and transverse scans. This is apparent from (1,0) peak and step peak data in Figs. 2-18 and 2-20 which show results of the time-dependence of the longitudinal and transverse widths, peak positions, peak intensities, and calculated integrated intensities at 1376 K (described in detail in the next section). However, temperatures were carefully selected such that the time-dependence of the scattering profile would not have a significant effect on the **q**-dependence of the peak, although it had a slight effect in the shape of the tails. It is important to note that these scattering data show a substantial variation in the time-evolution of the surface morphology over $\sim$ 100 K, which covers nearly the full range of temperatures for the step bunching region at negative current shown in the

phase diagram of Fig. 2-6. Further, the exact shape of the *tails* is not required in order to get a good measure of the facet sizes and step correlation lengths.

The scattering at both the (1,0) and step peak positions was analyzed with non-linear least-squares fits to several functional forms: a simple Lorentzian, a Lorentzian squared, and a Lorentzian to the power 1.5. By choosing the fits which resulted in the smallest chi-squared (χ^2_ν) values, it was straightforward to identify the lineshape which most consistently described the scattering. In the case of the scattering at (1,0), an additional constraint, chosen empirically, was applied by assuming the *same* lineshape described the scattering across the full range of temperatures, and for both positive and negative current directions. The functional form which best satisfied these requirements was determined to be a Lorentzian to the power 1.5 convoluted with the Gaussian resolution:

$$S(q) = \frac{S_0}{(1+\xi_{x0}^2(q-q_{x0})^2)^{3/2}}, \tag{2.9}$$

where q_{x0} is the peak position along either the longitudinal ($q_{\|}$) or transverse ($q_{\perp}$) directions, and ξ_{x0} is a characteristic length associated with the terrace width. The exponent 3/2 in Eq. 2.9 is not surprising since the usual form of the structure factor corresponding to exponentially decaying correlations in two-dimensions is $S(\mathbf{q}) = I_0/[1+\xi_{x0}^2(q_x-q_{x0})^2+\xi_{y0}^2 q_y^2]^{3/2}$. The distribution of facet sizes along the longitudinal and transverse directions can be determined from the HWHM of the scattering peaks. Additional attempts to modify the lineshape by allowing the exponent of the Lorentzian to vary yielded results comparable to those with the exponent fixed at 1.5 for the (1,0) peak.

To reiterate an important point regarding the consistency of the fits, the scattering profiles along consecutive $q_{\|}$ and $q_{\perp}$ scans were fit independently due to the gradual time development of the lineshapes. However, the profiles during the time of a single scan (either along $q_{\|}$ or $q_{\perp}$) were essentially undistorted, as can be seen from the symmetry of the scattering. At positive current one notes a sloping background contribution to the scattering for small $q_{\|}$ near (1,0) after a substantial time elapses

(see for example Fig. 2-24). This is due to the nearby broad step peak which undergoes a relatively large increase in intensity as the surface evolves from a faceted to a stepped morphology. The constant background term is measured far away from the (1,0) peak in θ, obtained from a fit when the (1,0) peak is weakest, then held fixed throughout the fits. The linear slope in the background along $q_{\|}$ is first allowed to float in the fits by at most 10% to account for the increasing step peak intensity and is finally fixed to the value determined when the (1,0) peak is smallest (ie. where the step peak has essentially saturated). The same procedure was applied for determining the background shape at the step peak, although in this case the sloping term in the background originated from the tails of the (1,0) peak (see Fig. 2-20).

Preliminary experiments revealed that one of the complicating features of this system is its continual evolution over time-scales of many hours (or even days). Hence, the approach to a "true" steady-state surface morphology can require very long times which are not readily accessible in an experiment. In fact, it was determined that a saturated surface morphology, eg. with well-established large facets, generally requires a long time to reverse, often making it necessary to *flash* the sample to high-temperatures several times in order to unfacet the surface. In order to extract useful information separating the time-dependence from other effects, such as temperature dependence or hysteresis, this problem had to be circumvented by simply limiting the time spent at one current direction within these high-temperature regions of the phase diagram. This was particularly important in the positive current regions, since these phases are accompanied by transverse meandering of the steps which can develop very large amplitude modulations with very slow dynamics. This will be discussed later in the context of chaotic step behavior and compared with what is predicted by the theoretical models.

Results of the Time-dependence after Quenching

Immediately following the heating run at negative current, the 8° miscut sample was flashed to 1525 K for 1 minute and quenched to 1413 K (−9.7 Amps) where a study was made of the time-dependence at (1,0). The results from fitting the lon-

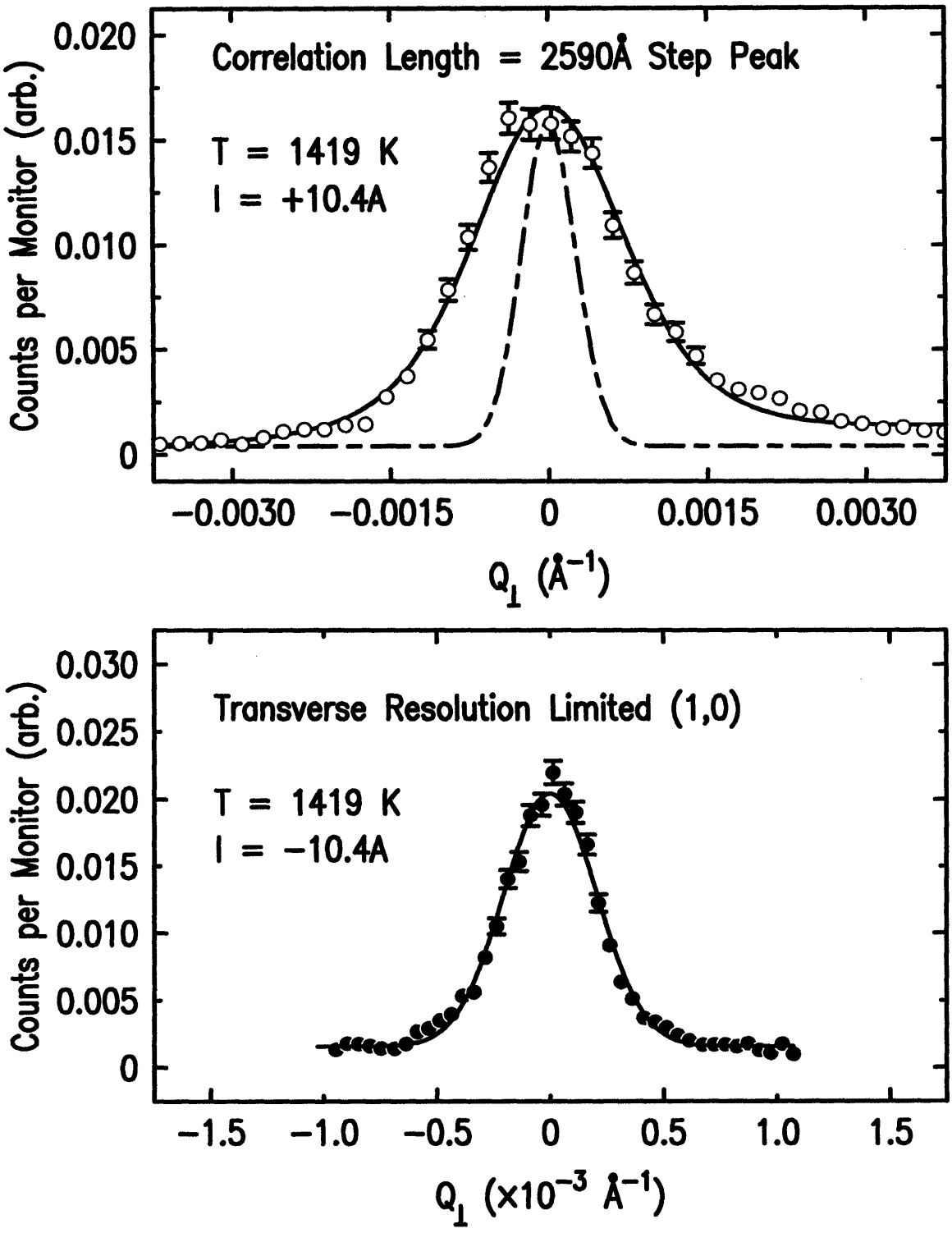

Figure 2-15: Steady-state morphology on a 4° miscut Si(111). Transverse scans at 1419K through (a) the step peak at +10.4A and (b) the (1,0) peak at -10.4A. The dashed line in the top panel is the transverse resolution profile.

gitudinal and transverse lineshapes are shown in Fig. 2-16. The first two points in this figure are peak amplitudes measured from the longitudinal scans (open circles) and transverse scans (closed circles) which indicate scattering just slightly above the background level of 1×10^{-3} counts per monitor count, and thus were not included in the lineshape analysis. Substantial development in the lineshape occurs only after approximately 20 minutes at this temperature, and is followed by a 2 orders of magnitude increase in the peak intensity over an additional 100 minutes at which point the integrated intensity saturates. Over the full 125 minutes at this temperature, the transverse facet width develops from 8000$\AA$ to about 12500$\AA$, the longitudinal facet width develops from 275$\AA$ to 410$\AA$, thus the ratio of the lengths ($\xi_\perp/\xi_\parallel$) is roughly constant. The longitudinal peak position ($q_{\parallel 0}$) is essentially constant throughout. The lattice expansion at these high temperatures accounts for the small shift from the integer (1,0) position.

A second quenching study was conducted at 1376 K (−8.6 Amps) after flashing the sample three times to 1525 K in order to unfacet the saturated surface structure. The results from the fits are shown in Fig. 2-17. The surface undergoes a much more rapid increase in peak intensity which changes non-linearly throughout most of the time studied at this temperature. Interestingly, the longitudinal and transverse facet widths do not develop significantly even after nearly 150 minutes while the integrated intensity saturates much earlier than at higher temperature. Regardless, the peak intensity increases substantially throughout the course of the measurements. Although the final peak widths are comparable to those measured in the quench at 1413 K, the intensity saturates at a larger value indicating that the former data (at 1413 K) might not have reached their final saturated value by the end of the 125 minutes elapsed in the measurements. This seems counterintuitive since one would expect that steady-state would be approached more rapidly with increasing temperature.

A cross-over at negative current from the stepped region to the step bunching region happens between about 1340 K and 1376 K, as is clearly seen from the data in Figs. 2-13 and 2-17, thus providing a lower bound on this transition to within 36 K

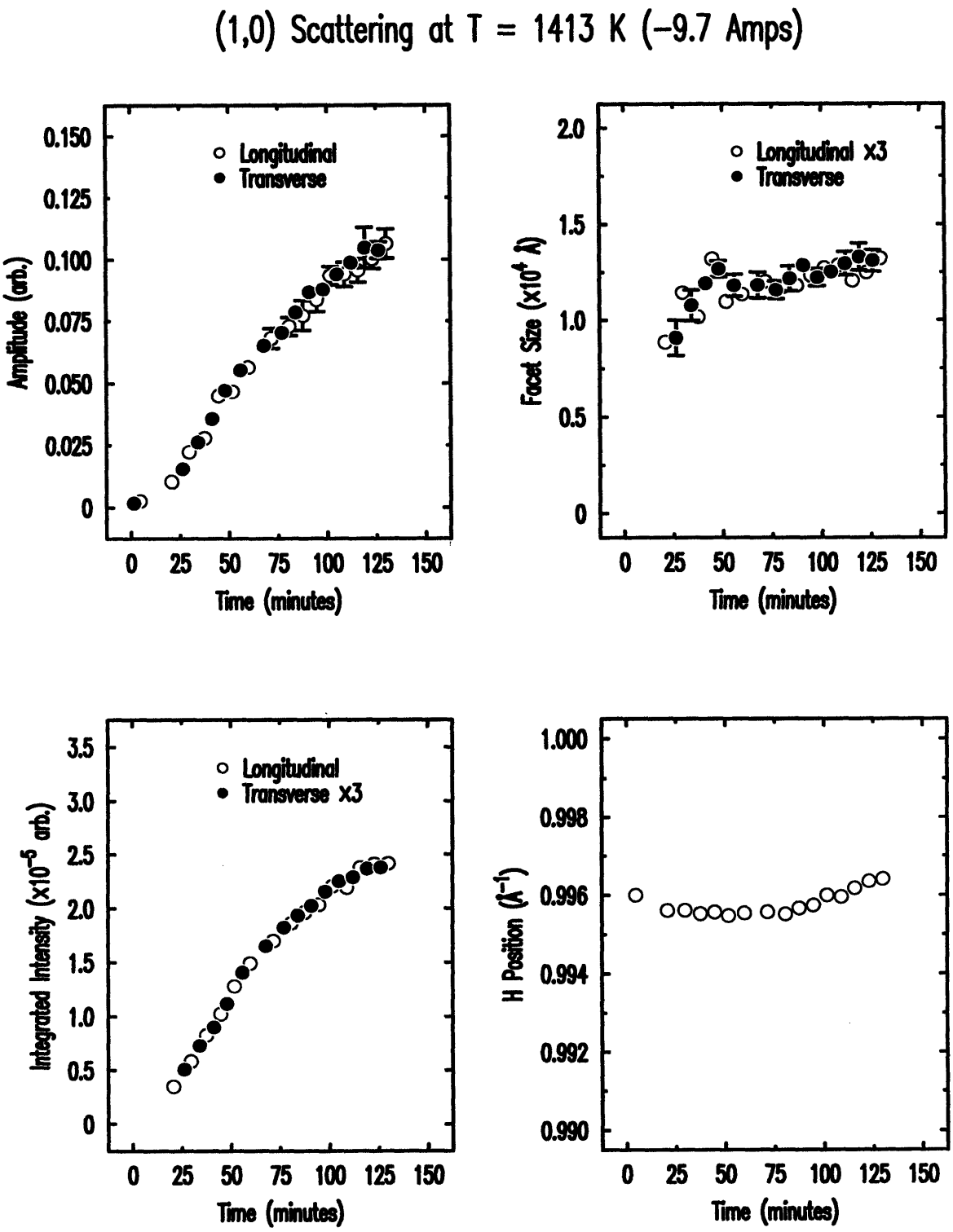

Figure 2-16: Results of the fits of the (1,0) peak showing time-dependent faceting after quenching from 1525 K to 1418 K.

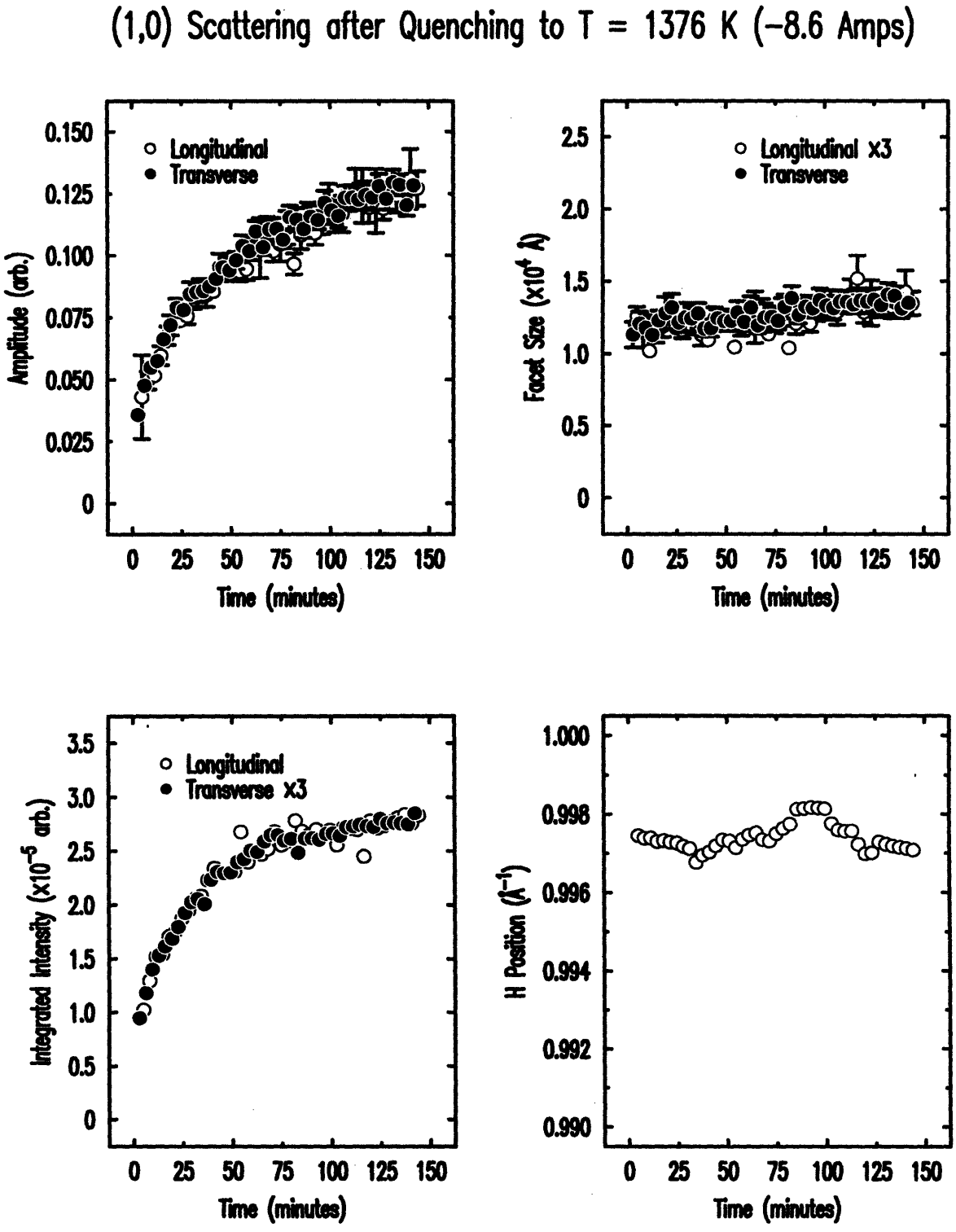

Figure 2-17: Results of the fits of the (1,0) showing time-dependent faceting after quenching from 1525 K to 1376 K.

for the 8° miscut sample. Further, the data in Figs. 2-16 and 2-17 show that faceting (or step bunching) occurs with dynamics which depend strongly on temperature. One will see in the next section that dynamical changes in the surface morphology will also depend on the direction of the current flow through the sample.

Results of the Time-dependence After Current Reversal

As shown in the phase diagram of Fig. 2-6, reversing the direction of current flow through the sample will induce a transformation in the surface morphology. This type of phase transition was studied at 1376 K, 1420 K, and 1473 K for the 8° miscut sample, with particular attention paid to the length-scales involved (eg. the facet size, and the step-step correlation lengths) as well as the time-scales and the reversibility of the morphology.

The time-dependence after current reversal of the (1,0) and step peaks was determined by first measuring the peak intensities as a function of time in order to estimate the rapidity of the intensity changes at this temperature. This was typically performed for both current directions and at both the (1,0) position and the step peak position, although the latter peak *position* is not constant in time. Once an estimate was made of the requisite x-ray counting times, it was straightforward to study the detailed time-dependence of the peak widths by performing consecutive scans over the transverse and longitudinal reciprocal coordinates ($q_{\|}$, and $q_{\perp}$).

The (1,0) and Step peak Behavior at T=1376 K, I=−8.6 Amps

The first current switching study was conducted at 1376 K where the initially stepped surface (at +8.6 Amps) underwent step bunching by switching to −8.6 Amps. The longitudinal (open circles) and transverse (closed circles) scans for the (1,0) peak are shown in Fig. 2-18 with the corresponding fits (solid lines) to Lorentzians to the power 1.5, similar to those used in the quenching studies. The top panels in Fig. 2-18 show scans of the (1,0) peak taken approximately 50 minutes after current reversal when the peak had developed sufficiently strong scattering. The bottom two panels

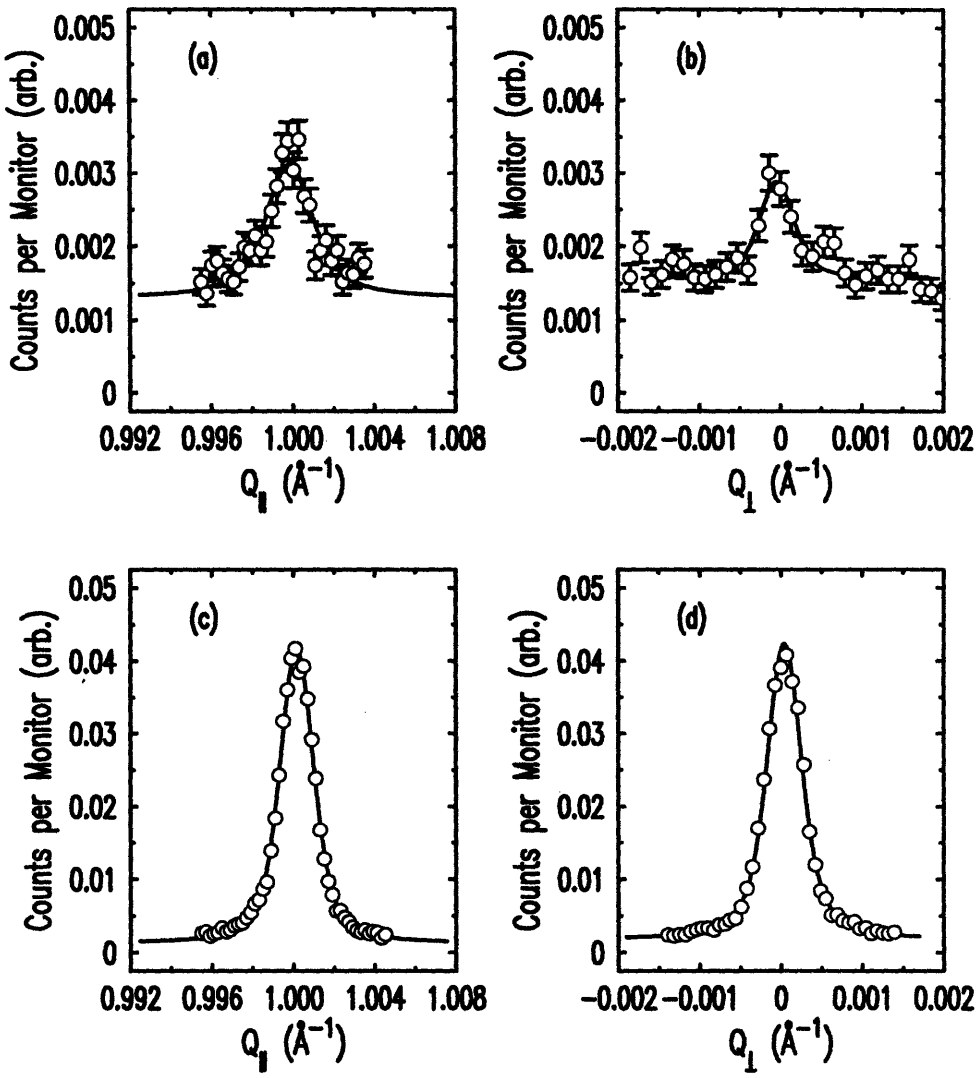

Figure 2-18: Longitudinal and transverse scans at (1,0) peak at 1376 K and −8.6 Amps at selected times after reversing the current direction. The solid lines are fits to a Lorentzian to the power 1.5.

show the last set of (1,0) scans at this current. Results from these fits are summarized in Fig. 2-19. The peak intensities at (1,0) were only slightly above the background level for the first two points shown, therefore there are no corresponding points for the integrated intensities and peak positions. This baseline value for the intensity shows clearly that the dynamics are very slow at this temperature, even after nearly one hour at which point faceting starts to develop relatively quickly.

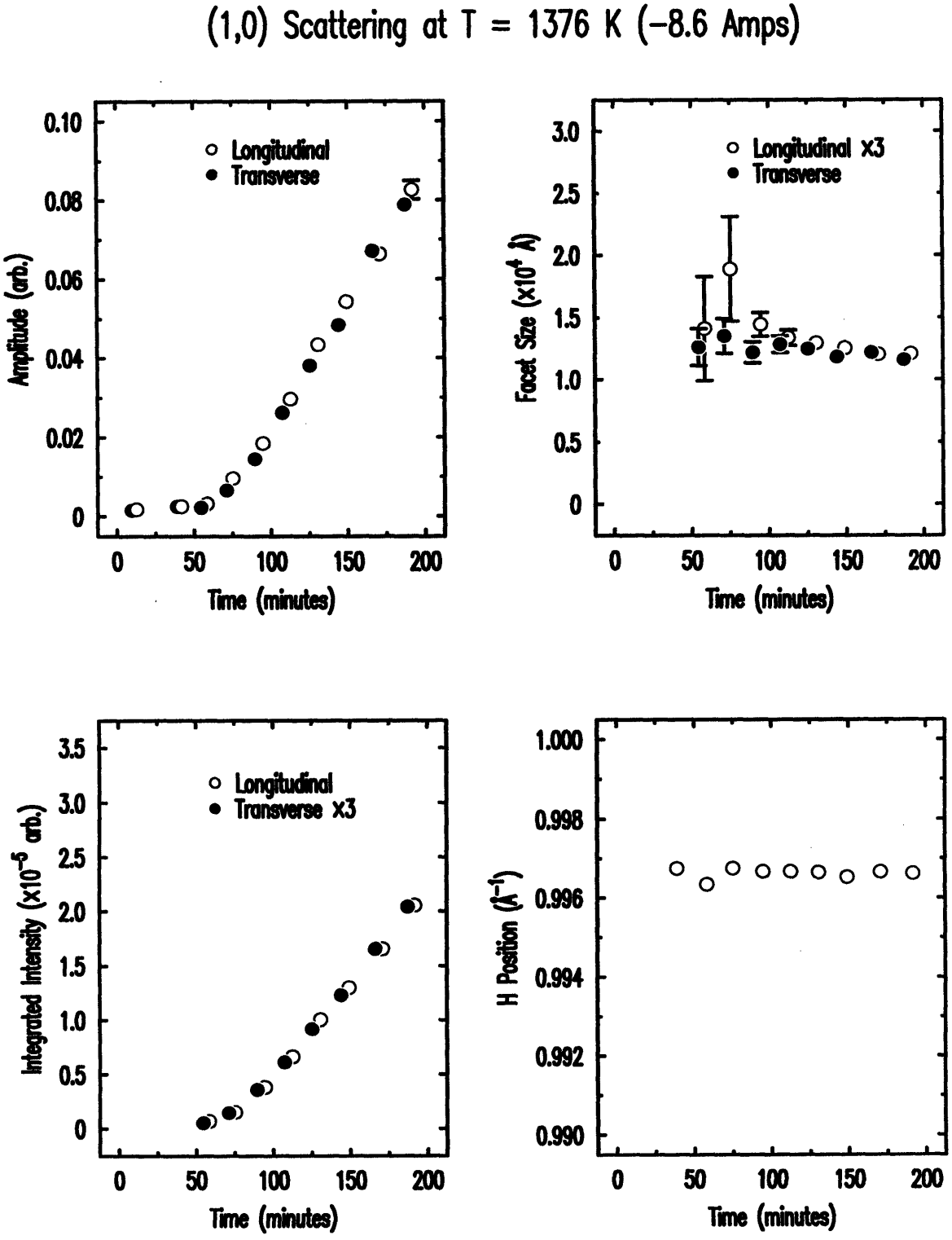

Figure 2-19: Results of the fits for the (1,0) peak at 1376 K (−8.6 Amps). The longitudinal facet size is multiplied by a factor of 3 for comparison with the transverse size. Similarly, the transverse integrated intensity includes this same factor of 3 showing that the integrated intensities following the same scaling. The first four peak intensity points in the first panel are barely above the background level.

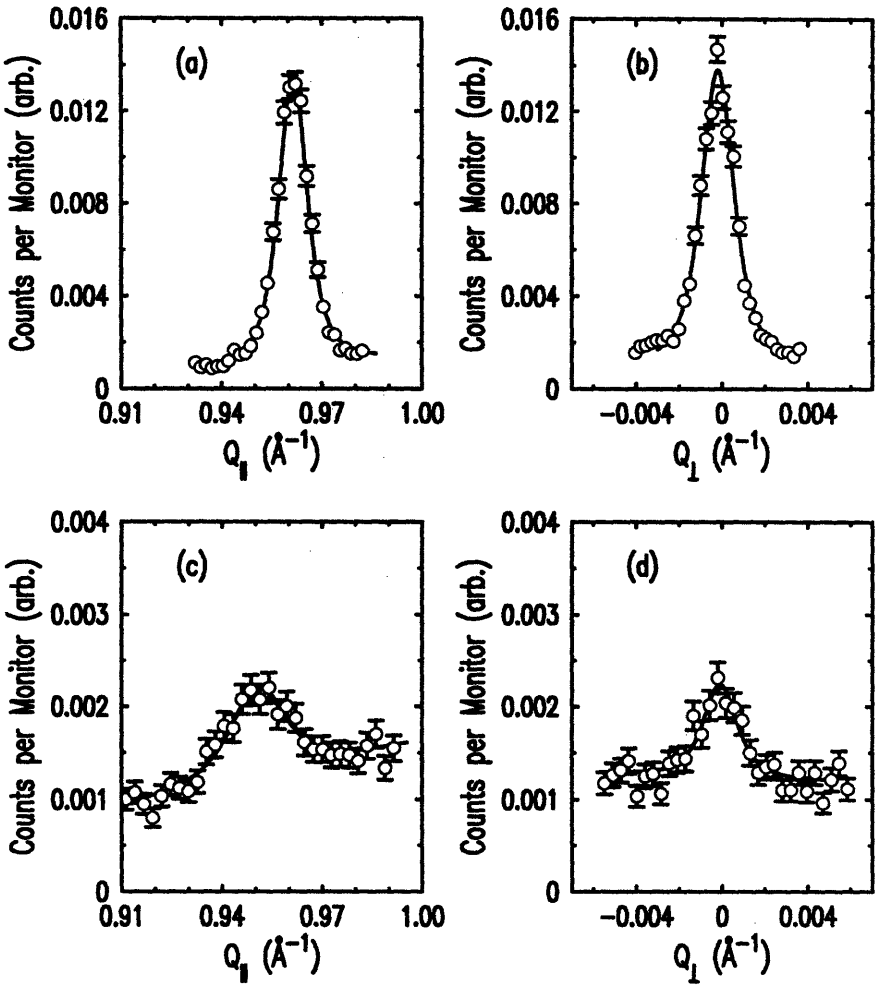

Figure 2-20: Longitudinal and transverse scans at the step peak at 1376 K (−8.6 Amps). The solid lines are fits to a Lorentzian to the power 1.75 as described in the text.

The x-ray scattering data in Fig. 2-20 show time-dependent step bunching at 1376 K and negative current (−8.6 Amps). The scattering lineshape which best described the step peak data was a Lorentzian to the power 1.75 convoluted with the resolution. The best-fit lineshape was determined by comparing fits to a pure Lorentzian, a Lorentzian-squared and a Lorentzian to a power η. In the latter form for the scattering shape, the exponent η was allowed to vary in the fitting routine for initial fits. By taking the average η from these fits then fixing η and comparing the chi-squares to the simpler Lorentzian forms, $\eta = 1.75$ gave the highest-quality fit and worked consistently well over the full range of the data, independent of temperature. This is consistent with the previous step peak data within the single-phase region

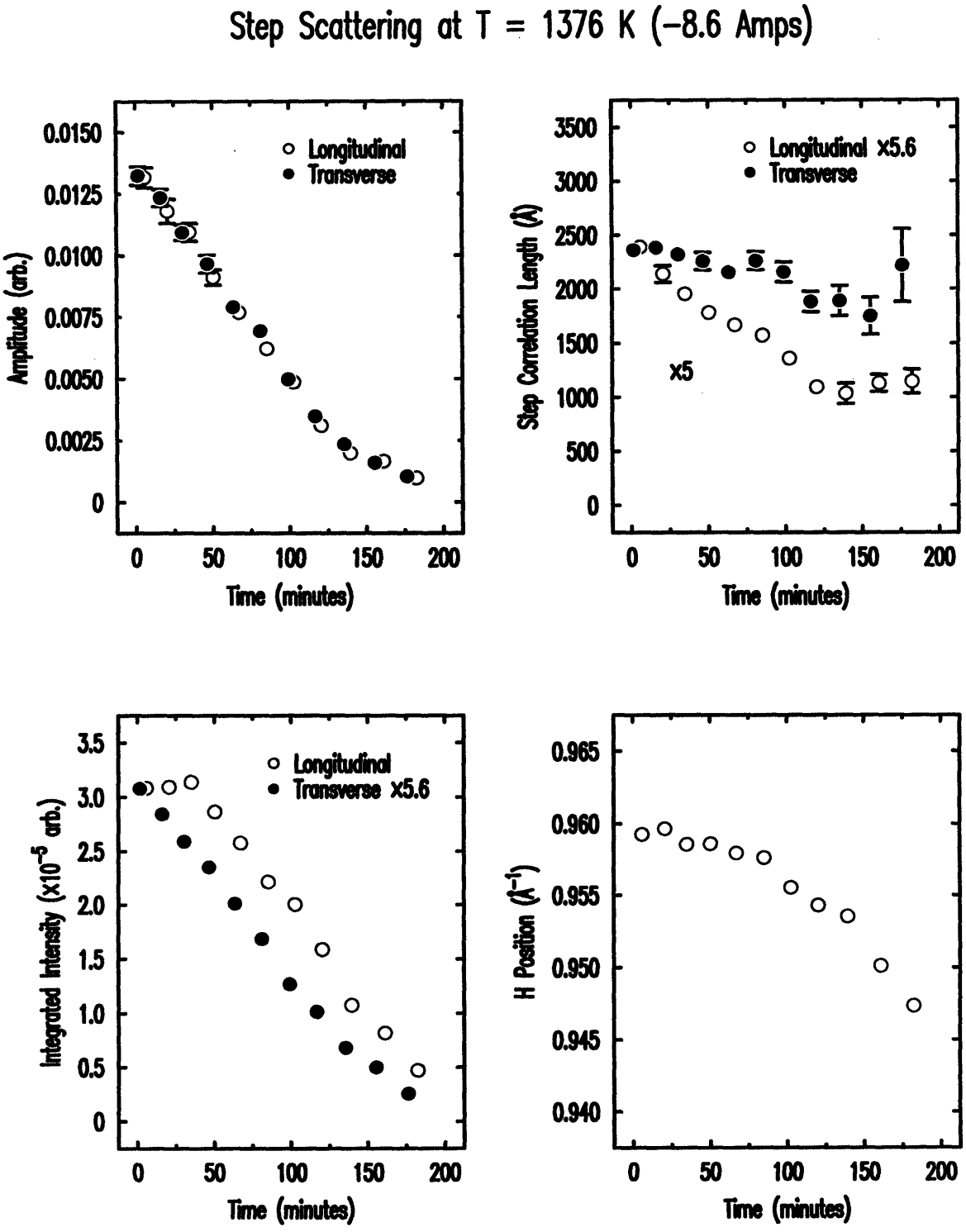

Figure 2-21: Results of the fits for the step peak at 1376 K (−8.6 Amps). The longitudinal step-step correlation length is multiplied by a factor of 5.6 for comparison with the transverse step-step correlation length. The transverse integrated intensity is multiplied by this same factor of 5.6.

described above. The slope in the longitudinal scans after long times is due to the tails of the (1,0) peak (not visible within the range of the plot), and this slope is included as a linear contribution to the fit. The results of the fits for the step peak are shown in Fig. 2-21. One observes that the transverse step-step correlation length ($\xi_\perp$) undergoes a time evolution starting from 2400$\AA$ at early times and decreases to 1750$\AA$ after 150 minutes where the integrated intensity has dropped by a factor of 6. The peak amplitude appears to drop almost linearly across most of the range of elapsed time. Step disordering occurs over this same time period, as shown by the longitudinal length which decreases from 400$\AA$ to about 200$\AA$. After the final scan in Fig. 2-21 the step peak is too weak and diffuse to measure.

The (1,0) and Step peak Behavior at T=1376 K, I=+8.6 Amps

Figures 2-22 and 2-24 show the x-ray data of the (1,0) and step peaks with their respective fits after reversing the current from −8.6 Amps back to +8.6A. The solid lines in the plots are fits to the same lineshape described above. Comparing the results from the (1,0) scattering data in Fig. 2-25 with that in Fig. 2-19 one sees that the instability toward unfaceting occurs with a far more rapid time dependence than the instability toward faceting. The most distinctive feature in this case is the broadening of the (1,0) peak, indicating that the facets decrease in size by about a factor of 2 both longitudinally and transversely before the (1,0) peak finally disappears.

At this same current direction the step-step correlation lengths increase gradually with time up to nearly 500$\AA$ longitudinally and 2500$\AA$ transversely at which point the integrated intensity saturates. These correlation lengths closely match those originally determined at this current direction prior to reversing the current. From the position of the step peak one obtains the time dependence of the step density. Note that the step density approaches its final value within about 100 minutes: the peak separation at this point is $0.996 - 0.9575 = 0.0385 \pm 0.005$, after which it remains nearly constant for the remaining 50 minutes. The step density is slightly larger than its original value before current reversal where the peak separation was 0.0367 ± 0.005. These values suggest that the step arrangements are essentially reversible.

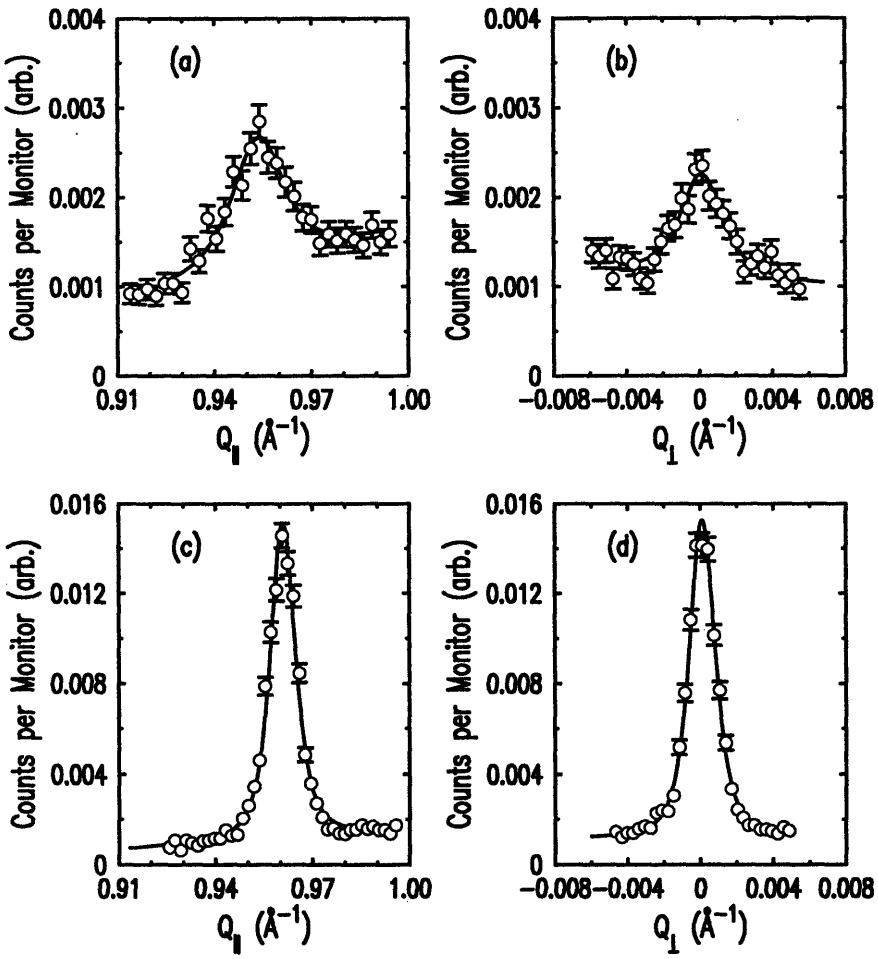

Figure 2-22: Longitudinal and transverse scans at the step peak at 1376 K (+8.6 Amps). The solid lines are fits to a Lorentzian to the power 1.75 as described in the text.

The relatively slow time evolution at 1376 K permitted consecutive scans of both the (1,0) peak and the step peak at −8.6 Amps and +8.6 Amps. The more rapid time-dependence at higher temperatures required independent measurements of the (1,0) and step peaks for each current direction.

Step Ordering at T=1420 K (I=+10 Amps)

These current reversal studies were repeated after first flashing the sample to 1525 K (at negative current) and then quenching to 1420 K (−10.0 Amps). The peak intensity and integrated intensity saturated to values comparable to those in Fig. 2-16 (for −9.7 Amps, 1413 K) within 70 minutes of quenching. Even though there is a

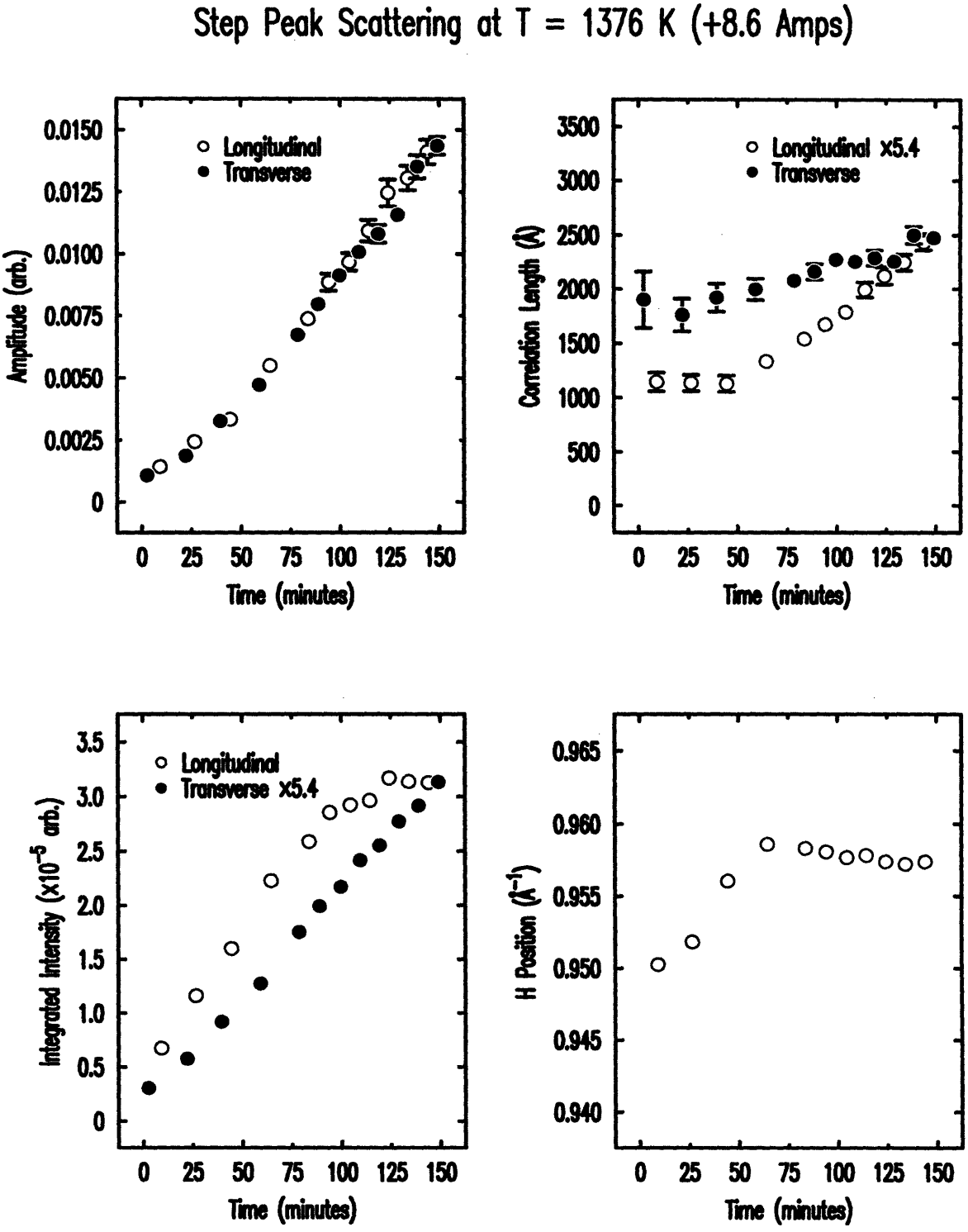

Figure 2-23: Results of the fits for the step peak at 1376 K (+8.6 Amps). The longitudinal step-step correlation length is multiplied by a factor of 5.4 for comparison with the transverse step-step correlation length. The transverse integrated intensity is multiplied by this same factor of 5.4.

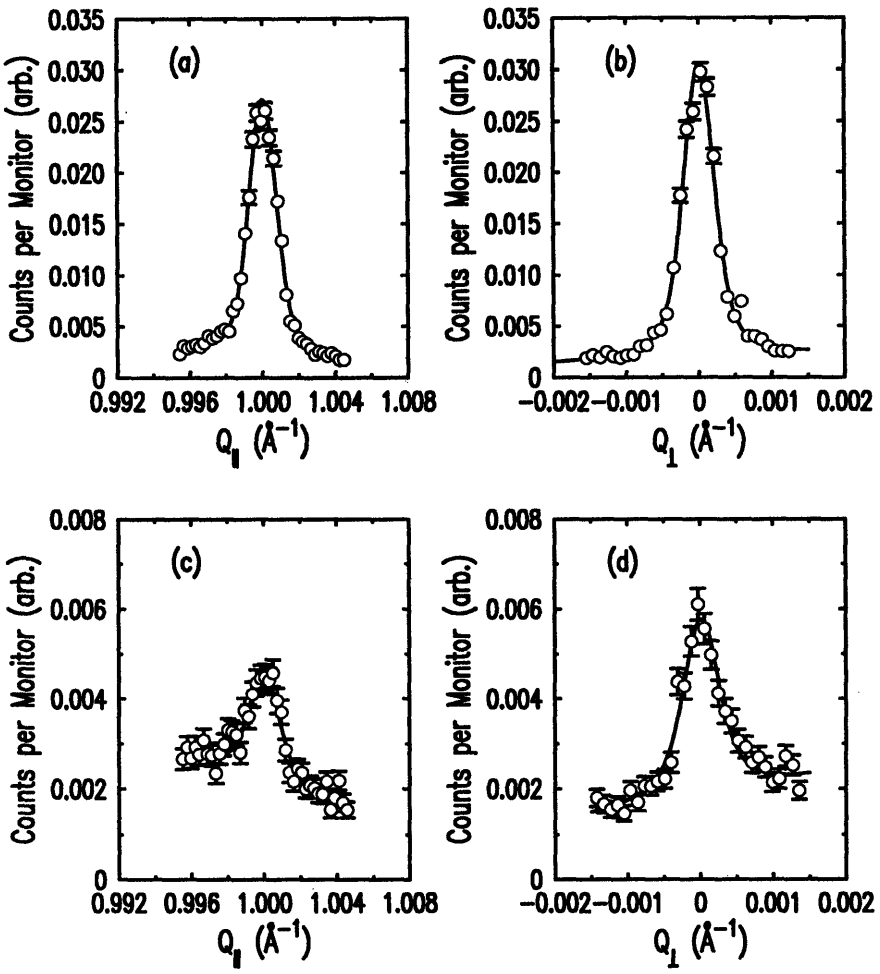

Figure 2-24: Longitudinal and transverse scans at (1,0) peak at 1376 K and +8.6 Amps. (a) and (b) are immediately after reversing the current direction, (c) and (d) are after approximately 50 minutes have elapsed. The solid lines are fits to a Lorentzian to the power 1.5.

7 K difference in the temperatures, one would expect relatively similar characteristics for these two quenches, which is not the case. Apparently the path toward steady-state is quite sensitive to the initial state of the sample, although the final peak characteristics such as the widths and intensities are essentially the same.

With this initially faceted surface state, the current was reversed to +10 Amps and x-ray data were taken of the step peak development as a function of time in the same manner as already described above. The top panels of Fig. 2-26 show an initially weak and broad step peak with a longitudinal correlation length of 250$\AA$ and a transverse correlation length of 1400$\AA$. The results of the fits for the step peak

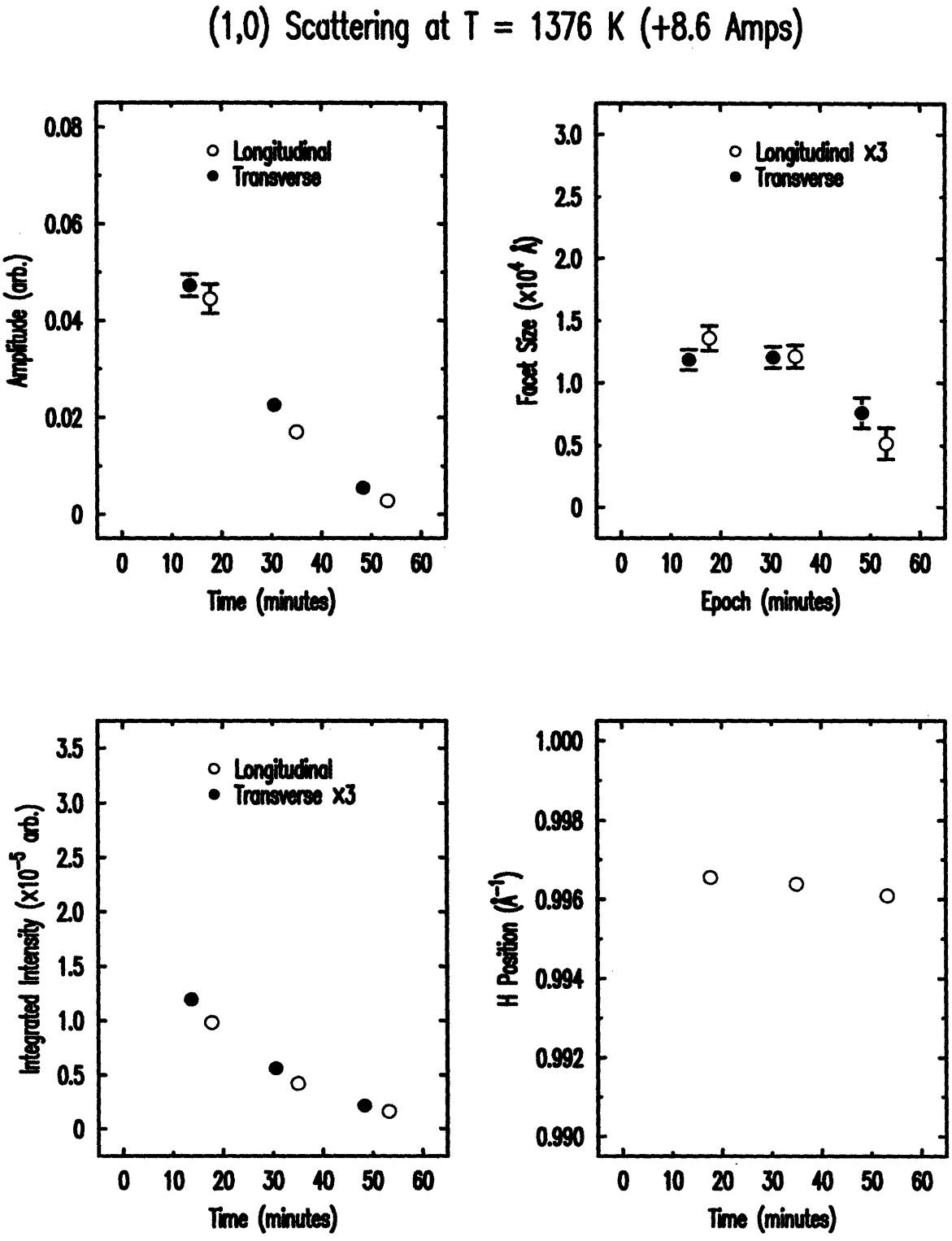

Figure 2-25: Results of the fits for the (1,0) peak at 1376 K (+8.6 Amps). The longitudinal facet size is multiplied by a factor of 3 for comparison with the transverse size. Similarly, the transverse integrated intensity includes this same factor of 3.

data are shown in Fig. 2-26 over a 50 minute interval. During the first 20 minutes the integrated intensity is almost constant as a function of time while there is a gradual increase in the peak intensity. This is followed by a roughly linear increase in the integrated intensity (see Fig. 2-26). The peak separation changes linearly after an initial rapid increase to 0.0495 and approaches a final separation of 0.041. The relatively short correlation lengths are 300$\AA$ longitudinally and 2000$\AA$ transversely (about 20 times smaller than the facet size in the longitudinal direction, and 10 times smaller transversely).

Step Disordering at T=1420 K (I=−10 Amps)

In Fig. 2-27, the results are shown for the step bunching study at −10 Amps. The step peak intensity and step-step correlation lengths behave almost reversibly from those measured at +10 Amps. The integrated intensity, on the other hand, decreases linearly across most of the range of time until the step peak is too weak and broad to measure. One sees a qualitatively similar step bunching behavior to that observed below the 7×7–1×1 reconstruction, however in the high-temperature case the step peak becomes far more diffuse than the step peak below the reconstruction transition. Recall that high step densities characterized by peak separations of almost 0.09 can be easily observed in this sample down to 160 K below the reconstruction transition. It is possible that at high temperatures, the disordering effect of step bunching leads to a loss of the local orientation of the stepped regions; that is, the angle with which the stepped regions make with respect to the (1,0) terraces is not a constant across the sample. Further evidence of this effect is seen in AFM images presented in the next section.

Unfaceting at T=1420 K (I=+10 Amps)

Before reversing the current back to +10 Amps at 1420 K, scans at the sharp (1,0) peak showed facets with a longitudinal extent of approximately 4500Å and a transverse width of 12100Å (a factor of 2.7 ratio in the lengths). The current was then reversed and *unfaceting* was studied as a function of time. The results from these

measurements are presented in Fig. 2-28. One observes an immediate and rapid decrease in the (1,0) peak intensity and integrated intensity over 45 minutes with the peak position remaining essentially unchanged. The facet size as measured from the peak widths evolves in a manner not unlike that observed during the time-dependence study at +8.6 Amps (1376 K). In particular, the transverse widths decrease substantially which is seen by a rather large broadening in the widths of the transverse scans. Throughout the 45 minutes of this study the longitudinal width remains precisely constant, with the final ratio of the transverse and longitudinal lengths reaching nearly unity before the facet peak vanishes.

Faceting at T=1420 K (I=−10 Amps)

Reversing the current back to −10 Amps (1420 K) yielded dramatically different behavior from that at +10 Amps particularly in the peak widths. Namely, the initial transverse and longitudinal scans through (1,0) revealed that the facets reached their maximum extent almost immediately, evolving only slightly during the 125 minutes spent at this temperature. Note that the integrated intensity does not saturate until nearly 100 minutes elapsed. We will see below that the facets can actually continue to evolve and increase in size after a long enough time has elapsed, although at this temperature the minimum required time exceeded that admissible during this run. However, this time-dependent study at −10 Amps was followed by several consecutive measurements of the longitudinal profile at different transverse ($q_\perp$) positions which revealed that the (1,0) peak essentially matched the shape of the resolution ellipse, which would indicate that the surface morphology was very close to being saturated.

Since the step bunching at 1420 K was basically saturated, four flashes at 1527 K (−13.8 Amps) were required in order to observe a significant temperature-dependent changes in the surface morphology. In order to insure that the faceting behavior was reproducible after flashing, the sample was cycled slowly up to the flashing temperature twice before finally quenching to a final temperature of 1473 K where a third current reversal study was conducted. It should be pointed out that the scans at the (1,0) peak after quenching to 1473 K showed behavior similar to that observed after

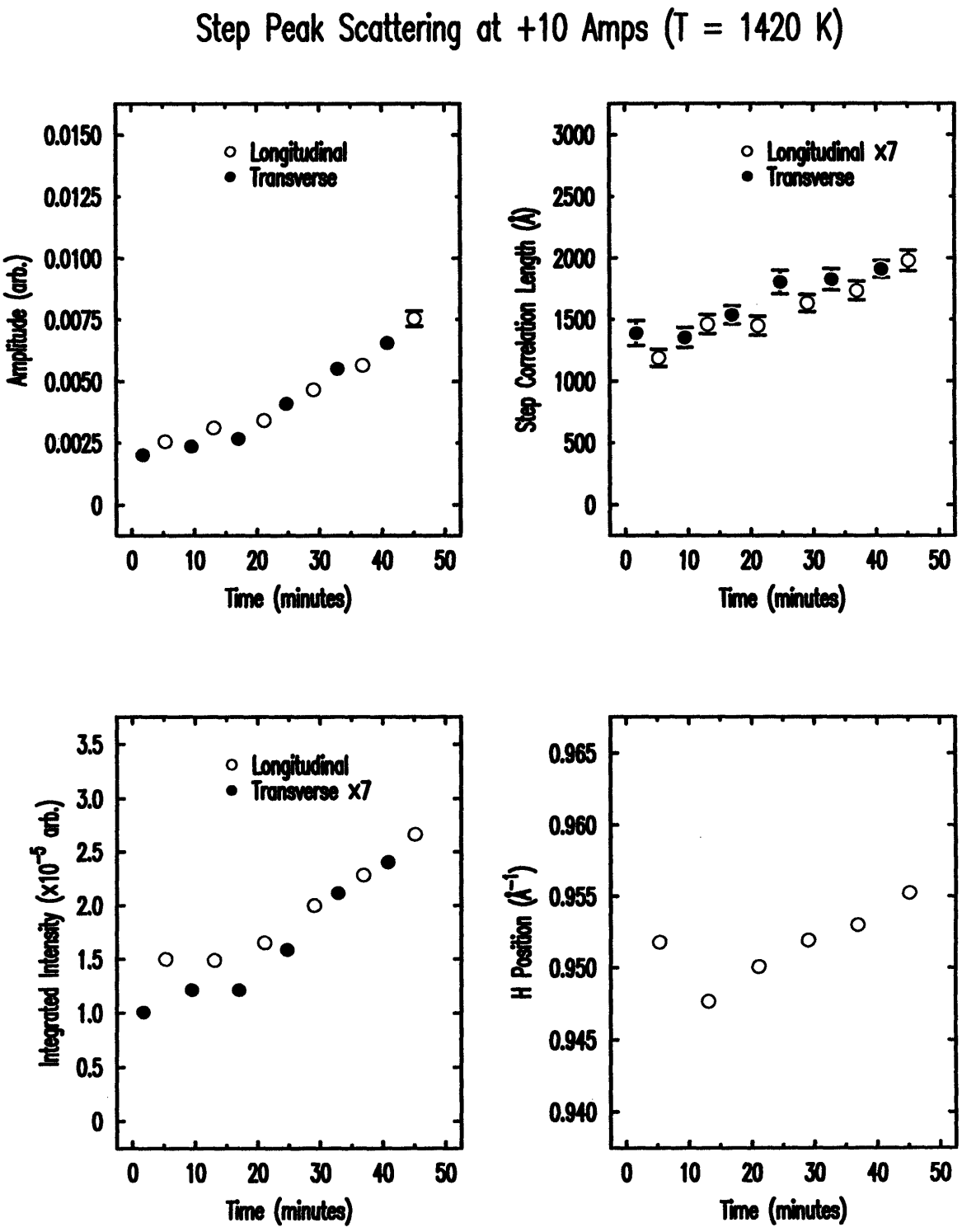

Figure 2-26: Results of the fits for the step peak at 1420 K (+10 Amps). The longitudinal step-step correlation length is multiplied by a factor of 7.0 for comparison with the transverse step-step correlation length. The transverse integrated intensity is multiplied by this same factor of 7.0.

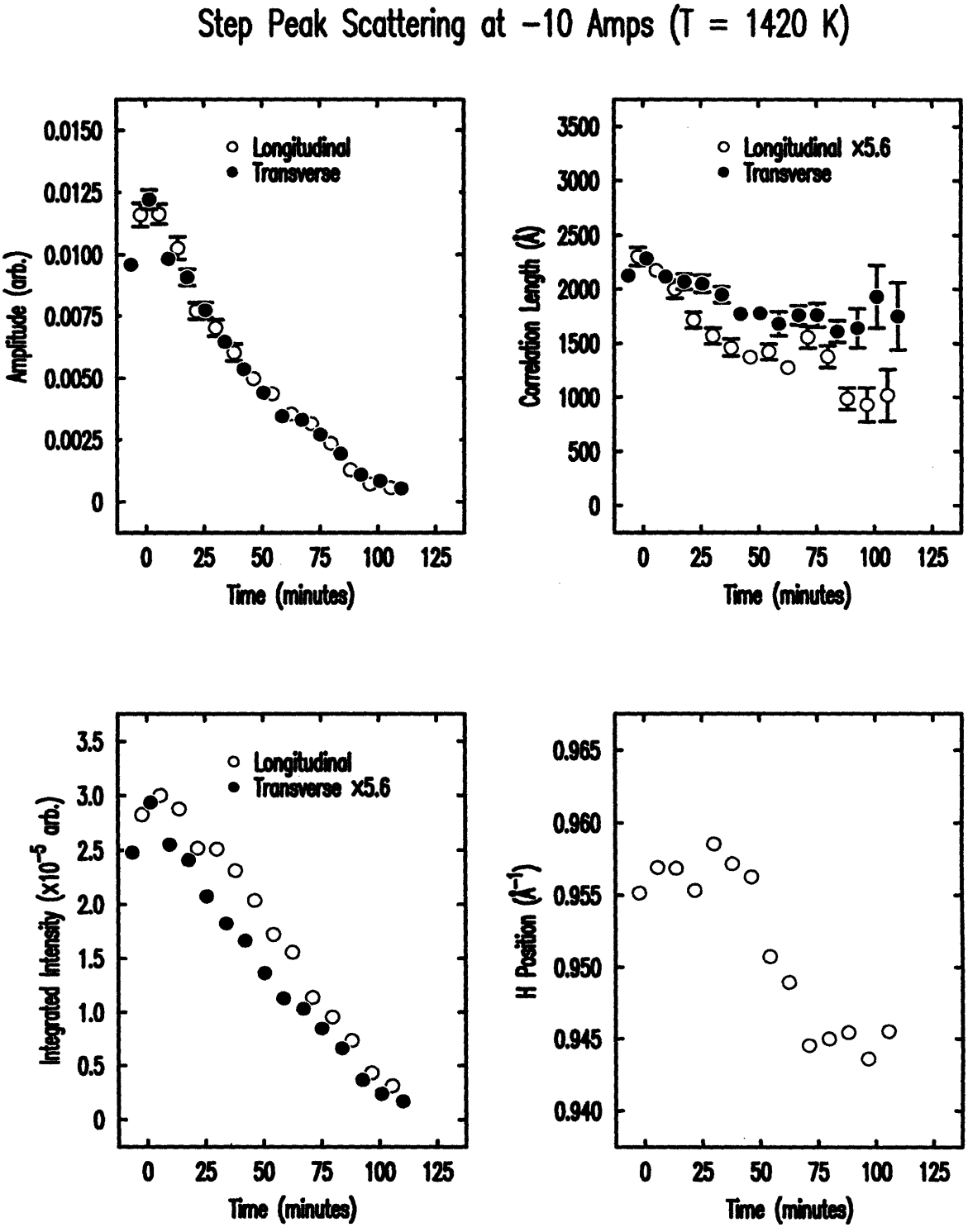

Figure 2-27: Results of the fits for the step peak at 1420 K (−10 Amps). The longitudinal step-step correlation length is multiplied by a factor of 5.6 for comparison with the transverse step-step correlation length. The transverse integrated intensity is multiplied by this same factor of 5.6.

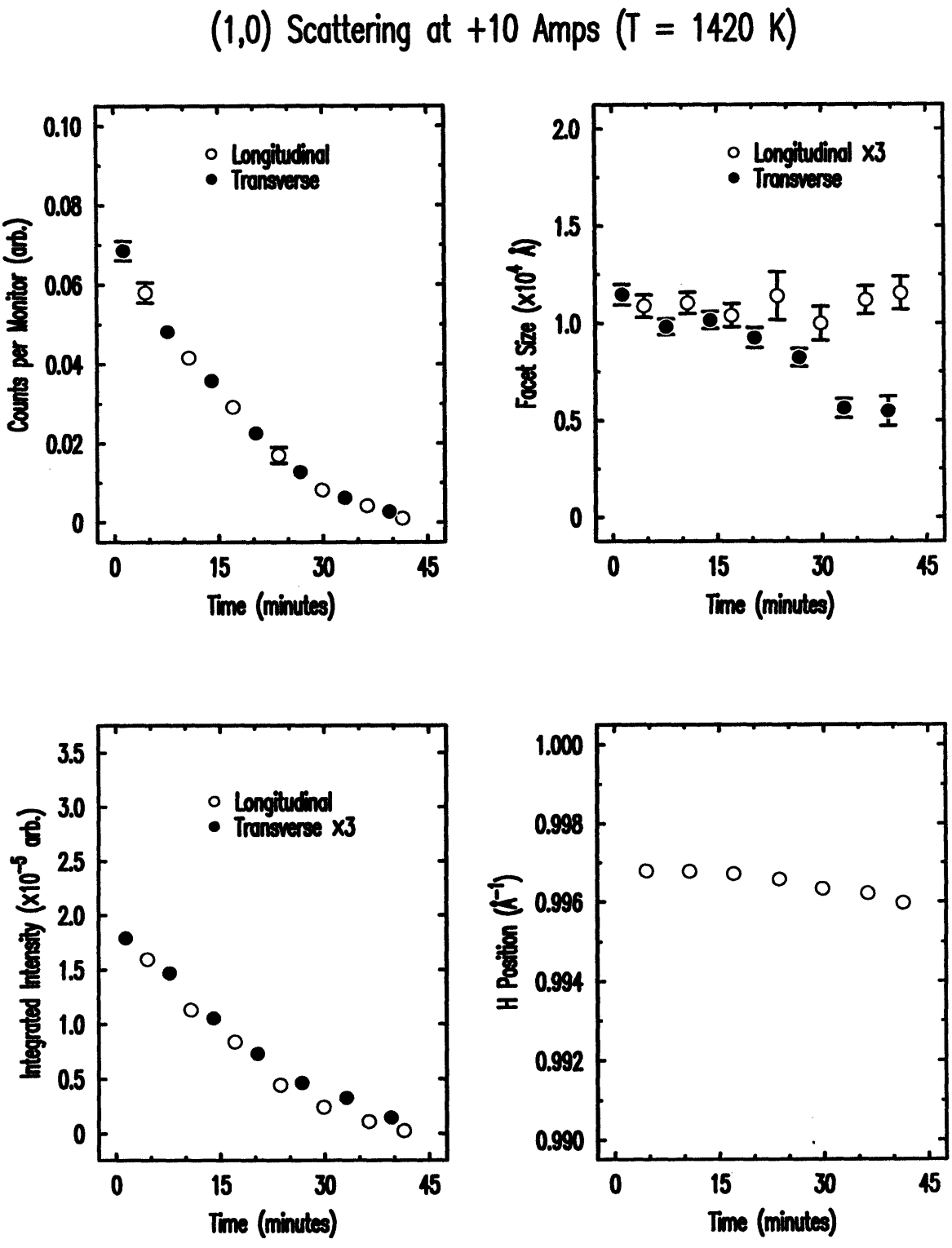

Figure 2-28: Results of the fits for the (1,0) peak at 1420 K (+10 Amps). The longitudinal facet size is multiplied by a factor of 3 for comparison with the transverse size. The transverse integrated intensity is likewise multiplied by a factor of 3.

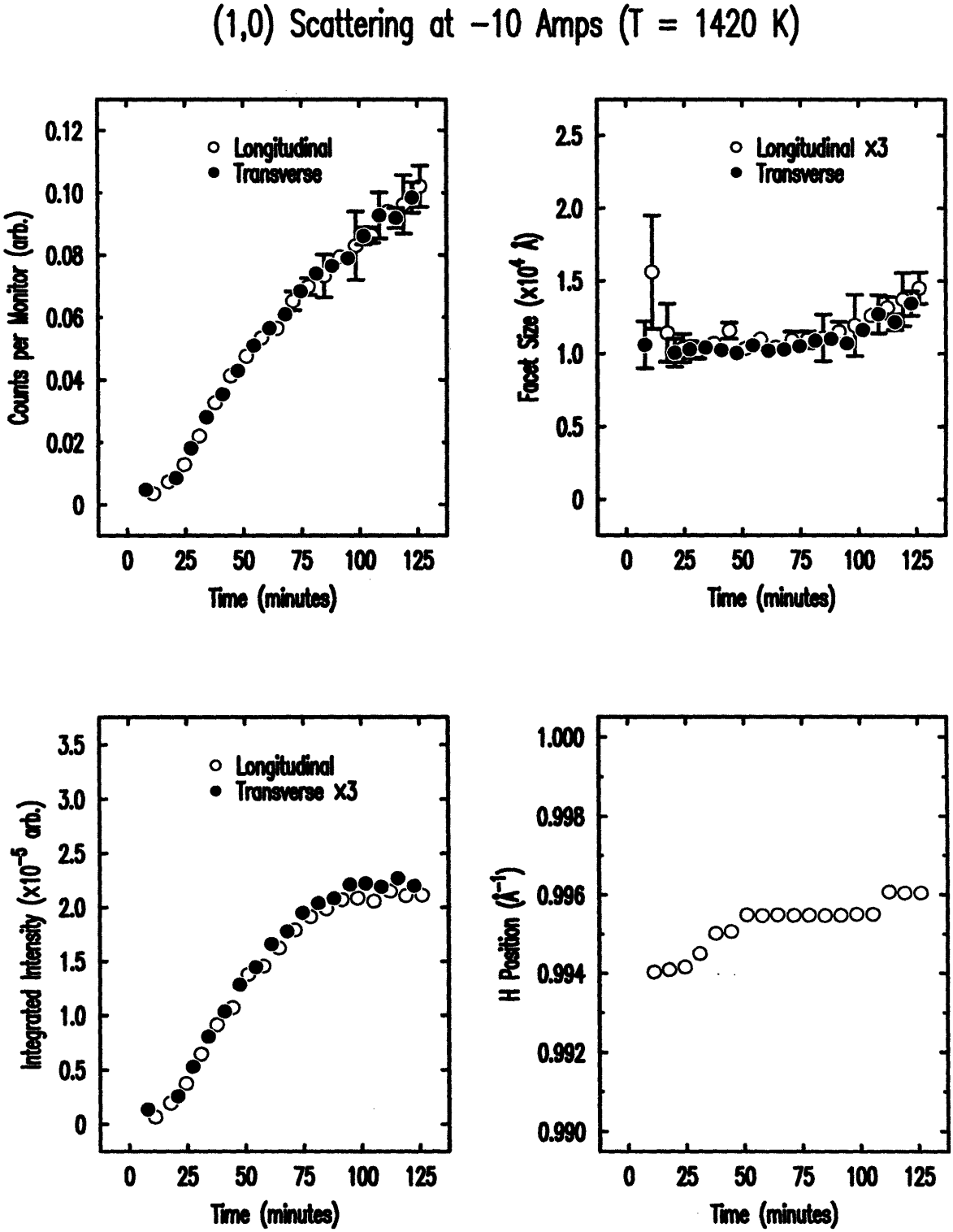

Figure 2-29: Results of the fits for the (1,0) peak at 1420 K (−10 Amps). The longitudinal facet size is multiplied by a factor of 3 for comparison with the transverse size. The transverse integrated intensity is likewise multiplied by a factor of 3.

the quench to 1420 K described above.

Step Ordering at T=1473 K (I=+11.8 Amps)

The results for the step peak data at +11.8 Amps (1473 K) are shown in Fig. 2-32. The longitudinal lengths (open symbols) have been multiplied by a factor of 5.6. The initial longitudinal step-step correlation length is only 200$\AA$, slightly larger than the 175$\AA$ measured at +10 Amps (1420 K). The transverse step-step correlation length of 1500$\AA$ is again comparable to the initial lengths measured at 1420 K, but is slightly smaller than the 1900$\AA$ observed in the initial measurements at 1376 K, lying just below one standard deviation in the calculated error bar. The longitudinal and transverse lengths at 1473 K have an anomalous behavior, similar to those at 1376 K, in that their ratio ($\xi_\perp/\xi_\parallel$) is initially very large (about 7.2) before ultimately converging to 5.6. The results of the step-step correlation length ratios for these two temperatures differ from the almost constant value of 5.6 measured at 1420 K. Of course, this anomalous evolution in the ratio of the lengths is also seen in the behavior of the integrated intensities. At both 1376 K and 1473 K with positive current the final ratio between the step-step correlation lengths ($\xi_\perp/\xi_\parallel$) converged to roughly 5.6, while at 1420 K and positive current this ratio was roughly 7.0. As the surface develops more highly correlated stepped regions, the step peak position moves toward smaller $q_\parallel$ from an initial peak separation of 0.0475 to its final value of 0.0345. These correspond to step densities which are slightly smaller than those measured at 1376 K and at 1420 K. This lack of agreement in the step densities at these three temperatures would be unsettling if this surface were uniformly stepped, since the surface must sustain a fixed macroscopic miscut. However, this is not the case at these temperatures as will be addressed in conjunction with the AFM images in the following section.

Step Disordering at T=1473 K (I=−11.8 Amps)

The disordering due to step bunching at −11.8 Amps is shown in Fig. 2-33 over a period of about one hour. The initial length ratio of 5.6 gradually increases to about

8.0 as the step peak slowly decays with time. The peak position data in Fig. 2-33 show that the step density is nearly constant for the first 30 minutes after which it rapidly increases in density to its final high-density value where the separation is 0.047, which agrees with the final values of 0.0496 and 0.051 determined at −8.6 Amps and −10 Amps, respectively. The constant peak position followed by an abrupt change at this temperature is similar to that observed at −10 Amps (1420 K), although the time-scale before the peak position begins to change is shorter by nearly 50%.

Rapid Unfaceting at T=1473 K (I=+11.8 Amps)

The results for the (1,0) peak at +11.8 Amps in Fig. 2-36 show a very rapid drop in both the peak intensity and integrated intensity over only 15 minutes. The facet dimensions again have a ratio ($\xi_\perp/\xi_\parallel$) of about 3.0 which is essentially constant with time. The longitudinal facet size changes by about a factor of 2 as the peak vanishes, with the width decreasing from its initial value of 3000$\mathring{A}$ to approximately 1500$\mathring{A}$ at the final time. A decrease in the time scale toward unfaceting of more than a factor of 3 is observed comparing the results at this temperature with those at 1420 K (+10 Amps). The peak intensity and integrated at 1473 K both scale with an exponential decay similar to those at 1420 K, although the characteristic change in the ratio of the lengths is not seen at these high temperatures due to the much shorter time constants.

Facet Growth at T=1473 K (I=−11.8 Amps)

Faceting on reversing the current to −11.8 Amps is shown in Fig. 2-37 over a long period of about 100 minutes. Immediately after the current reversal the peak intensity grows fairly rapidly while the longitudinal and transverse facet sizes are essentially unchanged. One can observe the onset of an approximately linear increase in the facet size with a concomitant saturation of the integrated intensity. During the first 40 minutes the ratio of the lengths ($\xi_\perp/\xi_\parallel$) is approximately 3, while the linear increase shows that the ratio approaches 2.25 after long times. The change in the ratio of the lengths is an artifact due to the failure in the approximation to the resolution which

becomes less precise when the peak widths are very sharp. This artifact also gives rise to the larger error bars for these data points. Thus, the overall characteristics in the peak widths are similar to those observed at -10 Amps and -8.6 Amps. Hence, it appears that there is a cross-over in behavior occurring approximately 40 minutes after switching current direction. Specifically, the (1,0) scattering widths continue to approach their resolution limit over a time-scale of about 100 minutes, even though the signal integrated intensity was saturated after the first 40 minutes. This behavior was not observed at the lower temperature points discussed above, even up nearly 200 minutes after current reversal, due to the slower dynamics at those temperatures. Recall that during the run at -10A faceting appeared to be almost saturated despite the fact that the length-scales had not reached their resolution limit.

The resolution limited (1,0) peaks correspond to facets of nearly macroscopic size extending on the order of 1 to 2 microns transversely and 0.7 microns longitudinally. This is in agreement with the AFM images and optical microscope images of this same 8° sample which was studied after quenching to room temperature from the faceted phase. These values are also consistent with previous surface diffraction results on smaller miscut samples [18, 20].

At positive current this stepped surface consists of steps which meander transversely. This cooperative behavior gives rise to micron size undulations perpendicular to $[11\bar{2}]$. During the course of these x-ray experiments, light from He-Ne laser ($\lambda = 6328\mathring{A}$) reflected from the sample surface revealed qualitative information about large length-scale surface undulations. Although there appeared to be some degree of reversibility of these undulations, no detailed studies were possible to determine the real-time dynamical behavior of large length-scale surface changes. These surface phenemona are described in the next section using Atomic Force Microscopy (AFM) imaging. However, it should be emphasized that the partially reversible changes observed in the x-ray experiments only strictly apply to structures with length-scales less than a couple of microns, and not to the larger surface undulations.

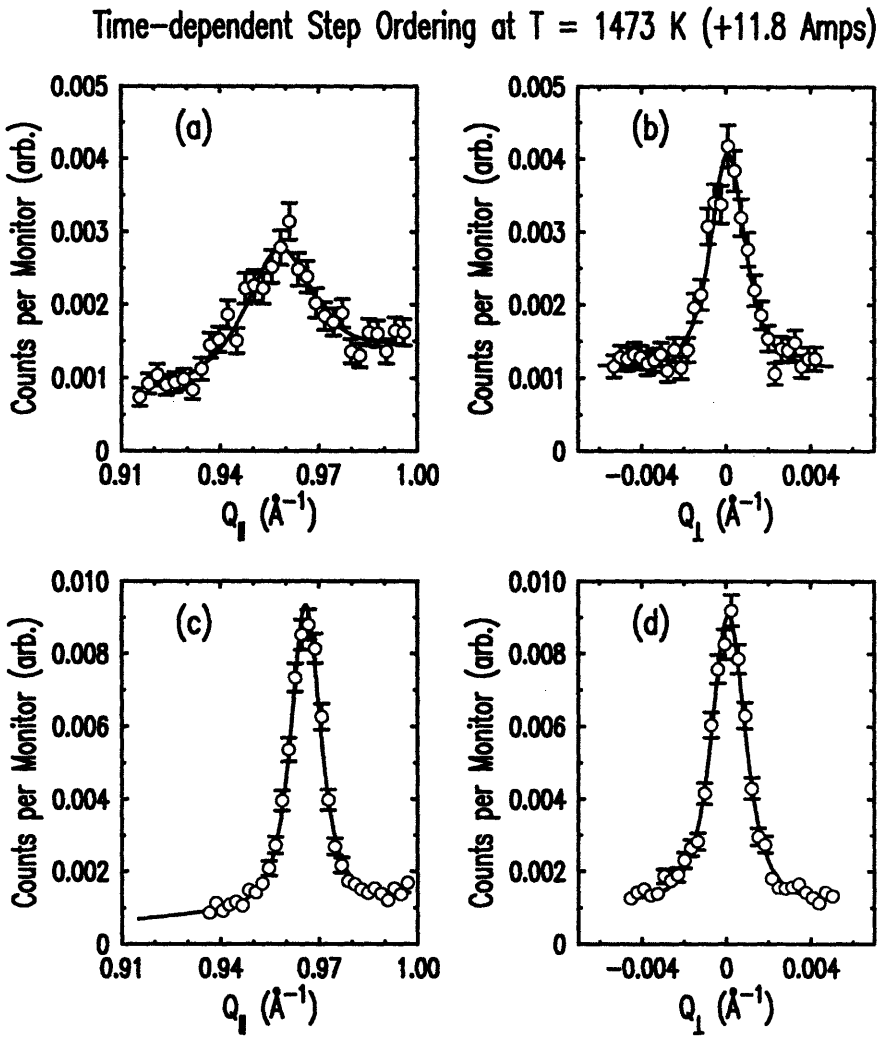

Figure 2-30: Longitudinal and transverse scans at the step peak at 1473 K (+11.8 Amps). The solid lines are fits to a Lorentzian to the power 1.75 as described in the text.

2.2.2 Optical and Atomic Force Microscopy Studies

This section describes the Optical and Atomic Force Microscopy studies of the surface structure for quenched vicinal Si(111). Following the x-ray experiments presented above, these Si(111) samples were quenched from high temperature to room temperature simply by switching off the current. The maximum sample cooling rate, determined mainly by radiative heat loss, is approximately 100 K/sec above 850 K.

Figure 2-38 shows a $100\times100\mu^2$ AFM image conducted in atmosphere showing a quenched surface which had been faceted by the action of electromigration at $\sim$ 1490 K with current in the step-up (negative) direction. The facet widths are roughly

1.5μ along the $[11\bar{2}]$ direction (vertical) and $> 10\mu$ in extent in the $[\bar{1}10]$ direction (horizontal). The step bunched regions wander dramatically, consistent with the step disordering observed in the x-ray diffraction data taken at this temperature and current direction. One should note that the longitudinal facet size exceeds the resolution of the x-ray experiment, and thus is substantially larger than expected.

A three-dimensional view of a similar faceted surface is shown in the AFM image of Fig. 2-38 for a 4° miscut sample. This sample was prepared at negative current in exactly the same manner as described previously, although it was heated immediately to $\sim$ 1520 K and then held at fixed temperature for several hours before quenching to room temperature. Facets of longitudinal extents varying from about 7μ to about 12μ are seen and these are separated by step bands which wander transversely. An approximate linear analysis of the facet structure can be made by examining Fig. 2-39 which shows a cross-section of the sample. One can see that the step bands on this sample have two inclinations toward and away from the $[11\bar{2}]$ direction. A single step band region is on average 5μ across measuring the distance from the upper side of one flat terrace to the bottom a step band. These "negatively" inclined step bands require steps which flow in the same direction as the current. Clearly, a "hill-like" distortion in the surface would be necessary before such a formation could occur since step barriers or generally not sufficient to induce a bias to destabilize the steps under electromigration. The microscopic mechanism for this anomalous step formation shown in Fig. 2-38 remains to be understood, it is most likely the result of electromigration combined with the relatively high sublimation rates at these high temperatures.

Fig. 2-41 shows an AFM image of the 8° miscut sample described above after quenching from a "faceted" surface state. This image was taken after extensive x-ray studies were conducted and thus had experienced a large amount of sublimation. This sample was quenched to 1060 K (within the two-phase reconstructed region) from a relatively low temperature of about 1270 K, before finally quenching to room temperature. This sample does not show the usual large flat <111> facet regions such as those shown in Fig. 2-38 probably due to the excessive amount of sublimation over

the long times involved in the experiment. One surprising feature apparent in this image is the long wavelength surface undulation in the [11$\bar{2}$] direction. A linear section analysis of these *aperiodic* undulations show an average peak-to-peak lateral distance of approximately 14μ and a vertical peak-to-valley distance of about 0.25μ.

Details of the "peak" and "valley" structures on this surface can be seen in Figs. 2-42 and 2-43 which are AFM images over a 5×5μ^2 area revealing terraces. It is not possible to discern 1×1 terraces from 7×7 terraces from these images since the native oxide on silicon limits the atomic resolution required to make this distinction. However, it is very likely that 1×1 terraces are predominant on this quenched surface despite the time spent in the two-phase reconstruction region before cooling to room temperature. The reason for this is simply because a nucleation barrier can prevent the development of 7×7 order which typically begins forming near step edges. On this surface the apparent terrace disorder would imply a large barrier against such nucleation. In Fig. 2-43, the "valley" of the surface shows nearly regularly spaced terraces with an average longitudinal extent of about 650Å, although the linear section analysis shows that no strong periodicity occurs. A large number of terraces distributed along the surface allow the valley and peak regions to vary almost smoothly in orientation. The absence of step bands could be the result of the slower quenching rate for this sample.

The two-dimensional projection of AFM data in Fig. 2-44 shows surface undulations caused by step wandering at positive current on a 4° miscut sample. This image shows the backside of the same quenched sample shown in Fig. 2-40. The light colored regions represent the "peaks" in the undulations while the darker colored regions represent the "valleys". The branch-like features in this image are the dominant characteristics of the transverse instability discussed with reference to the phase diagram of Fig. 2-6. These undulations are more apparent in Fig. 2-45 which shows a three-dimensional representation of similar data on the backside of the 8° discussed above. In this figure, positive current had induced a step ordering with a transverse instability resulting in dramatic transverse undulations in the surface with 10μ peak-to-peak distance along [$\bar{1}$10].

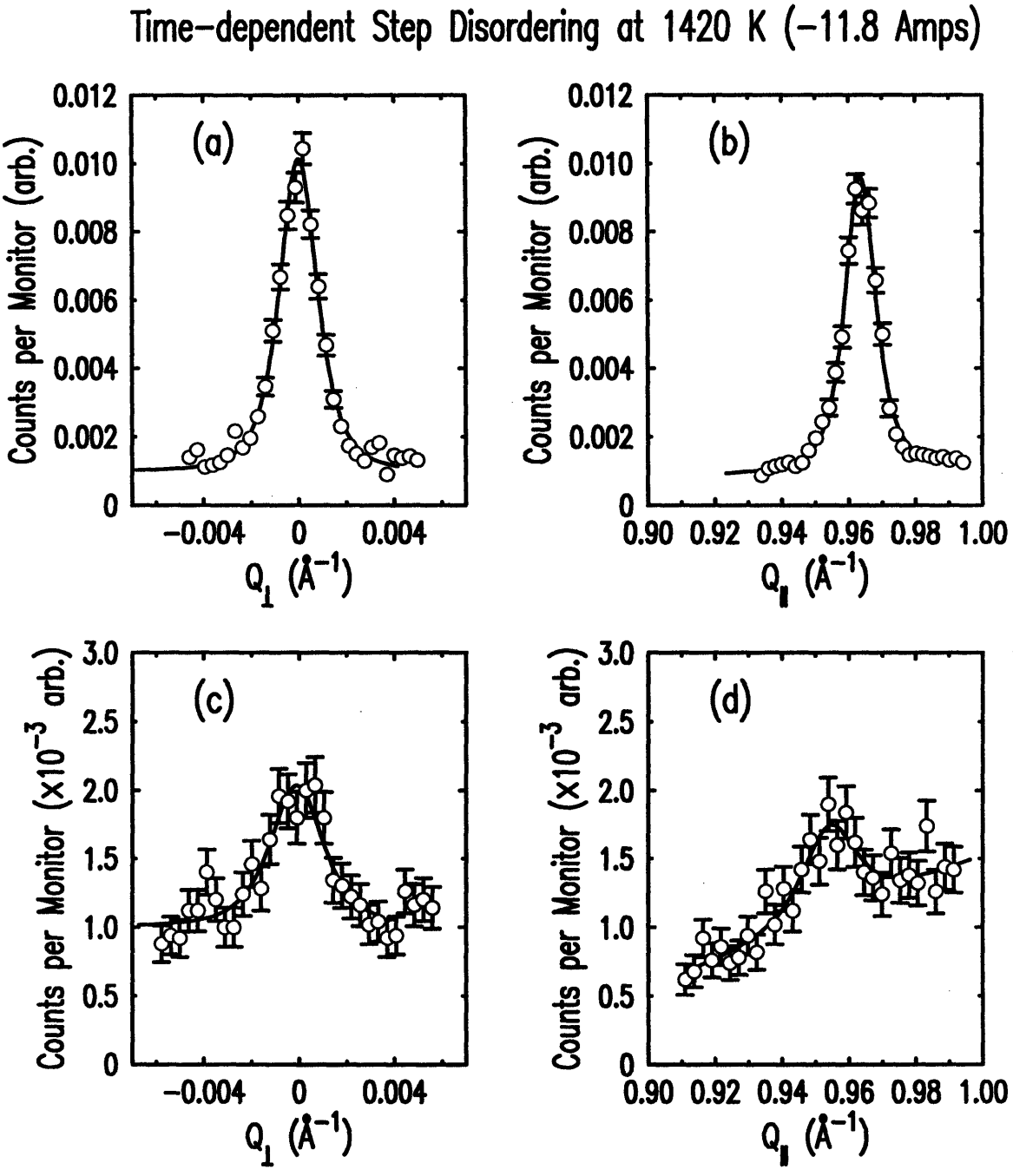

Figure 2-31: Longitudinal and transverse scans at the step peak at T=1473 K (−11.8 Amps). The solid lines are fits to a Lorentzian to the power 1.75 as described in the text.

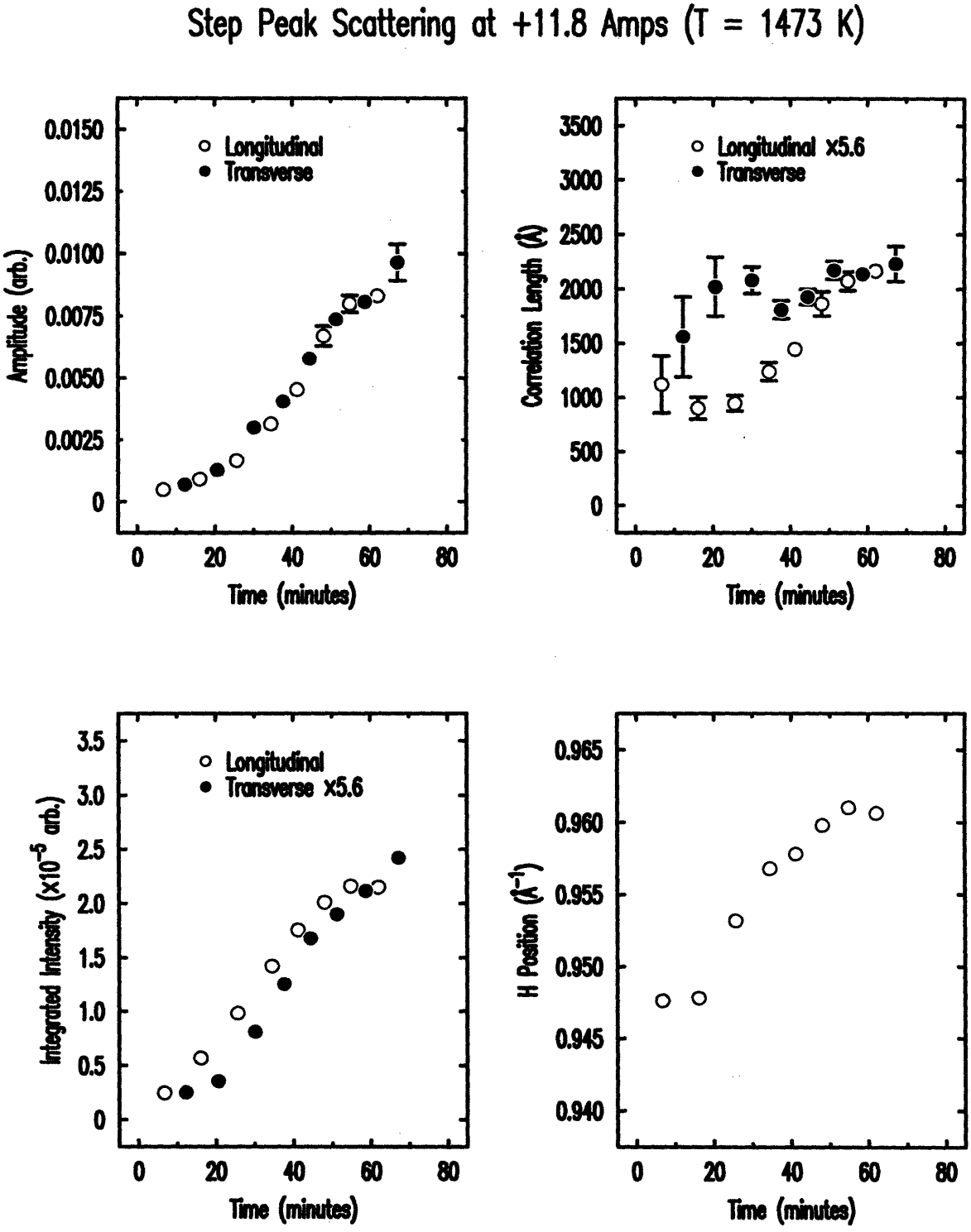

Figure 2-32: Results of the fits for the step peak at 1473 K (+11.8 Amps). The longitudinal step-step correlation length is multiplied by a factor of 5.6 for comparison with the transverse step-step correlation length. The transverse integrated intensity is multiplied by this same factor of 5.6.

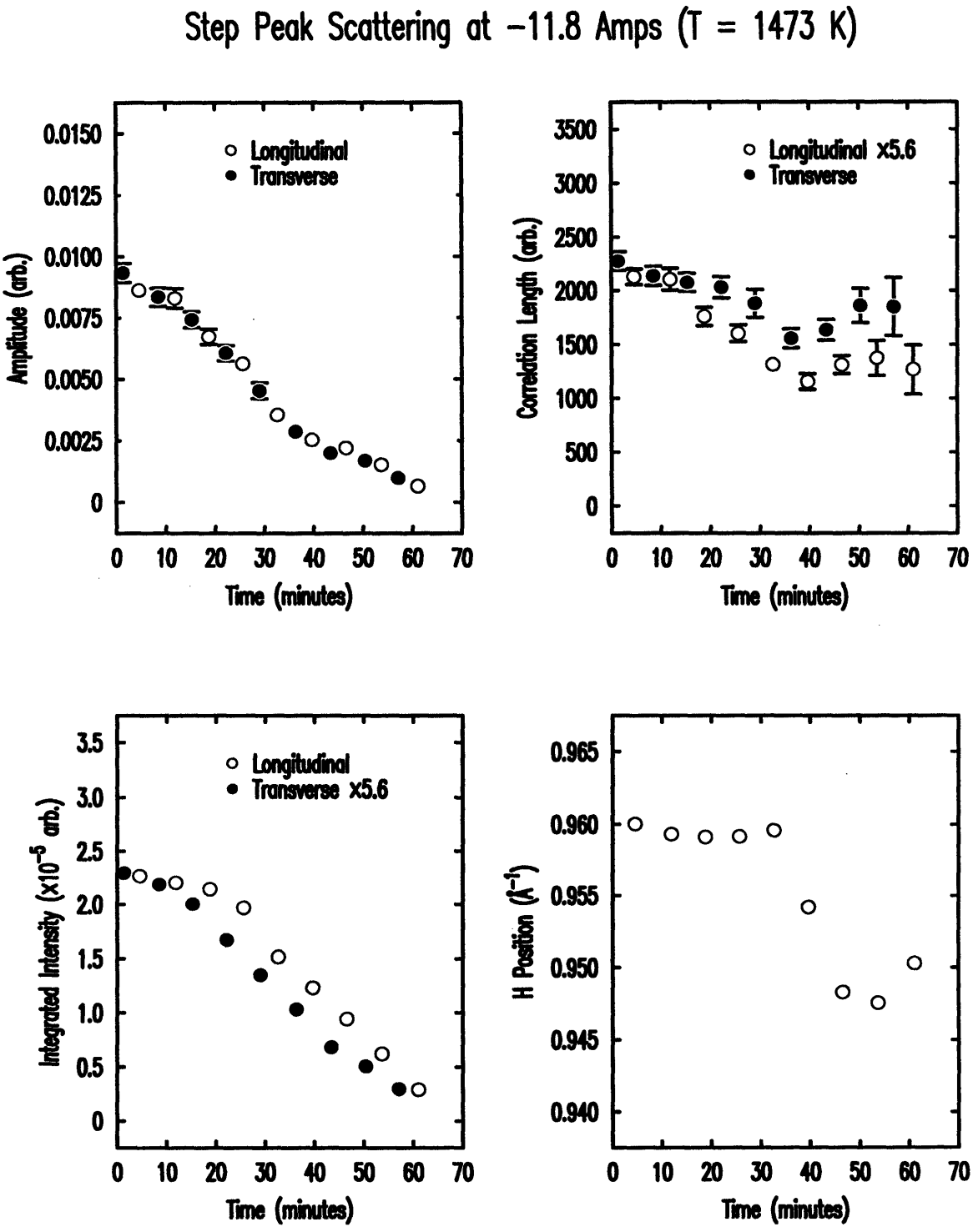

Figure 2-33: Results of the fits for the step peak at 1473 K (−11.8 Amps). The longitudinal step-step correlation length is multiplied by a factor of 5.6 for comparison with the transverse step-step correlation length. The transverse integrated intensity is multiplied by this same factor of 5.6.

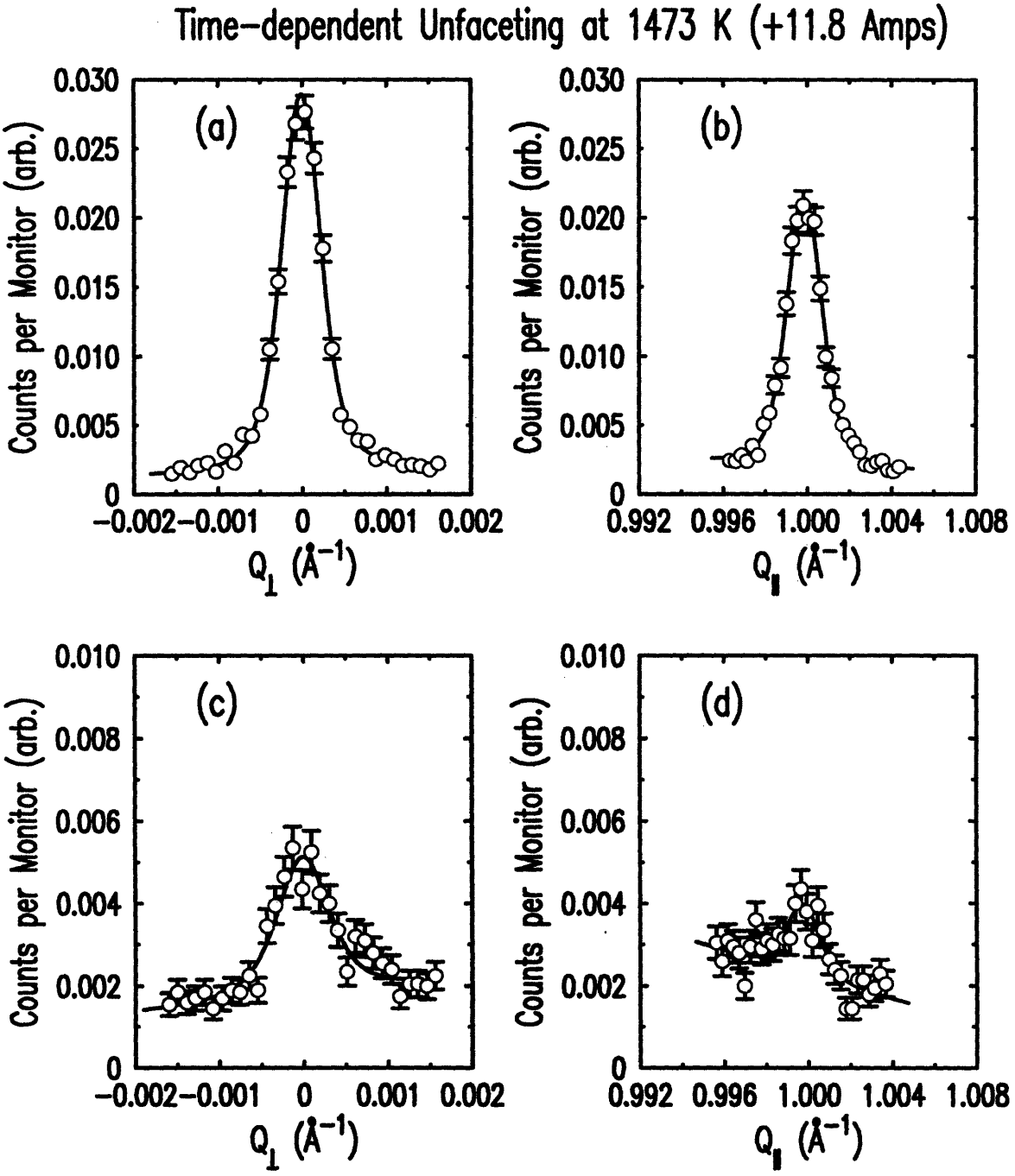

Figure 2-34: Longitudinal and transverse scans at (1,0) peak at 1473 K and +11.8 Amps. (a) and (b) are immediately after reversing the current direction, (c) and (d) are after approximately 15 minutes have elapsed showing a rapid unfaceting of the surface. The solid lines are fits to a Lorentzian to the power 1.5.

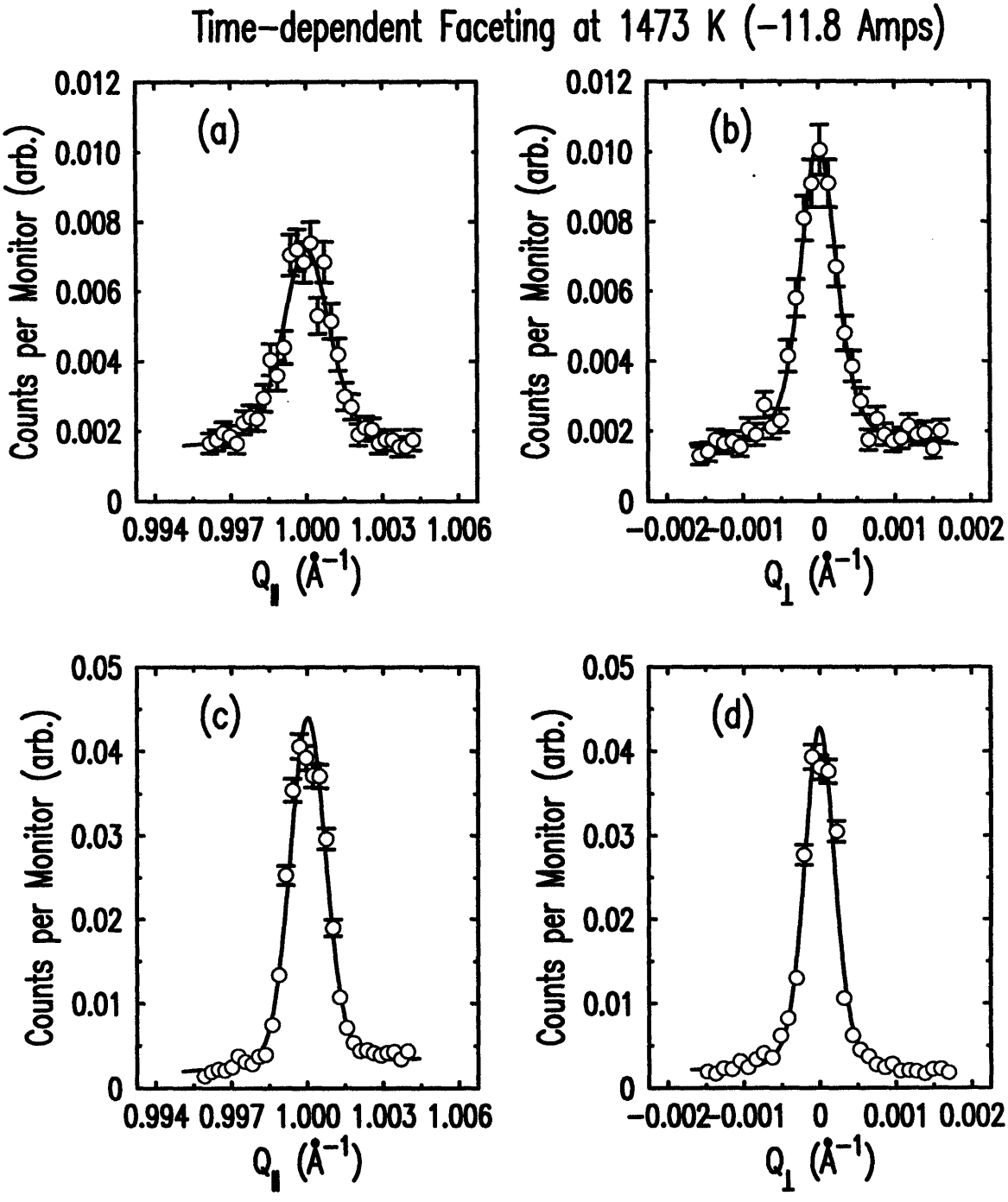

Figure 2-35: Longitudinal and transverse scans at (1,0) peak at 1473 K and −11.8 Amps. (a) and (b) are immediately after reversing the current direction, (c) and (d) are after approximately 100 minutes have elapsed. The solid lines are fits to a Lorentzian to the power 1.5.

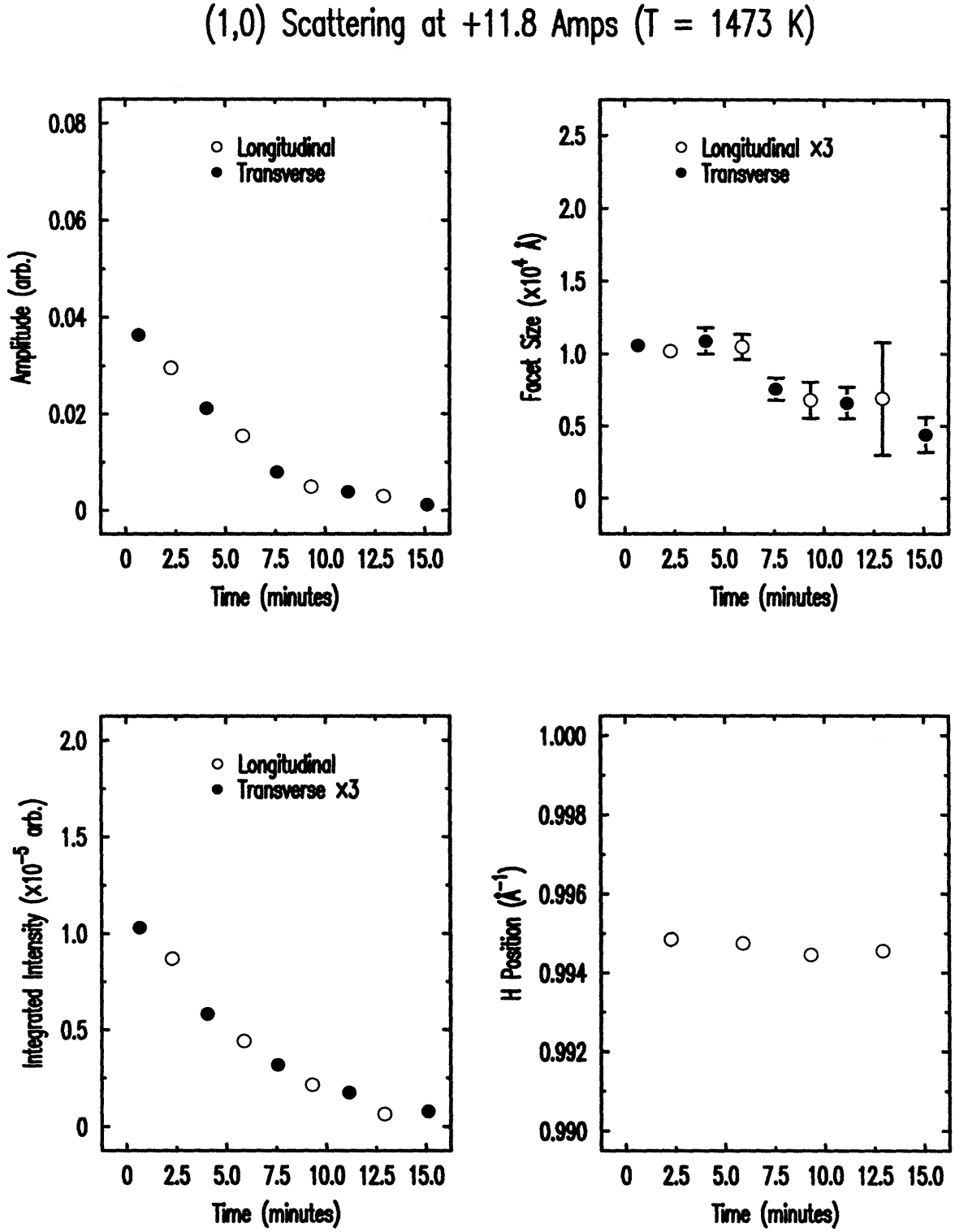

Figure 2-36: Results of the fits for the (1,0) peak at 1473 K (+11.8 Amps). The longitudinal facet size is multiplied by a factor of 3 for comparison with the transverse size. The transverse integrated intensity is likewise multiplied by a factor of 3.

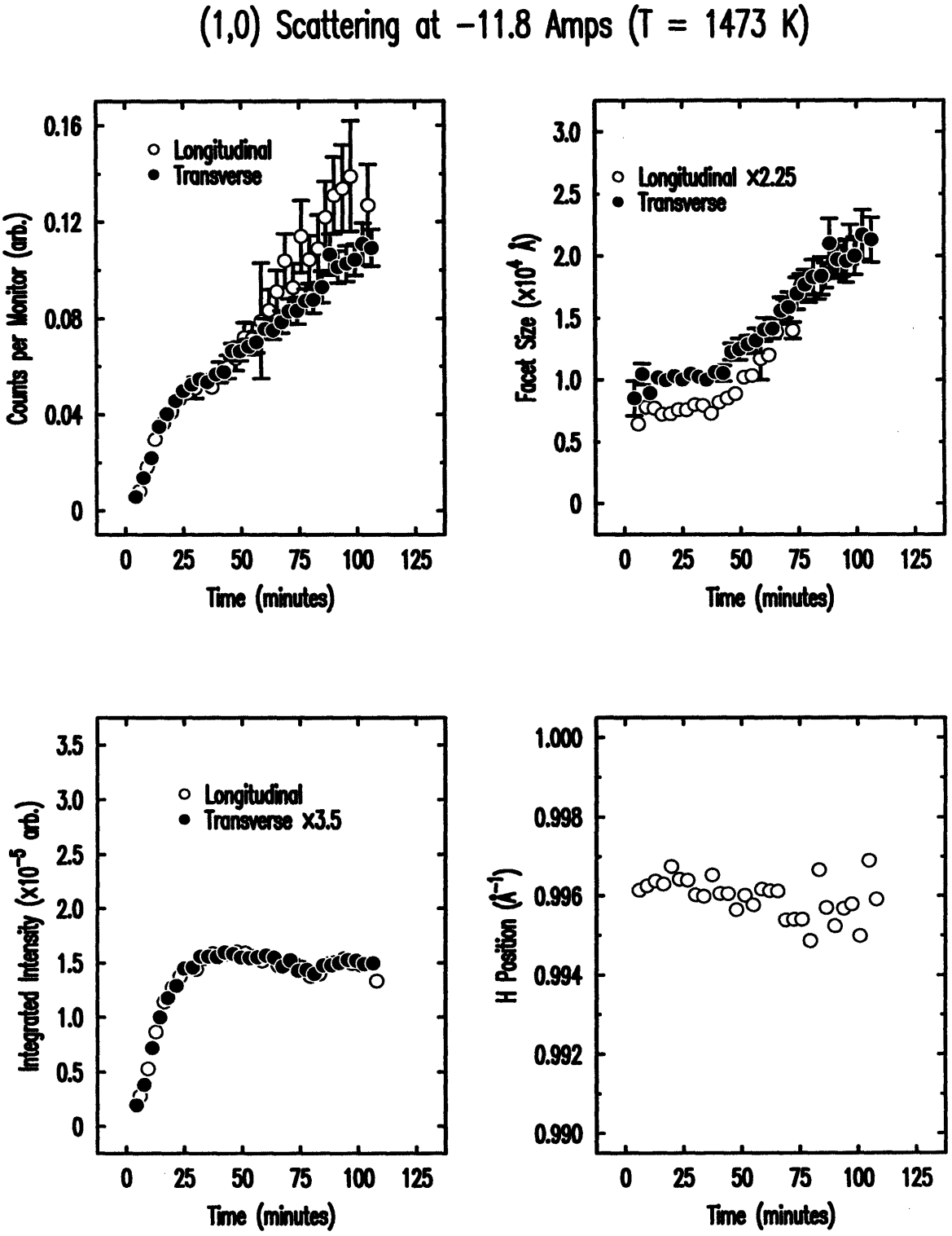

Figure 2-37: Results of the fits for the (1,0) peak at 1473 K (−11.8 Amps). The longitudinal facet size is multiplied by a factor of 2.25 for comparison with the transverse size. The transverse integrated intensity is likewise multiplied by a factor of 3.5. The difference in these two factors reflects the breakdown in the fitting approximation for these nearly resolution limited scans, as is indicated by the larger error bars.

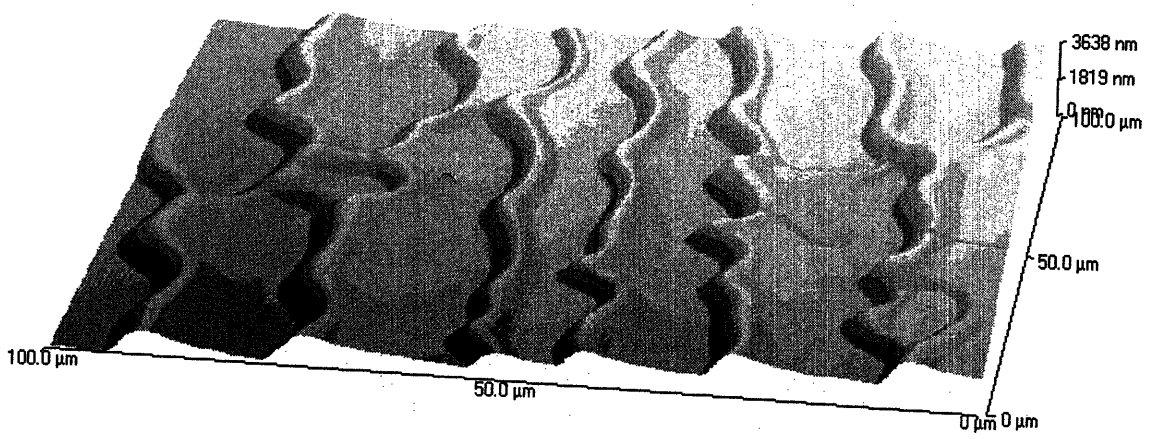

Figure 2-38: AFM image of a sample quenched from 1450K showing large facets with disordered stepped regions resulting from excessive sublimation under the influence of electromigration.

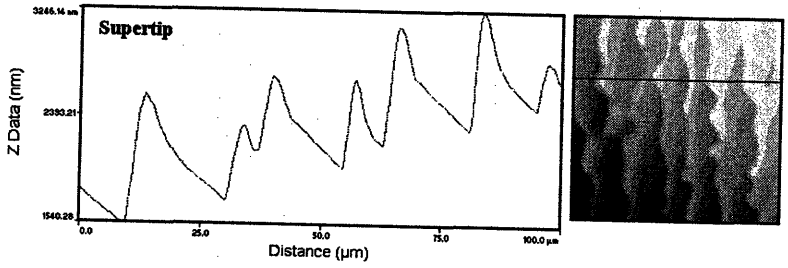

Figure 2-39: An linear slice from the AFM image in Fig. 2-38. This demonstrates that the stepped regions of the surface possess two oppositely inclined orientations.

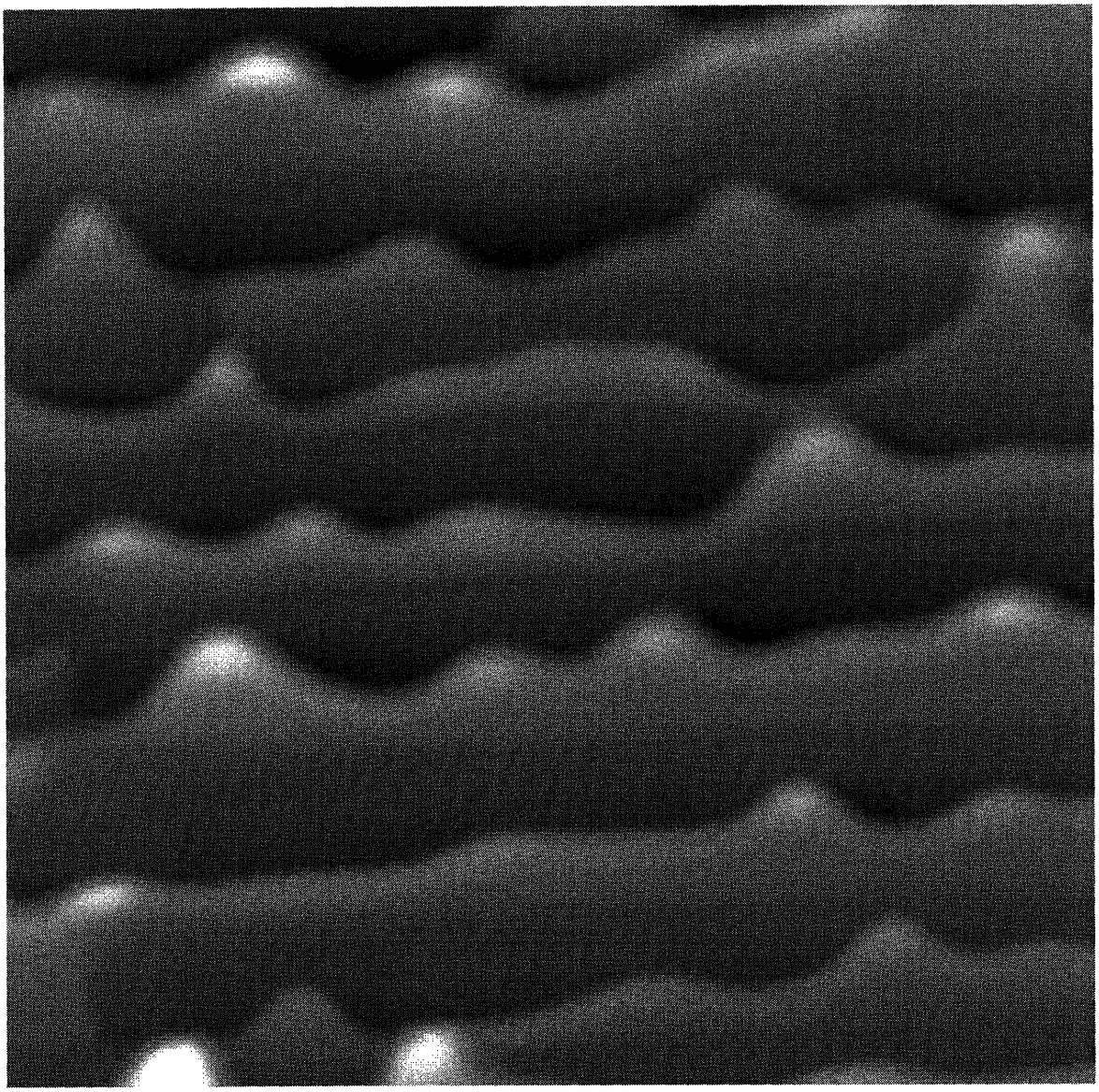

Figure 2-40: AFM imaging demonstrating electromigration-driven faceting at negative current. This sample was quenched to room temperature from a temperature of $\sim$1490 K. Facets are roughly 1.5μ along the [11$\bar{2}$] direction (vertical axis), and >10μ in extent in the [$\bar{1}$10] direction (horizontal axis). Wandering step bands indicate substantial step disorder.

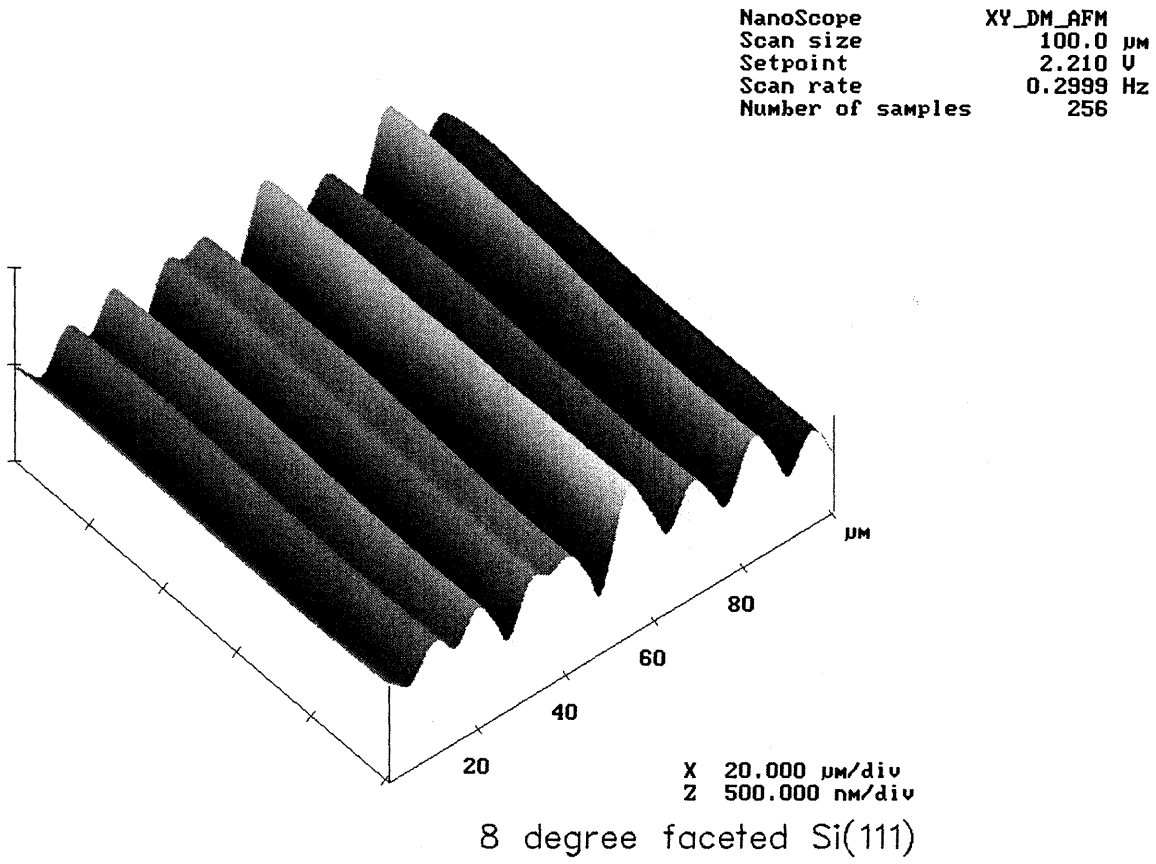

Figure 2-41: AFM image of quenched surface showing facet undulations after treating the sample at negative current.

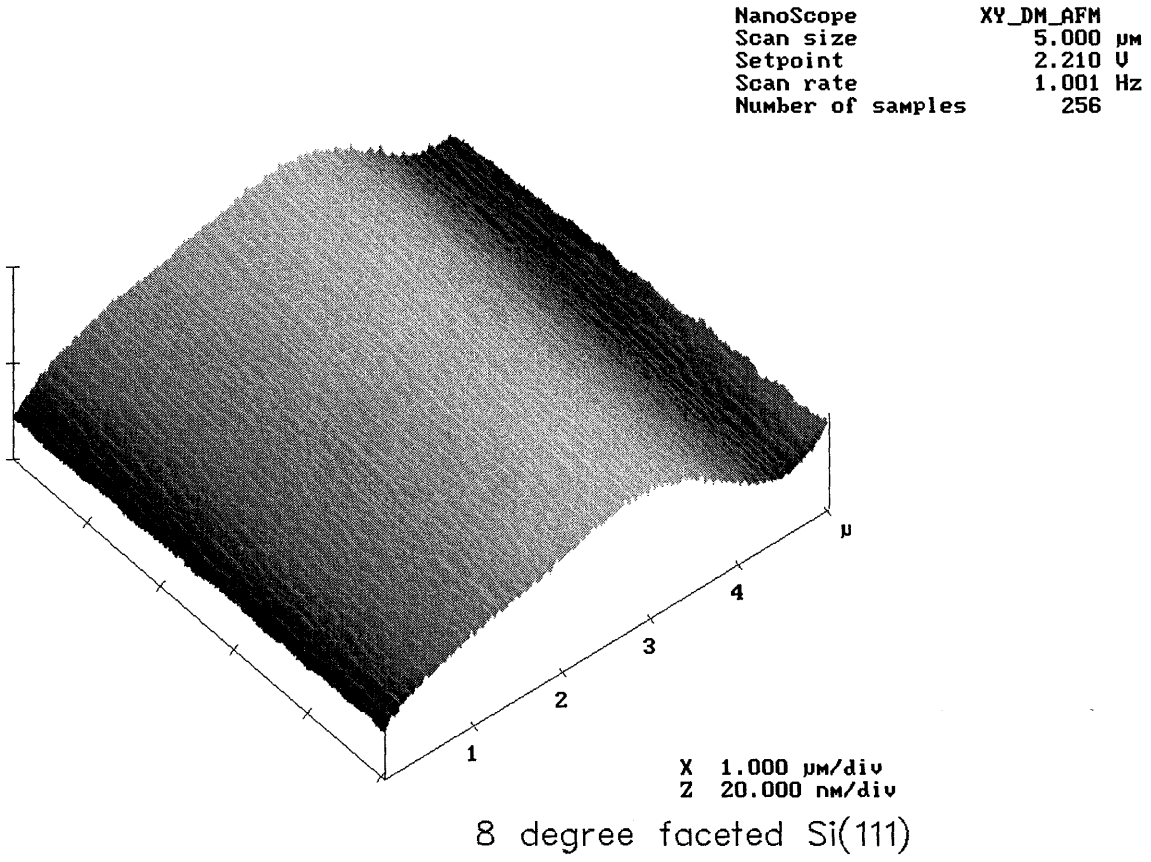

Figure 2-42: AFM image of a quenched surface showing a $5\times5\mu$ region near the peak of a single facet undulation.

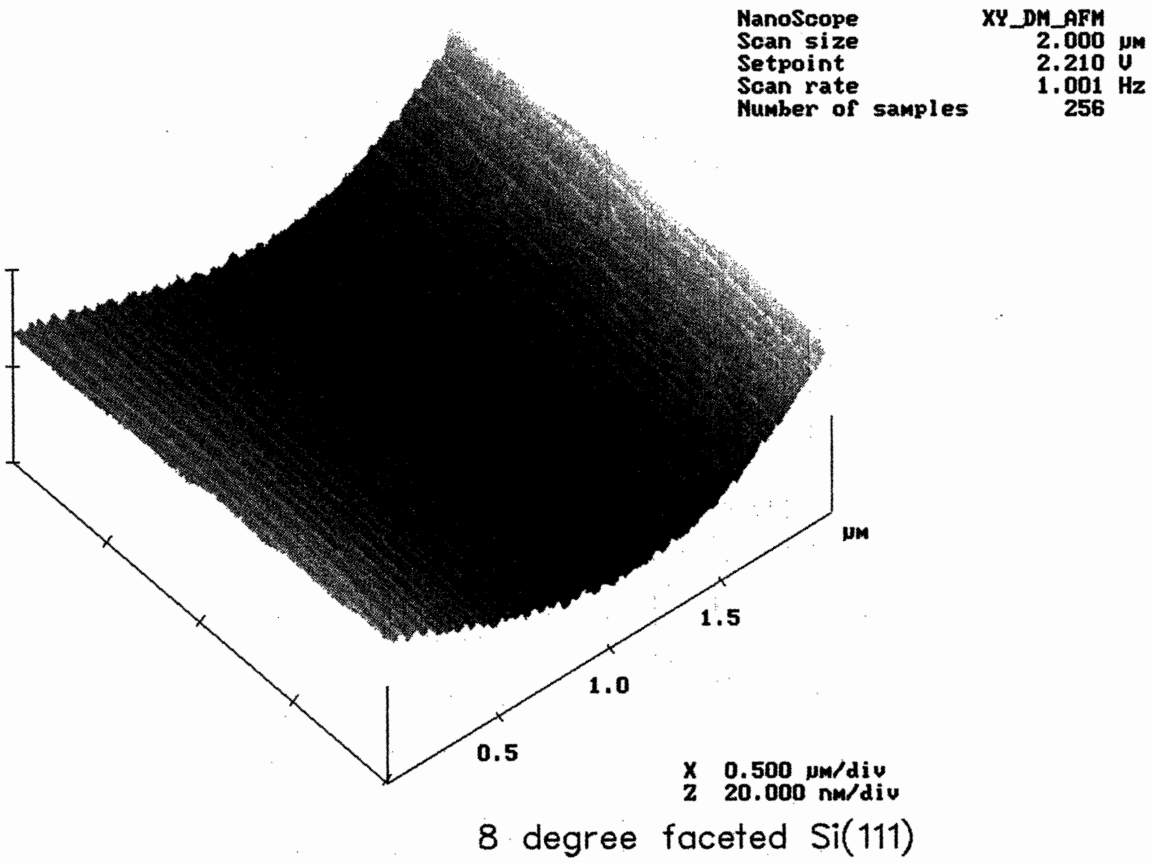

Figure 2-43: AFM image of a quenched surface showing a $5 \times 5\mu$ region near the valley of a single facet undulation. The terraces appear less disordered within this region of the surface than those observed in the peak regions.

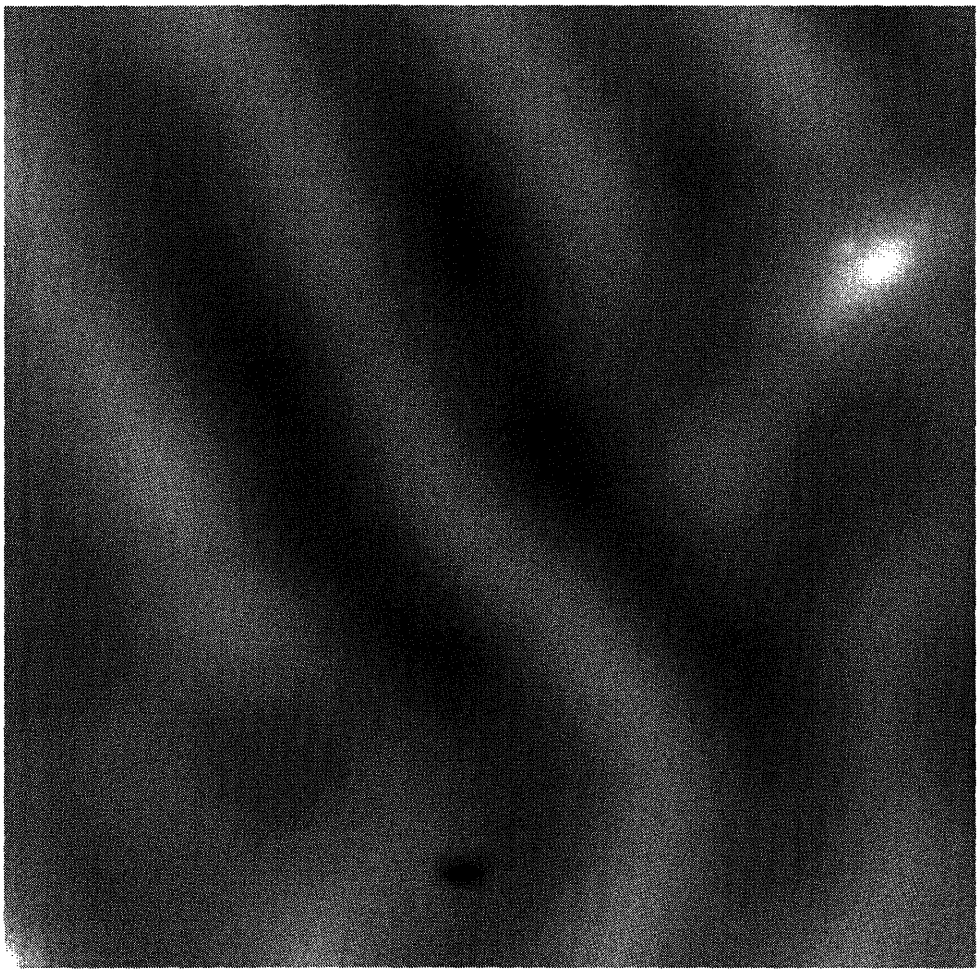

Figure 2-44: AFM image of a 4° miscut sample quenched from high temperature at positive current showing the large transverse undulations resulting from a transverse meandering of steps at positive current.

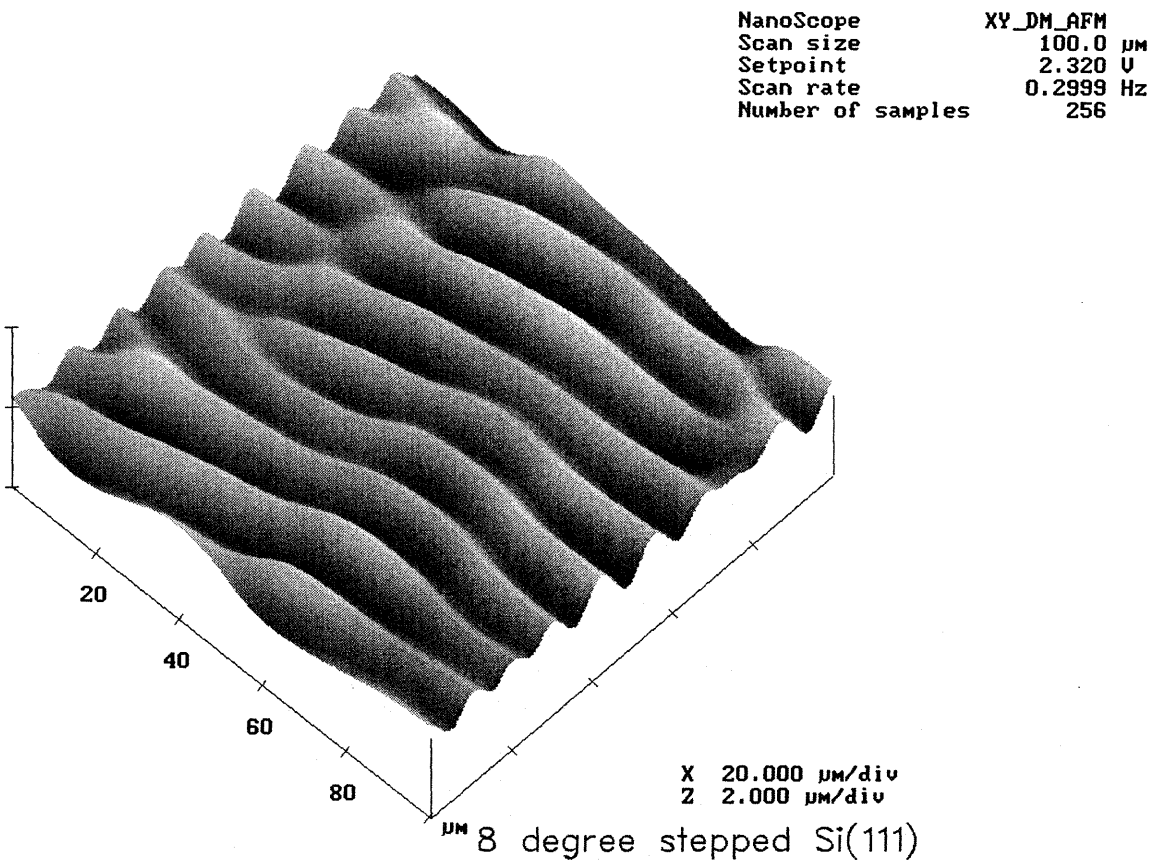

Figure 2-45: AFM image of an 8° miscut sample which was quenched from positive current in the stepped regime showing dramatic transverse undulations in the step pattern. The surface modulation is roughly perpendicular to $(11\bar{2})$. Note, the z scale is 2μ per division.

2.3 Models for Electromigration-driven Step Behavior

In this section, continuum and microscopic models describing the behavior of steps on surfaces under the action of an applied (electric) field are addressed and compared to the experimental results from the last section. The shortcomings of these theoretical models and the recent theoretical and experimental advancements that have been made in understanding the phenomena of electromigration-driven step behavior are discussed.

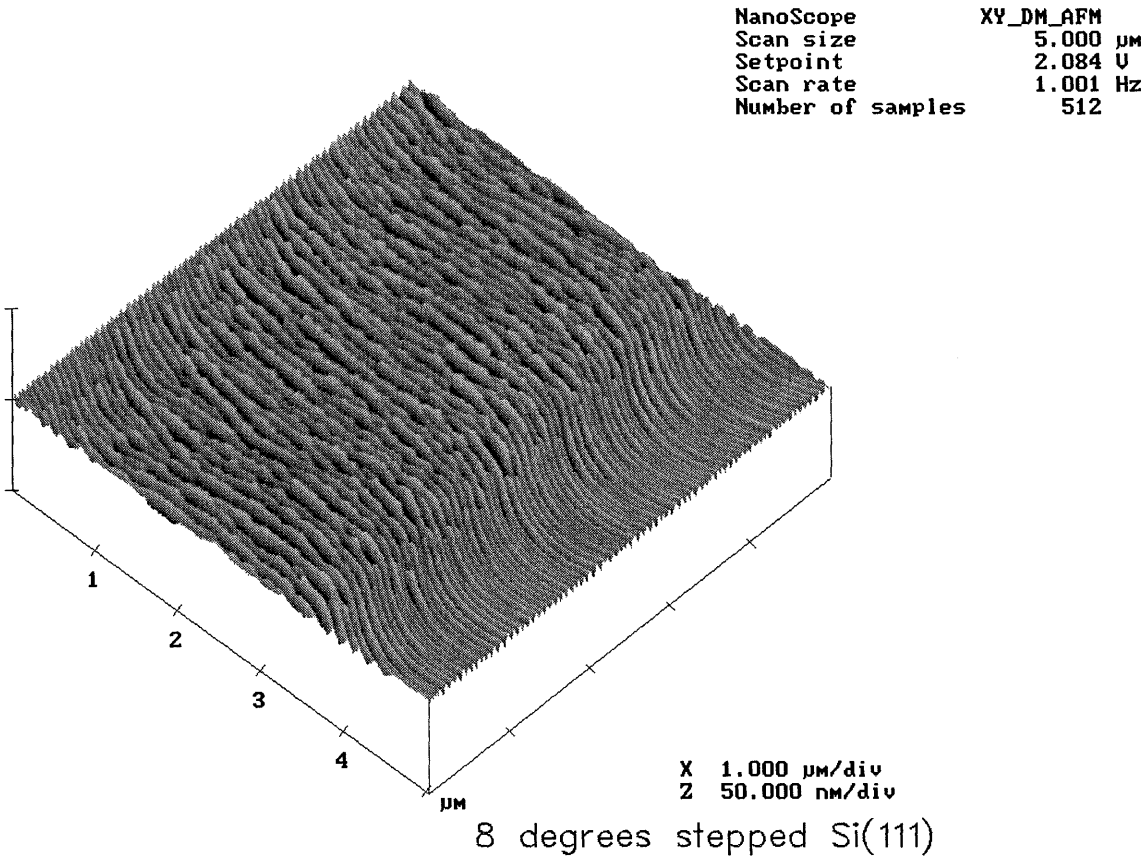

Figure 2-46: Detail from one of the branching points of the AFM image of Fig. 2-45 of an 8° miscut sample which was quenched from positive current in the stepped regime. Disordered 1×1 terraces are shown in the central portion of the image while smoothly varying terraces are observed on either edge. This image shows that the terrace disordering is greatest in the uppermost region of the branches. The z scale is 500 Å per division. Note, the scan direction of this image is orthogonal to that of Fig. 2-45 to maximize the resolution.

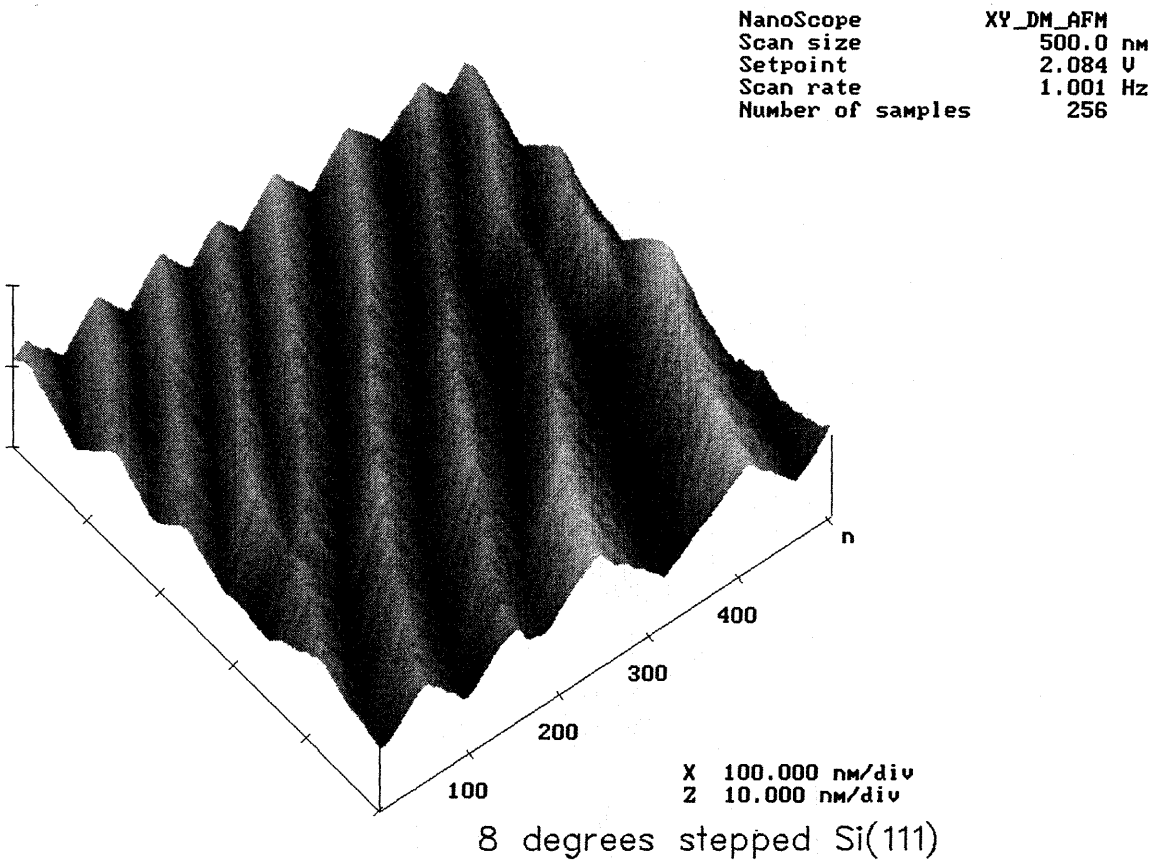

Figure 2-47: AFM image showing some of the details from the 1×1 terrace regions of the AFM image of Fig. 2-46. This image is from a 5000×5000Å^2 area roughly located in the upper right-hand corner of Fig. 2-46 along the smoothly varying terraces. The z scale is 100 Å per division. Although single steps are not distinguishable, small groups of steps can be resolved showing some regularity of the step arrangements consistent with the *in-situ* x-ray data.

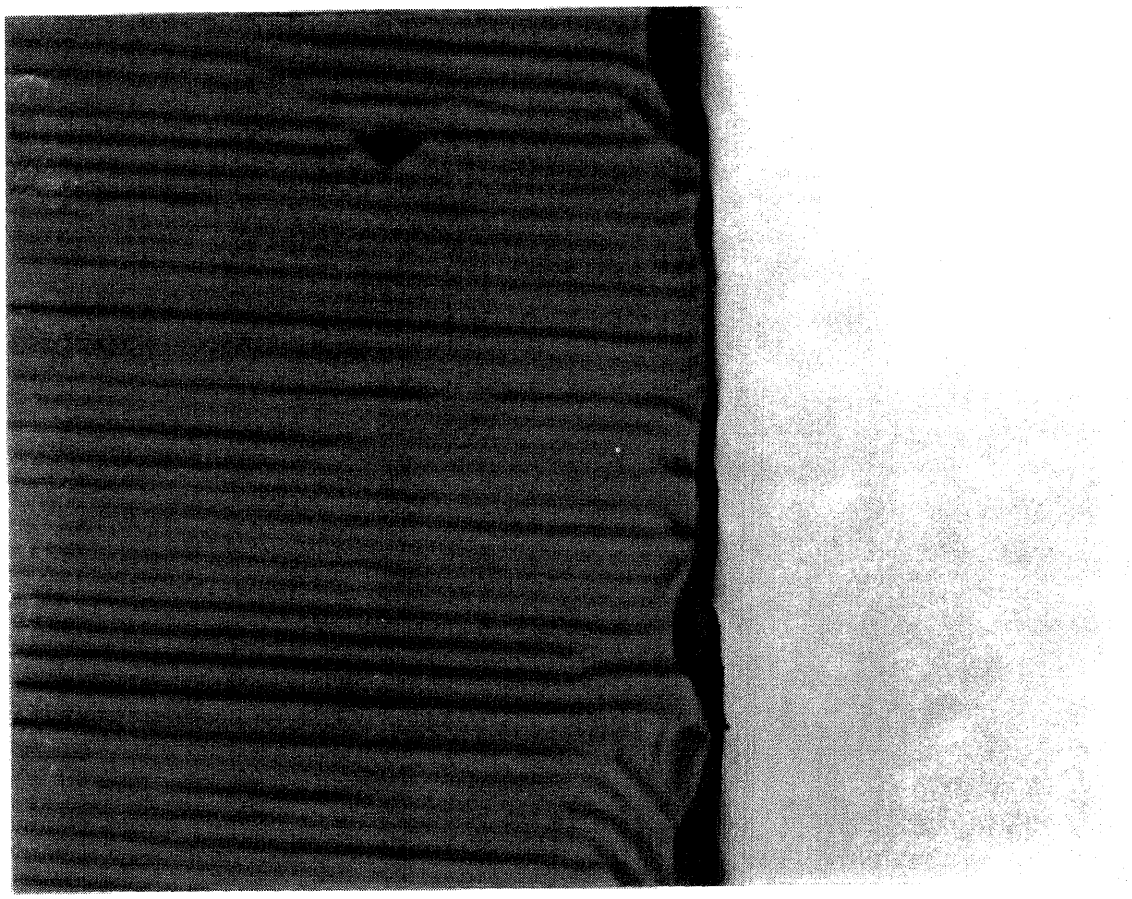

Figure 2-48: Optical microscope photograph of a quenched Si(111) sample showing large facets. This is the opposite of the same sample shown in Fig. 2-49.

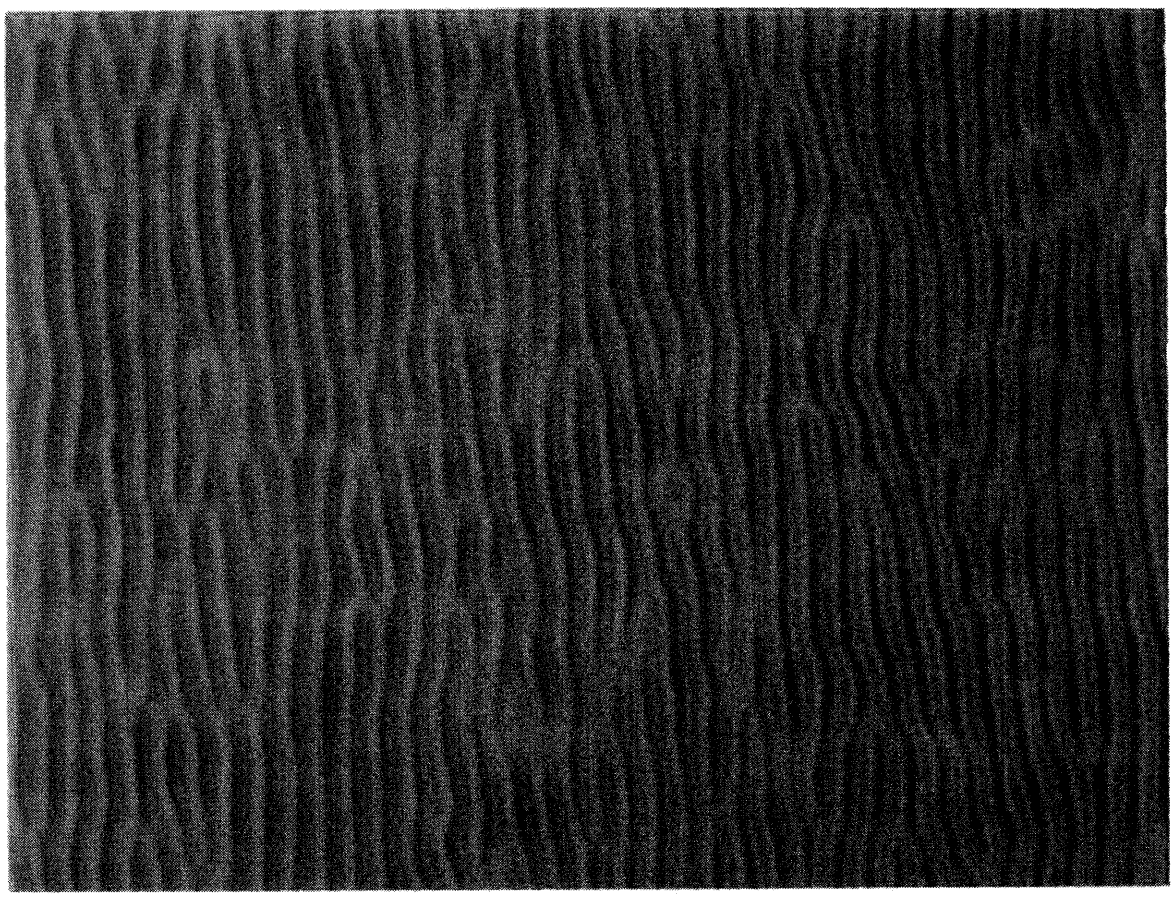

Figure 2-49: Optical microscope photograph of a quenched Si(111) sample showing large wavelength transverse undulations. This is the backside of the sample shown in Fig. 2-48.

2.3.1 A Continuum Model for Step Dynamics

A nonlinear continuum model recently developed by Misbah and Pierre-Louis (M-PL model) predicts that step bunching dynamics obey an equation with solutions which lead to a mixture of surface states yielding both solitons and spatio-temporal chaotic behavior [32]. The derivation, which is outlined below, starts with seemingly conventional approach using the Burton-Cabrera-Frank model [1] with the addition of electromigration and evaporation terms. As the resulting numerical solutions of this model reveal surface morphologies with overall features strikingly similar to those observed in experiment, it would be useful to present some of the details of this model. However, one should use caution in applying the results of this *one-dimensional* model to a two-dimensional surface as such a model is strictly valid only for relatively straight steps. Further caveats are provided in the discussion section.

In this model for step flow, many of the physical quantities relevant in experimentally realizable systems (such as adatom diffusion, electromigration, evaporation, and sticking at step edges) are explicitly included in order to obtain a realistic description of the step dynamics. For moderate temperatures, advacancies at the surface can be ignored. [A model including advacancies and adatoms under the influence of an electromigration force at sublimating temperatures is presented in ref.[33]. It is purported that advacancies can induce step instabilities even without an electromigrative term. However, there is no direct evidence that *any* advancies are present on the Si(111) surface at these temperatures.] In setting up the basic relationships for the model one can write a one-dimensional diffusion equation for the time-dependent adatom areal concentration field $c(\mathbf{r}, t)$ by imposing mass conservation:

$$\frac{\partial c}{\partial t} = D\nabla^2 c - \frac{c}{\tau} - \frac{DF}{k_B T}\frac{\partial c}{\partial z}. \tag{2.10}$$

The coordinate z is the displacement from the equilibrium position (along the miscut direction in the experimental system), τ is the desorption time for an adatom to leave the surface, and D is the usual adatom diffusion constant. The electromigration

force enters through the factor F which is defined such that positive F corresponds to an electric field exerting a force on the adatom in the direction of the field. As will be explained below this condition can be completely reversed in the case that enhanced electron densities in the vicinity of the adatoms change the effective charge of the adatom. The effect of adding advacancies to the system will be explained below. Also, the transverse wandering of steps is completely neglected as it adds an unnecessary level of complexity to the analysis. Despite these approximations, many of the salient features of step bunching can be ascertained from this simple model. The result of neglecting the meandering of steps in a full two-dimensional system will be discussed later.

In order to apply the above formalism to a stepped surface, one must establish the boundary conditions at each step edge. This requires some thermodynamic relationships relating the step kinetics to the parameters in the model equation (D, F and the thermal excitation energy k_BT). In the absence of an electromigration term, kinetics dictate that each step will advance by an amount which depends on the concentration gradient in the direction of motion. To see this, consider the simple steady-state case where adatoms impinge on the steps with a constant frequency. The velocity of each point on a step in the direction of the step normal would satisfy

$$v_n \Delta c_s = D\mathbf{n} \cdot \vec{\nabla} c \,. \tag{2.11}$$

The quantity Δc_s is simply the difference in the areal density of atoms on crossing a step and v_n is the kinetic coefficient. If kinetics are fast, the step concentration c is larger than the equilibrium concentration for a straight step (c_{eq}) by a factor $1 + \kappa\Omega\gamma/k_BT$. This can be calculated [1, 34] by first assuming that the chemical potentials of the step (a continuous capture center of adatoms) and the adatom gas are at equilibrium at both sides of a step, namely

$$\mu_s(p_s) = \mu(p_g, c) \,. \tag{2.12}$$

Expanding μ around its equilibrium value gives

$$(p_s - p_g)(\partial\mu_s/\partial p)_{p=p_g,c=c_{eq}} = (c - c_{eq})(\partial\mu_g/\partial c)_{p=p_g,c=c_{eq}}\,. \tag{2.13}$$

This expression can be simplified by assuming that the pressure in the solid phase, p_s, does reversible adiabatic work to change the surface area bounded by a step, Ω, and hence, from equilibrium thermodynamics, $\partial\mu_s/\partial p = \Omega$. Similarly, the gas of adatoms behaves approximately like an ideal gas, hence we make the approximation, $\partial\mu_g/\partial c = k_BT/c_{eq}$. According to Eq. 2.13, close to equilibrium the step concentration will satisfy

$$c - c_{eq} = \frac{c_{eq}\Omega}{k_BT}(p_s - p_g)\,. \tag{2.14}$$

Assuming mechanical equilibrium is established by the line tension of the steps, the quantity $(p_s - p_g)$ is equal to $\gamma\kappa$, where γ is the step tension and κ is the step curvature. Hence,

$$c - c_{eq} = \frac{c_{eq}\Omega}{k_BT}\gamma\kappa\,, \tag{2.15}$$

or,

$$c - c_{eq}(1 + \frac{\Omega}{k_BT}\gamma\kappa) = 0\,. \tag{2.16}$$

In the dynamical case, with electromigration force F driving the step motion, one gets a relationship analogous to Eq. 2.11, quoted here without proof.

$$\pm D[\frac{\partial c}{\partial n} - \frac{F}{k_BT}c]_{\pm} = v_{\pm}[c - c_{eq}(1 + \frac{\Omega}{k_BT}\gamma\kappa)]\,. \tag{2.17}$$

In this expression, the gas of adatoms is allowed to possess kinetic coefficients which take explicit account of the asymmetry in the flux on the upper $(-)$ and lower $(+)$ sides of the step (see the diagram in Fig. 3.1(a)). With this new kinetic coefficient,

$v_\pm$, and the electromigration driving force from Eq. 2.10, the essential mathematical machinery is available to calculate the step dynamics under the influence of an external electric field. The elastic contribution to the right hand side of this equation has been calculated in terms of the step spacing, l. To leading order in l, considering only nearest neighbor interactions, the elastic contribution is

$$\kappa\gamma = \frac{\partial \mathcal{E}}{\partial \lambda} = \frac{\partial}{\partial \lambda}\left(\frac{2(1-\sigma)^2 f^2}{\pi E}\left(\frac{1}{(\lambda_m - \lambda_{m-1} + l)^2} + \frac{1}{(\lambda_{m+1} - \lambda_m + l)^2}\right)\right) \quad (2.18)$$

where σ and E are the Poisson ratio and Young's modulus, respectively, and f is a force doublet (ie. units of force×length) which has its origin in the force-quadrupole interaction of an adatom with the surface mono-layer. To leading order the elastic energy, $\mathcal{E}$, arises as a result of the displacement of a single step from equilibrium due to the force exerted on it by the nearest neighboring steps. The origin of the step-step repulsion is explained rather elegantly by E. D. Williams [22] and can be calculated from first principles using standard elasticity theory [35]. The classical $1/l^2$ step-step repulsion is apparent in Eq. 2.18. (Note that Eq. 2.18, as it applies for homo-epitaxial step flow, was incorrectly stated in reference [32]. However, this has no effect on the results of their calculations.)

It is useful to note that the relationships in Eqs. 2.10 and 2.17 represent an improvement on an earlier model (due to Stoyanov [4]) in that the present treatment explicitly takes into account diffusion, evaporation, elastic interactions and the step tension. In Stoyanov's model, the evaporation is introduced indirectly as the origin of a "source" for the adatoms. However, the concentration field c for an adatom moving across a terrace will have the same form for both the Stoyanov model and the present model in the case of quasi steady-state step dynamics. This concentration field has solutions of the form

$$c = A cosh(z/\alpha_0) + B sinh(z/\alpha_0)\,, \quad (2.19)$$

where $\alpha_0 = \sqrt{x_s^{-2} + 1/4\xi^2}$, $x_s = \sqrt{D\tau}$ (the mean diffusion distance), and $\xi = k_B T/F$ (dimensions of length). This solution is identical for both the Stoyanov model and the

M-PL model, with the exception of the coefficients A and B, which can be calculated (through laborious algebra) from the kinetic equation 2.17. The positions of steps are indexed in terms of the one-dimensional (time-dependent) displacements from their equilibrium positions, $z = \lambda_m(t)$. In the M-PL model one can calculate the relationship for the step position for the mth step, z_m, as a function which relates the mth step to its neighboring steps ($m+1$ and $m-1$), yielding

$$
\begin{aligned}
(D\Omega c_{eq})^{-1}\dot{z}_m = {} & \mathcal{D}^{-1}(\Delta z_{m+1})\Big\{\alpha_0 e^{-\Delta z_{m+1}/2\xi}[1+\frac{A}{3\Omega c_{qe}}\Delta_2] \\
& -[\alpha_0 cosh(\alpha_0\Delta z_{m+1}) + (1/2\xi + d_-/x_s^2)sinh(\alpha_0\Delta z_{m+1})][1+\frac{A}{3\Omega c_{eq}}\Delta_1]\Big\} \\
& +\mathcal{D}^{-1}(\Delta z_m)\Big\{\alpha_0 e^{\Delta z_m/2\xi}[1+\frac{A}{3\Omega c_{eq}}\Delta_0] \\
& -[\alpha_0 cosh(\alpha_0\Delta z_m) + (-1/2\xi + d_+/x_s^2)sinh(\alpha_0\Delta z_m)][1+\frac{A}{3\Omega c_{eq}}\Delta_1]\Big\} \qquad (2.20)
\end{aligned}
$$

where

$$
\mathcal{D}(z) = [1 + d_+d_-/x_s^2 + (d_+ - d_-)/2\xi]sinh(\alpha_0 z) + \alpha_0(d_- + d_+)cosh(\alpha_0 z)\,.
$$

As illustrated in Fig. 2-50, the step spacing between two neighboring steps is defined to be $\Delta z_{m+1} \equiv z_{m+1} - z_m$, and $\Delta_i = \Delta z_{m+i}^{-3} - \Delta z_{m+i-1}^{-3} (i = 0,1,2)$. One recognizes immediately the similarity with the Stoyanov model [4] with an additional elastic contribution and with $d_+ = d_- = d$. The parameter $d_\pm = D/v_\pm$ is known as the Schwoebel length, which is the asymmetry for the sticking rate of adatoms to steps impinging from a lower terrace (+) compared to that from an upper terrace (−). This term has its origin in the modification of the surface potential near a step edge due to the increase and decrease in coordination of the surface and the detached adatom, respectively. In the case of non-equilibrium growth, the Schwoebel barrier [37] can cause the surface morphology to coarsen, but this factor can be neglected in the following calculation since the electromigration force should be the only source of asymmetry in the case of a uniformly stepped surface [40]. Thus, the sticking rate d is taken to be small but isotropic at each step. This assumption, along with

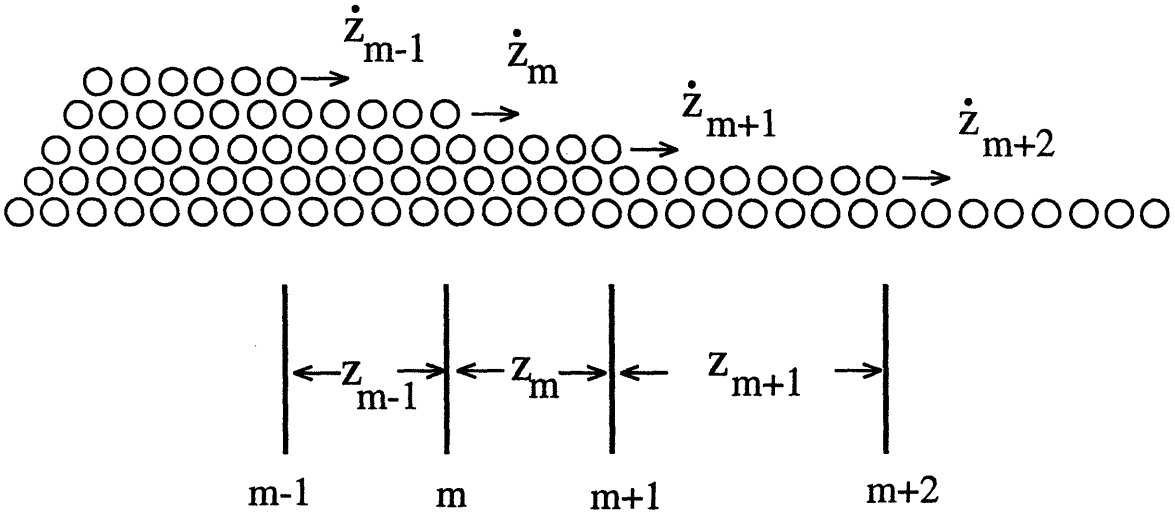

Figure 2-50: Mono-layer step model indicating the step coordinates (z_m) and step velocities ($\dot{z}_m$) used in Eqs. 3.9 and 3.11.

the above approximations, should permit for a reasonably corrigible model which can be adjusted to match experimental results. [It is useful to check that Eq. 2.20 gives a consistent description of the step dynamics when the electromigration term vanishes[29], ie. $F/2k_BT \equiv 1/2\xi \to 0$.]

Solving Eq. 2.20 is highly non-trivial since this involves handling an infinite set of equations. Fortunately, step bunching is one manifestation of step behavior which permits a continuum approximation, greatly simplifying the analysis of this dynamical equation. Specifically, the continuum (coarse grained) limit is a reasonable approximation in the case that the step-step spacing is much smaller than the diffusion length x_s, which is always the case during step bunching, even at extremely high temperatures.

One expands Eq. 2.20 in a series in powers of the inter-step parameter Δz_m, which is taken to be a continuous variable, thus the difference equation (2.20) becomes a differential equation which is certainly more appealing then an infinite set of coupled equations. To simplify the algebra it is useful to define $mh \equiv x$ and $W(x) = z_{m+1} - z_m$. Truncating the series by keeping only terms linear in Δz_m and up to fourth order in the derivatives $d(\Delta z_m)/dx \equiv W_x$ gives the resulting equation:

$$(1/\Omega D c_{eq})[W_t - (\Omega c_{eq}/\tau)W_x] = -[1/(2\xi d) - A/(\Omega c_{eq} x_s^2 l_0^3)]W_{xx}]$$

$$-(\frac{1}{6x_s^2} - \frac{A}{2\Omega c_{eq}\xi d l_0^3})W_{xxx} - (\frac{l_0^2[1/(2\xi d) - A/(\Omega c_{eq} x_s^2 l_0^3)]}{12} + \frac{A}{2l_0^4 d\Omega c_{eq}})W_{xxxx} \quad (2.21)$$

Misbah, et al. have shown that this differential equation can be re-written in terms of the step density, $m = 1/W \equiv m_{eq} + m_1$, by the following re-scaling of variables:

$$\mathcal{T} = \frac{D(\Omega c_{eq})^2 l_o^4}{(2Ad\xi^2)}\epsilon^2 t, \quad X = l_0^2[\frac{\Omega c_{eq}}{(A\xi)}]^{1/2}\sqrt{\epsilon}x \ , \quad \rho = \frac{x_s^4 l_0^2 (2\Omega c_{eq})^{1/2}}{[(2\xi)^{3/2}A^{1/2}d^2]}\epsilon^{3/2} m_1 \, ,$$

$$\text{and,} \quad \beta = \epsilon^{-1/2}\left[\frac{l_0^2 d(\xi\Omega c_{eq})^{1/2}}{(3x_s^2 A^{1/2})} - \frac{l_0^{-1}A^{1/2}}{(\xi\Omega c_{eq})^{1/2}}\right] .$$

The resulting equation which governs the step density is then

$$\rho_{\mathcal{T}} = -\rho_{XX} - \rho_{XXXX} - \beta\rho_{XXX} - \rho\rho_X \, . \quad (2.22)$$

Solutions to this nonlinear partial differential equation can be found be numerically. However, the advantage of rescaling should now be apparent to those who are conversant with problems in chaotic systems. By inspection of Eq. 2.22 there exist two limiting cases of interest to the problem at hand: one limit is marked by the absence of a dispersive ρ_{XXX} term, and the other is marked by the absence of the second order and fourth order terms. These limiting cases will depend in part on the value of β, which depends on the magnitude and direction (or sign) of the electromigration force, F, in Eq. 2.10. For the case were β is small, solutions of Eq. 2.22 are dominated by step behavior exhibiting spatio-temporal chaos. This evolution of step motion is shown in Fig. 2-51.

The results from numerical solutions of Eq. 2.22 for two values of the prefactor of the dispersive ρ_{XXX} term are shown in Figs. 2-51 and 2-52. Fig. 2-45 shows an AFM image of an 8° miscut Si(111) sample which had been prepared for several hours at high temperatures and thus had undergone substantial sublimation. These large-length scale electromigration-induced transverse undulations reveal many of the same features of the surface step pattern predicted from the M-PL model for $\beta = 0.5$. The

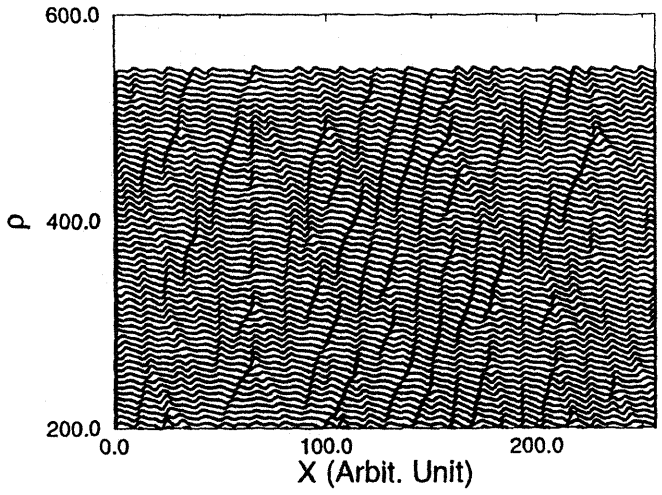

Figure 2-51: Spatiotemporal diagram taken from ref. [32] with $\beta = 0.5$ showing a chaotic (or disordered) step pattern. The X-axis is an arbitrary time coordinate and the Y-axis is a spatial coordinate. At t=0 the step array is assumed to be uniform.

chaotic step behavior in the model leads to distortions which are aperiodic in time (X-axis in the figure). Irregularly distributed branches appear in the surface profile due to this aperiodicity. As time progresses, these idealized steps appear to coalesce at localized points along the step direction, and then spread out leaving a pattern which has many branching points resulting in a self-similar surface morphology. For a two-dimensional surface one could expect a similar branch-like pattern to appear, provided the step curvature does not become so large that the elastic-limit approximation breaks down.

Figure 2-46 is a 1.0×1.0 μ^2 image showing detail one of the branching points of the AFM image of Fig. 2-45. The z scale is 500 Å per division. Disordered 1×1 terraces are shown in the central portion of the image while smoothly varying terraces are observed on either edge. The center of the image corresponds to one of the branching points. The terrace disordering is greatest in the uppermost region of the branches. This observation is in agreement with an absence of integer order scattering at (1,0) from this surface found in the x-ray experiment. Note, the scan

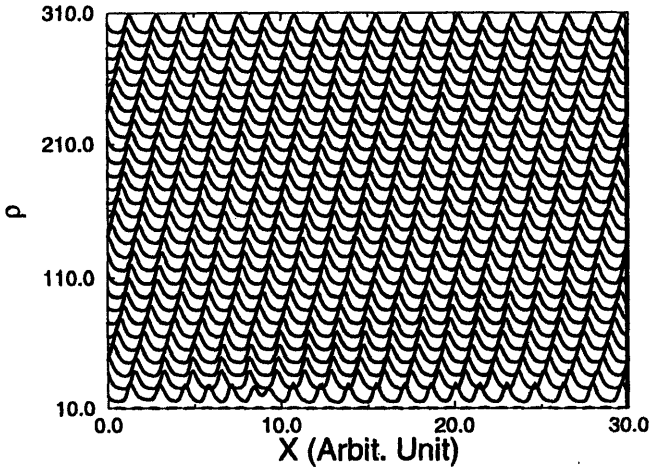

Figure 2-52: Spatiotemporal diagram taken from ref. [32] with $\beta = 3.0$. Step bunches appear to form ordered arrays with a periodic undulation. The X-axis is an arbitrary time coordinate and the Y-axis is a spatial coordinate.

direction of this image is orthogonal to that of Fig. 2-45 in order to optimize the resolution of the AFM instrument. The disorder of these terraces is evidently the result of long wavelength transverse step wandering.

The AFM image of Fig. 2-47 shows some of the details from the 1×1 unreconstructed terrace regions of the image of Fig. 2-46. This image is from an area 1.0×1.0 μ^2 located near in the upper right-hand corner of Fig. 2-46 in a region of smoothly varying terraces. The z scale is 100 Å per division. Although single steps are not distinguishable, small groups of steps can be resolved showing some regularity of the step arrangements with an average distance of more than 1000Å transversely, consistent with the *in-situ* x-ray data. It is of course not surprising that step groups do not appear to follow the pattern predicted from the M-PL model, although the 1×1 terraces themselves do tend to lead to effectively the same surface structure. This collective motion results in a terrace arrangement which follows qualitatively similar transverse motion over large length-scales reflected in the M-PL model. These steps tend to form regular kinks upon each terrace crossing and are distributed almost uniformly at least for short length-scales. This presumably gives rise to the relatively large transverse step-step correlation lengths measured in the x-ray scattering exper-

iment. The curved terrace regions of Fig. 2-47 form an array of large curvature and the spacing between the terraces is almost regular over short length-scales along the direction of the miscut.

Comments on the Continuum Models

Recently, a number of theorectical approaches [4] have been attempted to examine step dynamics on vicinal Si(111) surfaces using continuum approximations similar to that used in the previous section. In some of these models, it is argued that a phase transition occurs at a temperature where the diffusion length is equal to the terrace width. As explained in the above section, the continuum approximation can be satisfactorily applied to a one-dimensional array of steps in the limit that the diffusion length is much larger than the inter-step spacing, or equivalently, the size of the 1×1 terraces which separate the steps. In fact, this condition should be valid for *all* temperatures up to the melting temperature for silicon. As an order of magnitude estimate of the diffusion length, one can use results from recent calculations for the evaporation energy, $W = 4.6eV$, and the activation energy for diffusion, $E_d = 1.1eV$ [40]. Combining the diffusion coefficient, $D = a^2 \nu e^{E_d/k_B T}$, with the mean life of an adsorbed atom before evaporating, $\tau = \nu^{-1} e^{-W/k_B T}$, one can obtain an estimate of the diffusion length, $\lambda = \sqrt{D\tau} = a e^{(W-E_d)/k_B T}$. Evaluating this in the temperature regime of interest, one finds $\lambda = 2.0 \times 10^6 a$ at $T = 1400$ K, and $1.8 \times 10^5 a$, at $T = 1675$ K (the melting temperature for silicon!). Thus, the diffusion length in this approximation clearly exceeds the size of any of 1×1 terraces observable in experiments, even at very small miscuts down to 0.1° [3]. One should ask if there exist conditions which might lead to a dramatic reduction in the diffusion length above some temperatures. The phenomenon of surface melting probably will not lead to such a decrease in the diffusion length since this would tend to reduce the hopping energy E_d, thus increasing the difference $W - E_d$ and therefore the diffusion length, λ. The Schwoebel barrier discussed above is a possible candidate for introducing a mechanism to substantially reduce the diffusion length.

Establishing boundary conditions which consider large temperature changes in the

diffusion length as relevant is most likely not sufficient to determine the conditions which lead to a electromigration-induced phase transition. However, even in the M-PL model, the competition between the diffusion length and the effective length associated with the electromigration force, $F = 1/kT\xi$, determines the destabilizing condition. Therefore, it is plausible that a modification of the stability condition could result from the variation in the diffusion length, but the resolution of our experiment suggests that such a modification would be insignificant.

Following the x-ray diffraction study of the previous section, the 8° miscut Si(111) sample had been quenched from the two-phase region at 1050 K after many hours in the high temperature regime. Recall that this sample is polished on both sides. Therefore, using the conventional definition of current direction with respect to $<11\bar{2}>$ (ie. positive current follows the step-down direction), opposite sides of the sample will carry currents of opposite sign. Experimentally, this means that one can assess details of the surface for both positive and negative current from a single sample. For example, this quenched sample can have a "frozen" facet structure on one side, and a complimentary stepped structure on the opposite side, thus "frozen" from precisely the same temperature. Optical microscope photographs revealing these dramatic differences are shown in Figs. 2-48 and 2-49 for both sides of an 8° miscut Si(111) sample. It is apparent, therefore, that the direction of the electromigration force can be the *only* difference between these two quenched surface states since each side of the sample has the same miscut, and of course the same temperature. In fact, the miscut directions for each face will be as closely matched as is mechanically possible since the surfaces clearly remain parallel during the polishing process.

The overall features can be described as follows. Mesoscopic undulations of an irregular periodicity of the order of 10μ are observed, and the direction of the modulations differ by 90° between the two current directions. This shows that affect of the transverse step meandering on the surface morphology can be non-trivial, and should be addressed in the models. However, it is interesting that the apparently self-similar bifurcations, or branchings, observed in these images also appear in the M-PL model. Misbah and Pierre-Louis ascribe a step disordering due to spatio-temporal chaotic

behavior for the case with $\beta = 0.5$. For the case with $\beta = 3.0$, the steps form a regular array which is periodic in time resulting from a soliton mode expected from the Korteg de Vries type solutions of Eq. 2.22 [32].

2.3.2 A Microscopic Model of Electromigration

A microscopic model was developed [8] which predicts the site-to-site motion of a adatoms under the action of both an electric field and a wind force due to the scattering of electrons at the surface. In this local density functional approach, it was assumed that the site hopping of an adatom amounts to the exchange of an electron in the direction opposite to the motion of the adatom [42]. Therefore, ignoring the wind force, an effective current of negative charge also travels opposite to the adatom, resulting in an effective *positive* charge, Z_d, for the adatom. The calculated value of this effective charge is +0.05.

The contribution due to the wind force can be estimated using experimental values for the surface electron density, n_s. Although experimental results for n_s in Si(111) are not available, one can obtain a reasonable estimate for its temperature dependence from experimental results for Ge(111) which is expected to have roughly the same behavior. Figure 2-54 shows the estimated temperature dependence of n_s based on low-energy electron diffraction (LEED) experiments for Ge(111) [41]. The surface electron density is essentially zero in the (ordered) reconstructed phase. The increase in n_s through the stepped phase can be understood due to the weakly metallic-like nature of this disordered 1×1 surface. There is a jump in n_s at a temperature T_1 due to unmitigated metallicity indicative of *surface pre-melting*. The wind force due to an applied electric field $\vec{E}$ can be expressed as

$$\vec{F} = Z_w \vec{E} n l \sigma \,,$$

where Z_w is the effective charge n is the surface electron density, σ is the scattering cross-section electrons with an adatom at the Fermi energy, and l is the electron mean free-path between collisions [25].

The theoretical calculation started with an initially ordered arrangement of adatoms separated by a few lattice constants (about 8Å) which is subjected to an electromigration force. Taking a solitary adatom for the moment, one will find that the local effect of exchanging charge during the electric field-induced hopping is the key action which leads to the bias. The effect on a solitary adatom due to neighboring adatoms enters mainly as a small change in the relaxation of the surface in the vicinity of the rest atoms. Of course, evaluating this phenomenon in the presence of steps will add a great deal of complexity. The direct force can now be calculated within the local density functional theory in the following manner. The adatom hopping gives rise to a change in the electrostatic energy because the modification of the charge configuration. Taking the difference in the charge density between two configurations as $\rho(\mathbf{r}) - \rho'(\mathbf{r})$, the energy difference $\bar{\Delta}$ which arises from the presence of the electric field acting on these charge distributions is simply,

$$\bar{\Delta} = \Delta - \mathbf{E} \cdot \int d^3r \mathbf{r}[\rho(\mathbf{r}) - \rho'(\mathbf{r})], \tag{2.23}$$

where it is assumed that local changes in the charge distributions are not affected by the electric field. An effective charge associated with the direct force then follows from $-eZ_d\mathbf{E} \cdot \mathbf{a} = \bar{\Delta} - \Delta$, with $\mathbf{a}$ being the hopping vector connecting nearest T_4 and H_3 sites. This is the mechanism for the field-induced biased. Kandel *et al.* have numerically calculated a value of $Z_d = 0.05 \pm 0.006$. Summing the contributions from the wind force and the direct force, one gets two *special* temperature points, labeled T_1 and T_c in the diagram. Below T_1, adatom motion is determined by the direct force due to the electric field. At temperature T_1 there is a crossover where the wind force dominates the adatom motion. However, the occurrence of surface melting causes the value of Z_d to jump. The estimate of Z_d for temperature above T_c is 0.5, that is, closer to the valence charge of Si. Thus, the direct force dominates in this regime causing a second transition to appear.

The microscopic theory reveals that the competition between the wind force and

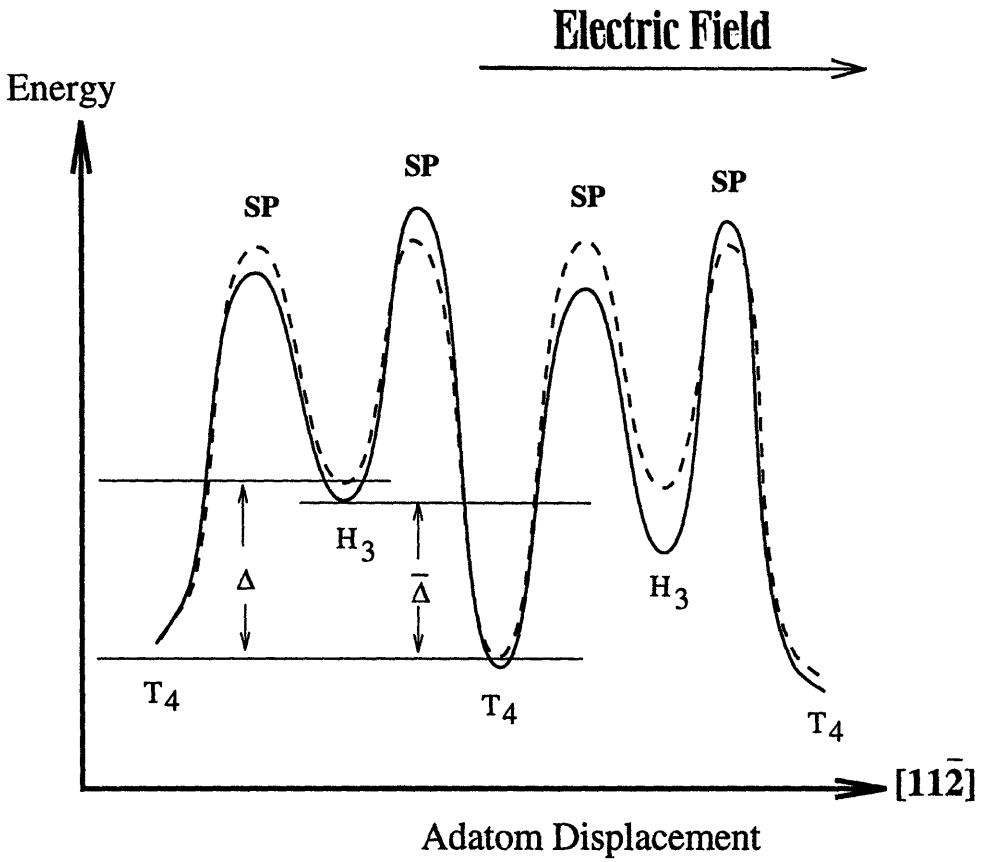

Figure 2-53: Energy landscape for Si(111) with a static biasing field (from ref. [8]). Hopping occurs between T_4 and H_3 sites, via saddle points (SP). The presence of steps are ignored in this model.

the direct force acting on the adatoms can naturally lead to multiple cross-over temperatures. The above arguments require an enhanced electron density due to surface melting and a jump in the value of Z_d, neither of which has been directly studied in experiments. It should be noted that surface melting should extend only to the first bilayer, in which case single atomic height steps could remain prevalent. This expectation has been confirmed in surface melting studies of Ge(111) [47]. It is reasonable to assume that a behavior similar to that of other elemental semiconductor materials might be observed for Si(111). The location of the transition temperatures will of course depending strongly on the details of the temperature dependence of the surface electron density.

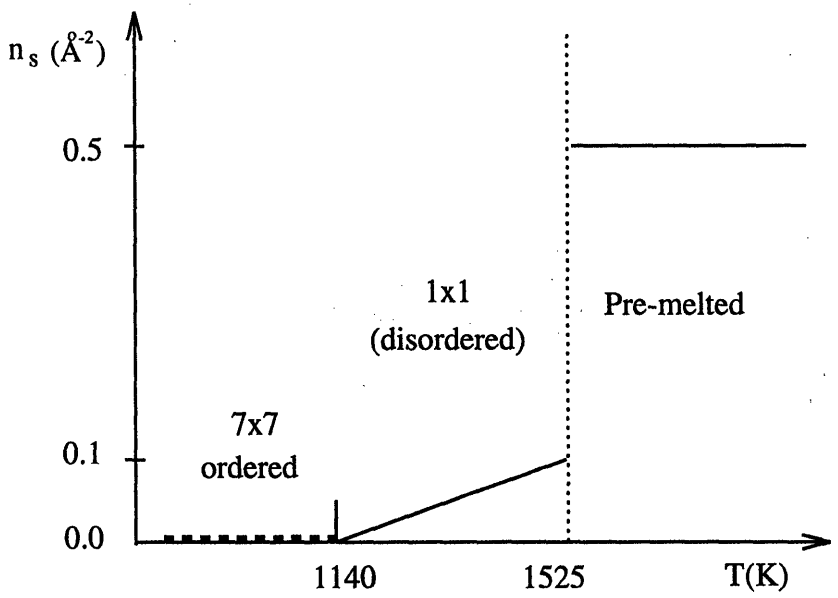

Figure 2-54: Estimate for the density of electrons at the surface of Si(111) proposed in ref. [8] to determine the crossover temperatures for step ordering. These values are estimates based on data for Ge(111) and Si(001). The dashed line below $T_{7\times7-1\times1}$ indicates a surface electron density of zero. The vertical dotted line marks a temperature where a jump in n_s might occur.

2.4 Summary

Studies of the step behavior on vicinal Si(111) have been conducted on surfaces miscut up to 8° toward <11$\bar{2}$>. An investigation of the effect of current reversal on the dynamics of step bunching and unbunching was completed at 1376K, 1420K, and 1470K for an 8° sample. The phase diagram in Fig. 2-6 shows the relevant temperature regions. The dashed line around 1140K represents the location of the reconstruction driven faceting transition which has an orientational dependence. Between 1370K and about 1470K the slow time evolution permitted independent measurements of the **q**-dependence of the scattering at the integer order facet peak (1,0) and at the step peak without significant distortion in the scattering profiles over periods ranging up to 200 minutes. The surface morphologies at these temperatures were essentially reversible, except after very long times at fixed current direction where either faceting or transverse step wandering could become saturated. Thus, a determination of the time dependence of the step correlation lengths, facet size and integrated intensities

was made for these temperatures over a substantial time range. The lower bound step–facet transition at ~1370K was also studied on heating from the single phase stepped region at negative current, and found to agree with the transition temperature measured on samples with smaller miscuts. In addition, a series of studies showing the time-dependence of the (1,0) peak were made on the 8° sample after quenching from above 1520K (an unfaceted surface) to 1406K and 1376K at negative current showing a continual development of the morphology over periods of up to 150 minutes. In some instances facets as large as $0.7\times2.5\mu^2$ were observed.

The scattering in the vicinity of the order-disorder transition at approximately 1520K (see diagram) was also examined for current both parallel (positive) and anti-parallel (negative) to $<11\bar{2}>$. This transition temperature was found to be independent of miscut for both current directions to within the experimental error. True "step-ordering" above 1520K at negative current was not observed in this set of experiments, as suggested by substantial diffuse scattering (and broadening) observed at both current directions for both the (1,0) peak and the step peak. Ex-situ optical microscopy on quenched samples revealed that large facets developed at positive current in the ordered stepped region above 1370 K and indicated a transverse instability consistent with that previously seen in other experiments on smaller miscut samples. The surface undulations which can appear at high-temperatures are of length-scales large enough to study with visible light. It would therefore be fruitful to augment the x-ray surface studies with *in-situ* specular reflection of diffraction studies from these surfaces.

Future experiments should reveal detailed information of the time-dependence, particularly if the q-dependence can be ascertained using a linear (position sensitive) detector. This would permit simultaneous measurement of scattering across a range of $\mathbf{q}$, greatly increasing the spatial and temporal resolution of the scattering experiment. It would also be interesting to address some of the basic assumptions taken in the microscopic model; namely, the enhancement of the surface electron density accompanying the purported incomplete melting of the Si(111) surface. To date, surface melting has not been confirmed experimentally on Si(111). The phenomenon

of surface melting of other semiconductor surfaces such as Ge(111) and Si(001) has been observed in electron diffraction experiments [9, 41, 45, 46]. Further theoretical work would also be helpful, particularly in illuminating the details of the step kinetics within the single-phase region above the 7×7–1×1 transition under electromigration.

Bibliography

[1] W. K. Burton, N. Cabrera, and F. Frank, Phi. Trans. R. Soc., **243**, 299 (1951).

[2] J. Villain, J. Phys. (France) **1**, 19 (1991).

[3] A. Latyshev, A. Krasilnikov, A. Aseev and S. Stenin, JETP Lett. **48** 529 (1988).

[4] Stoyan Stoyanov, Jap. Journ. Appl. Phys. **30**, 1-6 (1991).

[5] Stoyan S. Stoyanov, Hitoshi Nakahara, and Masakazu Ichikawa, Jap. Journ. Appl. Phys. **33**, 254 (1994).

[6] For a discussion of electromigration on semiconductor surfaces, see H. Yasunaga, A. Natori, Surface Science Reports, **15**, p. 205-80, 1992.

[7] Y. Homma, R. J. McClelland, and H. Hibino, Jap. Journ. Appl. Phys. **29**, **L** 2254 (1990).

[8] D. Kandel and E. Kaxiras, Phys. Rev. Lett. **76**, 1114 (1996).

[9] G. A. Held, J. L. Jordon-Sweet, P. M. Horn, A. Mak, and R. J. Birgeneau, Phys. Rev. Lett.**59**, 2075 (1987).

[10] See for example, P. R. Bevington and D. K. Robinson, *Data Reduction and Error Analysis for the Physical Sciences*, 2^{nd} Edition , (McGraw-Hill, Inc., New York, 1992).

[11] I. K. Robinson and D. J. Tweet, Rep. Prog. Phys. **55**, 599-651 (1992).

[12] G. A. Held and J. Brock, Phys. Rev. B **51**, 7262 (1995).

[13] G. A. Held and J. Brock, Phys. Rev. B **51**, 7269 (1995).

[14] C. Jayaprakash, C. Rottman, and W. F. Saam, Phys. Rev. B **30**, 6549 (1984).

[15] These experiments employed an ultra-high vacuum surface chamber and diffractometer which are described in D. L. Abernathy, Ph. D. thesis, Massachusetts Institute of Technology, Cambridge, Massachusetts, 1993.

[16] S. Song and S. G. J. Mochrie, Phys. Rev. B**51**, 10068 (1995).

[17] For a review of the equilibrium thermodynamics of faceting below the 7×7–1×1 reconstruction on vicinal Si(111), see E. D. Williams and N. C. Bartelt, Science **251**, 393 (1991).

[18] D. Y. Noh, K. I. Blum, M. J. Ramstad and R. J. Birgeneau, Phys. Rev. B **48**, 1612 (1993).

[19] For example, see E. D. Williams and N. C. Bartelt, Science **251**, 393 (1991) and references cited therein.

[20] M. J. Ramstad, R. J. Birgeneau, K. I. Blum, D. Y. Noh, B. O. Wells, and M. J. Young, Europhys. Lett. **24**, 653 (1993).

[21] S. Kodiyalam, K. E. Khor, N. C. Bartelt, E. D. Williams, and S. Das Sarma, Phys. Rev. B **51**, 5200 (1995).

[22] E. D. Williams, Surface Science **299/300**, 502 (1994).

[23] Extensive surface x-ray diffraction and laser diffraction data demonstrating the effect of impurity pinning of steps for 3° miscut Si(111) samples is presented by M. J. Ramstad, Ph. D. thesis, Massachusetts Institute of Technology, Cambridge, Massachusetts, 1996.

[24] E. Haeffner, Nature (London), **172**, 775 (1953).

[25] V. B. Fiks, Sov. Phys. Solid State, **1**, 14 (1959).

[26] R. J. Phaneuf, N. C. Bartelt, and Ellen D. Williams, Phys. Rev. Lett. **71**, 2284 (1993).

[27] H. Hibino and T. Ogino, Phys. Rev. Lett. **72**, 657 (1994).

[28] R. J. Phaneuf, E. D. Williams, and N. C. Bartelt, Phys. Rev. B **38**, 1984 (1988).

[29] G. S. Bales and A. Zangwill, Phys. Rev. B**41**, 5500 (1990).

[30] J. Krug, M. Plischke and M. Siegert, Phys. Rev. Lett.**70**, 3271 (1993).

[31] J. Krug and H. T. Dobbs, Phys. Rev. Lett.**73**, 1947 (1994).

[32] C. Misbah and O. Pierre-Louis, *Pulses and Disorder in a Continuum Version of Step Bunching Dynamics*, to be published (1996).

[33] C. Misbah, O. Pierre-Louis, and A. Pimpinelli, Phys. Rev. B **51**, 17283 (1995).

[34] I. Bena, C. Misbah and A. Valance, Phys. Rev. B **47**, 7408 (1993). This calculation was used to describe step-flow growth in the absence of an electromigration force, and is based on the Burton-Cabrera-Frank theory (see ref. [1]) for constitutive growth.

[35] L. Landau and E. Lifshitz, *Theory of Elasticity*, Vol. 7 (Pergammon Press, Oxford, 1970).

[36] B. Houchmandzadeh and C. Misbah, J. Phys. I France **5**, 685 (1995).

[37] R. Schwoebel and E. Shipsey, J. App. Phys., **37**, 3682 (1966).

[38] D. Kandel and J. D. Weeks, Phys. Rev. Lett. **69**, 3758 (1992).

[39] D. Kandel and J. D. Weeks, Phys. Rev. Lett. **72**, 1678 (1994).

[40] Efthemios Kaxiras, private communication.

[41] S. Modesti, et al., Phys. Rev. Lett. **73**, 1951 (1994).

[42] N. Takeuchi, A. Selloni, and E. Tosatti, Phys. Rev. B. **49**, 10757 (1994).

[43] Y. Mikata, T.Inoue, S. Takasu, T. Usami, T. Ohta, and H. Hirano; *Proceedings of the First International Symposium on Silicon Molecular Beam Epitaxy*, Proceedings (Electrochemical Society), Vol. 85-7, edited by J. C. Bean, (Pennington, NJ, 1985) p. 45-56.

[44] H. J. Shulz, Phys. Rev. B **22**, 5274 (1980).

[45] C. Alfonso, J. C. Heynard, and J. J. Métois, Surf. Sci. Lett. **291**, L745 (1993).

[46] J. Fraxedas, S. Ferrer, and F. Comin, Europhys. Lett. **25**, 119 (1994).

[47] Noboru Takeuchi, A. Selloni, and E. Tosatti, Phys. Rev. Lett. **72**, 2227 (1994).

Chapter 3

3D-XY behavior in liquid crystals with very wide nematic ranges

3.1 Introduction

The smectic-A (Sm-A) phase is defined by the establishment of a one-dimensional mass density wave in a three-dimensional (3D) fluid with the density wave along the direction of orientational order [1]. Many thermotropic liquid crystalline materials exhibit a phase transition between the nematic (N) phase and the Sm-A phase, and these systems have been the subject of numerous experimental and theoretical studies. The smectic-A phase of liquid crystal systems can be described by a density wave along the nematic director (perpendicular to the smectic layers) of the form $\rho=\rho_0 + \psi e^{i\phi} e^{iq_0 z}$. Figure 3-1 depicts the molecular arrangements for the nematic and the monolayer smectic-A_1 phases for a generic polar liquid crystal material. The order parameter associated with this sinusoidal density is $Re(|\psi|e^{iq_0 u})$, where the phase in the exponential is a function of the displacement, $u(\mathbf{r})$, of the layers along the z direction. Therefore, the critical behavior associated with fluctuations of this two-component ($n = 2$) order parameter is expected to be 3D-XY-like [1]-[4]. However, the experimental results to date have not established a clear case of 3D–XY universality [7, 21]. The nature of the N–Sm-A phase transition in liquid crystalline materials has been one of the most puzzling fundamental problems in the field of critical phenomena,

and is the subject of the experiments presented in this chapter.

Over the last two decades, the N–Sm-A transition has been studied in many liquid crystalline materials. However, none of the results of the experiments have shown a set of critical exponents in full agreement with the 3D–XY predictions. Moreover, the correlation-length critical exponents $\nu_{\|}$ and $\nu_{\perp}$ (where $\nu_{\|}$ and $\nu_{\perp}$ are the exponents describing the divergence of the correlation lengths parallel and perpendicular to the nematic director) have always been found to be anisotropic. The presence of two distinct values of the critical exponents describing the correlation length singularity is, of course, a serious violation of the scaling laws [5].

The broad range of critical exponents found experimentally has been attributed in part to the proximity of the systems to a tricritical point, depicted in the generic phase diagram of Fig. 3-2. The underlying physics was revealed experimentally by Ocko *et al.* [14] in a study of a series of binary liquid crystal mixtures. The crossover from first-order to second-order behavior can be understood in the context mean field theory where fluctuations are ignored. Following Ocko's discussion [15], one considers the nematic order parameter, S, to be at equilibrium close to T_{NA}. The free energy associated with the smectic order can be expressed in the usual Landau-Ginsberg form as:

$$\mathcal{F}_S = a_o + \frac{a_2}{2}|\psi|^2 + \frac{a_4}{4}|\psi|^4 \tag{3.1}$$

Including only the lowest order coupling term between the nematic and smectic order parameters, one can write for the free energy in the nematic phase as

$$\mathcal{F}_{NA} = \mathcal{F}_S - C|\psi|^2\delta S = \frac{1}{(2\chi)}\delta S^2 \tag{3.2}$$

where $\delta S \equiv S - S_o(T)$, and

$$\delta S = \chi C|\psi|^2 \tag{3.3}$$

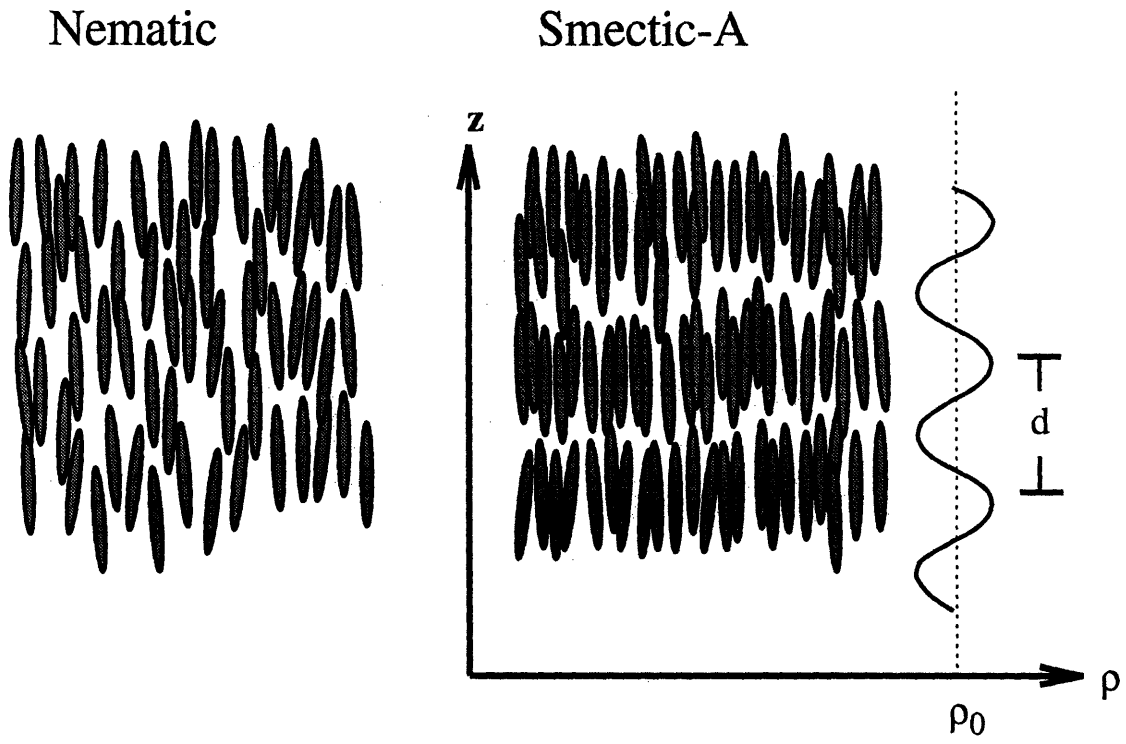

Figure 3-1: Diagram showing two of the many possible molecular arrangements for a nematic liquid crystal system. The diagram on the left shows the nematic (ordered fluid) phase. The diagram on the right depicts the salient features of the smectic-A phase, which is the most common stratified phase found in thermotropic liquid crystals. For the monolayer smectic-A_1, the mass density is described precisely by a pure sinusoid with an average layer separation d on the order of the molecular length.

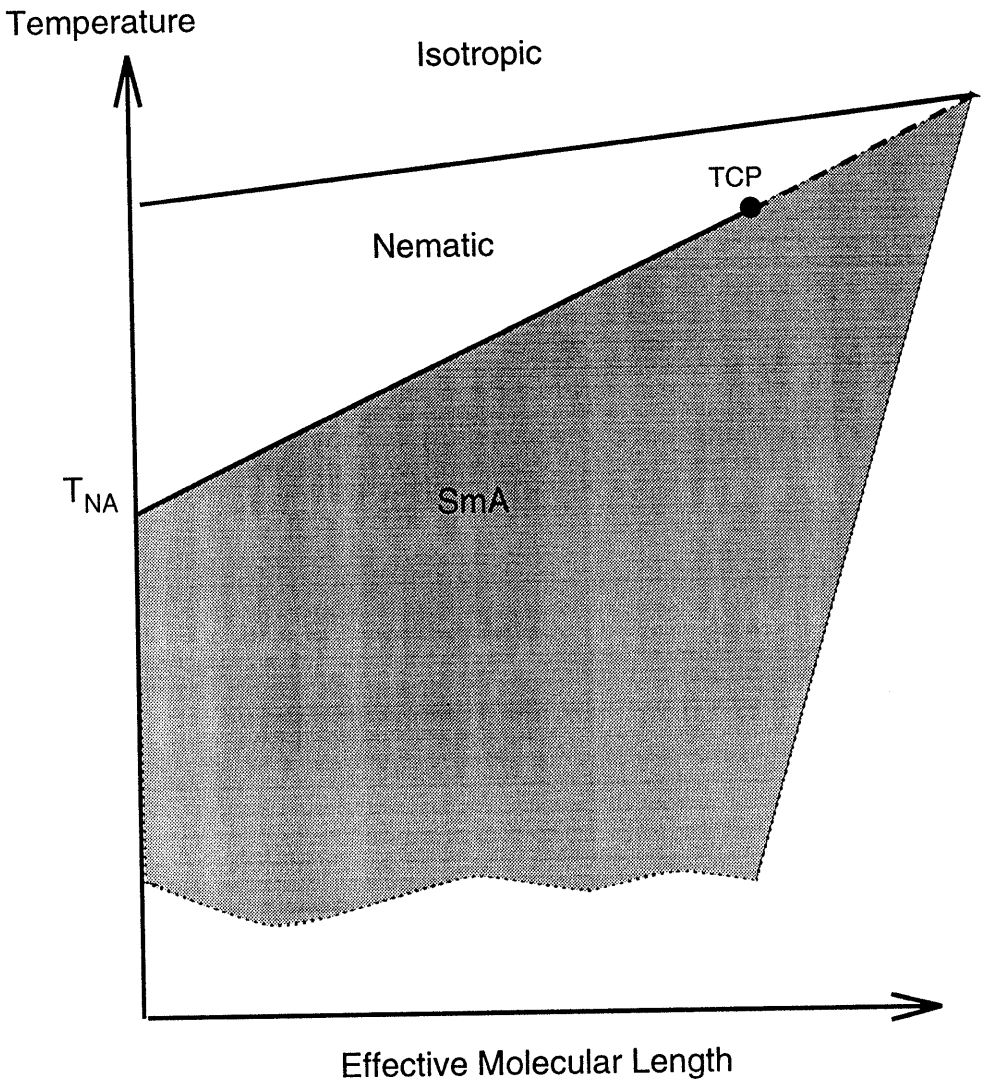

Figure 3-2: The phase diagram of a generic liquid crystal system showing the location of a tricritical point (TCP) separating a line of first-order transitions (dashed line) from a line of second-order transitions (solid line) at a temperature T_{NA} (the nematic–smectic-A transition temperature). A system consisting of a mixture of liquid crystals materials can possess an effective molecular length (the ordinate in the figure) which is typically intermediate between the molecular lengths of its constituents.

where the free energy has been minimized with respect to δS. Therefore,

$$\mathcal{F}_{NA} = a_o + \frac{a_2}{2}|\psi|^2 + \frac{a_4}{4}|\psi|^4 - \chi C^2|\psi|^4 + \frac{1}{(2\chi)}\chi^2 C^2|\psi|^4$$
$$= a_o + \frac{a_2}{2}|\psi|^2 + \frac{(a_4 - 2\chi C^2)}{4}|\psi|^4 . \qquad (3.4)$$

The tricritical point is determined from the zero value of the fourth-order term in Eq. 3.4 where a line of second-order critical points meets a line of first-order critical points. Therefore, an increasing nematic range, which corresponds to a *decreasing* χ, amounts to bringing the system further from the tricritical point. It is thus expected that systems with very large nematic ranges will possess critical behavior which is essentially unaffected by the tricritical point, and therefore should exhibit 3D XY-like critical behavior.

This argument can also be understood heuristically as follows. One would expect a continuous (second order) phase transition at T_{NA} in systems where the nematic order parameter is nearly saturated. This is simply due to the small energy required to create a layered smectic "droplet" within a nearly perfect nematic fluid. Conversely, a system with a narrow nematic range will not possess well-saturated nematic order. In this case, a large jump in the nematic order parameter would have to be achieved before local smectic order could develop; hence the transition should be first order [6]. Liquid crystal systems with narrow nematic ranges have been studied in many systems showing a first-order to tricritical to second-order crossover [12, 14, 16, 17, 22]. However, even in the tricritical region one finds $\nu_{\|} - \nu_{\perp} \simeq 0.1$ [14].

It is well-known that the analytical description of the critical singularities in heat capacity C_p, order parameter susceptibility σ, and correlation length ξ applies strictly to the *asymptotic* pure power law regime, i.e. for $T \rightarrow T_c$. Unfortunately it is often very difficult to carry out accurate measurements only in the asymptotic regime. However, Bagnuls and Bervillier have made an exact nonperturbative analysis of the ϕ^4 field theory model for d =3, n=1,2,3 and have evaluated numerically the universal aspects of the preasymptotic (first confluent corrections) regime [33, 36]. They have shown that their predictions for the 3D–XY (d=3, n=2) model describe well the heat

capacity of liquid helium near its normal-superfluid transition [40]. Moreover, recent ac-calorimetric studies of the critical heat capacity behavior have been reported for several polar liquid crystal compounds supporting this theory. These so-called "frustrated smectics" exhibit the nematic–monolayer smectic-A_1 (N–Sm-A_1) transition and are all characterized by wide nematic ranges ($\geq$ 45 K) [22, 23, 24, 25, 26]. In fact, the heat capacity C_p measurements for all of these systems were found to possess ideal 3D–XY behavior with a critical exponent $\alpha = -0.007 \pm 0.009$. Furthermore, first- and second-order corrections-to-scaling terms calculated within the preasymptotic theory were found to be important to accurately describe the C_p data [23, 24].

In this thesis, data for two compounds are discussed: the pure liquid crystal octyloxyphenylnitrobenzoyloxy benzoate (DB_8ONO_2), and the binary liquid crystal mixture pentylphenylcyanobenzoyloxy benzoate (DB_5CN) and cyanobenzoyloxypentylstilbene (C_5 stilbene). A detailed line-shape analysis is presented for the x-ray scattering data and an investigation is made of the effects alternate forms of the structure factor $S(\mathbf{q})$ might have on the resulting values of the correlation lengths $\xi_\parallel$ and $\xi_\perp$ and the smectic susceptibility σ. The dependences of $\xi_\parallel$, $\xi_\perp$, and σ on the reduced temperature $\tau = (T - T_c)/T_c$ are first analyzed using pure power-laws and effective critical exponents, as has been conventionally done for other N–Sm-A systems [14, 21]. This is followed by an analysis using the results of the preasymptotic theory which describe the correlation volume $\xi_\parallel \xi_\perp^2$, and the Sm-$A_1$ susceptibility σ in the nematic phase near the N–Sm-A_1 transition in both DB_8ONO_2 and DB_5CN + C_5 stilbene. Finally, using a minimal set of adjustable parameters and applying the results from heat capacity studies on these samples, it will be demonstrated that the thermodynamic quantities measured in the x-ray experiment are in very good agreement with 3D–XY predictions and that all of the known universal ratios are well obeyed. Thus, even though $\xi_\parallel$ and $\xi_\perp$ diverge differently, the above quantities are nevertheless accurately described by an orthodox 3D–XY model.

This chapter is organized as follows: The experimental results from the x-ray scattering studies of DB_8ONO_2 and DB_5CN + C_5 stilbene are presented in sections

3.2 and 3.3, respectively. In section 3.4, these same data are discussed in the context of a preasymptotic 3D-XY theory using the results from previously conducted heat capacity studies. Concluding remarks summarizing the results are presented in section 3.5. The details of the preasymptotic 3D–XY analysis of the heat capacity data on these samples can be found in Ref. [13].

3.2 X-ray Scattering Study of DB_8ONO_2

An x-ray scattering study was conducted for the N–Sm-A_1 phase transition in the pure liquid crystal compound DB_8ONO_2 which has the following molecular formula:

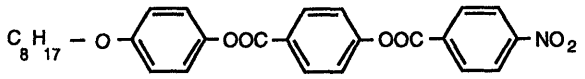

DB_8ONO_2

This molecule has a highly polar nitro group (NO_2) at the head, three benzene rings, and an alkyl group at the tail. The large diamagnetic moment of benzene conspires with the cigar-shaped geometry of the molecule to give a highly anisotropic volume diamagnetic susceptibility, $\chi_a \equiv \chi_{\parallel} - \chi_{\perp} \neq 0$. Thus, the mosaic (or angular spread) of the layer order can be reduced dramatically by orienting the sample in a magnetic field aligned parallel to the nematic director.

Our inspiration for studying this compound originated from a C_p study of binary mixtures of DB_8ONO_2 + $DB_{10}ONO_2$ [22]. In this system, a critical-to-tricritical crossover was observed. A mixture with 31.5 mole percent (X= 31.5) $DB_{10}ONO_2$, showed ideal 3D–XY heat capacity behavior, while a mixture with X=51.33 exhibited tricritical behavior ($\alpha = 0.50 \pm 0.04$). As the pure compound DB_8ONO_2 is substantially further away from this tricritical point than the X=31.5 mixture, it was deemed a very suitable candidate for observing ideal 3D–XY behavior. DB_8ONO_2 exhibits the phase sequence [27]

$$\mathrm{I} \underset{500K}{\longrightarrow} \mathrm{N} \underset{404.25K}{\longrightarrow} \text{Sm-A}_1 \underset{382.1K}{\longrightarrow} \text{Sm-}\tilde{\mathrm{C}} \underset{364.7K}{\longrightarrow} \text{crystalline},$$

and thus has a nematic range of 96 K. Neither the Sm-$\tilde{C}$ nor the crystalline phases were studied in the experiments described below.

The experiment was carried out using the high-resolution x-ray scattering configuration shown in Fig. 3-3. A Rigaku Ru-300 rotating-anode x-ray source operating at 12 kW, with a Cu K_α radiation was used. The spectrometer employed Si(111) single crystals as the monochromator and analyzer, in a nearly nondispersive configuration at the small scattering angles involved in the experiment. The resulting longitudinal resolution was $1.3\times10^{-4}\mathring{A}^{-1}$ half width at half maximum (HWHM). The transverse

in-plane resolution (in the plane of scattering) was $< 1 \times 10^{-5} \mathring{A}$, while the transverse out-of-plane (normal to the scattering plane), determined by the slits, was approximately Gaussian shaped with $0.04 \mathring{A}^{-1}$ (HWHM). A 160 mg sample of DB_8ONO_2 was placed in a beryllium cell 12×12×1.5 mm^3. The sample cell was mounted in a two-stage, nested, temperature controlled beryllium oven with a temperature stability of better than ±2 mK over several hours. This determined the experimental temperature resolution. Typical x-ray scans required between 1 and 15 minutes to complete except for reduced temperatures greater than 5×10^{-3} which took up to 2 hours. For the highest temperature data (above 5×10^{-3}) τ was determined to better than 1×10^{-4}. The vertical temperature gradient across the 12-mm height of the sample was only 1 mK, and a total sample area of $1 \times 3.5 mm^2$ was illuminated by the incident x-rays. The liquid crystal material was aligned in the nematic (ordered fluid) phase by a 6.5-kG electromagnet which was fixed to the θ-circle of the spectrometer. Measurements of the developing smectic order were carried out by performing longitudinal (parallel to the nematic director) and transverse scans at a series of constant temperatures in the nematic phase.

The DB_8ONO_2 sample was synthesized and purified at the Technical Institute of Berlin and is from the same batch as the material used in the heat capacity studies of DB_8ONO_2+$DB_{10}ONO_2$ mixtures in reference [22]. The N–Sm-A_1 phase transition temperature T_c was determined by the appearance of mosaic structure in the transverse scan as shown in Fig. 3-4(a). The mosaicity of the DB_8ONO_2 sample as measured from the θ width of our sharpest scan was 0.24° HWHM. At the start of the x-ray experiment the transition temperature T_c was 404.254 K, but T_c was found to drift slowly during the course of the experiment. A time-dependent transition temperature T_c could be used in the final analysis since the thermodynamic quantities of interest depend on the *reduced temperature* ($\tau \equiv (T - T_c)/T_c$), rather than the absolute temperature T. The reduced temperature is easily calculated from the values of T_c determined throughout the experiment. Drift rates of $dT_c/dt \simeq -45$ mK/day were observed over the first week of the experiment, after which this rate gradually slowed and for the remainder of the experiment had an approximately linear decrease of −20

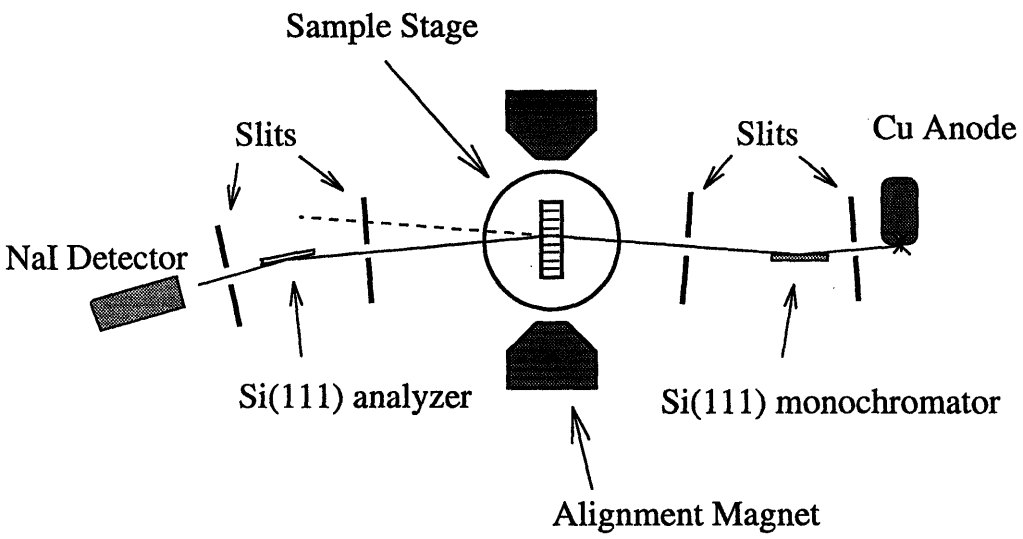

Figure 3-3: Diagram of the spectrometer configuration for high-resolution small-angle x-ray diffraction used in the bulk liquid crystal experiments. The angle between the detector arm and the direct beam (dashed line) defines 2θ. The aligning magnet is fixed with respect to the sample stage, and these make an angle θ with respect to the direct beam. Horizontal slits are used to reduce the background. The vertical slits which define the height of the beam are not shown here.

mK/day. Data obtained over an extensive period of time are internally consistent as a function of $(T - T_c)/T_c$. This observation is in concordance with the results from previous studies [28] which showed that the slow changes in sample purity at high temperatures due to annealed impurities do not affect the critical behavior.

In the nematic phase near the N–Sm-A_1 phase transition, the diffuse x-ray peak associated with the Sm-A_1 fluctuations was centered at $2\mathbf{q_0} = (0, 0, 0.2097\mathring{A}^{-1})$, which corresponds to a layer spacing $d = (2\pi/2q_0) = 29.96\mathring{A}$. No temperature dependence was found for the value of $2q_0$ in the nematic phase or in the Sm-A_1 phase just below the transition. Displayed in Fig. 3-4 are representative longitudinal scans (0, 0, $q_{\|}$) and transverse scans ($q_{\perp}$, 0, 0.2097) at four reduced temperatures showing the development of smectic order on approaching T_c. The top panel 3-4(a) shows scans in the Sm-A_1 phase just below T_c where the inset indicates structure in the peak indicative of mosaicity as the Sm-A_1 just becomes established.

One interesting feature of the DB_8ONO_2 data is the presence of a second diffuse x-ray peak centered at (0, 0, $0.6881q_0$), as can be seen in Fig. 3-5. This peak,

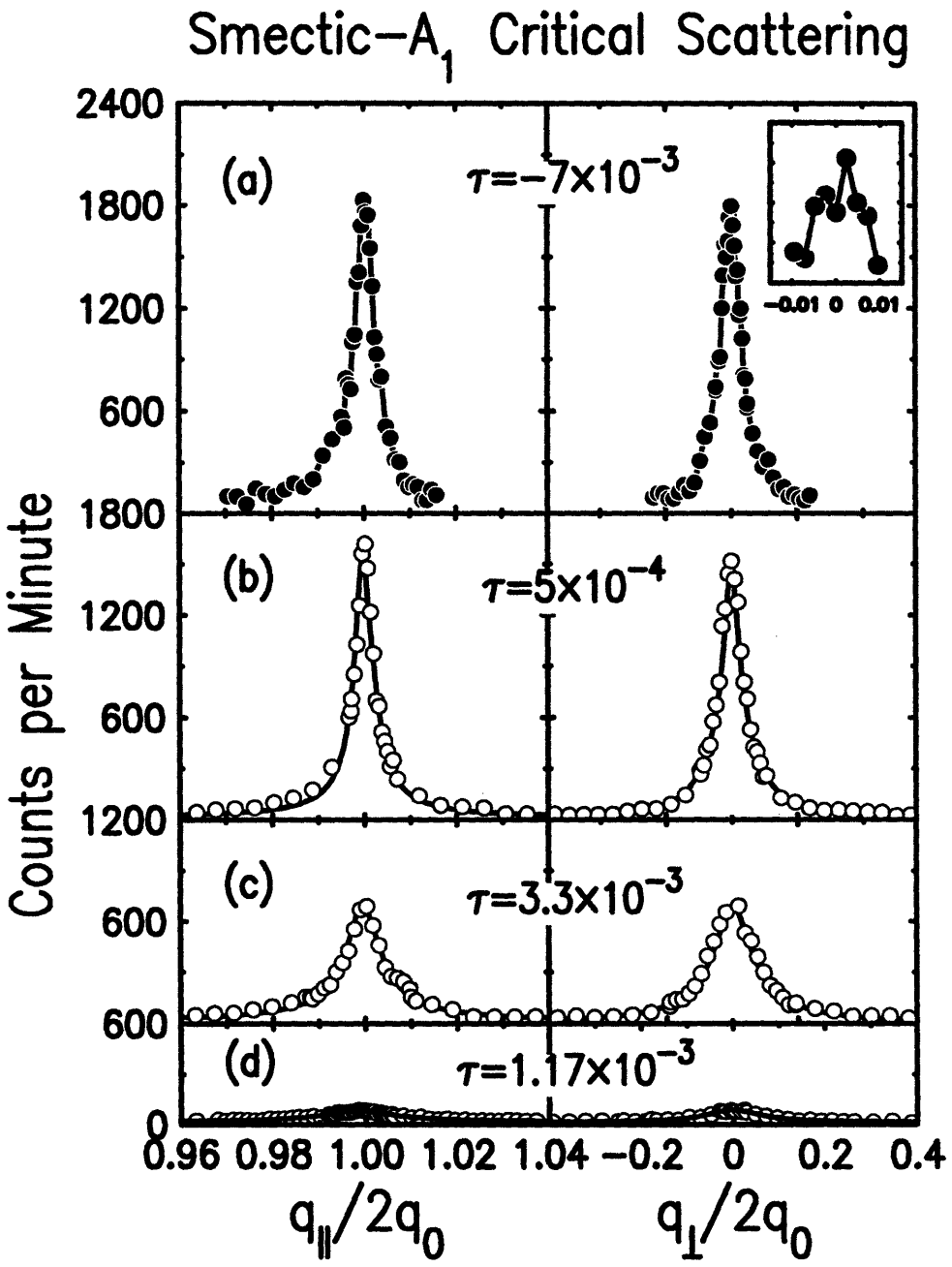

Figure 3-4: Representative scattering data showing longitudinal and transverse scans in DB_8ONO_2 at four reduced temperatures. The solid lines in (b)-(d) are fits with Eq. 3.5 convoluted with the resolution function. The lines is panel (a) are guides to the eye; the inset shows an example of how the mosaic is determined in the Sm-A_1 phase.

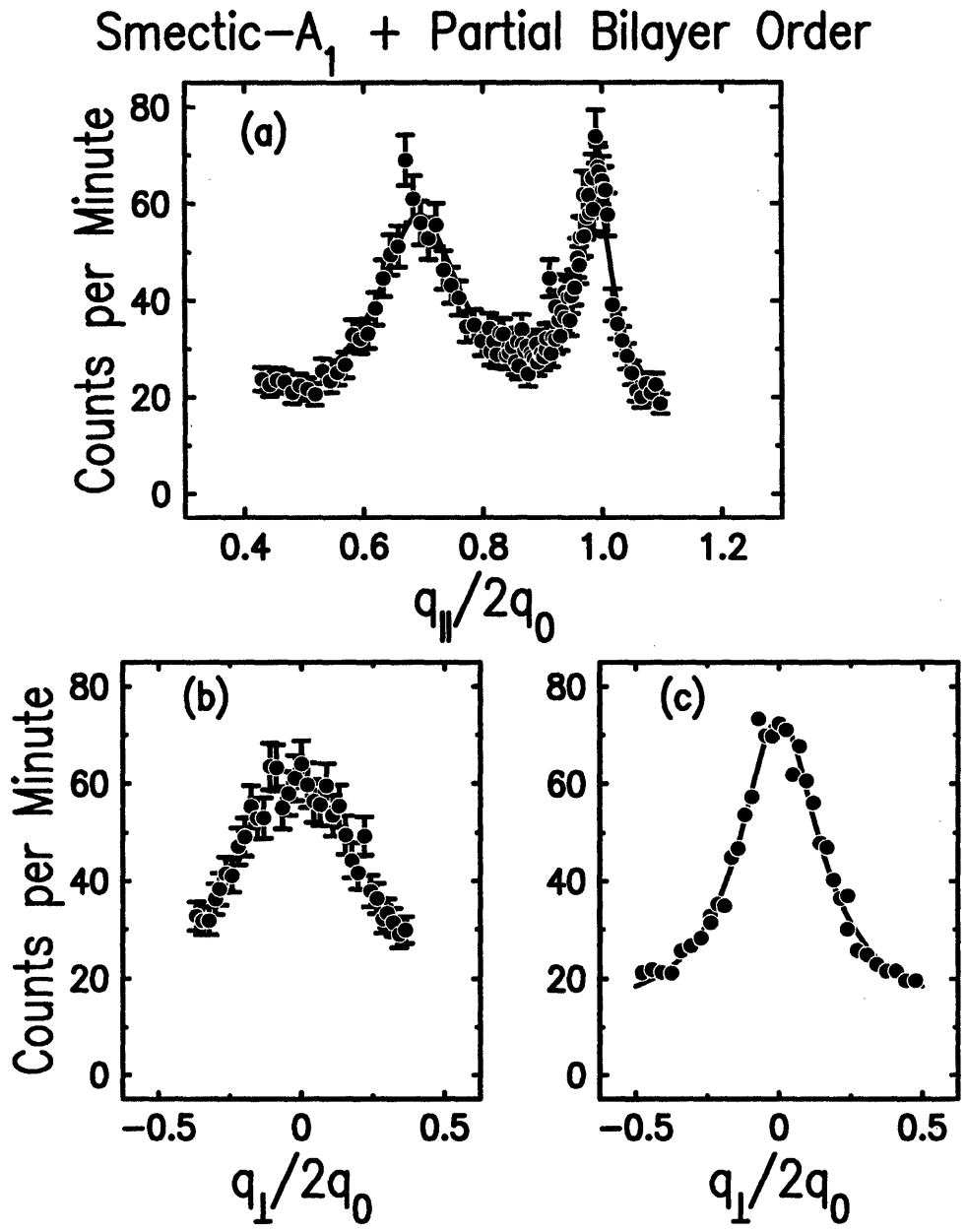

Figure 3-5: Longitudinal (a) and transverse (b) and (c) scans in DB_8ONO_2 showing Sm-A_d and Sm-A_1 ordering at $\tau = 1.2 \times 10^{-2}$. The Sm-$A_1$ peak is centered at $2\mathbf{q}_0$=(0, 0, 0.2097)Å^{-1}. The second diffuse peak at $\mathbf{q}_0'$=(0, 0, 0.1443)Å^{-1} is due to Sm-A_d order. Scan (b) is through the $\acute{q}_0$ peak, and scan (c) is through the $2q_0$ peak. The solid lines represent a fit of the $2\mathbf{q}_0$ to the lineshape of Eq. 3.5 including a Lorentzian contribution to the background due to $\acute{q}_0$.

associated with short-range partial bilayer (Sm-A_d) order, corresponds to a layer spacing $d' = (2\pi/q_0') = 43.54\AA$. Such Sm-$A_d$-like fluctuations are expected [29] in the nematic phase of a frustrated smectic system even if it does not exhibit a stable long-range ordered Sm-A_d phase at any temperature. The q_0' peak position, intensity, and width show no temperature dependence. All aspects of this weak, diffuse peak are absolutely stable not only in the nematic phase but also in the Sm-A_1 phase as low as 5 K below the N–Sm-A_1 phase transition. A similar diffuse peak has been detected in an x-ray study of the binary mixture DB_8ONO_2+$DB_{10}ONO_2$ at a q_0' value different from the q_0'' value of the quasi-Bragg spot associated with the long-range Sm-A_d phase observed in this mixture [30]. Although the Sm-A_d-like q_0' peak in DB_8ONO_2 becomes comparable in intensity to the Sm-A_1 peak only for $\tau<10^{-2}$, its presence was taken into account in the lineshape analysis of all the data. Both longitudinal and transverse scans through the q_0' peak could be well described by a Lorentzian, as shown in Figs. 3-5(a) and 3-5(b). This peak with a temperature-independent longitudinal HWHM of $1.59\times10^{-2}\AA^{-1}$ and a transverse HWHM of $5.58\times10^{-2}\AA^{-1}$ was treated as part of the background.

Critical x-ray scattering due to Sm-A_1 fluctuations in the nematic phase is described by the following structure factor expression:

$$S(\mathbf{q}) = \frac{\sigma}{1+\xi_{\|}^2(q_{\|}-2q_0)^2+\xi_{\perp}^2 q_{\perp}^2+c\xi_{\perp}^4 q_{\perp}^4}, \tag{3.5}$$

convoluted with the resolution function. No corrections for mosaicity were needed. A convenient way to incorporate the transverse correlation length in the analysis is through the ratio of the correlation lengths, $\xi_{\|}/\xi_{\perp}$. Thus, pairs of x-ray scans are fit with only three adjustable parameters: σ, $\xi_{\|}$, and $\xi_{\|}/\xi_{\perp}$. Note that this structure factor contains an empirically chosen quartic term $c\xi_{\perp}^4 q_{\perp}$ which is conventional in analysis of N–Sm-A data [21, 31]. The need for a quartic term, which most probably has its origin in splay-mode director fluctuations, is dictated by the non-Lorentzian wings of transverse scans at large τ [31]. Figure 3-5(c) displays the results of fitting a transverse scan at $\tau=1.2\times10^{-2}$ with Eq. 3.5 allowing $c \neq 0$ and with a Lorentzian

(i.e., $c = 0$). It is clear from the scans that a fourth-order correction term is required to fit these data adequately. The coefficient c is a freely adjustable parameter in the fits and its temperature dependence is shown in Fig. 3-6(a). One sees that c is very small near T_c, and never becomes larger than $\frac{1}{4}$ at large reduced temperature, which is in agreement with the results of fits to x-ray data for other N–Sm-A systems [14, 21]. This temperature dependence of the parameter c reflects a crossover in the *transverse* shape of the scattering, which changes away from the simple Lorentzian shape near T_c to a Lorentzian squared far above T_c where c is largest.

It has recently been argued [32] that a more correct form for Eq. 3.5 should have the quartic term $\xi_s^4 q_\perp^4$ instead of $c\xi_\perp^4 q_\perp^4$, where ξ_s is a splay correlation length; it is further argued that ξ_s should be constrained to a power law critical behavior $\xi_s \tau^{-\nu}$ characterized by a critical exponent ν_s. The empirical ν_s and ξ_{s0} values reported for octyloxyphenylcyanobenzoyloxy benzoate (8OPCBOB) are $\nu_s \simeq 0.41$ and $\xi_{s0} = 2.33\mathring{A}$ [32]. Figure 3-7 displays our quantity $c^{1/4}\xi_\perp$ as a function of τ for DB_8ONO_2. These points can be fitted nicely by a pure power law with an exponent equal to 0.35±0.05. Thus, Fig. 3-7 demonstrates that the treatments of the transverse line-shape with Eq. (1) or with a form that includes a $\xi_s^4 q_\perp^4$ splay term are equivalent as, of course, they must be since they are algebraically identical except for the power-law constraint imposed in Ref. [32]. It has also been argued [32] that the critical behavior of ξ_s affects the criticality of the correlation length $\xi_\perp$. As shown below, the statistics of our data analysis do not show such a trend. The uncertainty in the determination of $\xi_\perp$ from fitting the data with different $S(\mathbf{q})$ has no significant effect on the values of the effective critical exponents, at least within the experimental standard deviations.

Results for DB_8ONO_2 using Pure Power-law Analysis

The values of $\xi_\parallel$, $\xi_\perp$, and the smectic susceptibility σ obtained from fits to the x-ray profiles with Eq. 3.5 are shown in Fig. 3-8. These quantities have been fit over the range $2\times10^{-5}<\tau<1.2\times10^{-2}$ with pure power-law expressions having the forms

$$\xi_\parallel = \xi_{\parallel 0}\tau^{-\nu_\parallel},\ \xi_\perp = \xi_{\perp 0}\tau^{-\nu_\perp},\ \sigma = \sigma_0\tau^{-\gamma}.$$

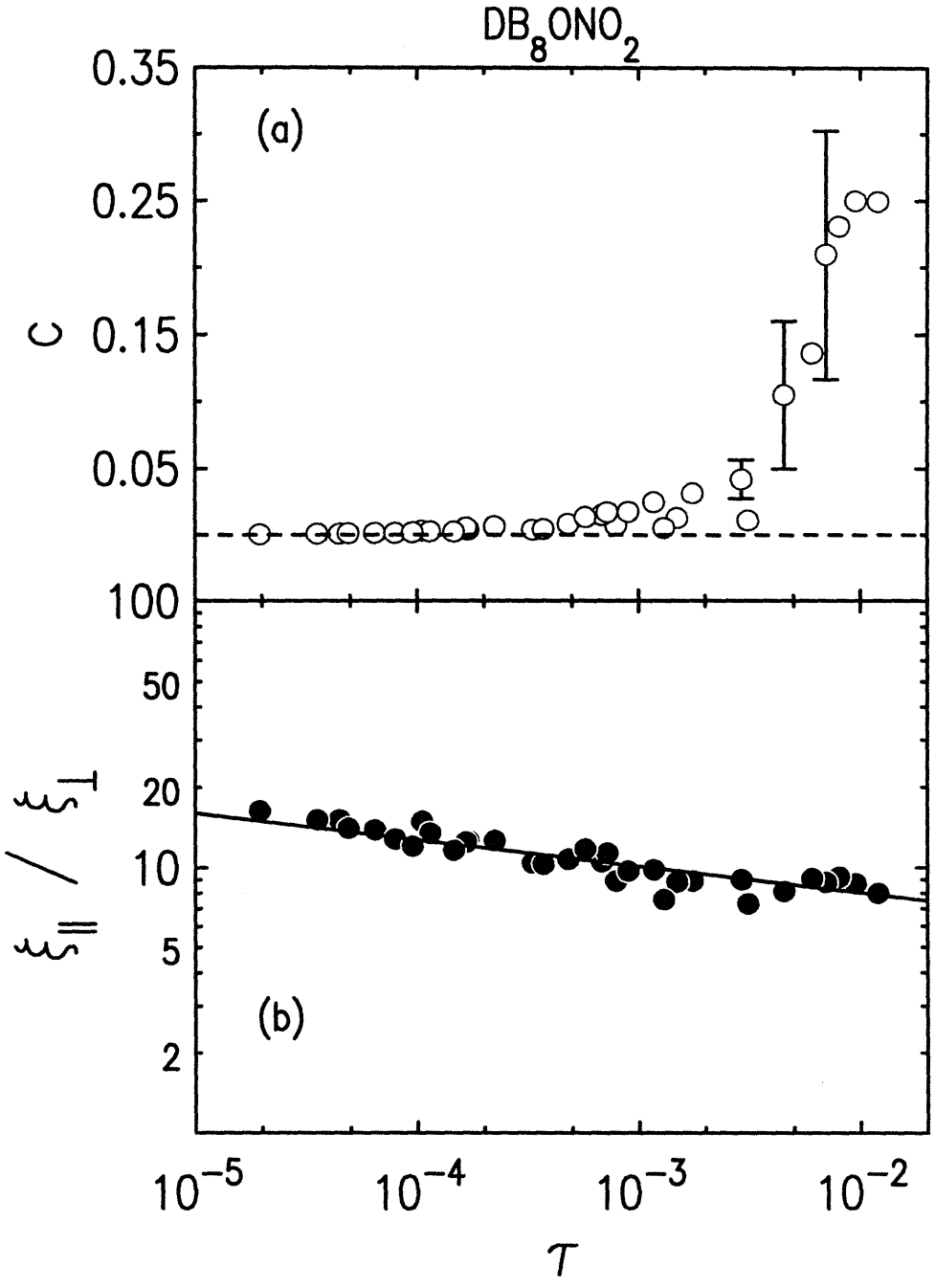

Figure 3-6: (a) Fourth-order coefficient c in Eq. 3.5 obtained from least-squares fits to the x-ray profile. The error bars for $\tau < 3 \times 10^{-4}$ are smaller than the size of the points. (b) Ratio $\xi_{\|}/\xi_{\perp}$ of correlation lengths. The best-fit line has a slope $\Delta\nu = \nu_{\|} - \nu_{\perp} = 0.10$.

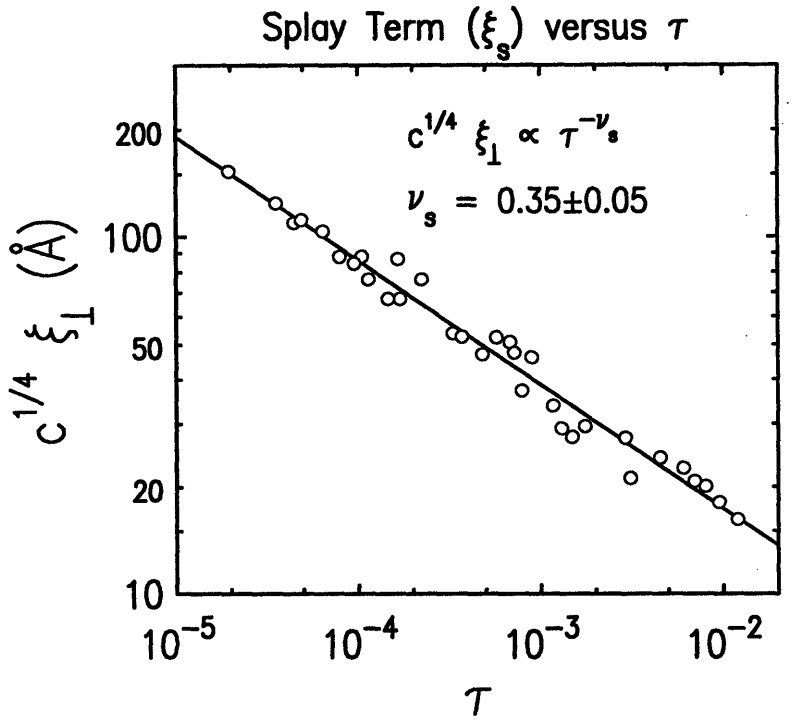

Figure 3-7: Dependence of $\xi_s \equiv c^{1/4}\xi_\perp$ on reduced temperature. The line represents the empirical form $\xi_{s0}\tau^{-\nu_s}$ with $\xi_{s0} = 5.14\mathring{A}$ and $\nu_s = 0.35 \pm 0.05$.

The 3D–XY values for the critical exponents are $\nu_\parallel = \nu_\perp = 0.669 \pm 0.001$ and $\gamma = 1.316 \pm 0.002$ [33]. As can be seen from table 3.1, the final values $\nu_\parallel = 0.69 \pm 0.03$ and $\gamma = 1.28 \pm 0.05$ seem to agree with the 3D–XY values within the experimental uncertainties but the value $\nu_\perp = 0.59 \pm 0.03$ clearly does not. The observed anisotropy in the correlation length exponents is reflected in the temperature dependence of the ratio $\xi_\parallel/\xi_\perp$, which is shown in Fig. 3-6(b).

To demonstrate the effects of the quartic term on the values of the critical exponents, the data were also fit by setting c equal to zero in Eq. 3.5 for all temperatures, and by using the empirical Lorentzian term with a power-law correction given by [14, 31]

$$S(\mathbf{q}) = \frac{\sigma}{\xi_\parallel^2(q_\parallel - 2q_0)^2 + (1 + \xi_\perp^2 q_\perp^2)^{1-\eta_\perp/2}}, \tag{3.6}$$

where $-2 < \eta_\perp < 0$ is an empirical τ dependent exponent that is freely adjustable in the fits. This form of S(q), like Eq. 3.5, changes from Lorentzian near T_c (where

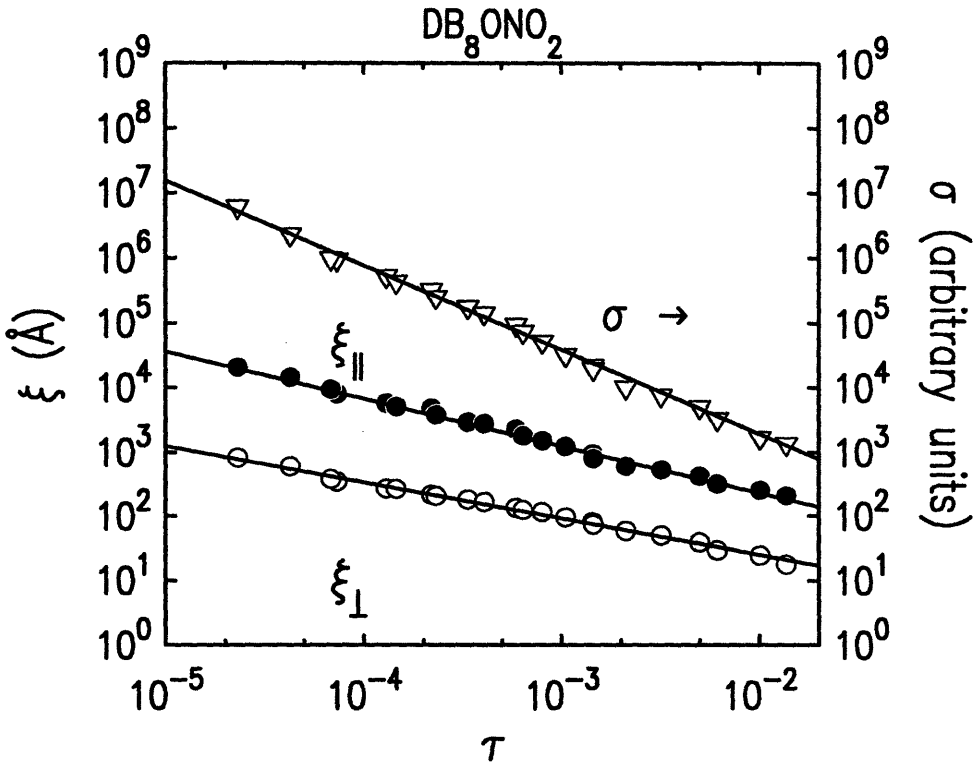

$$\sigma = \sigma_0 t^{-\gamma} \qquad (\gamma = 1.28 \pm 0.05)$$

$$\xi_{\parallel} = \xi_{\parallel 0} t^{-\nu_{\parallel}} \qquad (\nu_{\parallel} = 0.69 \pm 0.03)$$

$$\xi_{\perp} = \xi_{\perp 0} t^{-\nu_{\perp}} \qquad (\nu_{\perp} = 0.59 \pm 0.03)$$

Figure 3-8: Smectic-A_1 susceptibility σ and the longitudinal and transverse correlation lengths $\xi_{\parallel}$ and $\xi_{\perp}$ near the N–Sm-A_1 transition in DB_8ONO_2, as obtained from fitting the x-ray profiles to Eq. 3.5. The lines are least-squares fits with pure power laws, and the fitting parameters are given in the first line of Table 3.1. The σ values have been shifted up by a factor of 4 to improve clarity.

S(q)	$\xi_{\|0}$ (Å)	$\nu_{\|}$	$\xi_{\|0}$ (Å)	$\nu_{\perp 0}$	σ_0	γ
Eq. 3.5, $c \neq 0$	8.74	0.69	1.75	0.59	1.33	1.28
	±0.44	±0.03	±0.09	±0.03	±0.05	±0.05
Eq. 3.5, $c = 0$	9.01	0.71	2.55	0.59	1.77	1.27
	±0.50	±0.03	±0.14	±0.03	±0.10	±0.05
Eq. 3.6	8.39	0.69	1.00	0.60	1.39	1.27
	±0.46	±0.04	±0.05	±0.04	±0.08	±0.06

Table 3.1: Summary of results for DB_8ONO_2. Least-squares values of the amplitudes and effective critical exponents for $\xi_{\|}$, $\xi_{\perp}$, and σ using the pure power-law forms of Eqs. 3.5 and 3.6.

$\eta_{\perp} \simeq 0$) to Lorentzian squared far from T_c (where $\eta_{\perp} = -2$). The profiles were almost as well fit with Eq. 3.6 as Eq. 3.5 with $c \neq 0$, but the Lorentzian form provided poorer fits. Figure 3-9 shows the values for $\xi_{\perp}$ obtained using these three structure factor forms. Comparable effects are also obtained for $\xi_{\|}$ and σ, and Tabel 3.1 lists the amplitudes and effective exponents obtained from power-law fits. It is evident from Fig. 3-9 and Table 3.1 that the fourth-order term in Eq. 3.5 has no significant effect on the values of the experimental critical exponents although the amplitudes vary depending on the assumed form for S(q). Equivalent results have been obtained previously [14].

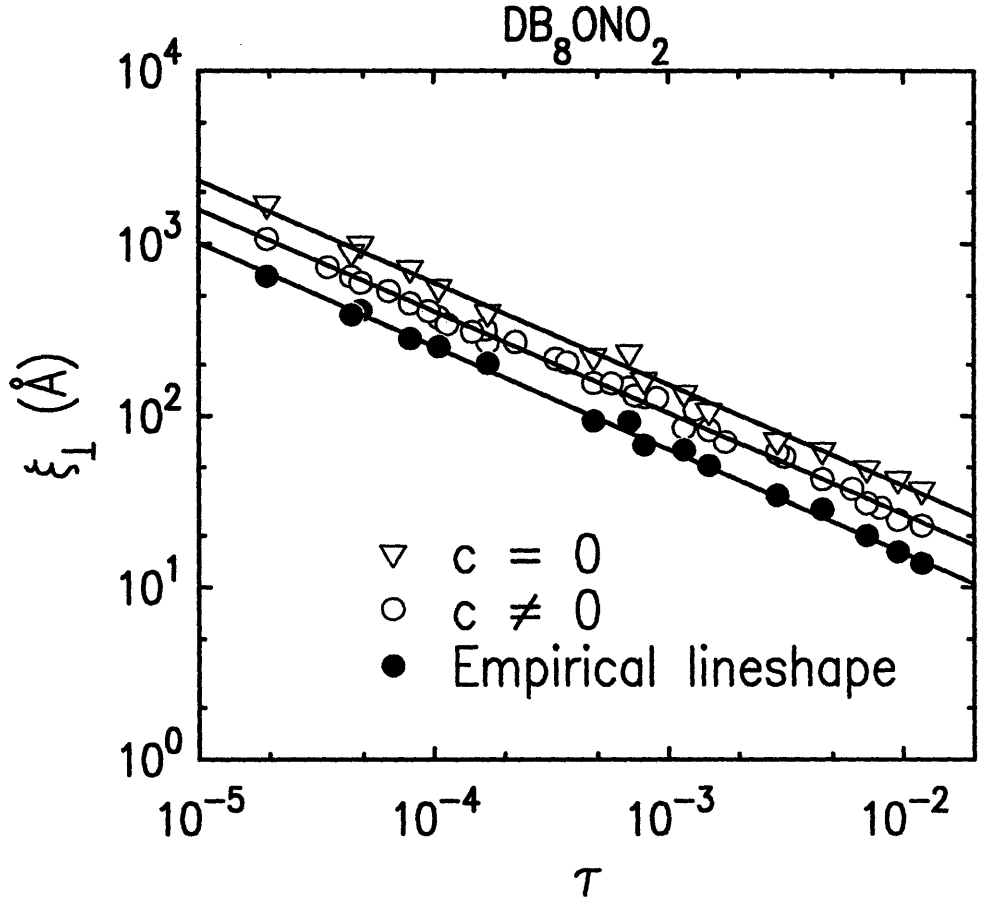

Figure 3-9: Influence of the form of the structure factor S(**q**) on the transverse correlation length $\xi_\perp$ in DB_8ONO_2. The points denoted by open circles (○) and the triangles (▽) were obtained by fitting the x-ray profile of Eq. 3.5 with $c \neq 0$ and $c = 0$, respectively. The solid points (●) came from fits to the profile in Eq. 3.6 with $\eta_\perp$ taken to be a freely adjustable parameter at each temperature. A subset of the DB_8ONO_2 data shown in Fig. 3-8 were used here. The least-squares parameters for the power-law fits shown by the straight lines are given in Table 3.1.

3.3 X-ray Scattering Study of DB_5CN+C_5 stilbene

An x-ray scattering study was also conducted for the N–Sm-A_1 phase transition in the binary liquid crystal mixture pentylphenylcyanobenzoyloxy benzoate (DB_5CN) and cyanobenzoyloxypentylstilbene (C_5 stilbene). The constituents of this mixture have the following molecular formulas:

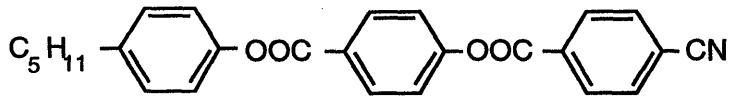

DB_5CN

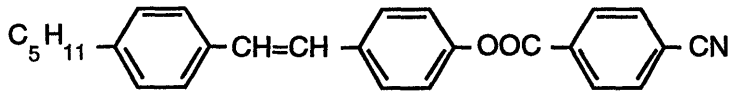

C_5 stilbene

with molecular masses of 413.48g and 395.50g, respectively. Note, these molecules both have the highly polar cyano group at the head, three benzene rings, and an alkyl group at the tail. These compounds were synthesized and purified at the Centre de Recherche Paul Pascal [4], and they are from the same batch that was used for an earlier C_p investigation [12]. The x-ray sample is a mixture containing 49.5 mole percent C_5 stilbene, which was previously used for a high-resolution x-ray study of the N–Sm-A_1 transition [13]. The phase sequence for this sample is

$$\underset{}{\mathrm{N}} \underset{424.3\ \mathrm{K}}{\longrightarrow} \mathrm{Sm\text{-}A_1} \underset{\sim 398\ \mathrm{K}}{\longrightarrow} \mathrm{Sm\text{-}\tilde{A}} \underset{383.6\text{–}386\ \mathrm{K}}{\longrightarrow} \mathrm{Sm\text{-}A_2},$$

where 382–384.4 K represents a broad Sm-$\tilde{A}$+Sm-A_2 coexistence range. The transition temperatures cited above are somewhat lower than those reported previously [4, 12] due to a slow drift in transition temperatures with time over the very long period of x-ray observations. With a large nematic range of 120 K, DB_5CN + C_5 stilbene is expected to yield critical behavior qualitatively similar to that of DB_8ONO_2.

The experiment was conducted using the same spectrometer, scattering configuration, and resolution as was described in the last section. The sample was aligned in the

nematic (N) phase in a 6.5 kG magnetic field by cycling the temperature slowly across the N–Sm-A_1 transition until a sample mosaicity of 0.12° HWHM was obtained. As explained in the previous section regarding the DB_8ONO_2 experiment, the DB_5CN + C_5 stilbene sample had a small linear drift in T_c which was observed over the long period of measurements, and this was taken into account in the data reduction. The initial T_c for DB_5CN+C_5 stilbene was 424.302 K, in very good agreement with those obtained from C_p data. The diffuse Sm-A_1 scattering peak is centered at (0, 0, $2q_0$), where $2q_0=2\pi/d$ and d is the Sm-A_1 layer spacing: $2q_0=0.2097\mathring{A}^{-1}$ for DB_8ONO_2 and $2q_0=0.2115\mathring{A}^{-1}$ for DB_5CN+C_5 stilbene, independent of temperature near the N–Sm-A_1 transition.

Longitudinal and transverse x-ray scans through (0, 0, $2q_0$) were carried out over the reduced temperature range $5\times10^{-6}<\tau<1.2\times10^{-2}$, where $\tau \equiv(T-T_c)/T_c$. As explained in the previous section, each pair of scans describing the lineshape was fit simultaneously with the standard structure factor, S(**q**), for Sm-A_1 fluctuations in the nematic phase: $S(\mathbf{q})= \sigma/[1 + \xi_{\|}^2(q_{\|} - 2q_0)^2 + \xi_{\perp}^2 q_{\perp}^2 + c\xi_{\perp}^4 q_{\perp}^4]$. The parameter c is a freely adjustable empirical coefficient for the $q_{\perp}^4$ term. Variants on the transverse lineshape, including Lorentzians to an arbitrary power, yield identical results for the temperature dependence of $\xi_{\perp}$ [13, 35].

The critical behaviors of $\xi_{\|}$, and $\xi_{\perp}$ and σ are first described in terms of effective critical exponents by fitting these quantities with simple power laws. Figure 3-10 shows the values for the longitudinal and transverse correlation lengths and the smectic susceptibility determined from the diffuse x-ray scattering along with their corresponding fits to pure power laws. The resulting exponents are $\nu_{\|}$=0.73±0.03, $\nu_{\perp}$=0.57±0.03, and γ=1.30±0.05 for DB_5CN+C_5 stilbene. These results compare very well with those for DB_8ONO_2 which had $\nu_{\|}$=0.69±0.03, $\nu_{\perp}$=0.59±0.03, and γ=1.28±0.05. Hence, both systems are close to the 3D–XY values: $\nu_{\|} = \nu_{\perp} = \nu_{XY} = 0.669 \pm 0.001$ and $\gamma_{XY} = 1.316 \pm 0.002$ [33, 36]. It is clear that although $\gamma=\gamma_{XY}$ and $\nu_{\|}$ is close to ν_{XY}, $\nu_{\perp}$ is less than ν_{XY} and, as in other liquid crystal systems, there is an anisotropy, $\nu_{\|}-\nu_{\perp} \simeq 0.16 \pm 0.03$ (slightly larger than the value 0.10 ± 0.03 measured for DB_8ONO_2). Similar results have been reported previously for the N–

S(q)	$\xi_{\|0}$ (Å)	$\nu_{\|}$	$\xi_{\|0}$ (Å)	$\nu_{\perp 0}$	σ_0	γ
Eq. 3.5, $c \neq 0$	7.91	0.73	1.84	0.57	1.22	1.30
	±0.34	±0.03	±0.08	±0.03	±0.05	±0.05
Eq. 3.5, $c = 0$	10.42	0.74	2.37	0.59	2.13	1.32
	±0.70	±0.05	±0.16	±0.04	±0.11	±0.07
Eq. 3.6	8.56	0.75	1.17	0.59	1.67	1.30
	±0.46	±0.04	±0.06	±0.03	±0.09	±0.06

Table 3.2: Summary of results for DB_5CN+C_5 stilbene. Least-squares values of the amplitudes and effective critical exponents for $\xi_{\|}$, $\xi_{\perp}$, and σ using the pure power-law forms of Eqs. 3.5 and 3.6.

Sm-A_1 transition in the alkyloxybenzoyloxy cyanostilbenes T_7 and T_8 [21] as well as in octyloxyphenylbenzoyloxy benzoate (80PCBOB) [32]. Reference [32] misstates the data analyses carried out in previous experiments such as [21].

Figure 3-11 shows the value of the quartic term c from fits to S(**q**) along with the ratio of the correlation lengths, $\xi_{\|}/\xi_{\perp}$. One notes from this figure that c has the same qualitative behavior for DB_5CN+C_5 stilbene as that obtained for DB_8ONO_2 shown in Fig. 3-6. As in the analysis of the DB_8ONO_2 data discussed in the last section, three forms for S(**q**) were tested: a simple Lorentzian, ie. Eq. 3.5 with $c = 0$; the non-Lorentzian given by Eq. 3.5; an empirical Lorentzian with a power-law correction, given by Eq. 3.6. Table 3.2 shows the results from fits using these three modified forms for the structure factor. These results demonstrate clearly that the effective critical exponents obtained are about the same for all three choices of the structure factor, S(**q**).

As discussed above for the DB_8ONO_2 data, replacing the quartic term with the so-called splay correlation length term, $\xi_s^4 q_s^4$, (proposed by Bouwman and de Jeu) yields essentially identical results for $\xi_{\perp}$. Fitting the DB_5CN + C_5 stilbene data using Eq. 3.5 one finds that $\xi_s \equiv c^{1/4}\xi_{\perp}$ is well described by $\xi_{s0}\tau^{-\nu_s}$ with $\xi_{s0} = 2.056\mathring{A}$ and $\nu_s = 0.46$.

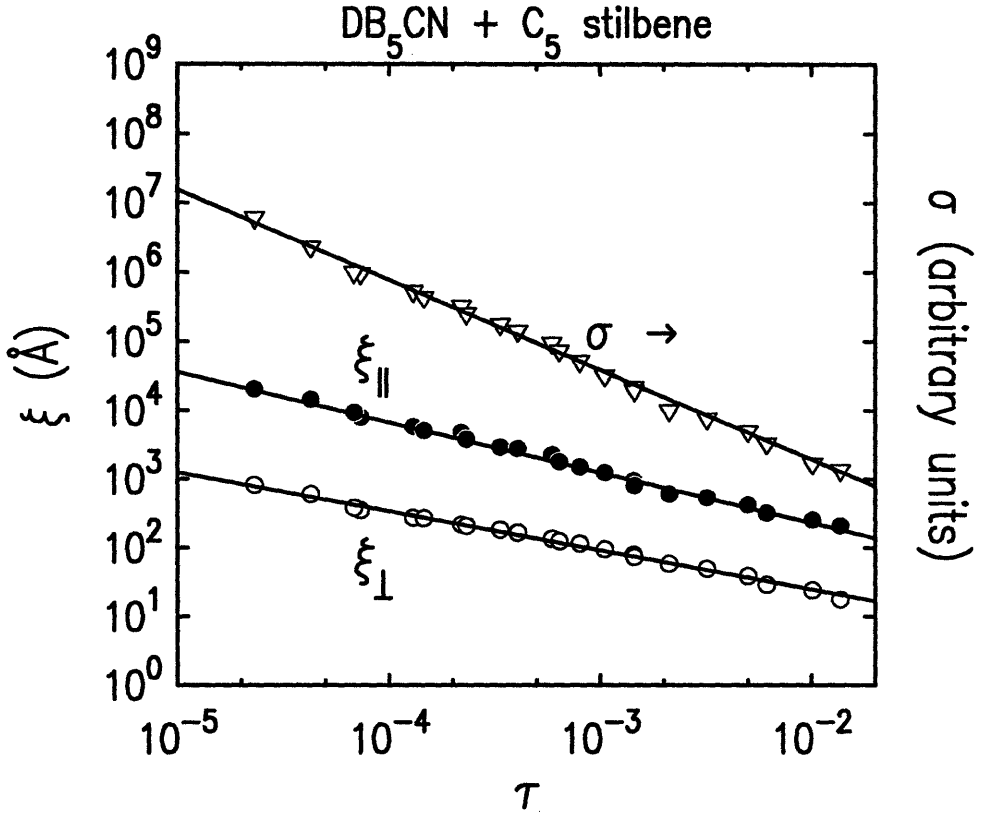

$$\sigma = \sigma_0 t^{-\gamma} \qquad (\gamma = 1.30 \pm 0.05)$$

$$\xi_{\parallel} = \xi_{\parallel 0} t^{-\nu_{\parallel}} \qquad (\nu_{\parallel} = 0.73 \pm 0.03)$$

$$\xi_{\perp} = \xi_{\perp 0} t^{-\nu_{\perp}} \qquad (\nu_{\perp} = 0.57 \pm 0.03)$$

Figure 3-10: The reduced temperature dependence of the Smectic-A_1 susceptibility σ and the longitudinal and transverse correlation lengths $\xi_{\parallel}$ and $\xi_{\perp}$ near the N–Sm-A_1 transition in DB_5CN+C_5 stilbene, as obtained from fitting the x-ray profiles with Eq. 3.5. The solid lines are least-squares fits with the indicated pure power laws, and the fitting parameters are given in the first line of Table 3.2. The σ values have been shifted up by a factor of 4 to improve clarity.

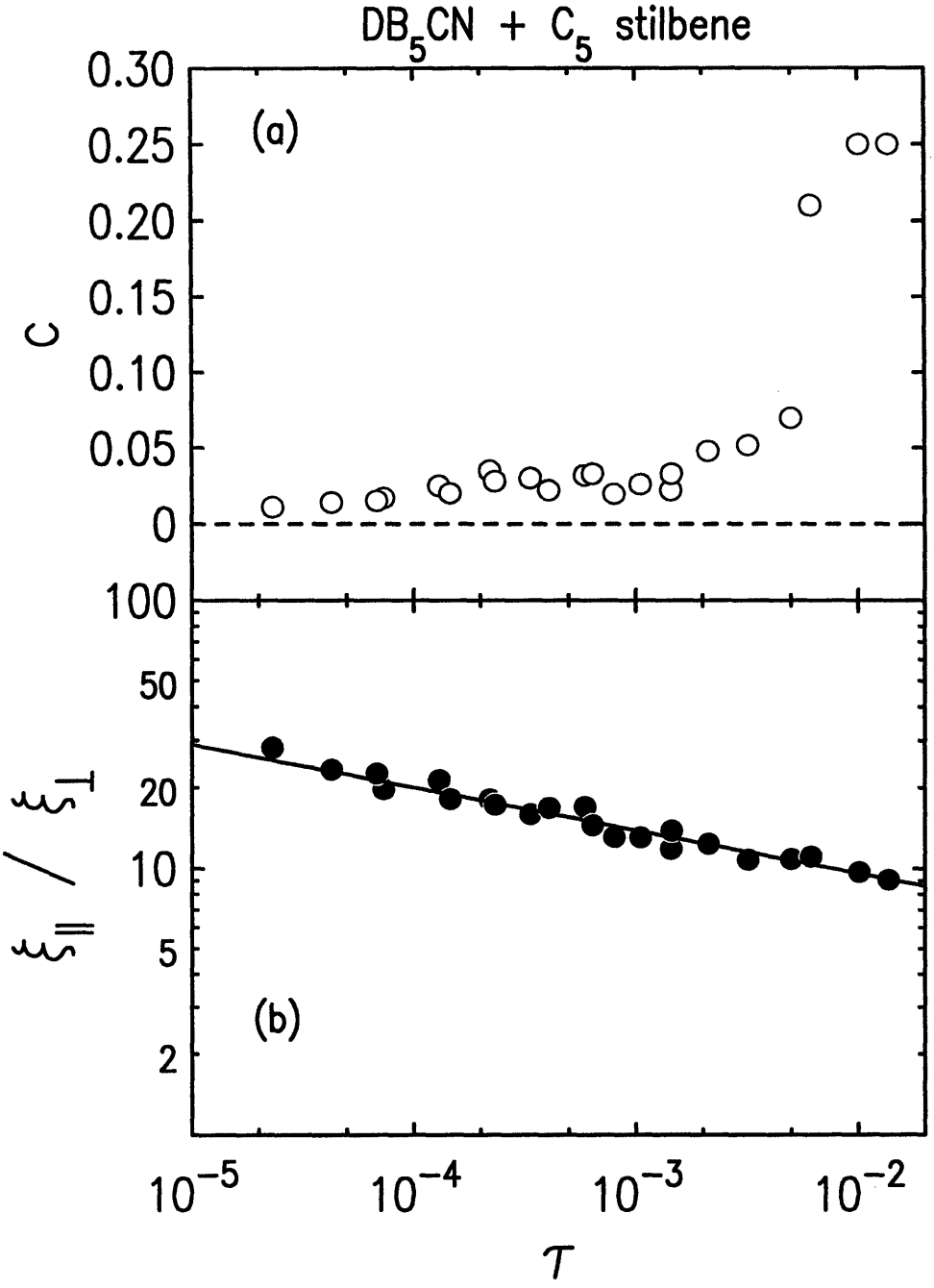

Figure 3-11: Pure power-law results for DB_5CN+C_5. (a) Fourth-order coefficient c in Eq. 3.5 obtained from least-squares fits to the x-ray profile, and (b) ratio $\xi_{\parallel}/\xi_{\perp}$ of correlation lengths obtained from fits to $S(\mathbf{q})$ and the c values shown. The line in (b) is a fit to a power-law form with a slope $\Delta\nu = \nu_{\parallel} - \nu_{\perp} = 0.16$.

3.3.1 Remarks on the Correlation Length Anisotropy

The x-ray scattering measurements on DB_8ONO_2 and DB_5CN+C_5 stilbene reveal that although the effective critical exponents $\nu_{\|}$ and γ conform well with 3D–XY universality, $\nu_{\perp}$ does not. Thus, these systems behave similarly to many other previously studied systems; namely, the correlation length exponents are anisotropic with $\nu_{\|} - \nu_{\perp}$ equal to 0.10±0.03 for DB_8ONO_2, and 0.16±0.03 for DB_5CN+C_5 stilbene. The lineshape analysis provides no evidence that this anisotropy is the result of the way the transverse line shapes were analyzed, in obvious disagreement with the suggestion of Ref. [32]. It should be stressed that the detailed form of reasonable choices for the structure factor $S(\mathbf{q})$ has no significant influence on the values of the effective critical exponents that are obtained from the pure power-law analysis.

3.3.2 Violation of 3D-XY Universality

Renormalization-group theory predicts that within a given universality class certain scaling relationships connecting critical exponents must exist. One such test of universality can be made through the hyperscaling relation, $d\nu = 2 - \alpha$, which is derived from simple free-energy considerations. This free-energy argument can be generalized for the anisotropic case where $\nu_{\|} \neq \nu_{\perp}$. Thus, two-scale-universality gives

$$\nu_{\|} + 2\nu_{\perp} + \alpha = 2 \tag{3.7}$$

as the anisotropic hyperscaling relation [3]. The x-ray and C_p results quoted above for DB_8ONO_2 yield $\nu_{\|} + 2\nu_{\perp} + \alpha = 1.86 \pm 0.07$ when Eq. 3.5 is used as the structure factor and 1.88±0.09 when Eq. 3.6 is used for the structure factor. From the results for DB_5CN+C_5 stilbene one finds that $\nu_{\|} + 2\nu_{\perp} + \alpha = 1.86 \pm 0.07$ using Eq. 3.5, and $\nu_{\|} + 2\nu_{\perp} + \alpha = 1.92 \pm 0.07$ using Eq. 3.6. Figure 3-12 shows the x-ray results using Eq. 3.5 along with their respective error bars. The dashed line in Fig. 3-12 indicates values of $\nu_{\|}$ and $\nu_{\perp}$ which exactly satisfy the hyperscaling relation of Eq. 3.7 with $\alpha = \alpha_{XY} = -0.007$, and the theoretical 3D-XY values are indicated by the filled circle. One should note that although $\nu_{\|}$ is quite close to the expected 3D-XY model value, $\nu_{\perp}$

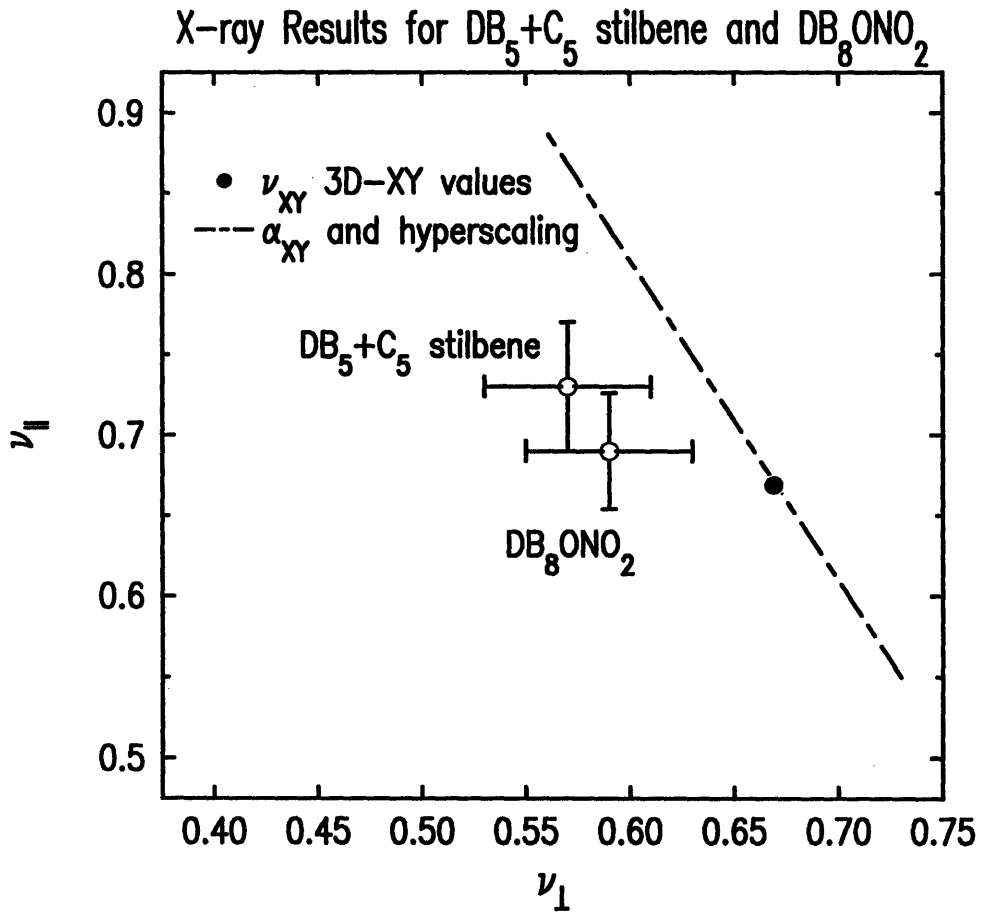

Figure 3-12: Hyperscaling violation for DB_8ONO_2 and DB_5CN+C_5 stilbene. The filled circle shows the location of the predicted 3D-XY values for the correlation length exponents ($\nu_{XY} = 0.669$). The dashed line indicates values of ($\nu_\parallel$, $\nu_\perp$) which satisfy hyperscaling with $\alpha = \alpha_{XY} = -0.007$. The error bars shown correspond to 95% confidence limits discussed in the text.

deviates markedly from the theoretical predictions for both samples. The uncertainty limits for the x-ray results are 95% confidence limits based on a propagation-of-error treatment using the uncertainties listed in Table 3.2 and $\Delta(\alpha)=\pm 0.003$. Thus it would appear that hyperscaling is violated in these two systems.

These apparent violations in polar N–Sm-A_1 systems arise from the use of effective exponents $\nu_\parallel$ and $\nu_\perp$ obtained from the use of pure power laws to describe the critical behavior of $\xi_\parallel$ and $\xi_\perp$. A preasymptotic analysis of the x-ray data using corrections-to-scaling terms, presented in the next section, shows that indeed hyperscaling is obeyed.

3.4 Preasymptotic Analysis of X-ray Data

In the previous two sections, high-resolution x-ray studies near the N–Sm-A_1 transition in DB_8ONO_2 and DB_5CN + C_5 stilbene were presented along with pure power-law analyses yielding effective critical exponents for the smectic order parameter susceptibility, γ, and for both longitudinal and transverse correlation lengths, $\nu_{\|}$ and $\nu_{\perp}$, respectively. However, as was observed from range-shrinking analyses in heat capacity studies on theses sample, conventional power-law analysis suffers from internal inconsistencies [13, 23, 24, 35]. Specifically, the nonasymptotic theory of Bagnuls and Bervillier [33, 40] shows that the critical heat capacity requires corrections to scaling. The heat capacity result from the theory gives $\Delta C_p^{\pm} = A^{\pm} t^{-\alpha}[1 + D_1^{\pm} t^{\Delta_1} + D_{2\mathrm{eff}}^{\pm} t] + B_c$, where for the 3D-XY model exponent one calculates $\alpha = -0.0066$, $\Delta_1 = 0.524$, $D_1^{+} = -0.461\theta_0^{\Delta_1}$, the term $D_{2\mathrm{eff}}^{\pm} t$ contains both second corrections-to-scaling and analytic correction terms, and B_c is a non-singular critical term. The heat capacity data for both DB_8ONO_2 and DB_5CN + C_5 stilbene were analyzed with the preasymptotic theory, and clearly demonstrate that first correction coefficients are large and must be retained for fitting C_p when $t \geq 10^{-4}$ [13, 23, 24, 35]. Moreover, the full nonasymptotic theoretical predictions for an ideal 3D–XY transition show that the corrections-to-scaling terms for C_p, as well as the correlation length, and the susceptibility are interrelated, and all depend on a single non-universal temperature scaling parameter θ_0 that can be evaluated from the C_p analysis alone.

In experiments, x-ray data typically extend well beyond the range of reduced temperature where asymptotic pure power-law theory is valid. Thus, a self-consistent description of the x-ray data is expected to require the preasymptotic theory. However, it is important to emphasize that prior to these results, x-ray studies of the critical behavior at the N–Sm-A_1 transition in liquid-crystal systems have failed to explicitly include corrections-to-scaling terms. In this section, results from an analysis of the x-ray data using the preasymptotic 3D–XY theory are presented for both DB_8ONO_2 and DB_5CN + C_5 stilbene.

Results of the Preasymptotic Theory

According to the pre-asymptotic theory, the thermodynamic quantities such as the correlated volume, $\xi^*(t^*)$, the smectic susceptibility, $\sigma^*(t^*)$, and the heat capacity, $C_p^*(t^*)$, can be expressed in the dimensionless form,

$$f^*(t^*) = X_1(t^*)^{-e}[1 + X_2(t^*)^{\Delta_1}]^{X_3} \times [1 + X_4(t^*)^{\Delta_1}]^{X_5} + X_6\,, \tag{3.8}$$

where e is the exponent which describes the critical divergence of the appropriate thermodynamic quantity (for example the correlation length) and X_6 is non-zero only for the heat capacity C_p. The corrections-to-scaling exponent Δ_1 is a universal quantity calculated from the theory and is equal to 0.524 ± 0.004 for the 3D-XY model. The quantities X_i are well determined numerically in the preasymptotic critical domain for the region $t^* \equiv \theta_0\tau < 10^{-2}$. Thus, this expression should be valid in the x-ray scattering experiments since the lower limit of the preasymptotic domain corresponds roughly to $\tau \sim 3 \times 10^{-3}$, which is well inside the range of data obtained for both DB_8ONO_2 and $DB_5CN + C_5$ stilbene.

The scaling relations of interest for both the x-ray experiments of the last two sections and the previously conducted heat capacity experiments can be written using the theoretically determined values for the 3D-XY model. These are

$$\xi = \xi_0\tau^{-\nu} \times [1 + 0.375(\theta_0\tau)^{0.524}] \times [1 + 29.76(\theta_0\tau)^{0.524}]^{0.232} \tag{3.9}$$

$$\xi_\parallel\xi_\perp^2 = (\xi_{\parallel,0}\xi_{\perp,0}^2)\tau^{-3\nu}[1 + 1.1262(\theta_0\tau)^{0.524}] \times [1 + 29.76(\theta_0\tau)^{0.524}]^{0.696} \tag{3.10}$$

$$\sigma = \sigma_0\tau^{-\gamma} \times [1 + 0.512(\theta_0\tau)^{0.524}] \times [1 + 24.55(\theta_0\tau)^{0.524}]^{0.46} \tag{3.11}$$

$$\Delta C_p = A\tau^{-\alpha} \times [1 - 0.461(\theta_0\tau)^{\Delta_1} + D_2^{\text{eff}}t] + B_c\,, \tag{3.12}$$

for the correlation length, correlated volume, smectic susceptibility, and heat capacity, respectively. In the above expressions, the quantity $\theta_0\tau$ is a theoretical scaling field, τ is the experimentally measurable reduced temperature, and θ_0 is a system-dependent quantity which is fixed at the value determined from the C_p analysis using Eq. 4.12. This is an important fact connecting the C_p studies with the results from the x-ray

experiments presented in sections 4.2 and 4.3.

Experimentally, measurements of heat capacity involve an integration over correlated *volumes*, thus it will prove convenient to work with the product $\xi_{\|}\xi_{\perp}^2$ when analyzing the correlation lengths for the x-ray data. In order to analyze the x-ray data, it is useful to express the correlated volume and smectic susceptibility in terms of a system dependent amplitude multiplied by a pure scaling function. Multiplying equations 4.10 and 4.11 by θ_0 to an appropriate power, one has

$$\xi_{\|}\xi_{\perp}^2 = (\xi_{\|,0}\xi_{\perp,0}^2)\theta_0^{3\nu} \times F_1(\theta_0\tau) \tag{3.13}$$

and

$$\sigma = \sigma_0\theta_0^{\gamma} \times F_2(\theta_0\tau)\,. \tag{3.14}$$

Thus, the bare correlation volume and bare susceptibility, which are system dependent, can be separated from the functions $\mathrm{F}_1(\theta_0\tau)$ and $\mathrm{F}_2(\theta_0\tau)$ which depend on the quantity θ_0 and the reduced temperature.

It is now proposed that one may apply the existing theoretical results for the isotropic 3D–XY model to the x-ray data, and thus analyze the smectic susceptibility σ, and the correlation volume $\xi_{\|}\xi_{\perp}^2$ using the results from the analysis of the heat capacity data to determine the value of θ_0 for DB_8ONO_2 and DB_5CN+C_5 stilbene. The correlation volume is related directly to the free energy by two-scale factor universality [19] and thus may exhibit ideal 3D–XY behavior even though $\xi_{\|}$ and $\xi_{\perp}$ separately deviate slightly from the 3D–XY predictions. Regardless, no theory explicitly accounts for the anisotropy in the correlation lengths [3, 7, 10].

Stauffer et al. [19] developed a method for demonstrating universality from experimentally measured critical properties. This led directly to the idea of two-scale factor universality, which can be expressed in the following form:

$$\frac{\bar{F}_{sing}\xi^3}{k_BT} = \frac{\bar{F}_{sing}\xi_{\|}\xi_{\perp}^2}{k_BT} = Y \equiv \text{Universal constant}\,.$$

$\bar{F}_{sing}$ is the singular free energy density with units of (volume)$^{-1}$, Y is a universal constant whose value is independent of the system studied within a given universality class [19], and the correlated volume is expressed in terms of the quantities measured in the x-ray experiment. As described in detail in reference [13], the free energy was evaluated by integrating the preasymptotic 3D-XY heat capacity expression of Eq. 4.12.

Application of the Preasymptotic Theory to the X-ray data

Data of $\xi_{\|}\xi_{\perp}^2$ as a function of τ for both DB_8ONO_2 and DB_5CN+C_5 stilbene along with the quantity $k_BTY/\bar{F}_{sing}$ (solid line) are shown in Fig. 3-13, where Y is the only adjustable parameter and is independent of temperature. The value of Y was found to be -0.267 for DB_8ONO_2 and -0.285 for DB_5CN+C_5 stilbene. Note that the solid lines, obtained by integrating the heat capacity, fit the results from the x-ray data very well across the full range of reduced temperature, and thus provide strong evidence that the expectations of the preasymptotic theory are correct.

In addition to the above test of the preasymptotic theory, an explicit analysis was also conducted using the results of expressions 4.10 and 4.11 for the correlated volume and smectic susceptibility, respectively. The scaled correlated volume, $F_1(\theta_0\tau) \equiv \xi_{\|}\xi_{\perp}^2/(\xi_{\|}\xi_{\perp}^2)_0\theta_0^{3\nu}$ and scaled smectic susceptibility, $F_2(\theta_0\tau) \equiv \sigma/\sigma_0\theta_0^{\gamma}$, are shown in Figs. 3-14 and 3-15 for both DB_8ONO_2 and DB_5CN+C_5 stilbene. The exact 3D-XY exponents $\nu = 0.669$ and $\gamma = 1.316$ are used in these expressions. The values of θ_0 determined from the C_p fits are 0.48 for DB_8ONO_2, and 0.41 for DB_5CN+C_5 stilbene. The solid curves correspond to the preasymptotic expressions while the dashed lines show the pure power-law expectations. In order to obtain the fits in Figs. 3-14 and 3-15, a *single* adjustable parameter was required; the bare correlated volume, $(\xi_{\|}\xi_{\perp}^2)_0$, for $F_1(\theta_0\tau)$, and the bare smectic susceptibility, σ_0, for $F_2(\theta_0\tau)$.

In Figs. 3-14 and 3-15 one can see that the x-ray data clearly deviate from the pure power law beyond 10^{-3} in reduced temperature. Although this curvature in the data is slight, it shows the same trend for both DB_8ONO_2 and DB_5CN+C_5 stilbene at large τ. It is unlikely that this is a result of simple systematic errors in the scattering

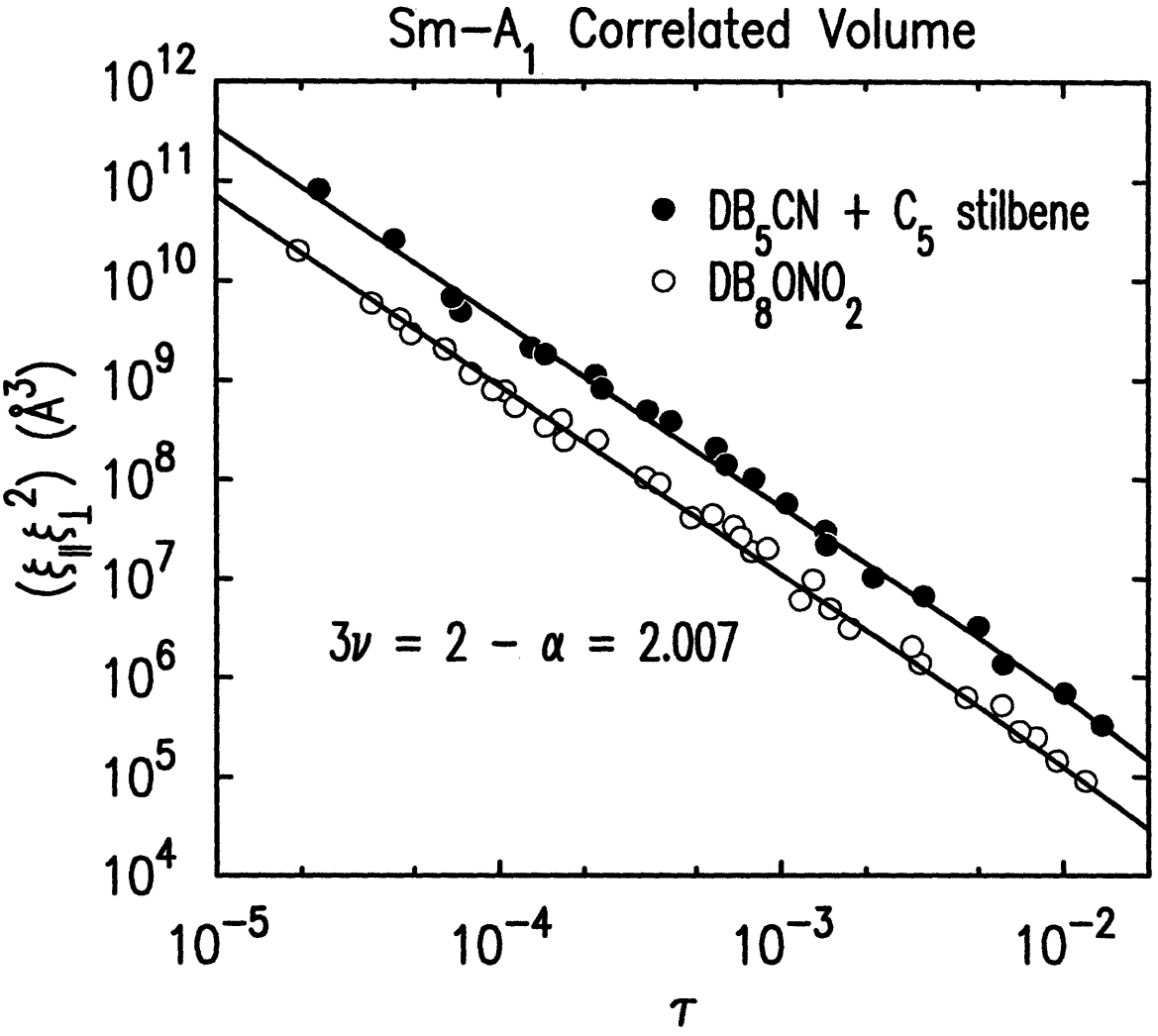

Figure 3-13: Temperature dependence of the Sm-A_1 correlated volume $\xi_\parallel \xi_\perp^2$ for DB_8ONO_2 and DB_5CN+C_5 stilbene. The solid fitting line $k_B TY/\bar{F}_{sing}$ has *one* adjustable parameter, the temperature-independent constant Y. The error bars are equal to the size of the points for both data sets. Data for DB_8ONO_2 are shifted down by a factor of 5 in order to improve the clarity of the display.

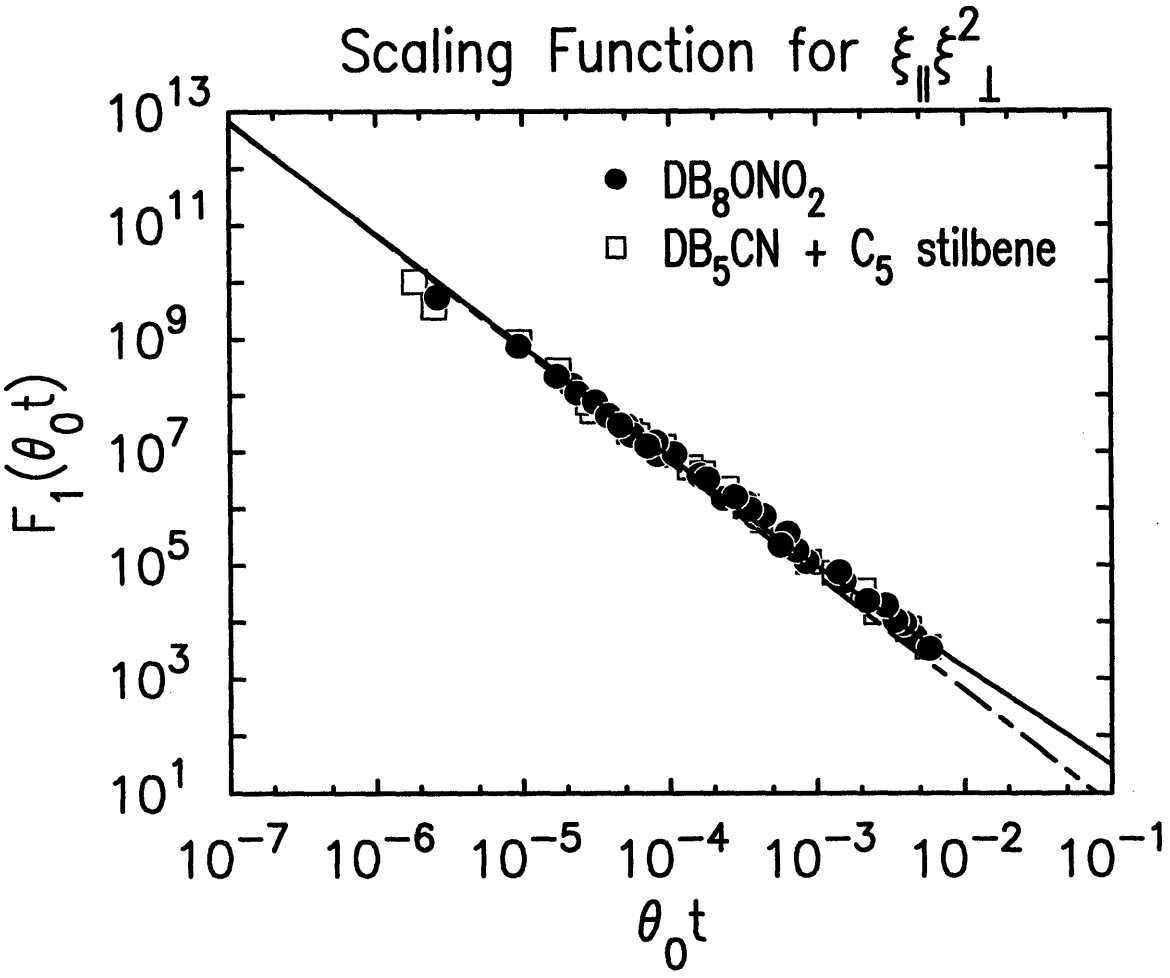

Figure 3-14: Correlated volume for DB_8ONO_2 and DB_5CN+C_5 stilbene and showing that a single universal curve describes the critical behavior. Note, the error bars are equal to the size of the points for both data sets.

data. The results from both the conventional analysis and the preasymptotic analysis are shown in tables 3.3 and 3.4. Note that ξ_ν^2 values as determined from best-fits of the data are comparable for both analyses.

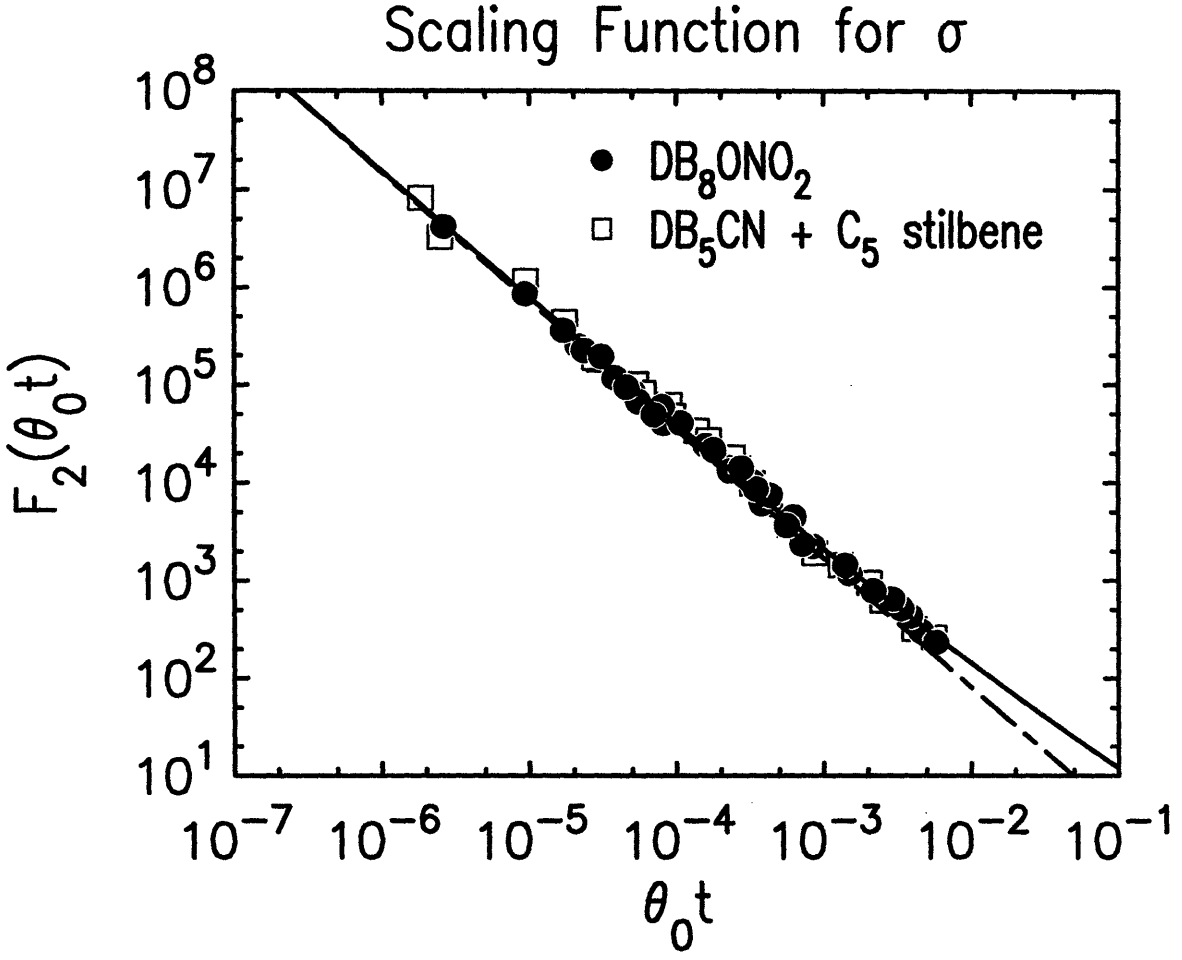

Figure 3-15: Smectic susceptibility scaling function for DB_8ONO_2 and DB_5CN+C_5 stilbene showing that a single universal curve describes the critical behavior. Note, the error bars are equal to the size of the points for both data sets.

Liquid Crystal Compound	Asymptotic (Pure Power-Law)					
	$(\xi_{\|}\xi_{\perp}^2)_0$	$3\nu_{\text{eff}}$	χ_ν^2	σ_0	γ_{eff}	χ_ν^2
DB_8ONO_2	26.92 ± 1.30	1.87 ± 0.09	1.71	1.33 ± 0.05	1.28 ± 0.05	1.75
DB_5CN + C_5 stilbene	23.20 ± 1.11	1.88 ± 0.09	1.50	1.22 ± 0.05	1.30 ± 0.05	1.10

Table 3.3: Summary of results from fits to the pure power-law 3D–XY theory.

Liquid Crystal Compound	Preasymptotic (3D–XY theory)					
	$(\xi_{\|}\xi_{\perp}^2)_0$	3ν	χ_ν^2	σ_0	γ	χ_ν^2
DB_8ONO_2	7.07 ± 0.37	2.007	1.98	0.849 ± 0.036	1.316	1.56
DB_5CN + C_5 stilbene	6.74 ± 0.35	2.007	1.76	0.825 ± 0.035	1.316	1.64

Table 3.4: Results from fits to the Preasymptotic 3D–XY expressions of Eqs. 4.9 – 4.12. Note, the values for 3ν and γ are fixed to the 3D-XY values.

3.5 Discussion

There are a number of issues which should be clarified about the analysis of the x-ray data. It had been common practice to use the conventional pure power-law analysis of x-ray data even for liquid crystal systems where heat capacity clearly showed the need for corrections-to-scaling terms. The reason for this is that x-ray data of $\xi_{\|}$, $\xi_{\perp}$, and σ generally showed statistically insignificant curvature over the full range of reduced temperature, and thus any corrections to pure power laws were considered inconclusive. Moreover, the anisotropy in the correlation lengths could not be explicitly accounted for in these analyses since the correction terms result from an isotropic theory. Further limitations in typical x-ray experiments are due to the relatively few data points obtained (about 20-40 points over nearly three decades of reduced temperature) in comparison with the several hundred data points in C_p studies, and thus range shrinking tests could not be adequately conducted. Universality has typically been salvaged by the success of anisotropic hyperscaling tests using the effective exponents ($\nu_{\|}$, $\nu_{\perp}$, and α_{eff}). However, the results presented above show obvious problems with this assumption; namely, these two large nematic range systems fail to obey hy-

perscaling although ideal 3D-XY behavior was observed in the heat capacity studies. Nevertheless, the rather large values for θ_0 determined from the C_p studies suggest that an analysis of the x-ray data must also include these corrections to scaling.

Note: The extent of the preasymptotic domain, estimated from the C_p analysis, can be approximately set at $\theta_0\tau \sim 2\times10^{-3}$. The effect of higher order correction terms are not are not considered in the analysis above as they are relevant only outside of the preasymptotic limit. The possibility of a crossover from isotropic ($\nu_{\|} = \nu_{\perp} = \nu_{XY}$) to anisotropic critical behavior has been predicted by Patton and Andereck [10]. These calculations treat the coupling between the smectic order parameter and nematic director fluctuations. However, neither a quantitative description of the crossover nor a treatment of corrections-to-scaling has been made within their model, and thus our results are unable to test these predictions.

3.6 Conclusions

The correlation volume $\xi_{\|}\xi_{\perp}^2$, the smectic order-parameter susceptibility σ, and the heat capacity C_p of DB_8ONO_2 and DB_5CN+C_5 stilbene are in excellent agreement with exact theoretical *preasymptotic* 3D-XY predictions. The importance of correction terms for $\xi_{\|}\xi_{\perp}^2$ and σ is clearly demonstrated and this is consistent with the use of correction terms in the analysis of C_p data. Several universal features of the 3D-XY model are obeyed [13] except for the anisotropy in the correlation lengths $\xi_{\|}$ and $\xi_{\perp}$, while hyperscaling is recovered. Excellent agreement of the x-ray correlated volume measurements with the two-scale factor universality predictions involving the free energy density determined solely from C_p data is also demonstrated. Moreover, this internally consistent analysis shows that few adjustable parameters are required to describe both $\xi_{\|}\xi_{\perp}^2$ and σ. These results combined with the successful description of the heat capacity ΔC_p show that the exact preasymptotic theory for the isotropic 3D-XY model correctly describes the critical behavior at the N–Sm-A_1 transition in these systems. It is anticipated that a theory which explicitly includes the length anisotropy should be able to explain the results for our correlated volume data.

Bibliography

[1] P. G. de Gennes, Solid State Commun. **10**, 753 (1972); P. G. de Gennes, in *The Physics of Liquid Crystals* (Clarendon, Oxford, 1974); P. G. de Gennes, Mol. Cryst. Liq. Cryst. **21**, 49 (1973).

[2] B. I. Halperin, T. C. Lubensky, and S. K. Ma, Phys. Rev. Lett. **32**, 292 (1974); C. Dasgupta and B. I. Halperin, *ibid.* **47**, 1556 (1981).

[3] T. C. Lubensky, J. Chim. Phys. **80**, 31 (1983).

[4] T. C. Lubensky, J. Chim. Phys. **80**, 31 (1983), and references cited therein.

[5] See for example Shang-Keng Ma, *Modern Theory of Critical Phenomena*, (Benjamin/Cummings Publishing Company, Inc., Reading, Massachusetts, 1976), pg. 91.

[6] J. D. Litster, R. J. Birgeneau, M. Kaplan, C. R. Safinya, and J. Als-Nielsen, in *Ordering in Strongly Fluctuating Condensed Matter Systems*, Vol. 50 of NATO Advanced Study Institutes Series, Ser. B: Physics, edited by Tormod Riste, (Plenum, New York, 1980), p. 357.

[7] D. R. Nelson and J. Toner, Phys. Rev. B **24**, 363 (1981); J. Toner,, *ibid.* **26**, 462 (1982).

[8] J. Prost, Adv. Phys. **33**, 1 (1984).

[9] P. Barois, J. Pommier, and J. Prost, in *Solitons in Liquid Crystals*, edited by L. Lam and J. Prost (Springer-Verlag, New York, 1989), Chap. 6.

[10] B. R. Patton and B. S. Andereck, Phys. Rev. Lett. **69**, 1556 (1992).

[11] D. L. Johnson, J. Chim. Phys. **80**, 45 (1983), and references cited therein; C. W. Garland and M. Meichle and B. M. Ocko and A. R. Kortan and C. R. Safinya and L. J. Yu and J. D. Litster and R. J. Birgeneau, Phys. Rev. A, **27**, 3234, (1983), and references cited therein.

[12] J. Thoen, H. Maynissen, and W. VanDael, Phys. Rev. Lett. **52**, 204 (1984).

[13] C. W. Garland, G. Nounesis, M. J. Young, and R. J. Birgeneau, Phys. Rev. E **47**, 1918 (1993), note that the value $2q_o = 0.2115\mathring{A}^{-1}$ cited therein is a typographical error; the correct value is $2q_o = 0.2481\mathring{A}^{-1}$.

[14] B. M. Ocko, R. J. Birgeneau, and J. D. Litster, Z. Phys. B **62**, 487 (1986).

[15] B. M. Ocko, Ph.D thesis, Massachusetts Institute of Technology, Cambridge, Massachusetts, 1984.

[16] K. J. Stine and C. W. Garland, Phys. Rev. A **39**, 3148 (1989).

[17] D. Brisbin, R. D. Hoff, T. F. Lockhart, and D. L. Johnson, Phys. Rev. Lett. **43**, 1171 (1979).

[18] L. Chen, J. D. Brock, J. Huang, and S. Kumar, Phys. Rev. Lett. **67**, 2037 (1986).

[19] D. Stauffer, M. Ferer, and M. Wortis, Phys. Rev. Lett. **29**, 345 (1972).

[20] K. K. Chan, P. S. Pershan, L. B. Sorensen, and F. Hardouin, Phys. Rev. A **34**, 1420 (1986).

[21] K. W. Evans-Lutterodt *et al.*, Phys. Rev. A **36**, 1387 (1987).

[22] G. Nounesis, C. W. Garland, and R. Shashidar, Phys. Rev. A **43**, 1849 (1991).

[23] C. W. Garland, G. Nounesis, and K. Stine, Phys. Rev. A **39**, 4919 (1989).

[24] C. W. Garland, G. Nounesis, K. Stine, and G. Heppke, J. Phys. (Paris) **50**, 2291 (1989).

[25] C. W. G. L. Wu and S. Pfeiffer, Phys. Rev. A **46**, 973 (1992).

[26] L. Wu, C. W. Garland, and S. Pfeiffer, Phys. Rev. A **46**, 6761(E) (1992).

[27] V. N. Raja *et al.*, Phys. Rev. A **37**, 303 (1988).

[28] C. W. Garland *et al.*, Phys. Rev. A **27**, 3234 (1983).

[29] P. Barois, T. C. Lubensky, and J. Prost, J. Phys. (Paris) **46**, 391 (1985).

[30] G. Nounesis, K. Blum, C. W. Garland, R. J. Birgeneau, S. Pfeiffer and R. Shashidar (unpublished).

[31] J. Als-Nielsen *et al.*, Phys. Rev. Lett. **39**, 1668 (1977).

[32] W. G. Bouwman and W. H. de Jeu, Phys. Rev. Lett. **68**, 800 (1992).

[33] C. Bagnuls and C. Bervillier, Phys. Rev. B **32**, 7209 (1985).

[34] K. Ema, C. W. Garland, G. Sigaud, and N. H. Tinh, Phys. Rev. A **39**, 1369 (1989).

[35] G. Nounesis *et al.*, Phys. Rev. E **47**, 1910 (1993).

[36] C. Bervillier, Phys. Rev. B **34**, 8141 (1986).

[37] D. L. Johnson, J. Chim. Phys. **80**, 45 (1983).

[38] S. Sprunt, L. Solomon, and J. D. Litster, Phys. Rev. Lett **53**, 1923 (1984).

[39] C. Dasgupta, J. Phys. (France) **48**, 957 (1987).

[40] C. Bagnuls and C. Bervillier, Phys. Rev. Lett. **112A**, 9 (1985).

[41] J. C. LeGuillon and J. Zinn-Justin, Phys. Rev. Lett. **39**, 95 (1977).

[42] J. C. LeGuillon and J. Zinn-Justin, Phys. Rev. B **21**, 3976 (1980).

[43] R. Shashidar *et al.*, Mol. Cryst. Liq. Cryst. Lett **1**, 89 (1985).

[44] X. Wen, C. W. Garland, and G. Heppke, Phys. Rev. A **44**, 5064 (1991).

[45] J. D. Litster and R. J. Birgeneau, Phys. Today **35**, No. 5, 261 (1982).

[46] K. G. Wilson, Phys. Rev. Lett. **28**, 540 (1972). See also S. K. Ma, *Modern Theory of Critical Phenomena* (Benjamin, Reading, 1976), Sec. IX.6.

[47] C. W. Garland, in *NATO ASI Ser. B Geometry and Thermodynamics*, edited by J.-C. Toledano (Plenum, New York, 1990), pp. 221–254.

[48] C. R. Safinya, W. A. Varady, L. Y. Chiang, and P. Dimon, Phys. Rev. Lett. **57**, 432 (1986).

[49] J. C. Chen and T. C. Lubensky, Phys. Rev. A **14**, 1202 (1976).

[50] L. Wu *et al.*, Phys. Rev. Lett. **72**, 376 (1994).

[51] J. Prost and P. Barois, J. Chim. Phys. **80**, 65 (1983).

[52] J. Wang and T. C. Lubensky, J. Phys. (France) **45**, 1653 (1984).

[53] K. Ema, G. Nounesis, C. W. Garland, and R. Shashidar, Phys. Rev. A **39**, 2599 (1989).

[54] S. Kumar, L. Chen, and V. Surendranath, Phys. Rev. Lett. **67**, 322 (1991).

[55] P. Barois, C. Coulon, and J. Prost, J. Phys. (Paris) Lett. **42**, L107 (1981).

Chapter 4

Density Wave Systems with Higher Harmonics

4.1 Introduction

The monolayer order of the Sm-A_1 phase in liquid crystals is perhaps one of the simplest encountered in density wave systems as it is the result of a symmetry breaking defined by the establishment of uniaxial order with only two components, a magnitude and phase [1]. Despite its apparent simplicity, many theoretical and experimental advances were required in order to elucidate the nature of the phase transition between the nematic and Sm-A_1 phases in these systems; some of these advances were presented in Chapter 3. There are many solid-state and soft condensed-matter systems which exhibit similar physical phenomena characterized by density wave order. The normal-incommensurate phase transition in charge density wave (CDW) systems is one example found in solid-state materials such as $NbSe_3$ [2]. The itinerant antiferromagnetic metal, chromium, is the "classic" spin density wave system familiar to solid-state physicists and serves as a model example which has been throughly studied [3]. The phenomenon of two-dimensional (2D) freezing from the bond-orientationally ordered hexatic fluid to a 2D solid is a particularly interesting example of density wave ordering.

In the previous chapter, detailed studies were presented showing the critical be-

havior associated with fluctuations of smectic-A_1 (Sm-A_1) order in the nematic phase near the N–Sm-A_1 transition in two polar thermotropic liquid crystalline materials. One should recall from these studies that the phase transitions and critical fluctuations in such systems are characterized by a two-component order parameter $\psi e^{i\phi}$ which is associated with a sinusoidal density wave $\rho=\rho_0+\psi e^{i\phi}e^{iq_0z}$ in three dimensions (3D). Hence the critical behavior associated with fluctuations of the order parameter is expected to be 3D-XY-like. In fact, this expectation was confirmed by the high resolution x-ray scattering experiments on DB_8ONO_2 and DB_5CN + C_5 stilbene. These results combined with the results from ac-calorimetry experiments showed clearly that many features of the N–Sm-A_1 phase transition in liquid crystals are well described by the 3D–XY model, although the correlation lengths exhibit weakly anisotropic critical behavior [13].

In the layered Sm-A_1 phase, the mass density is described by a single sinusoid and thus ρ has only one Fourier component. However, it is possible to find systems which exhibit density wave order requiring several Fourier components; thus, the density takes the form, $\rho = \rho_0 + \psi_n e^{inq_0z}$, where n$\geq$2. One of the more interesting examples of such systems is found in hexatic liquid crystals which can have long-range *bond orientational* order between the molecules with short-range *positional* order. Such bond orientational order is described by a multi-component order parameter with a six-fold symmetry. The hexatic order observed in experiments [8] exhibited critical behavior which was beautifully described by a multi-critical theory [5, 6, 8] detailing the scaling relation between successive harmonics of the order parameter, ψ_n, and the fundamental order parameter, ψ_1. However, for several years, observations of critical fluctuations at the higher harmonics in these and other condensed-matter systems had eluded experimental study since such critical scattering is extremely weak.

Until very recently no experiments had been reported on the critical fluctuations associated with the higher harmonics of sine-wave order parameter systems. This lack of experimental results had left many open questions, specifically in relation to the critical divergence of the correlation lengths for the higher harmonics. Theoretical treatment [7, 8] typically assumed that all correlation lengths in the system were

equal; this was a plausible assumption although no data existed to confirm this. To date only one system has shown critical scattering in the disordered phase of a multi-component sine-wave order parameter system; this liquid crystal system is the subject of the experiments presented in this chapter.

A high resolution x-ray scattering study was completed detailing the order parameter and critical fluctuations associated with both the first and second harmonics at the N–Sm-A_2 transition in the polar thermotropic liquid crystal material 4′-*n*-heptyloxycarbonylphenyl-4′-(4″-cyanobenzoyloxy) benzoate (7APCBB). The liquid crystal compound 7APCBB has the molecular formula

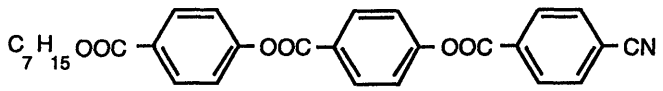

7APCBB

and the phase transition temperature sequence is [43, 44]

$$\mathrm{I} \underset{482K}{\longrightarrow} \mathrm{N} \underset{415.8K}{\longrightarrow} \text{Sm-}A_2 \underset{413.3K}{\longrightarrow} \text{Sm-}C_2.$$

This material was synthesized and first characterized at the Technical University of Berlin [43]; the sample investigated was from the same synthetic batch as that used previously for C_p measurements [44]. The Sm-A_2 phase has a bilayer structure with the layer thickness d=2L, where L is the molecular length [7], while Sm-C_2 is the corresponding tilted bilayer phase. The Sm-A_2 →Sm-C_2 phase transition was not studied in this experiment.

One interesting feature of this system is that it exhibits a *uniaxial* bilayer order and therefore the harmonic components characterizing this are centered at distinct positions in reciprocal space separated by integer multiples of the fundamental, $q_0\hat{\mathbf{z}}$. The nematic temperature range is quite wide for this system (66.2 K), implying that the nematic order parameter should be well saturated close to the N–Sm-A_2 transition; hence, this transition is expected to be second order and 3D-XY-like. This has been confirmed by a high resolution calorimetric study [44]. Analysis of C_p(N–Sm-A_2) data yielded the critical exponent $\alpha = -0.029$ when α was a freely

adjustable parameter, and a statistically equivalent fit was obtained with α fixed at the 3D–XY value ($\alpha = -0.007$).

The results of the present x-ray experiment revealed that the first-harmonic order parameter and critical fluctuations are very close to those expected for a 3D–XY systems with a very small correlation length anisotropy. Moreover, it was found that the second-harmonic susceptibility, χ_2, both above and below T_c exhibited the behavior predicted by Aharony and coworkers [5, 6, 8] who developed a multicritical scaling theory for the 3D–XY model. Theoretically, the exponents describing correlation functions of the order parameters ψ_n were derived from the d-dimensional XY model which described the leading order parameter ψ_1. Although these experiments confirmed the theoretical predictions for the second harmonic susceptibility, χ_2, fits of the second harmonic structure factor $S_2(\mathbf{q})$ to a single Lorentzian shape yielded correlation lengths $\xi_{\|2}$ and $\xi_{\perp 2}$ which seemed to scale very differently than their first harmonic counterparts. In fact, close to the transition, the second harmonic lengths were at least an order of magnitude smaller than the first harmonic lengths at the same temperature.

A different scaling of the correlation lengths ξ_n's for the different harmonics would imply that the N–Sm-A_2 transition involves more than one critical length scale and that it cannot be simply described by the XY model. Furthermore, the fitted exponents $\nu_{\|2}$ and $\nu_{\perp 2}$ severely violated the hyperscaling relation $\nu_{\|2} + 2\nu_{\perp 2} = 2 - \alpha$, with no explanation. These experimental findings motivated renewed theoretical work [21]. In the following section, several results from recent developments in the theory are presented. Specifically, it is predicted that all the harmonics are still dominated by the critical behavior of the XY model, and therefore that $\xi_n^2 = X_n \xi_1^2$, where X_n is a universal number. However, since X_n may be quite small, the structure factor of the n^{th} harmonic, $S_n(\mathbf{q})$, may be strongly influenced by its bare (non-critical) value. Furthermore, since at the transition $S_n \sim q^{-(2-\eta_n)}$, with large values of η_n, deviations from the Lorentzian shape are also important. These new theoretical results succeed in describing the results from the x-ray study of 7APCBB and results from more recent work which consisted of additional measurements on the same system [10]. Data

from these two studies are presented in Sec. 3.3.

4.2 Results of the Theory for the Higher Harmonics

One defines the "local" n'th harmonic order parameters as the slowly varying complex functions $\psi_n(\mathbf{r})$ determining the density:

$$\rho(\mathbf{r}) = \rho_0 + \mathrm{Re}\sum_{n=1}^{\infty}\psi_n(\mathbf{r})\exp(iq_0nz)\,. \tag{4.1}$$

Thus, the density contains a background (average) contribution from ρ_0 and modulated contributions from the ψ_n's. The first term, ψ_1, is the fundamental order parameter, while the higher harmonics ($n \geq 2$) are often referred to as secondary order parameters. In the most general case, one should treat all the ψ_n's as competing order parameters. In the absence of couplings, each ψ_n would undergo a separate XY-like phase transition, at a temperature T_n, described by a free energy

$$\begin{aligned}\mathcal{H}_n = \int d^d\mathbf{r}\Big\{&\frac{1}{2}r_{n0}[|\psi_n(\mathbf{r})|^2 + \xi_{\|nb}^2|\nabla_\|\psi_n(\mathbf{r})|^2 \\ &+\xi_{\perp nb}^2|\nabla_\perp\psi_n(\mathbf{r})|^2] + u_n|\psi_n(\mathbf{r})|^4\Big\}\,.\end{aligned} \tag{4.2}$$

Coupling terms are introduced through the interaction Hamiltonian

$$\mathcal{H}_{n,\mathrm{int}} = \mu_n\int d^d\mathbf{r}(\psi_1^n(\mathbf{r})\psi_n^*(\mathbf{r}) + \psi_1^{*n}(\mathbf{r})\psi_n(\mathbf{r}))\,. \tag{4.3}$$

where μ_n is the coupling strength. This interaction favors a *lock-in* of wavevectors with $\mathrm{q}_n = nq_1$. The correlation functions of the secondary order parameters, ψ_n's with $n > 1$, can in principle be derived from Eqs. (4.2) and (4.3).

Assuming T_n to be far enough below T_1, one has a transition at $T_c = T_1$, with the leading two component order parameter ψ_1. Near this transition, one can neglect the self-interaction of the ψ_n's and set $u_n = 0$ in Eq. (4.2). Thus the ψ_n's for $n > 1$ can be treated in the harmonic approximation and one can solve the partition function for ψ_n exactly in terms of the correlation functions of ψ_1. For example, the average

density modulation with the wave vector $nq_0\hat{\mathbf{z}}$ is determined by

$$\Psi_n = \langle\psi_n\rangle = \mu_n\chi_{nb}\langle\psi_1^n\rangle\,, \tag{4.4}$$

where $\chi_{nb} = 1/r_{n0}$ is the bare susceptibility for the n'th harmonic. Since χ_{nb} is not singular at T_1, the singularity comes only from $\langle\psi_1^n\rangle \propto |t|^{\beta_n}$, where $t = (T - T_c)/T_c$, $\beta_n = 2 - \alpha - \phi_n$ and ϕ_n is the crossover exponent associated with n'th order anisotropy near the rotationally invariant XY model fixed point [5]. Specifically, ϕ_2 is the crossover exponent when a symmetry breaking field results in a uniaxial anisotropy term; this term is proportional to $\mathrm{Re}(\psi_1^2) = x^2 - y^2$. Experiments on bond orientational harmonics confirmed these predictions for ϕ_n from integer $n = 1$ up to and including $n = 7$ [8].

Defining $\psi_n(\mathbf{q})$ as the Fourier transform of $\psi_n(\mathbf{r})$, the above theory can now be extended to the structure factor [17, 18],

$$S_n(\mathbf{q}) = \langle\psi_n(\mathbf{q})\psi_n^*(\mathbf{q})\rangle = S_{nb}(\mathbf{q}) + \mu_n^2 S_{nb}(\mathbf{q})^2\langle\psi_1^n(\mathbf{q})\psi_1^{*n}(\mathbf{q})\rangle\,, \tag{4.5}$$

or, equivalently

$$S_n(\mathbf{q}) = \langle\psi_n(\mathbf{q})\psi_n^*(\mathbf{q})\rangle = S_{nb}(\mathbf{q}) + \mu_n^2 S_{nb}(\mathbf{q})^2\tilde{S}_n\,, \tag{4.6}$$

where one defines the bare n'th harmonic structure factor,

$$S_{nb}(\mathbf{q}) = \frac{k_B T\chi_{nb}}{1 + \xi_{\|nb}^2 q_\|^2 + \xi_{\perp nb}^2 \mathbf{q}_\perp^2}\,, \tag{4.7}$$

and the correlation function,

$$\tilde{S}_n = \langle\psi_1^n(\mathbf{q})\psi_1^{*n}(\mathbf{q})\rangle\,.$$

Here, $\tilde{S}_n$ has to be calculated with the XY model Hamiltonian $\mathcal{H}_1$. The definition of ψ_n in Eq. 4.1 implies that the experimentally measured $\mathbf{q}$'s differ from those in Eqs. 4.5 and 4.7 by $nq_0\hat{\mathbf{z}}$. Based on the experimental evidence, one can ignore the

possibility that the peak in S_n is shifted away from $nq_0\hat{\mathbf{z}}$, thus this parameter can be constrained in the calculations.

Asymptotically close to T_1, and for very small $\mathbf{q}$, $S_{nb}(\mathbf{q})$ is practically temperature independent, and the divergent part of S_n is proportional to $\tilde{S}_n$. However, the experimental data usually extend over a range of momenta $\mathbf{q}$ in which the $\mathbf{q}$-dependence of S_{nb} cannot be ignored, as is shown in the discussion of these data below. This fact may be associated with the physical nature of the polar material, where the smectic-A_2 phase may be close to the transition into the smectic-A_1 phase.

The correlation function $\tilde{S}_n(\mathbf{q})$ is dominated by the critical behavior of the XY model represented by $\mathcal{H}_1$. The asymptotic form of $\tilde{S}_n(\mathbf{q})$ is expected to scale as $\chi_n f_n(q\xi_1)$, where f_n is a universal scaling function [15], and χ_n is the susceptibility for the n'th harmonic. Using a scaling model for the behavior of harmonics of the free energy [5, 9], ie.

$$F(t, h_n) \sim |t|^{2-\alpha} \sum_n g_n(h_n/|t|^{\phi_n}) ,$$

one can write for the latter term,

$$\chi_n = \partial^2 F/\partial^2 h \sim |t|^{2-\alpha-2\phi_n} \sim |t|^{-\gamma_n} ,$$

where ϕ_n is the usual crossover exponent. For $q\xi_1 \ll 1$, $f_n(q\xi_1)$ may be expanded in powers of $q\xi_1$, and thus be approximated by a Lorentzian, that is $f_n(x) = 1/[1 + X_n x^2 + O(x^4)]$, with $x \equiv q\xi_1$ and X_n is a universal amplitude ratio [15]. Rewriting $\tilde{S}_n = \chi_n/[1 + \xi_n^2 q^2 + ...]$, this yields $\xi_n^2 = X_n \xi_1^2 = X_n \xi_{10}^2 |t|^{-2\nu}$, that is, *all* the harmonic correlation lengths scale with the *same* XY model correlation length exponent ν, but with different amplitudes. The ratios of these amplitudes, X_n, are universal. The ϵ-expansion calculations [21] confirm these expectations, and explicitly show that X_n can be small compared to unity, causing the $\mathbf{q}$-dependence of $\tilde{S}_n$ to become dominant only very close to T_c. For $x \gg 1$, $f_n(x) \sim x^{-(2-\eta_n)}$, with $2 - \eta_n = \gamma_n/\nu$. For $n > 1$, η_n is quite large, and significant deviations from the Lorentzian shape are expect at large $q\xi_1$. Following Fisher and Burford [16], one can approximate the crossover between

these two limits and express the universal scaling form as

$$f_n(x) = \frac{(1 + A_n x^2)^{\eta_n/2}}{1 + (X_n + A_n \eta_n/2)x^2}. \tag{4.8}$$

The explicit calculation of $\tilde{S}_2$ using an ϵ-expansion in $d = 4 - \epsilon$ dimensions yielded the following results. First, one finds that ξ_2 scales with the same exponent as ξ_1, and second, the quantity $X_2 \equiv (\xi_n/\xi_1)^2$ is universal and has the value $\epsilon/20 - \epsilon^2/100 + \mathcal{O}(\epsilon^3) \approx 0.04$ in three-dimensions (ie. $\epsilon = 1$). The resulting form of the correlation function for $n = 2$ can then be written as

$$\tilde{S}_2(\mathbf{q}) = \frac{k_B T \chi_2 [1 + A_2(\xi_{\|1}^2 q_\|^2 + \xi_{\perp 1}^2 \mathbf{q}_\perp^2)]^{\eta_2/2}}{1 + (X_2 + A_2\eta_2/2)(\xi_{\|1}^2 q_\|^2 + \xi_{\perp 1}^2 \mathbf{q}_\perp^2)}, \tag{4.9}$$

with $\chi_2 \sim |t|^{-\gamma_2}$. In summary, eqs. 4.5, 4.7, and 4.9 form the theoretical predictions, to be compared with experimental data below. At this stage A_2 must be determined from experiment.

4.3 Experiment: The N–Sm-A_2 transition in 7APCBB

X-ray scattering data in the nematic phase were taken using the IBM-MIT beamline X20B at the National Synchrotron Light Source at Brookhaven National Laboratory. The diffraction experiment utilized a triple-axis spectrometer with a bent Si(111) monochromator and flat Si(111) analyzer together with horizontal and vertical collimating slits. The longitudinal resolution was 3.54×10^{-4} Å^{-1} (HWHM), the transverse in-plane resolution was less than 10^{-5}Å^{-1}, while the out-of-plane resolution was 0.02Å^{-1} (HWHM). The relatively strong scattering observed in the Sm-A_2 phase permitted measurements using the Cu $K\alpha$ radiation from a conventional rotating-anode x-ray source. The details of the spectrometer are essentially identical to those described in Chapter 3. The sample was sealed in a beryllium cell having a temperature stability of better than 0.002 K, and an applied magnetic field of 0.65 T aligned the nematic director in the scattering plane, resulting in a mosaicity in the Sm-A_2 phase of 0.3° (HWHM). This mosaicity is comparable to that measured in both DB_8ONO_2

and DB_5CN+C_5 stilbene discussed in the last chapter. The rapid linear drift of $\sim$ −0.006 K per hour in the transition temperature T_c was taken into account in the data reduction. As expected theoretically and as demonstrated in previous experiments [28], T_c drifts due to quenched impurities have no effect on the observed critical behavior.

Critical fluctuations of Sm-A_2 order within the nematic phase lead to diffuse scattering centered at (0, 0, q_0) and (0, 0, $2q_0$) with q_0=0.1080 $\AA^{-1}$. The experimental procedure included a complete set of scans carried out at both q_0 and $2q_0$ for each temperature. The value of T_c was determined by observing the onset of smectic mosaicity for the q_0 peak. Several such sweeps across the phase transition were done during the experiment. Figures 4-1 and 4-2 show typical longitudinal ($q_{\|}$) and transverse ($q_{\perp}$) scans through the q_0 and $2q_0$ peaks at various reduced temperatures $t \equiv (T-T_c)/T_c$. It is immediately evident from Figs. 4-1 and 4-2 that the scans at $2q_0$ are much broader than those at q_0, which implies that the relevant correlation lengths of the $2q_0$ fluctuations are much shorter than those of the q_0 fluctuations. Thus, it is clear that the previous theoretical assumptions that the correlation lengths for the successive harmonics are identical cannot be correct.

The critical scattering associated with the first harmonic was analyzed using essentially the same approach described in Chapter 3. X-ray scans above T_c were fit to the usual x-ray structure factor [31]

$$S(\mathbf{q}) = \frac{k_B T \chi_1}{1 + \xi_{\|1}^2 (q_{\|} - q_0)^2 + \xi_{\perp 1}^2 q_{\perp}^2 + c_1 \xi_{\perp 1}^4 q_{\perp}^4}, \tag{4.10}$$

convoluted with the instrumental resolution function. χ_1 is the susceptibility and $\xi_{\|1}$ and $\xi_{\perp 1}$ are the correlation lengths along the longitudinal and transverse directions associated with the order parameter $\psi_1 e^{i\phi}$. The quartic term, needed to describe the non-Lorentzian transverse line shape for the q_0 fluctuations, has a freely adjustable coefficient c_1. One finds that c_1 exhibits the same kind of temperature dependence seen typically for N–Sm-A_1 and other N–Sm-A [35] systems.

Susceptibility and correlation lengths for the q_0 peak in the nematic phase are

shown in Figs. 4-1 together with power law fits using $\chi_1(t) = \chi_{10}|t|^{-\gamma}$, $\xi_{1\|}(t) = \xi^0_{1\|}|t|^{-\nu_\|}$, and $\xi_{1\perp}(t) = \xi^0_{1\perp}|t|^{-\nu_\perp}$. For all of the data, the 1 standard deviation errors in χ and ξ are smaller than the size of the plotted symbols. However, T–T_c has a typical uncertainty of 0.012 K due to the combined effects of the uncertainties in T_c in a given run and the T_c drift rate. For the q_0 peak, the least squares values of the critical exponents and amplitudes are $\gamma_1 = 1.34 \pm 0.14$, $\nu_{\|1} = 0.70 \pm 0.07$ and $\xi^0_{\|1} = 7.0\mathring{A}$, $\nu_{\perp 1} = 0.64 \pm 0.07$, and $\xi^0_{\perp 1} = 0.83\mathring{A}$. These exponent values agree within the errors with the 3D–XY values calculated from theory: γ_{XY}=1.316±0.002 and ν_{XY}=0.669±0.001 [41, 42], and the length anisotropy itself is quite small, $(\nu_\| - \nu_\perp)_1 = 0.06 \pm 0.03$. The latter is obtained from fits to $\xi_{\|1}/\xi_{\perp 1}$ directly. In order to stress how close these q_0 results are to 3D–XY behavior, the lines shown in Fig. 4-5 represent fits with exponent values fixed at XY values $\gamma = \gamma_{XY}$, $\nu_{\|1} = \nu_{\perp 1} = \nu_{XY}$.

In figure 4-4, results from fits of the second harmonic scattering data are shown using the conventional modified Lorentzian form

$$S(\mathbf{q}) = \frac{k_B T \chi_2}{1 + \xi^2_{\|2}(q_\| - 2q_0)^2 + \xi^2_{\perp 2} q^2_\perp + c_2 \xi^4_{\perp 2} q^4_\perp}, \tag{4.11}$$

analogous to Eq. 4.10 with $c_2 = 0$. That is, these data are fit fairly well with a pure Lorentzian for most of the range of temperatures. The power-law fits to χ_2, $\xi_{\|2}$, and $\xi_{\perp 2}$ values obtained from these fits yield surprising results: namely, $\gamma_2 = 0.41 \pm 0.09$, $\nu_{\|2} = 0.31 \pm 0.04$ and $\xi^0_{\|2} = 27.1\mathring{A}$,$\nu_{\perp 2} = 0.23 \pm 0.04$, $\xi^0_{\perp 2} = 5.2\mathring{A}$ and $(\nu_\| - \nu_\perp)_2 = 0.08 \pm 0.04$ These clearly differ from the corresponding exponents for the first harmonic. The error bars represent 1 standard deviation statistical errors together with the effects of the uncertainty in T_c. The ratio of scattering wave vectors $2q_0/q_0$ is 2.000±0.003 both above and below T_c with no systematic temperature dependence. The ratio of diffuse intensities χ_2/χ_1 varies from $\sim 4\times10^{-2}$ at t=3×10^{-3} (where the q_0 fundamental scattering is quite weak) to $\sim 4\times10^{-4}$ at t=3×10^{-5}.

The scattering at the second harmonic can now be analyzed using the approximate form for the structure factor given by Eqs. 4.5 and 4.9 keeping in mind the universal

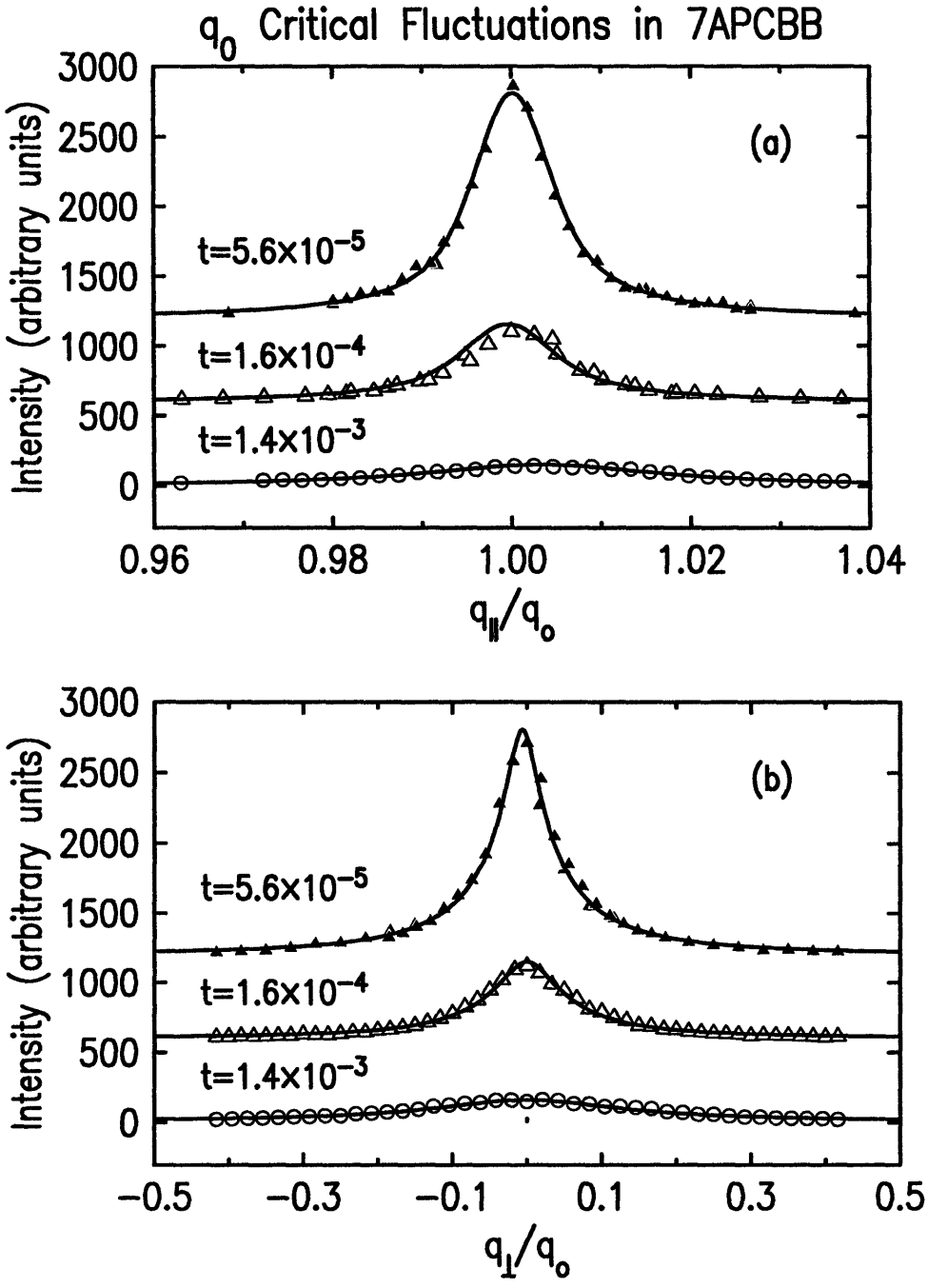

Figure 4-1: (a) Longitudinal x-ray scans through the q_0 peaks in 7APCBB at various reduced temperatures, $t = (T - T_c)/T_c$. (b) Corresponding transverse x-ray scans. For clarity, each scan is shifted by 600 counts/s in intensity. The solid lines are the results of least squares fits to Eq. 4.10, as explained in the text, convoluted with the instrumental resolution.

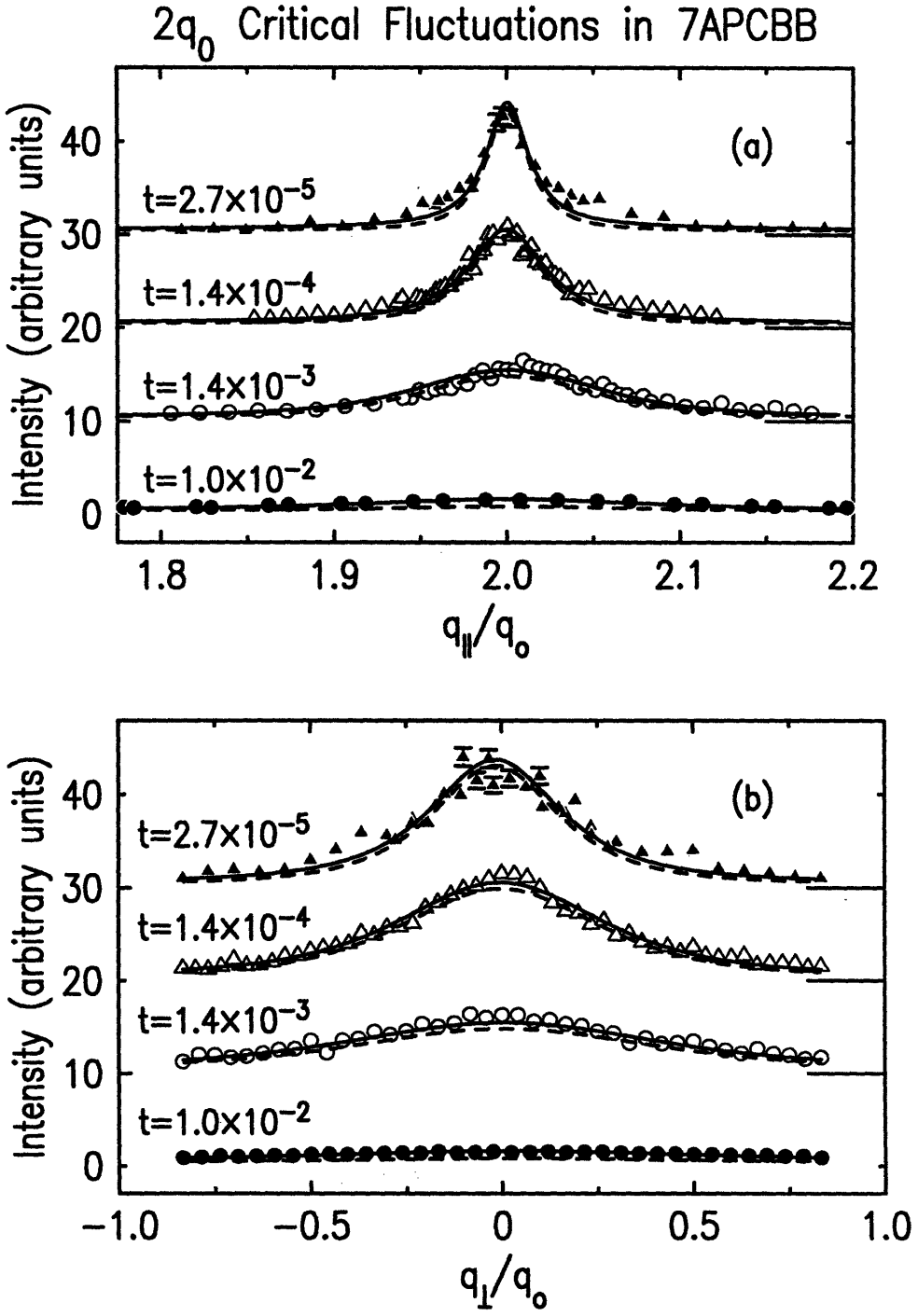

Figure 4-2: (a) Longitudinal x-ray scans through the $2q_0$ peaks in 7APCBB at various reduced temperatures, $t = (T - T_c)/T_c$. (b) Corresponding transverse x-ray scans. For clarity, each scan is shifted by 10 counts/s in intensity. The solid lines are the results of least squares fits to Eq. 4.5, as explained in the text, convoluted with the instrumental resolution. The dashed lines corresponds to the contributions from the second term of Eq. 4.5. The data at $t = 1.0 \times 10^{-2}$ (and at 8 lower temperatures) were taken with a lower resolution and then normalized to match the intensity of the earlier measurements in the overlap region.

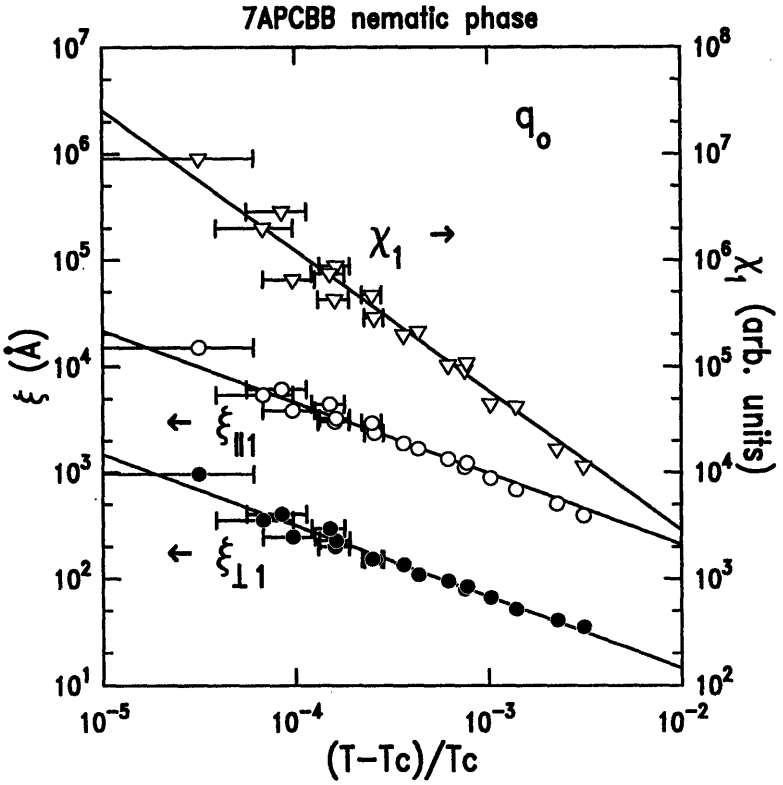

Figure 4-3: The susceptibility χ_1 for the first harmonic at q_0 in the nematic phase of 7APCBB. The solid line shows a single power law with the 3D-XY exponent $\gamma_1 = \gamma_{XY} = 1.316$. Also shown are data for the longitudinal and transverse correlation lengths for the first harmonic, $\xi_{\|1}$ and $\xi_{\perp 1}$, respectively, with the XY model exponent $\nu = 0.669$.

relationship $\xi_n = \xi_1\sqrt{X_n}$. One will notice that the data around $t \sim 10^{-2}$ are fitted excellently by a simple Lorentzian around $2q_0\hat{\mathbf{z}}$, with correlation lengths which show little temperature dependence. In order to interpret this, one can assume that far away from the transition Eq. 4.5 is dominated by the bare structure factor, $S_{nb}(\mathbf{q})$. From the data at $t = 10^{-2}$ shown in fig. 4-2 one sees that the contribution due to the second term in Eq. 4.5 (dashed line) is small. Fits to S_2 for scans at $t = 10^{-2}$ with Eq. 4.7 then yield the values $\xi_{\|2b} = 80\mathring{A}$ and $\xi_{\perp 2b} = 11\mathring{A}$. Furthermore, the amplitude χ_{nb} can be fixed at the value found by these fits. Having set the bare second harmonic structure factor, $S_{2b}(\mathbf{q})$, at these values for all temperatures, X_2 is also fixed at its ϵ-expansion value of 0.04, and $\xi_{\|1}$ and $\xi_{\perp 1}$ at their values determined from $S_1(\mathbf{q})$ at each temperature (shown in Fig. 4-5). The value of η_2 is also fixed to $2 - \gamma_2/\nu \approx 1.5$ using the predictions from the multicritical theory of reference [5]. Using Eq. 4.9 in

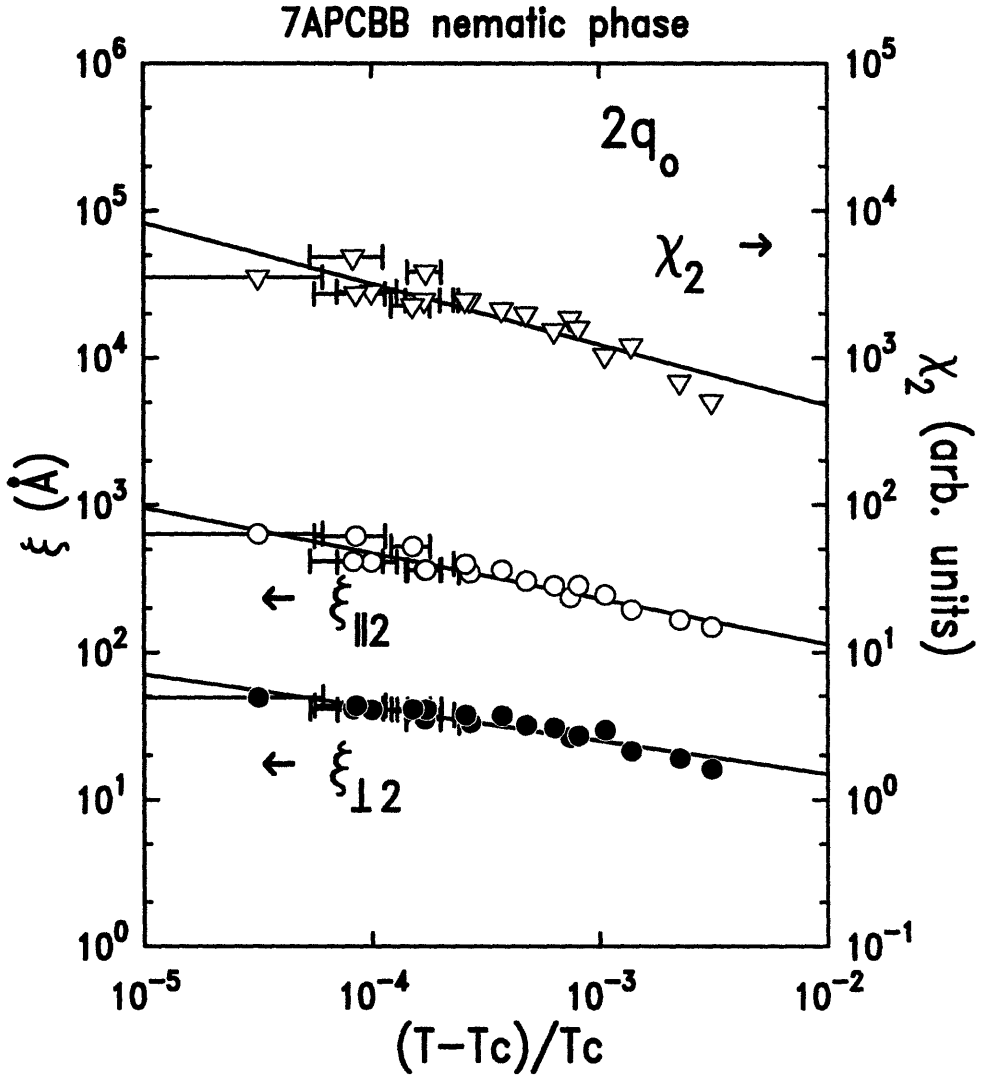

Figure 4-4: Results from fits of the second harmonic scattering to the pure Lorentzian form of Eq. 4.10 for $c = 0$. Data are shown for the smectic susceptibility χ_2 for the second harmonic at $2q_0$ in the nematic phase of 7APCBB. The solid line shows a single power law with the 3D-XY exponent $\gamma_2 = \gamma_{XY} = 0.41 \pm 0.09$. Also shown are data for the longitudinal and transverse correlation lengths for the second harmonic, $\xi_{\|2}$ and $\xi_{\perp 2}$, respectively, with exponents $\nu_{\|2} = 0.31 \pm 0.04$ and $\nu_{\perp 2} = 0.23 \pm 0.04$, for the longitudinal and transverse lengths, respectively.

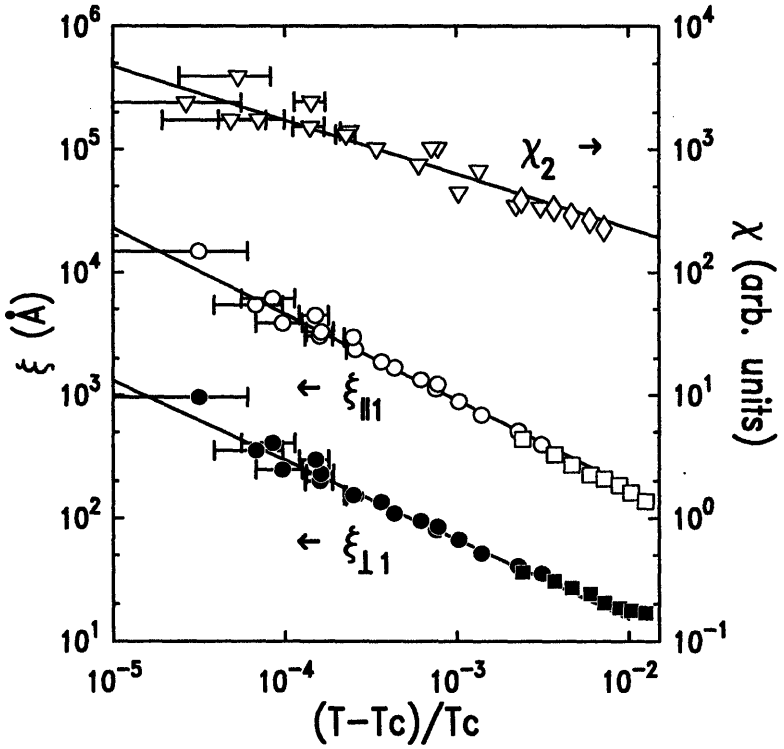

Figure 4-5: The susceptibility χ_2 for the second harmonic at $2q_0$ in the nematic phase of 7APCBB. These data include 8 additional data points (farthest from T_c) taken on the same sample at a later date and normalized to match the intensity of the earlier data [10]. The solid line shows a single power law with the exponent $\gamma_2 = 0.44$. Data are shown for the longitudinal and transverse correlation lengths for the first harmonic, $\xi_{\|1}$ and $\xi_{\perp 1}$, respectively, with the XY model exponent $\nu = 0.669$.

Eq. 4.5, the structure factor S_2 was then fitted in the range $10^{-5} < t < 10^{-4}$, ie. close to T_c, and found to yield good fits for $A_2 \approx 0.01$.

At these temperatures, S_2 is dominated by the second term in Eq. 4.5 (see top of Fig. 4-2). Setting $A_2 = 0.01$ for all T, one is left at each temperature with the single adjustable parameter $\mu_2\chi_2$. Finally, from fits of $S_2(\mathbf{q})$ at each temperature, the value of $\mu_2\chi_2$ was found. As can be seen from Fig. 4-2, the fits to both the transverse and longitudinal scans over the complete temperature range from $t \sim 10^{-2}$ to $t \sim 10^{-5}$ are very good, comparable in quality to the pure Lorentzian fits. This gives strong support to the above theory. The critical second harmonic susceptibility so-obtained is also shown in Fig. 4-5. Fits to a single power law give $\gamma_2 = 0.44 \pm 0.1$, again in agreement with the theoretical prediction $\gamma_2 = 0.32 \pm 0.04$ [5].

In addition to studying the diffuse scattering above T_c, measurements were made

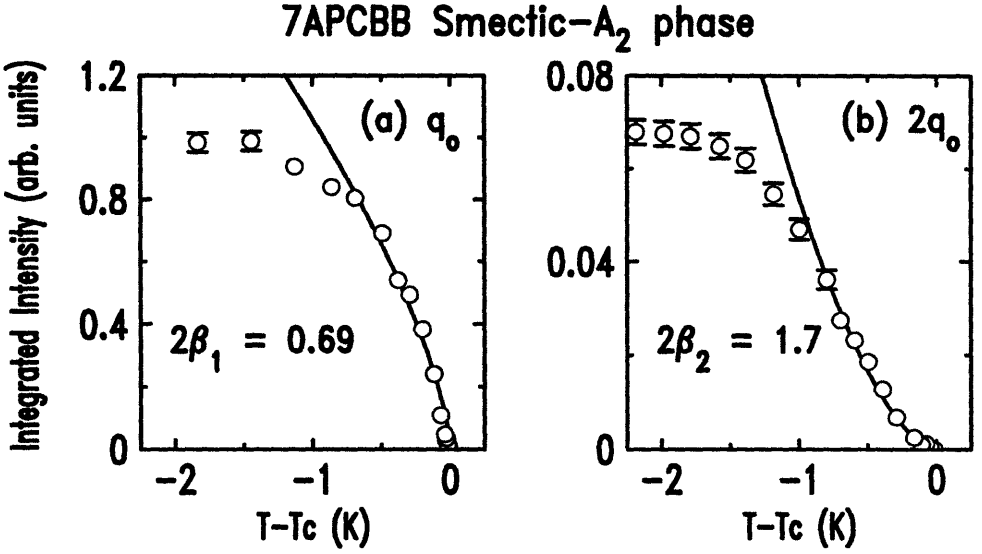

Figure 4-6: (a) The Bragg intensity versus temperature at q_0, integrated over the central mosaicity. The solid line is a single power law $|T - T_c|^{2\beta_1}$ with $2\beta_1 = 0.69$; (b) Bragg intensity versus temperature at $2q_0$, integrated over the central mosaicity. The Lorentz factor, $sin2\theta$, has been removed so that the relative intensity of (b) to (a) corresponds to $\sim |\psi_2/\psi_1|^2$ times the ratio of the molecular form factors squared. The solid line is a single power law $|T - T_c|^{2\beta_2}$ with $2\beta_2 = 1.7$.

of the integrated intensity $I(q_n)=\int d\mathbf{q}S(\mathbf{q} - n\mathbf{q})$ of the quasi-Bragg peaks in the Sm-A_2 phase. The diffuse scattering in the tails was cut off in order to make a reasonable determination of the pure quasi-Bragg component in the peaks. The temperature dependences of the Bragg intensities $I(q_0)$ and $I(2q_0)$ are shown in Fig. 4-6. The ratio of $I(2q_0)/I(q_0)(\sim |\psi_2/\psi_1|^2)$ in the Sm-A_2 phase is ~ 0.07 at $T = T_c - 2$ K. This corresponds to a relative value of the order parameters of $|\psi_2/\psi_1| \sim 0.26$, with an uncertainty arising from the molecular form factor which is not well known for 7APCBB [19]. Note that the intensities for both q_0 and $2q_0$ begin to saturate at about 1 K below T_c, presumably due to the pretransitional effects of the Sm-A_2–Sm-C_2 phase transition which occurs at T_c–T= 2.5 K in this sample. Fits of the data in the Sm-A_2 phase to single power laws for $|T - T_c| < 0.8$ K yield $\beta_1 = 0.39 \pm 0.04$ and $\beta_2 = 0.76 \pm 0.04$ in reasonable agreement with theoretical 3D-XY values $\beta_1 = 0.346 \pm 0.001$ and $\beta_2 = 0.85 \pm 0.07$. To emphasize this agreement, q_0 and $2q_0$ data are each shown with single power laws of the form $|T - T_c|^{2\beta}$ using the 3D XY values for β_1 and β_2.

Comments

Proving uniqueness as well as further optimization of the parameters would require a detailed theoretical expression replacing the approximate Eq. 4.5, as well as more precise experimental data. It would be most valuable to search for similar effects in other systems with XY-like DW ordering, and in systems exhibiting critical fluctuations in other secondary order parameters. Recently, results from an normal-incommensurate transition in the solid-state material Rb_2ZnCl_4 were found revealing critical scattering at the first three harmonics (secondary satellite peaks) of the incommensurate modulation in the ordered phase which was well described by the 3D-XY model critical exponents [22]. However, no critical scattering was observed in that study *above* T_c at any of the harmonics of the fundamental. Such complete absence of higher harmonic critical scattering is very puzzling since substantial scattering had been observed at the higher harmonics in the ordered phase. It was argued that the small susceptibility of the higher harmonics might be a general feature of solid-state materials as there is no particular reason for a softening of modes with wave vectors at the secondary satellite positions. Futher, it was emphasized that Rb_2ZnCl_4 might have many complicating features due to its solid-state nature causing it to behave differently from 7APCBB. For example, as was pointed out by Zinkin et al., scattering at structural phase transitions involves phonon processes associated with both the higher harmonics of the order parameter, and with secondary order parameters. The latter one-phonon scattering contribution arises from the higher Fourier components of the structural distortion. The Rb_2ZnCl_4 system had the additional complication of requiring two length-scales to describe the critical scattering. No such behavior was observed in 7APCBB.

The anomalously large scattering which occurs in 7APCBB is apparently due to the relatively large coupling between the n'th harmonic with the primary order parameter and large bare susceptibility. As seen from Eqs. 4.4 and 4.5, the chances to observe higher harmonics are increased when the couplings among the harmonics, represented by the coupling coefficients μ_n, are strong, and when the bare suscepti-

bilities, χ_{nb} are large; that is the T_n's are not too far from each other. Despite the contrasts between the behavior observed in the liquid crystal experiment and that reported for Rb_2ZnCl_4, it appears that the results for both systems concord in their observations of the critical behavior below T_c. It remains to be seen whether other density wave systems will yield results consistent with those observed in 7APCBB above T_c.

4.4 Conclusions

Using synchrotron x-ray techniques it has been possible to measure the critical behavior above T_c associated with both the first- and second-harmonic critical fluctuations. We have also measured the relative intensities of the first- and second-harmonic density wave order parameter scattering below T_c. The first-harmonic critical behavior is found to be 3D–XY-like, albeit with a small length anisotropy as is normally observed at N–Sm-A transitions. The second-harmonic susceptibility above T_c and the integrated Bragg intensity below T_c both are accurately predicted by the XY-model multicritical scaling theory [5, 6, 8]. However, a simple interpretation for the second harmonic lengths disagreed strongly with predictions of current density wave systems, and thus stimulated a re-examination of the theory. The resulting theoretical advances yield predictions for the behavior of the structure factor associated with fluctuations in the n'th harmonic density wave order parameter $\psi_n(\mathbf{q})$. Namely, the n'th structure factor $S_n(\mathbf{q})$ is affected by a coupling between $\psi_n(\mathbf{q})$ and the leading order parameter $\psi_1(\mathbf{q})$, and by its bare $\mathbf{q}$-dependence. Moreover, the correlation lengths characterizing fluctuations in the order parameters $\psi_n(\mathbf{q})$ are found to scale with a universal ratio, $X_n = (\xi_{n0}/\xi_{10})^2$, and are described by a *single* exponent ν. The theoretical calculations give $X_2 = \epsilon/20 - \epsilon^2/100 + \mathcal{O}(\epsilon^3)$ in an ϵ-expansion in $4 - \epsilon$ dimensions. This new theory is completely consistent with the experimental data on the second harmonic critical fluctuations in 7APCBB. Clearly, these theoretical advances should have consequences for the description of *all* 3D density wave phase transitions and possibly 2D systems as well.

Bibliography

[1] J. D. Litster and R. J. Birgeneau, Phys. Today **35**, No. 5, 261 (1982).

[2] R. F. Fleming, D. E. Moncton, J. D. Axe, and G. S. Brown, Phys. Rev. B **30**, 1877 (1984).

[3] For a review, see E. Fawcett, Rev. Mod. Phys., **60**, 1, (1988).

[4] B. I. Halperin and T. J. Lubensky [Solid State Commun. **14**, 997 (1974)] argued that the fluctuations of the director can convert the nematic-smectic phase transition into a first order one. M. A. Anisimov, V. P. Voronov, V. E. Podnek and F. Kholmurodov, Pis'ma Zh. Eksp. Teor. Fiz. **45**, 336 (1987) [JETP Letters **45**, 425 (1987)] reported experimental results confirming that possibility. However, the latter were obtained for the region near a tricritical point where the fourth-order interaction vertex is anomalously small. Far from the tricritical point one effectively expects an XY-like second order behavior, and the director fluctuations are not expected to play an essential role.

[5] A. Aharony *et al.*, Phys. Rev. Lett. **57**, 1012 (1986).

[6] R. A. Cowley and A. D. Bruce, J. Phys. C **11**, 3577 (1978).

[7] D. R. Nelson and B. I. Halperin, Phys. Rev. B **19**, 2457 (1979).

[8] J. D. Brock *et al.*, Z. Phys. B**74**, 197 (1989).

[9] L. Wu, M. J. Young, Y. Shao, C. W. Garland, R. J. Birgeneau, and G. Heppke, Phys. Rev. Lett. **72**, 376 (1994).

[10] Yongmei Shao, M.S. thesis, Massachusetts Institute of Technology, Cambridge, Massachusetts, 1994.

[11] E. V. Gurovich, E. I. Kats and V. V. Lebedev, JETP **73**, 473 (1991).

[12] E. I. Kats, V. V. Lebedev and A. R. Muratov, Phys. Rep. **228**, 1 (1993).

[13] The integration over ψ_n also generates changes in the effective Hamiltonian $\mathcal{H}_1$. In the case of ψ_2, there arises a non trivial q-dependent negative contribution to the fourth order vertex in ψ_1. This contribution may turn the transition first order. However, if the contribution does not change the sign of the total vertex the phase transition remains of second order and belongs to the same XY universality class.

[14] The definition of ψ_n in Eq. (1) implies that the experimentally measured $\mathbf{q}$'s differ from those in Eqs. (5) and (6) by $nq_0\hat{\mathbf{z}}$. Based on the experimental evidence, we ignore the possibility that the peak in S_n is shifted away from $nq_0\hat{\mathbf{z}}$.

[15] For a recent review on universal scaling functions and universal amplitude ratios, see e. g. V. Privman, P. C. Hohenberg and A. Aharony, in *Phase Transitions and Critical Phenomena*, edited by C. Domb and J. L. Lebowitz (Academic, New York, 1991), Vol. 14, p. 1.

[16] M. E. Fisher and R. J. Burford, Phys. Rev. **156**, 583 (1967).

[17] E. V. Gurovich, E. I. Kats, and V. V. Lebedev, JETP **73**, 473 (1991).

[18] E. I. Kats, V. V. Lebedev, and A. R. Muratov, Phys. Rep. **228**, 1 (1993).

[19] B. M. Ocko, A. R. Kortan, R. J. Birgeneau, and J. W. Goodby, J. Phys. **45**, 113 (1984).

[20] K. G. Wilson, Phys. Rev. Lett. **28**, 540 (1972). See also S. K. Ma, *Modern Theory of Critical Phenomena* (Benjamin, Reading, 1976), Sec. IX.6.

[21] R. R. Netz and A. Aharony, *Scaling Behavior of Quartic Correlation Functions*, to be published.

[22] M. P. Zinkin *et al.*, *Synchrotron X-ray scattering study of the Normal-Incommensurate phase transition in* Rb_2ZnCl_4, submitted for publication (1996).

[23] A recent and very readable review of density waves in solid-state materials can be found in G. Grüner, *Density Waves in Solids*, (Addison-Wesley Co., Reading, Massachusetts, 1994).

Chapter 5

Smectic-A Fluid Antiphase Domain Ordering

A high-resolution x-ray diffraction study has been carried out on a binary liquid crystal mixture of pentylphenylcyanobenzoyloxy benzoate (DB_5CN) + cyanobenzoyl oxypentyl-stilbene (C_5 stilbene) that is 49.5 mole % C_5 stilbene. This mixture exhibits on cooling the phase sequence monolayer smectic-A (Sm-A_1) – smectic-A fluid antiphase (Sm $\tilde{A}$) – bilayer smectic-A (Sm-A_2). We observe the presence of a coexistence region between the Sm$\tilde{A}$ phase and the Sm-A_2 phase, contrary to previous work which reported a new smectic-A crenelated phase. The high resolution of this diffraction experiment allows us to quantify directly the behavior of the smectic-A fluid antiphase domain ordering and the evolution of the system to Sm-A_2 order via a two-phase coexistence region. These results are compatible with previous high-resolution heat capacity measurements on the same sample.

5.1 Antiphase Domain Order in Polar Compounds

Thermotropic liquid crystal systems possess rich intermolecular and entropic interactions which allow for a multitude of ordered structures, and a wide variety of order-disorder transitions [1]. In fact, smectic liquid crystalline order alone is realized in more than ten classes, the best known being the smectic-A phases which

were discussed at length in Chapters 3 and 4. The simplest structure of this class is the monomeric smectic-A_m (Sm-A_m), which can occur in nonpolar rodlike mesogenic molecules. Smectic-A polymorphism is typically observed in molecules with long (three-ring) aromatic cores and a polar head group which provides the molecule with a longitudinal dipole moment. Studies of mixtures of these dipolar mesogens have revealed a variety of interesting phases within the SmA class: In particular, the partial bilayer Sm-A_d, the monolayer Sm-A_1, the bilayer Sm-A_2, and a more exotic biaxial phase intermediate between the latter two–the "smectic-A fluid antiphase" (Sm$\tilde{A}$) [2, 3, 4, 6]. The hallmark of the Sm$\tilde{A}$ phase is the establishment of a long-period polarization wave within the layers [8, 9, 10, 11].

It is known that for a range of concentrations, binary mixtures of the polar cyano mesogens pentylphenylcyanobenzoyloxy benzoate (DB_5CN) and cyanobenzoyl oxypentylstilbene (C_5 stilbene) exhibit a smectic fluid antiphase Sm$\tilde{A}$ between the Sm-A_1 and Sm-A_2 phases [4].

A partial phase diagram of this system is shown in Fig. 5-1. Depicted in Fig. 5-2(a) are real space sketches of several SmA structures, including Sm$\tilde{A}$, which possesses a centered rectangular two-dimensional lattice with m=a/2 [8]. Reciprocal space pictures of the x-ray scattering associated with these structures are shown in Fig. 5-2(b). Sm$\tilde{A}$ order is analogous to the antiphase domain order which occurs in binary alloys. It consists of two-dimensionally ordered slabs; hence this phase is characterized by the usual density modulation normal to the layers and an in-plane wavevector modulated at $q_\perp = q_T^0$, where $q_\perp$ is the transverse component in (q_H, q_K, q_L) space.

It has been reported that a *new* smectic-A fluid antiphase intermediate between the Sm$\tilde{A}$ phase and the Sm-A_2 phase occurs for these systems, and this has been designated as crenelated smectic-A or Sm-A_{cren} [8]. The Sm-A_{cren} phase differs from the Sm$\tilde{A}$ phase in its in-plane order. In essence, the periodic antiphase domains are proposed to be slabs of different thicknesses with m<a/2 while the longitudinal order remains unchanged. We will show [7] that the region of the phase diagram for DB_5CN and C_5 stilbene between the Sm$\tilde{A}$ and Sm-A_2 phases corresponds a broad two-phase coexistence region, as opposed to a new type of smectic-A fluid antiphase.

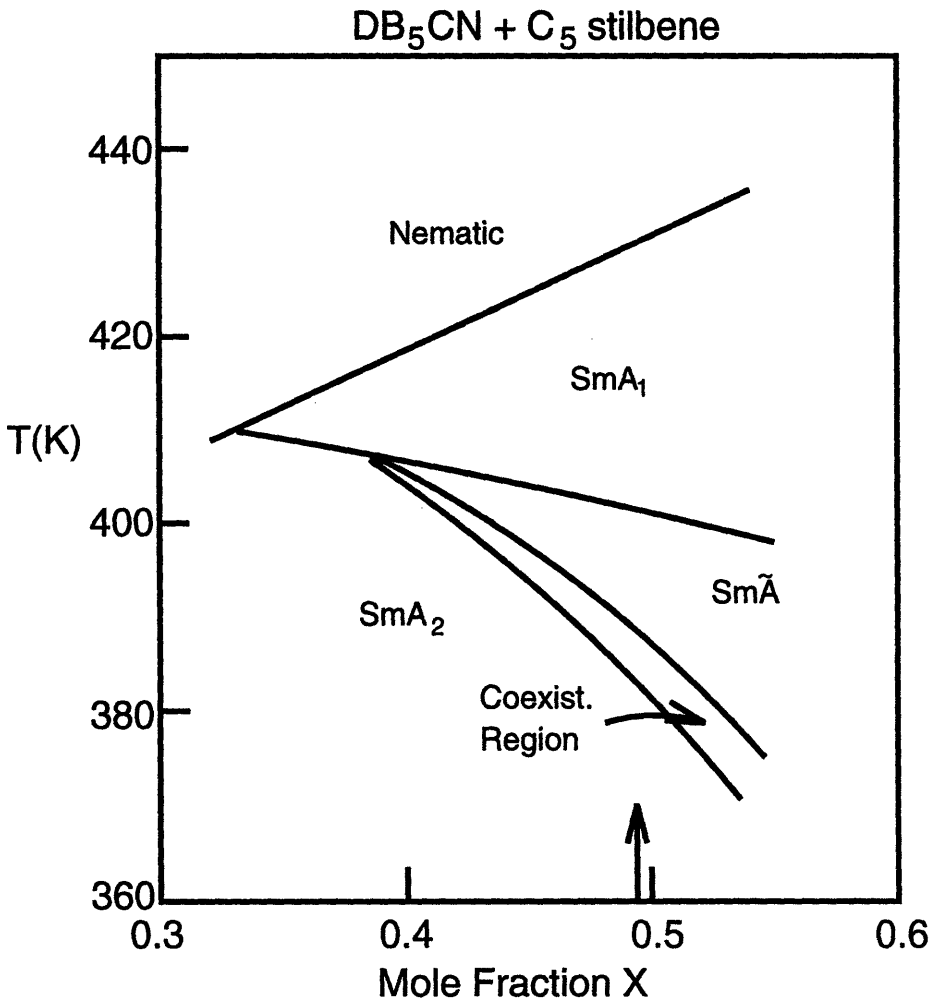

Figure 5-1: Partial phase diagram for mixtures of DB_5CN + C_5 stilbene, taken from Ref. [4]. The narrow region labeled "coexist" was formerly assigned to the Sm-A_{cren} phase but is now ascribed to a broad coexistence of SmÃ and Sm-A_2 phases. The arrow indicates the mole fraction of C_5 stilbene for the composition studied in this work.

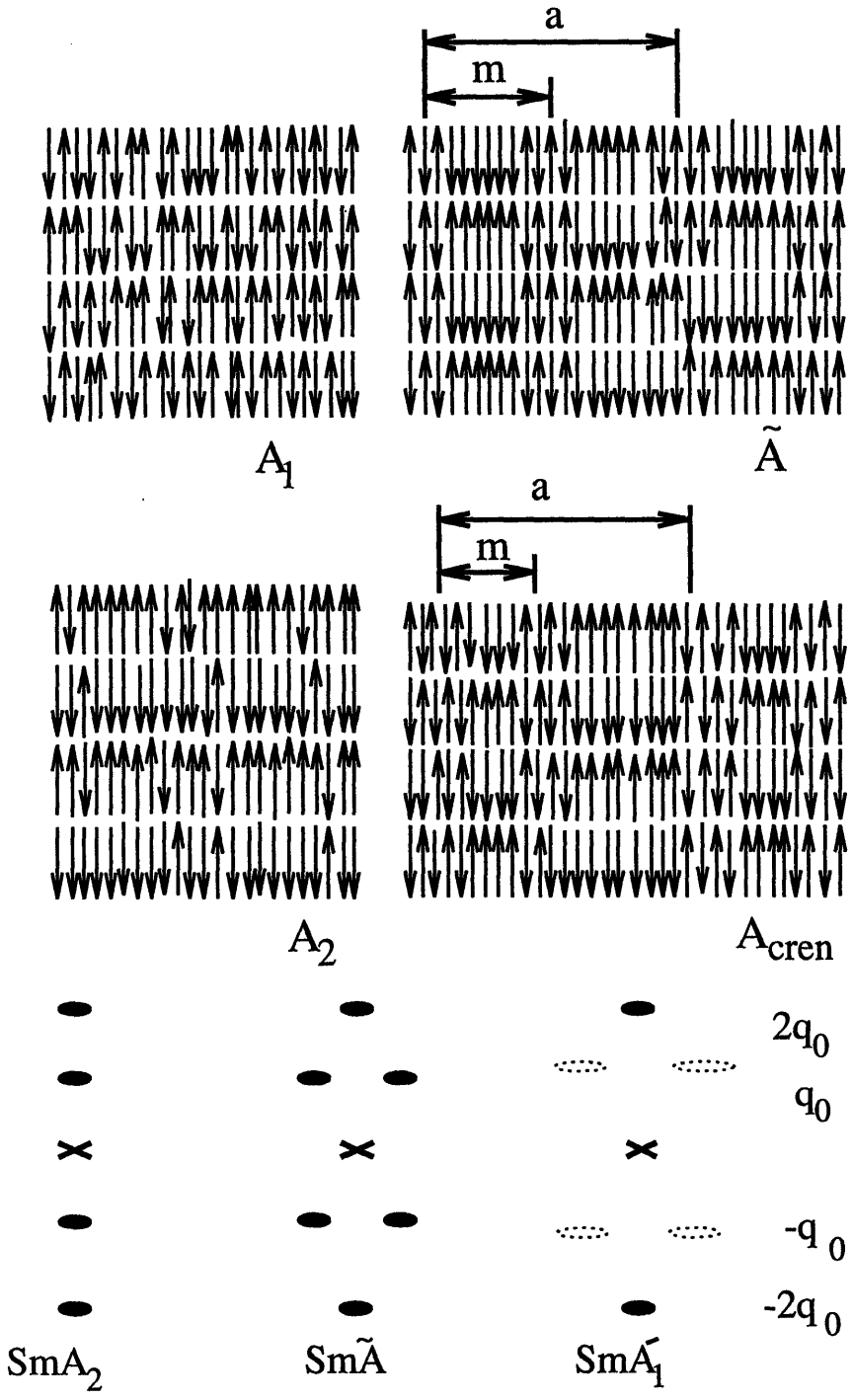

Figure 5-2: (a) Schematic structures for monolayer Sm-A_1, bilayer Sm-A_2, and the fluid antiphase Sm-$\tilde{A}$ (a centered rectangular structure with $m = a/2$); also shown is a structure for the purported Sm-A_{cren} phase where $m < a/2$. (b) The corresponding reciprocal space x-ray scattering patterns. The dashed elliptical areas represent diffuse scattering due to short-range fluctuations. The filled elliptical areas represent sharp quasi-Bragg peaks.

This chapter is organized as follows: First, a description of the experimental apparatus and the sample is given in section 5.2. Results for the Sm-A_1 phase with its concomitant Sm$\tilde{A}$ fluctuations, the Sm$\tilde{A}$ phase, the Sm-A_2 phase, and the (Sm$\tilde{A}$+Sm-A_2) two-phase coexistence region will be presented in section 5.3. A discussion comparing these results with previous heat capacity, optical and electron microscopy, and x-ray diffraction experiments will be given in section 5.4.

5.2 Experimental Details

The compounds used were synthesized and purified at the Centre de Recherche Paul Pascal [4], and they are from the same batch that was used for an earlier C_p investigation [12]. This x-ray sample is a mixture containing 49.5 mole % C_5 stilbene, which was previously used for a high-resolution x-ray study of the N–Sm-A_1 transition [13]. The phase sequence for this sample is

$$\begin{array}{ccccccc} \text{Sm-}A_2 & — & \text{Sm}\tilde{A} & - & \text{Sm-}A_1 & - & \text{N} \\ 383.6\text{–}386\text{K} & & \sim 398\text{K} & & 424.3\text{K} & & \end{array}$$

where 382–384.4K represents a broad Sm$\tilde{A}$+Sm-A_2 coexistence range. The transition temperatures cited above are somewhat lower than those reported previously [4, 12] due to a slow drift in transition temperatures with time over the very long period of x-ray observations.

The experiment was conducted using Cu K_α radiation from a Rigaku RU–300 rotating-anode machine operating at 7 kW, and a triple–axis spectrometer with Si(111) monochromator and analyzer crystals set in a dispersive configuration. The instrumental resolution for the in-plane longitudinal direction was well approximated by a Lorentzian with a half width at half maximum (HWHM) of 1.4×10^{-4}Å^{-1}. The transverse in-plane resolution was considered perfect ($< 10^{-5}$Å^{-1}), while the transverse out-of-plane resolution was well approximated by a Gaussian with a HWHM of 0.03Å^{-1} and was set by incoming and outgoing slits with matching angular acceptance. Evacuated flight paths with narrow slits positioned before and after the sample reduced the background count rate to 0.25 counts per second. The beam had

a spot size of 1.5×3 mm^2 at the sample position.

A sample of mass 180 mg was sealed with indium in a beryllium cell 12×12×1.5 mm^3. This cell was placed in a two-stage oven constructed from two beryllium cylinders which were individually temperature controlled throughout the experiment to ±10mK. The sample was aligned in the nematic (N) phase in a 5.5 kG magnetic field by cycling slowly across the N-Sm-A_1 transition until the sharpest transverse scan was obtained. With this technique it was possible to obtain a sample mosaicity of 0.5° HWHM in the Sm-A_1 phase in the vicinity of the N-Sm-A_1 transition.

5.3 Results

We learned from chapter 3 that the Sm-A_1 phase is characterized by a sinusoidal one-dimensional mass density wave in a three-dimensional fluid. Short-range, fluidlike order between molecules is observed in the direction transverse to this density wave. As is well known, in an x-ray scattering experiment the Sm-A_1 ordering gives rise to a single quasi-Bragg peak at $(0,0,2q_o)$ due to Landau-Peierls scattering which has the reciprocal space form $(q_{\|} - q_0)^{-2+\eta}$. For DB_5CN and C_5 stilbene in the N phase near the N-Sm-A_1 transition $2q_0$=0.2481$\AA^{-1}$, which equals 2π/L with an effective molecular length L is 25.33$\AA$ [13]. This value is consistent with Levelut *et al.* who report that L is close to the value 26.8$\AA$ for this system with X=0.46, the small difference being mainly due to slightly different mole fractions X. Well below the N-Sm-A_1 transition, Sm-A_1 monolayer type order is well established, hence changes in the mosaic are gradual and there is no measurable change in the longitudinal $2q_o$ linewidth with temperature. However, despite this essentially "frozen" smectic-A_1 order, there are fluctuations of in-plane domain order [8, 9] which become larger with decreasing temperature. From a.c. calorimetry measurements on this mixture [12] we know that the Sm-A_1–Sm$\tilde{A}$ transition is accompanied by significant pretransitional energy fluctuations over a large range in temperature, indicative of the presence of short-range Sm$\tilde{A}$-like order in the Sm-A_1 phase.

In the x-ray experiment these Sm$\tilde{A}$ fluctuations are demonstrated by the appear-

ance of weak diffuse spots off-axis which were first detectable about 7K above the Sm-A_1–SmÃ transition temperature. Figure 5-3 shows five transverse scans along ($q_\perp$, 0, q_0) at temperatures within the Sm-A_1 phase and two scans in the SmÃ phase. Figure 5-4 shows the corresponding longitudinal scans in which q_L is varied, with q_H held fixed at q_T^0. The diffuse scattering data in the Sm-A_1 phase were fitted with the empirical form first suggested by Chen and Lubensky [14] for the N-SmC transition:

$$\sigma(\vec{q}) = \frac{\sigma_o}{1+\xi_\parallel^2(q_\parallel - q^o)^2 + C_\perp q_\perp^2 + D_\perp q_\perp^4}, \tag{5.1}$$

where $q_\parallel$ is the L component and $q_\perp$ is the H component of the scattering vector in (q_H, q_K, q_L) space and the quadratic coefficient $C_\perp$ is negative. The results of these fits are shown in Figs. 5-3 and 5-4. Following Martinez-Miranda, Kortan, and Birgeneau [15], we have defined a length scale using the half width at half maxima of the peaks, which corresponds to the size of the smectic-A fluid antiphase domains:

$$\xi_\parallel(q_\perp^o) = \frac{\xi_\parallel^o}{\left[1+\frac{1}{2}C_\perp(q_\perp^o)^2)\right]^{1/2}} \tag{5.2}$$

$$\xi_\perp(q_\perp^o) = \frac{\sqrt{2D_\perp}}{\left\{-C_\perp + \left[C_\perp^2 + 4D_\perp\left(\frac{1-C_\perp^2}{2D_\perp}\right)\right]^{1/2}\right\}^{1/2} - \sqrt{-C_\perp}}, \tag{5.3}$$

where $q_T^0=(-C/2D)^{1/2}$ is the peak wave vector in the transverse direction. Below the Sm-A_1–SmÃ transition, these off-axis diffuse peaks become resolution limited in radial scans, thus confirming long-range order in the SmÃ phase. Pure transverse scans in the scattering plane reveal a mosaic with a roughly Gaussian angular distribution.

The size of the modulation repeat distance $\underline{a}=2\pi/q_T^0$ increases on cooling, which is clearly shown in Fig. 5-3 by the change in q_T, the off-axis peak position of the ($q_\perp$, 0, q_0) scans. The monotonic trend of the in-plane modulation distance $\underline{a}$ with temperature is indicated by the variation of q_T^0 shown in Fig. 5-5(a). The value of q_T^0 decreases to 0.020Å^{-1} on cooling (corresponding to $\underline{a}$ = 315 Å) at the point where

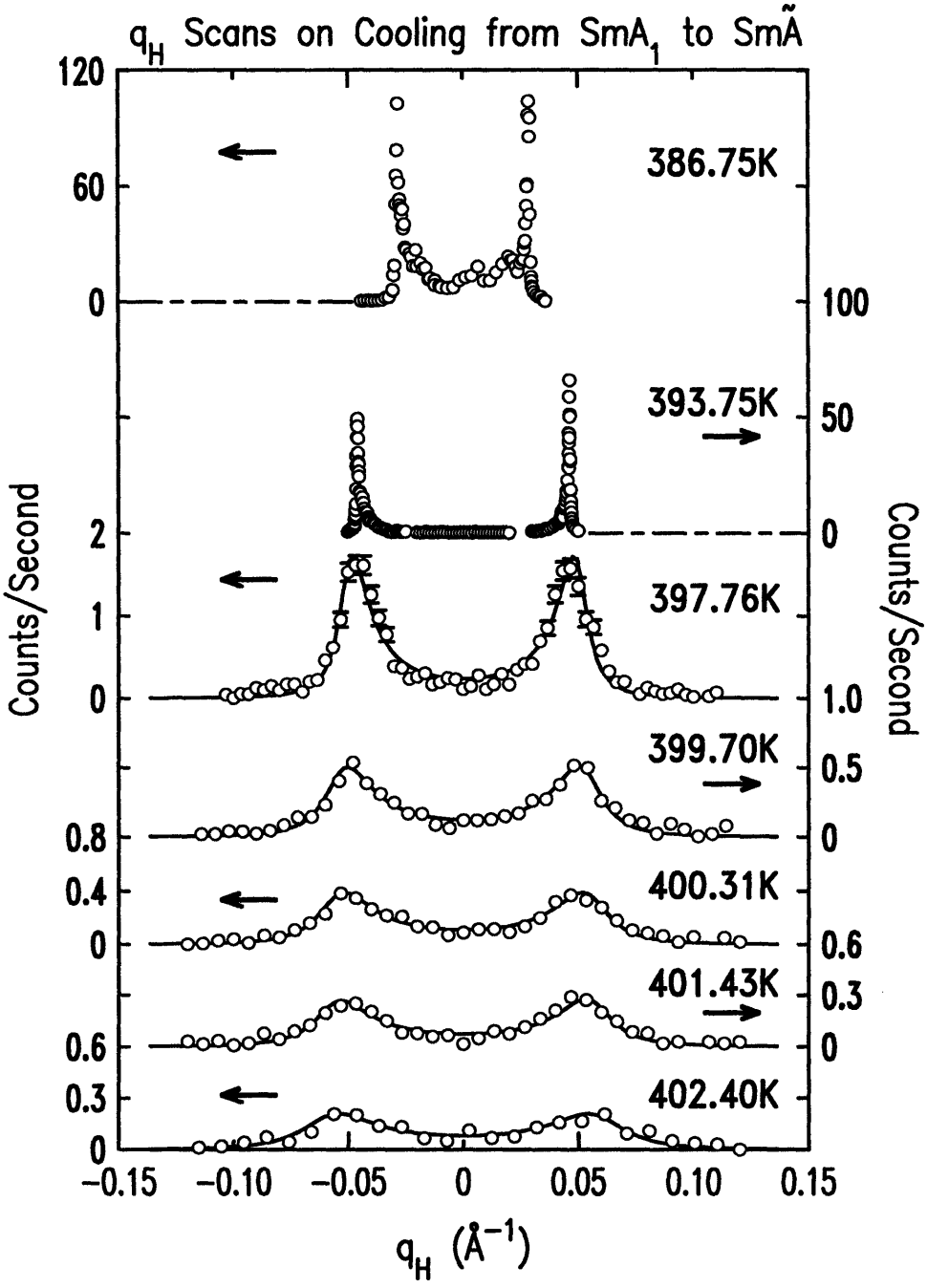

Figure 5-3: Scans along q_H with $q_L = q_0$ in the Sm-A_1 and -Ãphases. The five scans with $T > 396$K are in the Sm-A_1 phase, and the diffuse peaks are fitted with Eq.(1). The arrows indicate the intensity scale associated with each scan. The two scans at $T < 396$K are in the Sm-Ã phase. The solid lines are fits to the scattering profile described in the text.

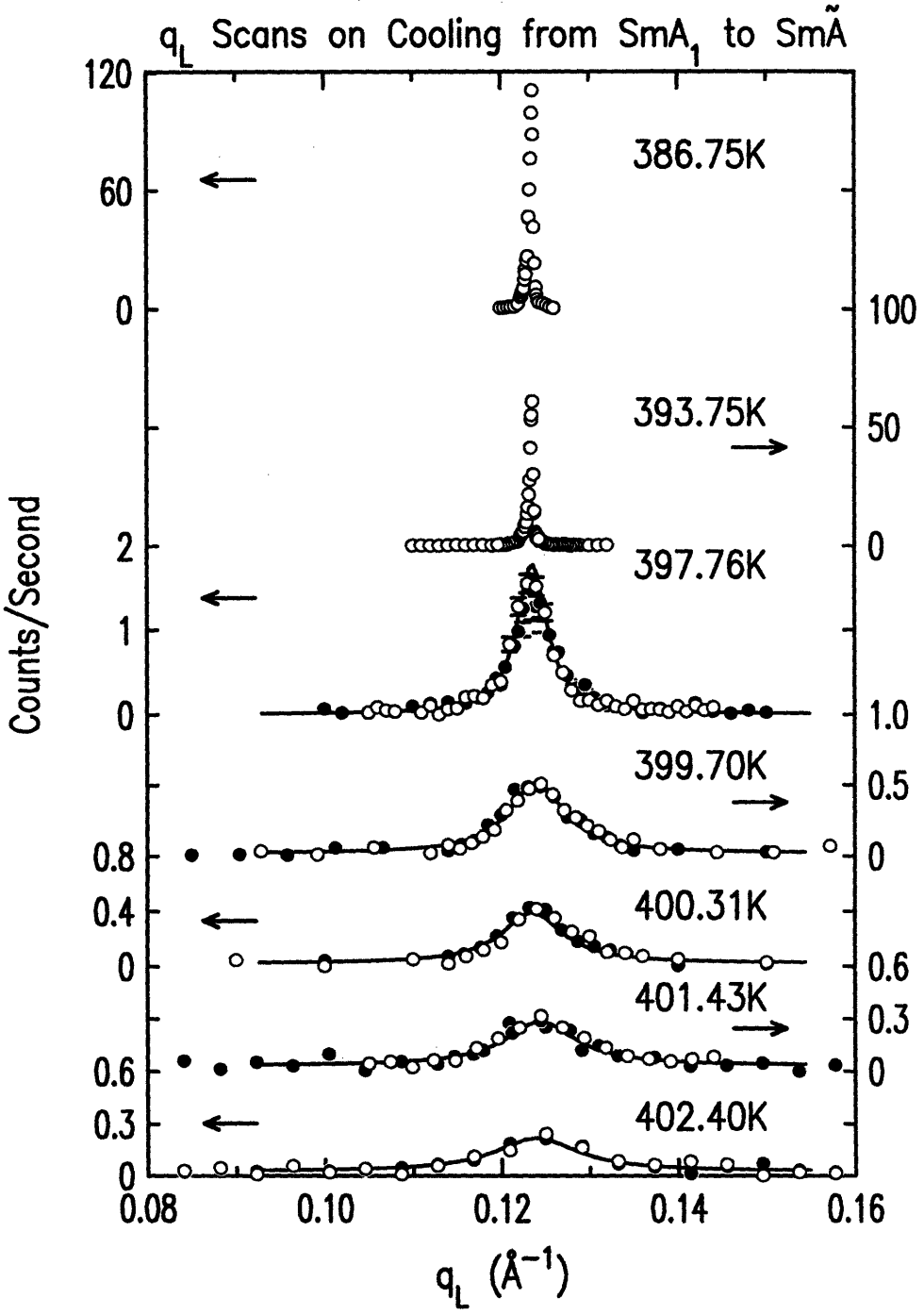

Figure 5-4: Scans along q_L through with $q_H = q_T^0$ in the Sm-A_1 and Sm-Ã phases. The open circles are for data along $(+q_T^0,0,q_L)$ and the closed circles are for $(-q_T^0,0,q_L)$. phases. The five scans with $T > 396$K are in the Sm-A_1 phase, and the diffuse peaks are fitted with Eq.(1). The arrows indicate the intensity scale associated with each scan. The two scans at $T < 396$K are in the Sm-Ã phase. The solid lines are fits to the scattering profile described in the text.

two-phase SmÃ+Sm-A_2 coexistence begins. The smooth curve through the q_T^0–T data in the SmÃ phase represents an empirical fit with the quadratic form

$$(q_T^0 - 0.02) = 0.01(T - 384.4)^{1/2}.$$

Note that this formula when extrapolated to higher temperatures is still in good agreement with the q_T^0 values determined from diffuse off-axis peaks in the Sm-A_1 phase.

The position of the (0,0,2q_0) peak, shown in Fig. 5-5(b), changes linearly with T in the SmÃ phase and in the Sm-A_1 phase above $\sim$ 400 K. An extrapolation of these Sm-A_1 values to 426 K yields $2q_0$=0.2479$\AA^{-1}$; this is in good agreement with the value $2q_0$=0.2481$\AA^{-1}$ determined from the diffuse Sm-A_1 scattering in the nematic phase [13]. One can see from Fig. 5-5(b) that near the Sm-A_1–SmÃ transition, there is a noticeable deviation for the monotonic increase in $2q_0$ with temperature, probably due to greater "dimerization" in the fluid antiphase than in the Sm-A_1. The scatter in the data points in this region is due to uncertainties in both $\Delta T = T - T_c(A_1 - \tilde{A})$ due to T_c drifts and $2q_0$ resolution ($\pm 1 \times 10^{-4}$Å^{-1}). The values of q_0 for the off-axis (q_T^0, 0, q_0) peaks have also been determined as a function of temperature. For the diffuse peaks in the Sm-A_1 phase, we find that (q_0)>(1/2)($2q_0$), where ($2q_0$) is determined from the position of the (0,0,$2q_0$) Bragg peak; the ratio (q_0)/($2q_0$) ranged from 0.5041 at 402.40 K to 0.5010 at 397.76 K. In the SmÃ phase and in the SmÃ+Sm-A_2 coexistence region, it was found that (q_0)/($2q_0$)=0.5 within the resolution ($\pm$0.0007) for all temperatures. These observations are in agreement with those reported by Levelut [8].

The peak intensities I_T of the off-axis diffuse scattering in the Sm-A_1 phase are shown in Fig. 5-6(a). Finally, the correlation lengths $\xi_\perp$ and $\xi_\parallel$ determined from the diffuse (q_T^0, 0, q_0) peaks using Eqs.(1)–(3) are shown in Fig. 5-5(b). The uncertainties in these ξ values are moderately large, but note that $\xi_\parallel$ and $\xi_\perp$ only differ by a factor of approximately 2.2.

Before considering the SmÃ + Sm-A_2 coexistence region, let us first describe the

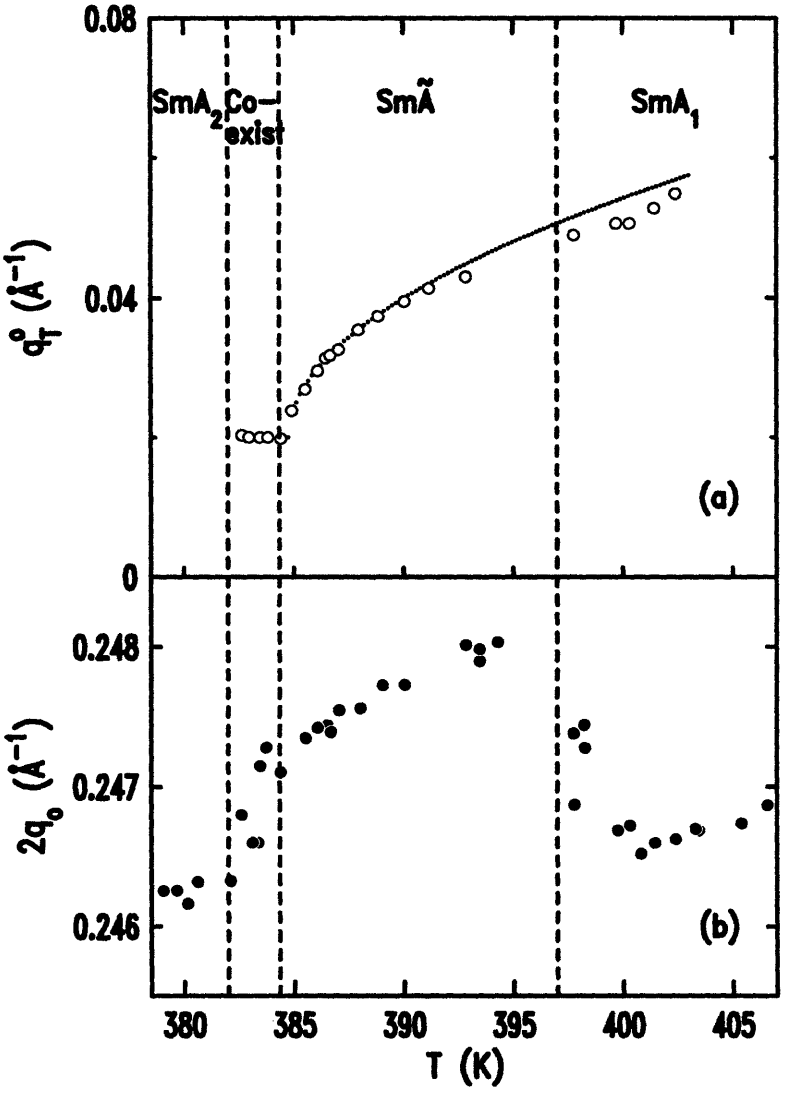

Figure 5-5: Scattering wave vectors for DB_5CN and C_5 stilbene: (a) Transverse position q_T^0 of the off-axis $(\pm q_T^0,0,q_0)$ peaks in the SmÃ and Sm-A_1 phases. The smooth curve through these q_T^0 points in the SmÃ phase has the empirical form described in the text $(q_T^0 - 0.02) = 0.01(T-384.3)^{1/2}$, and the dashed curve in the Sm-A_1 phase is an extrapolation of this form to higher T. (b) Longitudinal position of the $(0,0,2q_0)$ peak across the entire range of temperature for this experiment.

low temperature Sm-A_2 phase. The Sm-A_2 bilayer phase occurs when antiferroelectrically aligned molecular dimers form a double layer structure as shown in Fig. 5-2. The reciprocal space picture is described by fundamental scattering centered at (0,0,q_0), and second harmonic scattering centered at (0,0,2q_0) [16, 17]. Fluidlike order within the Sm-A_2 layers is present as in the Sm-A_1 phase, and there is no off-axis (q_T^0, 0, q_0) scattering in the Sm-A_2 phase.

In the temperature range 382–384.4 K between the Sm$\tilde{A}$ phase region and the Sm-A_2 phase region, a detailed study was made of the scattering profiles for off-axis ($\pm q_T^0$, 0, q_0) peaks and on-axis (0,0,q_0) and (0,0,2q_0) peaks. This is the temperature region where a new modulated structure, the Sm-A_{cren} phase with a regular array of two different thickness antiphase slabs with m<a/2, has been proposed to exist [8]. Contrary to that description, our results demonstrate that the transformation between the Sm$\tilde{A}$ and Sm-A_2 phases occurs via a broad two-phase coexistence region. Figure 5-7 shows θ rocking curves through the (0,0,q_0) peak as a function of T. Figure 5-8 shows the temperature variation of the intensity for the (q_T^0, 0, q_0) off-axis and (0,0,q_0) on-axis peaks over the coexistence range where the Sm$\tilde{A}$ transforms into Sm-A_2. As the system is cooled through the two-phase coexistence region, the q_T^0 and q_0 positions of the off-axis (q_T^0, 0, q_0) peak do not change but the intensity of this peak decreases smoothly. At the same time, the intensity of the on-axis (0,0,q_0) peak grows, as shown in both Figs. 5-7 and 5-8. This behavior is exactly what one would expect if domains of Sm-A_2 phase appear with decreasing temperature at the expense of the domains of Sm$\tilde{A}$.

Heuristically one could describe the evolution from modulated antiphase Sm$\tilde{A}$ order to Sm-A_2 bilayer order as a simple permeation of the molecules between layers, This process can be energetically favorable since it would tend to keep the global curvature of the layers constant as the temperature is decreased. In this case it would result that some in-plane domains increase in extent at the expense of neighboring domains. The transition to bilayer order then marks the onset of a single domain orientation for the molecular dimers. One might anticipate a transition first to a intermediate structure which has two different sizes of in-plane antiphase domains

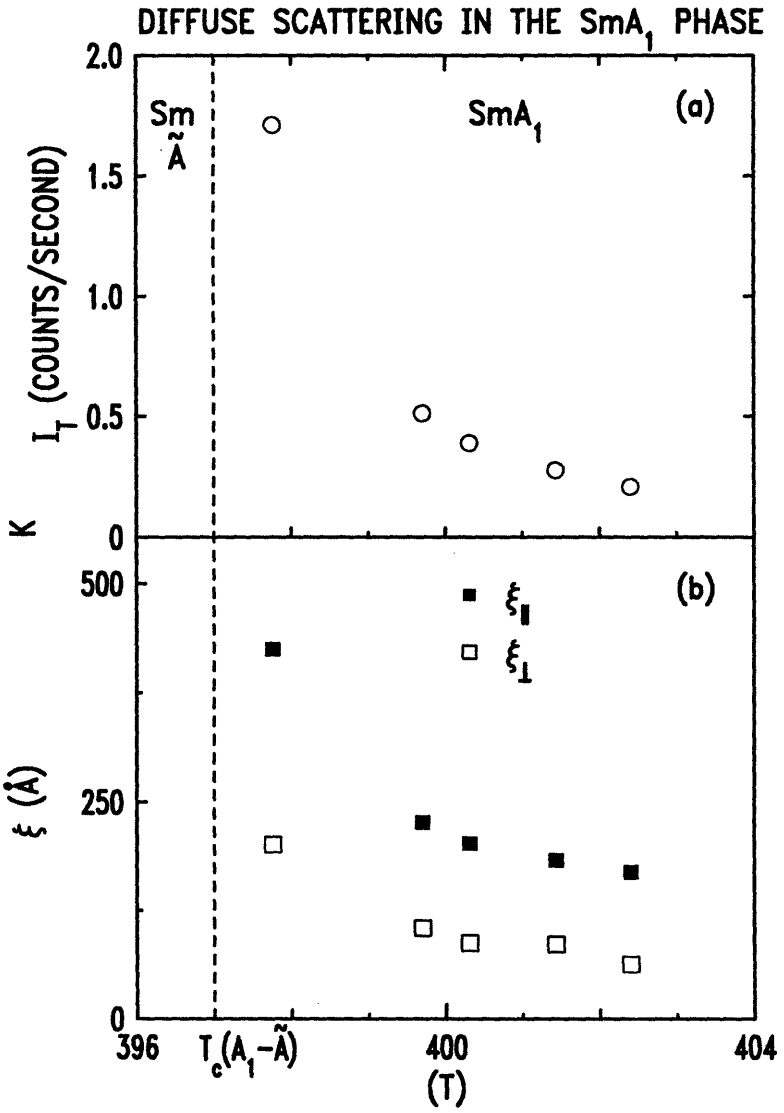

Figure 5-6: Intensity and correlation length data for diffuse (q_T^0, 0, q_0) off-axis peaks in the Sm-A_1 phase: (a) Peak intensities I_T(◯) and (b) Longitudinal and transverse correlation lengths $\xi_{\|}$ (□) and $\xi_{\perp}$ (□) for the in-plane modulation obtained from Eqs.(2)–(3) and fits to the off-axis scattering profile with Eq.(1).

(with m<a/2). This is the purported Sm-A_{cren} phase.

The presence of two separate types of order, Sm-A_2 and Sm$\tilde{A}$, is evident by comparing the mosaics of the on-axis and off-axis peaks. A contour plot of the scattering intensities observed in the coexistence region is shown in Fig. 5-9. If the scattering were produced by a single ordered phase , there would be only one mosaic distribution as measured from θ rocking curves. However, the dramatic difference between the angular widths of the on-axis $(0,0,q_0)$ and off-axis $(\pm q_T^0, 0, q_0)$ peaks rules out the possibility of a single phase. We should point out that scattering at $(0,0,2q_0)$ can result from both Sm-A_2 and Sm$\tilde{A}$ ordered domains, so both contributions must be considered in the analysis of that mosaic. Figure 5-10 shows mosaic data at two temperatures within the coexistence region. At T=383.35K we observe the mosaics of the off-axis $(\pm q_T^0, 0, q_0)$ peaks to be consistent with the on-axis $(0,0,2q_0)$ mosaic but strikingly different from the on-axis $(0,0,q_0)$ mosaic. This is to be expected since Fig. 5-8 shows that the integrated intensity of the $(0,0,q_0)$ peak at this temperature is weak relative to its saturation value below 382 K. Hence, the Sm-A_2 contribution at $(0,0,2q_0)$ will be qualitatively insignificant. In contrast to this, Sm-A_2 domains are quite large compared to Sm$\tilde{A}$ domains at T=382.65K as seen from the integrated intensities shown in Fig. 5-8. Thus, their contribution to the scattering at $(0,0,2q_0)$ should be quite substantial, resulting in a q_0-like mosaic for the $(0,0,2q_0)$ peak, as observed. However, the mosaic of the $(0,0,q_0)$ peak remains distinctly different from the mosaics at $(+q_T^0, 0, q_0)$ and $(-q_T^0, 0, q_0)$. One can observe noticeable differences not only between the absolute angular widths of the mosaics but also between the features in each peak. Since these features do not reflect the symmetry of reciprocal space, they can be attributed to the mosaicity, probably originating from domains which lack perfect azimuthal symmetry about the scattering vector $\vec{q}$=(0,0,q). This is expected, given that the spectrometer is configured to integrate over a wide out-of-plane momentum transfer. This comparison of the two off-axis peaks with the two on-axis peaks shows clearly the presence of two distinct mosaics. More precisely, we observe the disappearance of Sm$\tilde{A}$ ordered domains with the simultaneous development of Sm-A_2 ordered domains on cooling through a $\sim$ 2.4-K–wide coexistence

region.

The final experiment designed to distinguish SmÃ+Sm-A_2 coexistence from a Sm-A_{cren} phase involved scans through the off-axis harmonics ($\pm nq_T^0$, 0, q_0) of the SmÃ fundamental ($\pm q_T^0$, 0, q_0). The data shown in Fig.5-11 were obtained at 383.75K, which is in the coexistence region. In addition to observing the large on-axis (0,0,q_0) peak and the off-axis (q_T^0=0.022$\AA^{-1}$, 0, q_0) peak, we made a careful search at the ($2q_T^0$, 0, q_0) and ($3q_T^0$, 0, q_0) positions. One can easily determine the relative proportion of the antiphase domains from the magnitude of off-axis harmonics. Long counting times were used in order to achieve a good signal-to-noise ratio in these regions of weak scattering. The third harmonic is observed at (+0.066, 0, q_0), but there is no indication of the second harmonic at ($2q_T^0$, 0, q_0). It should be noted that the latter is not allowed by symmetry even in multiple scattering for either the SmÃ or Sm-A_2 phases separately but could occur in a two-phase coexistence region via double scattering between domains of each phase. Such ($\pm 2q_T^0$, 0, q_0) peaks were indeed reported in Ref.[7] and were interpreted as evidence of a Sm-A_{cren} ordered structure. The excess scattering at the low-q side of the third harmonic peak is due in part to the long tails of the fundamental peak, and to mosaic broadening. The relatively weak integrated intensity of this third harmonic peak compared to the fundamental allows us to ascribe a nearly pure sinusoidal shape to the polarization modulation transverse to the smectic mass density wave. Thus, the fluid antiphase domains are separated by broad domain walls even when SmÃ ordering is as fully developed as possible and SmÃ coexists with the Sm-A_2 phase.

It should be noted that for the run during which the data of Figs. 5-8–5-11 were obtained, the lateral position q_T^0 of the off-axis ($\pm q_T^0$, 0, q_0) peaks was q_T^0=0.022$\AA^{-1}$ instead of 0.02 $\AA^{-1}$ as observed in the run shown in Fig. 5-5. Such slight variations in the maximum $\underline{a}$ value observed in the coexistence region from run to run are of no conceptual importance.

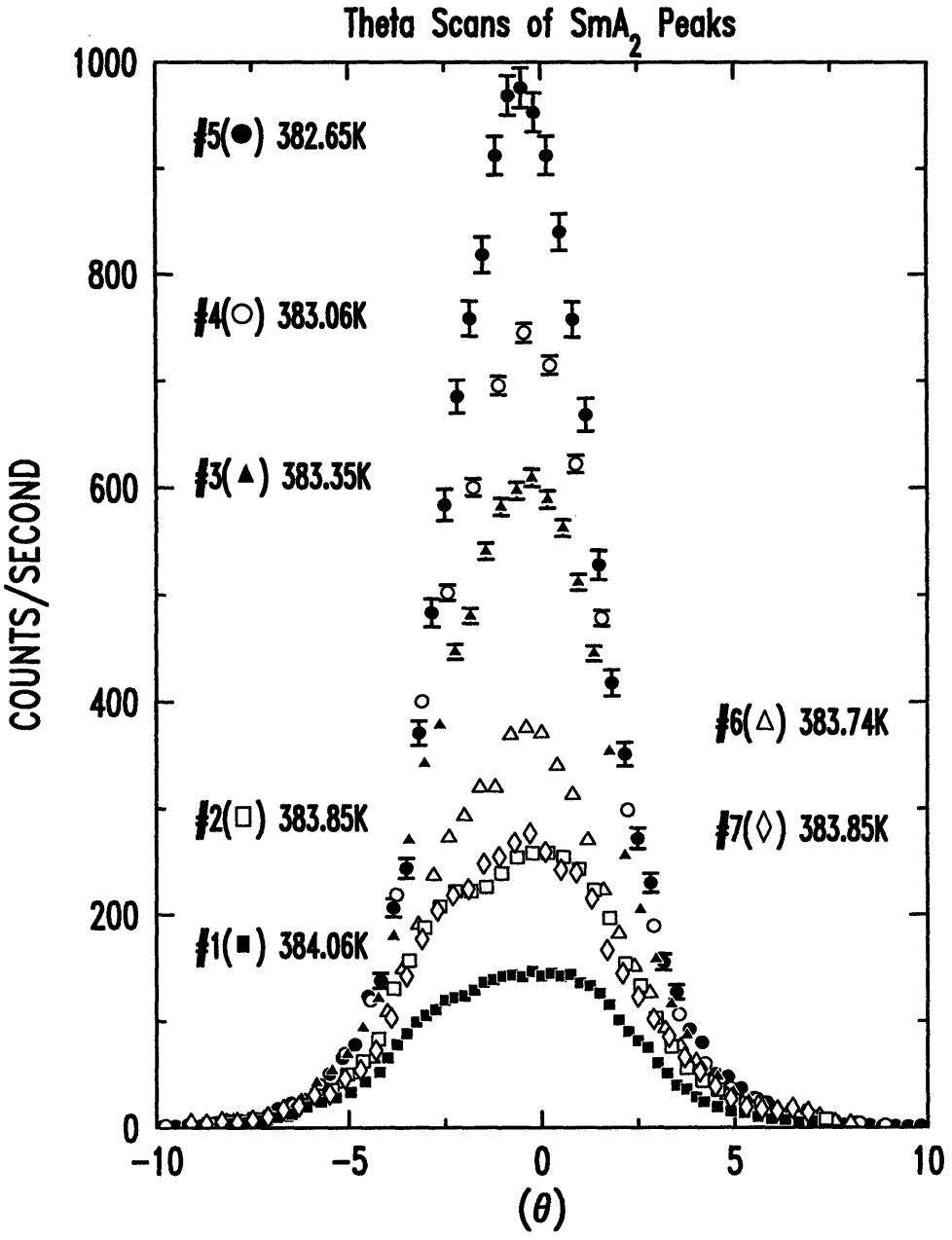

Figure 5-7: θ rocking curves at constant radial wave vector through the $(0,0,q_0)$ peak in the SmÃ+Sm-A_2 coexistence region. The run numbers 1–7 are in chronological order, i.e., the sample was first cooled (1–5) and the reheated (6 and 7).

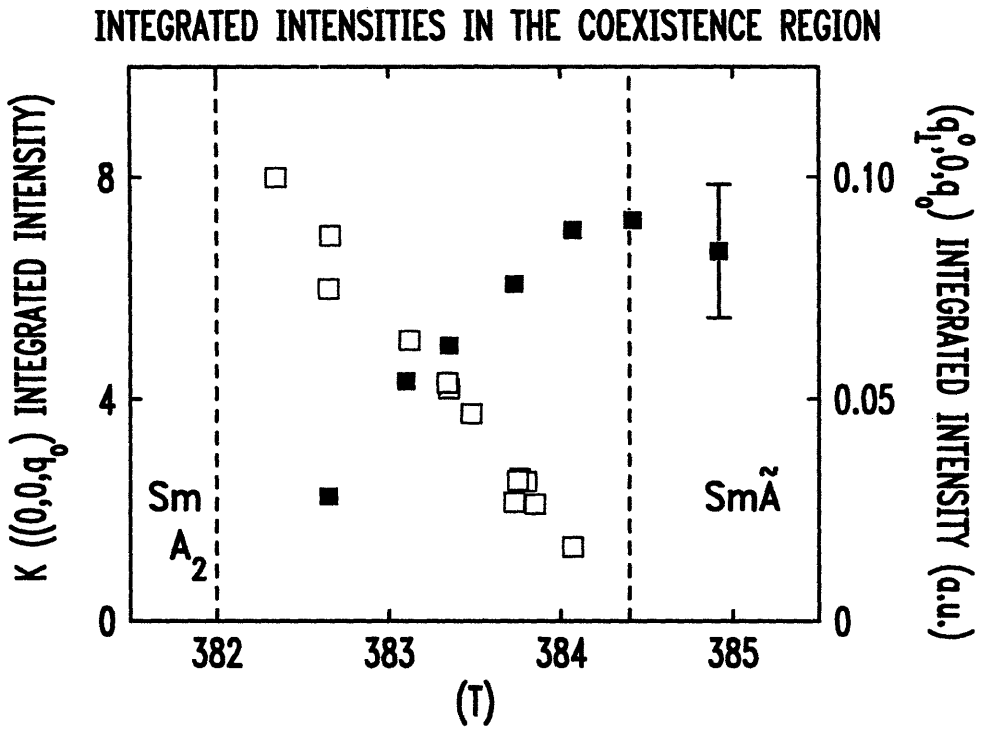

Figure 5-8: Detail of x-ray intensity data in the SmÃ + Sm-A_2 coexistence region. The integrated intensities of the (0,0,q_0) bilayer peak (open squares) and the (q_T^0,0,q_0) fluid antiphase peak (filled squares) are shown.

5.4 Discussion

This section will present a discussion of five issues — the fluctuations of SmÃ-like short range order in the SmA_1 phase, the nature of the SmA_1–SmÃ transition, the evolution of long-range lateral modulations in the SmÃ phase, the two-phase coexistence region associated with the SmÃ-SmA_2 transition, and the scattering behavior at q_0 and $2q_0$ in the SmA_2 phase.

5.4.1 Fluctuations in the SmA_1 phase

The presence of in-plane SmÃ-like fluctuations in a SmA_1 phase has been detected previously in x-ray [8, 10], viscosity [3], and calorimetry [12] studies. The detailed behavior of the pre-transitional energy fluctuations for both DB_5CN and C_5 stilbene and DB_6CN and C_5 stilbene mixtures is shown in Fig. 5-12. It is clear from this figure that ΔC_p^+ data above $T_c(A_1$-Ã) do not follow a simple power-law behavior,

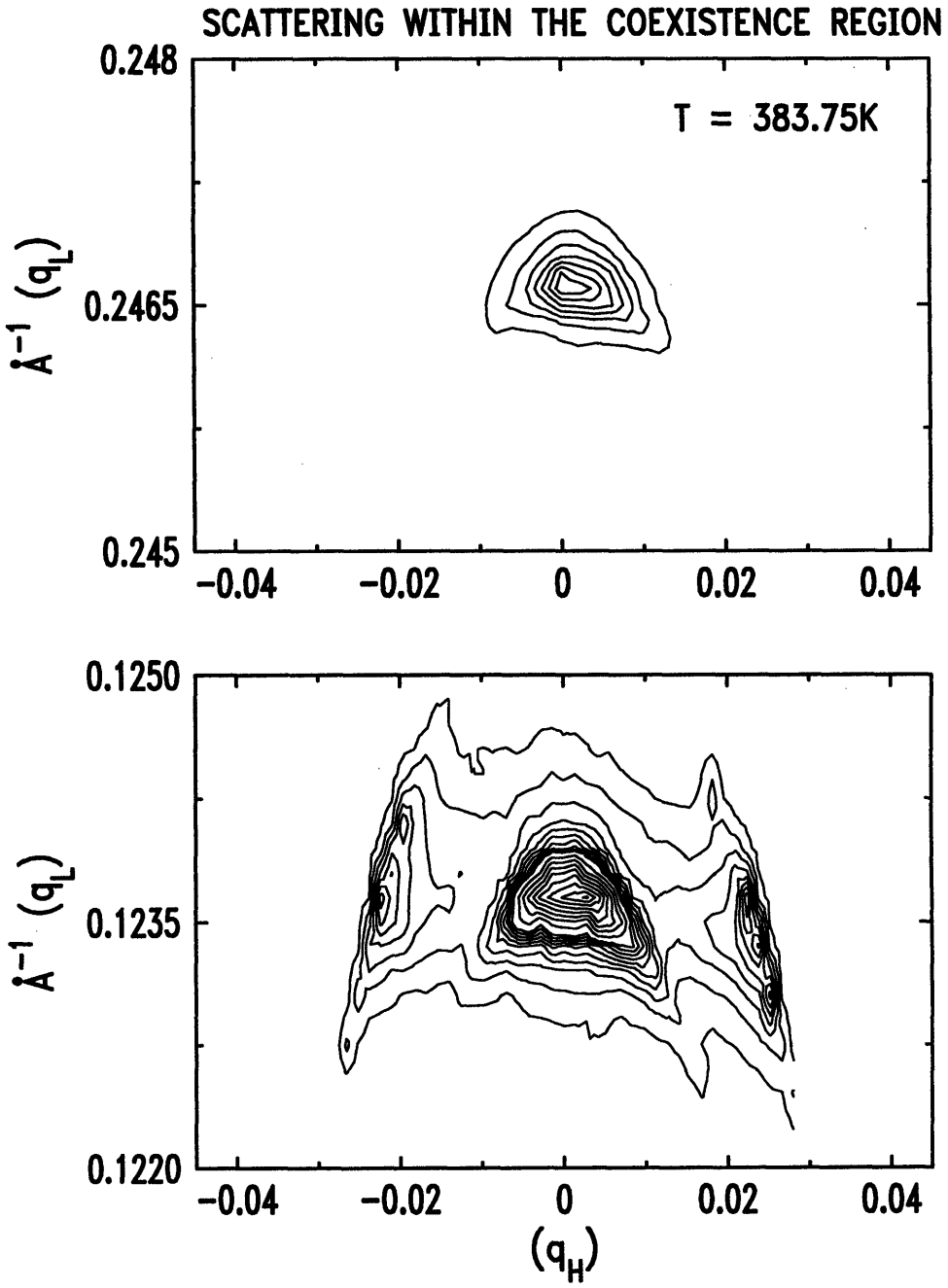

Figure 5-9: Contour plot of scattering intensities observed at 383.75K in the SmÃ + Sm-A_2 coexistence region. Features at ($\pm q_T^0$, 0, q_0) arise from SmÃ scattering; that at (0,0,q_0) from Sm-A_2 scattering, and that at (0,0,2q_0) from both SmÃ and Sm-A_2 scattering. Note the mosaic broadening of the off-axis (q_T^0,0,q_0) peaks.

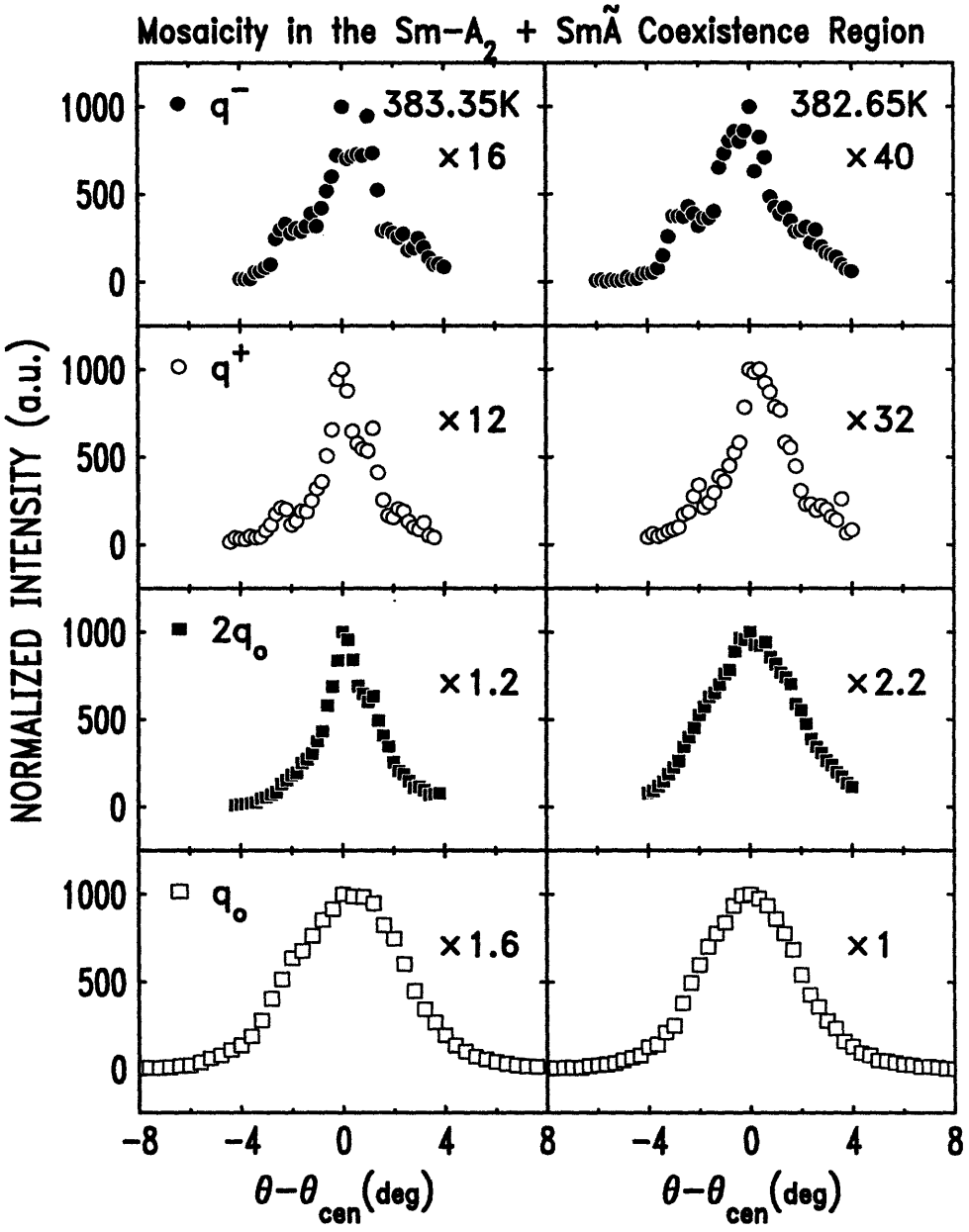

Figure 5-10: Comparison of mosaicity widths at T=383.35K (left panel) and 382.65K (right panel) during a slow cooling run. q^+ and q^- are the off-axis peaks centered at $(0.022\text{Å}^{-1},0,q_0)$ and $(-0.022\text{Å}^{-1},0,q_0)$, respectively. q_0 is the on-axis $(0,0,q_0)$ bilayer peak. $2q_0$ is the on-axis $(0,0,2q_0)$ peak with contributions from both SmÃ and Sm-A_2 scattering. The factor by which I(experimental) was multiplied to obtain the normalized intensity is given for each scan.

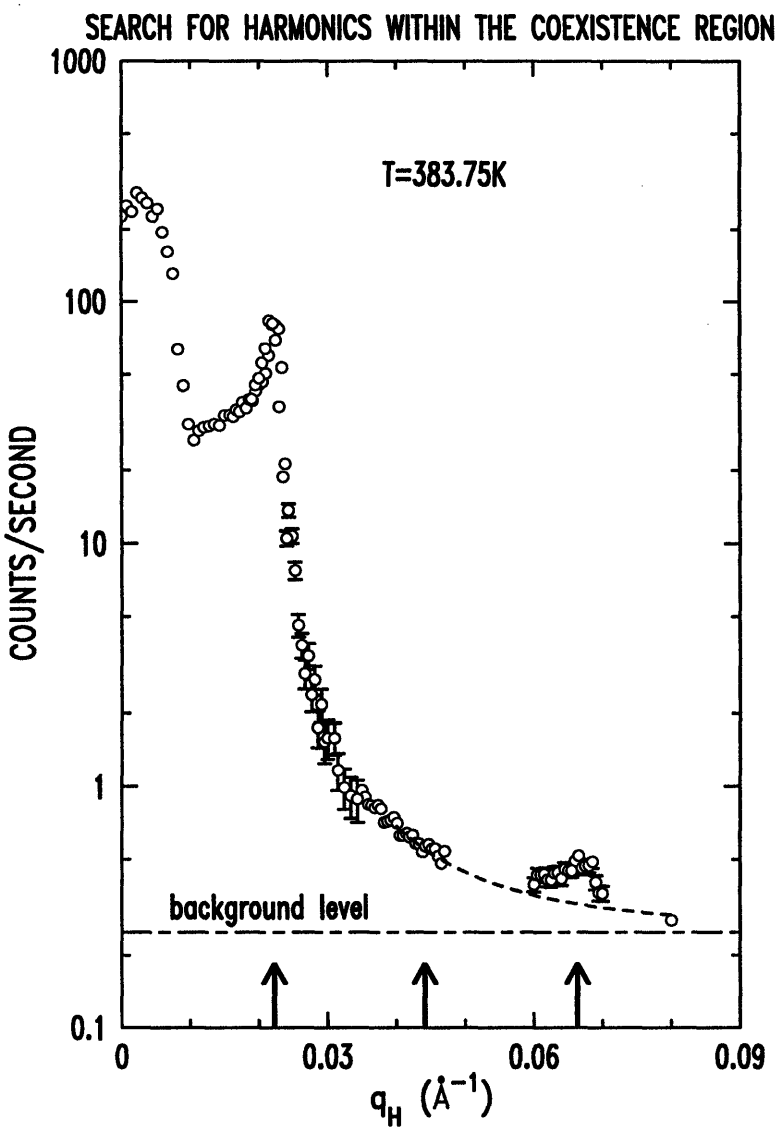

Figure 5-11: Third harmonic ($3q_T^0$,0,q_0) at q_H=0.066$\AA^{-1}$ compared to the fundamental (q_T^0,0,q_0) at q_H = 0.022$\AA^{-1}$ showing that the SmÃ phase in a SmÃ + Sm-A_2 coexistence mixture exhibits a nearly sinusoidal polarization wave transverse to the smectic mass density wave. Note that the second harmonic at (0.044,0,q_0) is not allowed by symmetry for a SmÃ + Sm-A_2 two-phase mixture and is not observed within the instrumental resolution. The error bars for points with $q_H > 0.035$ are comparable to the size of the symbols since long counting times were employed. The dashed curve for $q_H > 0.048\AA^{-1}$ represents the large q_H scattering expected in part due to long tails for the fundamental peak and in part due to mosaic broadening.

but the qualitative trend in the experimental ΔC_p values is similar to that predicted from a "weak crystallization" theory of the SmA_1–Sm$\tilde{A}$ transition [18]. Although the present x-ray data shown in Fig. 5-6 for ($q_\perp$,0,q_0) scans in the SmA_1 phase are too sparse to test power-law analyses of $\xi_\parallel$ and $\xi_\perp$, one can make a consistency check between the behavior of $\Delta C_p{}^+$ and the correlation lengths.

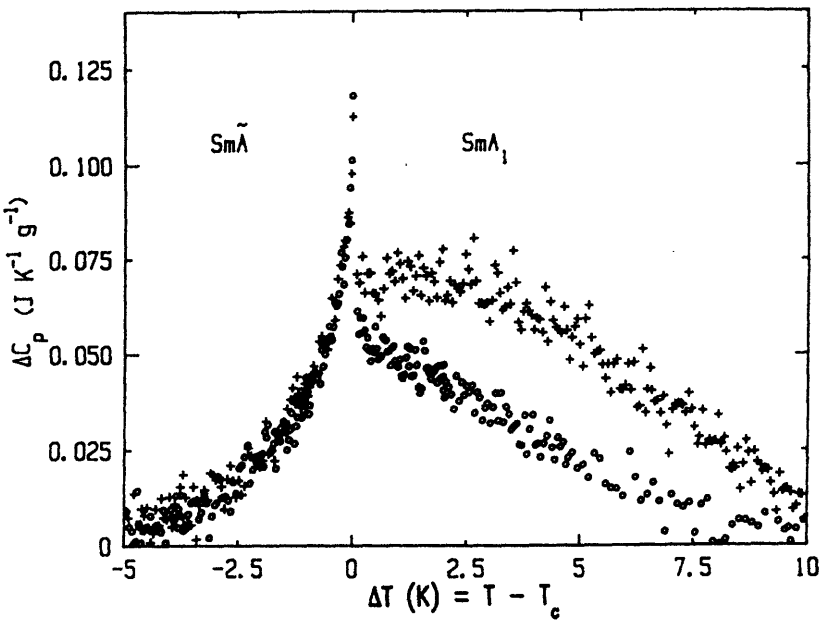

Figure 5–12: C_p data showing excess heat capacity in the vicinity of the Sm-A_1–Sm-$\tilde{A}$ phase transition. Data from ref. [12] for DB_5CN and C_5 stilbene with $X = 0.492$ (open circles) and for DB_5CN and C_5 stilbene with $X = 0.505$ (plus signs) are shown. T_c indicates the very weakly first-order phase transition.

The concept of two-scale universality states that $\bar{F}_c\xi_{vol}/k_BT$, where $\bar{F}_c$ is the critical free energy per unit volume and ξ_{vol} is the correlation volume, should be a dimensionless constant for a given universality class [19]. In the present case, the correlation length in the y direction is unknown but can be assumed to vary with T in the same way as $\xi_\perp$ does. Thus one expects for Sm$\tilde{A}$ fluctuations,

$$\bar{F}_c\xi_\parallel\xi_\perp^2/T = C \tag{5.4}$$

where C is a constant independent of T. Integrating the ΔC_p^+ data in Fig. 5-12 to obtain $\bar{F}_c$ as a function of ΔT and choosing the x-ray transition temperature to be 397 K (see Fig. 5-6), we obtain C = −1.7 at 397.76 K, −2.8 at 399.70 K, −2.4 at 400.31 K, −2.9 at 401.43 K, and −2.6 at 402.40 K. The fact that C is roughly constant while $\xi_\parallel \xi_\perp^2$ and $\bar{F}_c$ are each varying by a factor of ~ 20 is an indication of consistency between the ΔC_p^+ data and the diffuse x-ray scattering results.

Another test of internal consistency for the SmÃ fluctuation behavior is to consider the ratio $\xi_\parallel \xi_\perp / I_T$. If simple power-law behaviors $\xi \sim (\Delta T)^\nu$ and $I \sim (\Delta T)^\gamma$ were to hold, this ratio would vary as $(\Delta T)^{\eta\nu}$, almost independent of ΔT, since scaling gives $\gamma = (2-\eta)\nu$ and $\eta \ll 1$. For the five data points shown in Fig. 5-6, we obtain an approximately constant value for this ratio, which demonstrates that I_T indeeds scales like $\xi_\parallel \xi_\perp$.

It should also be noted that in the SmA_1 phase $(q_0) > 0.5(2q_0)$, where (q_0) is the L component of the off-axis $(q_T{}^0, 0, q_0)$ diffuse peak and $(2q_0)$ is that of the on-axis $(0,0, 2q_0)$ condensed peak. The ratio $(q_0)/(2q_0)$ locks in at 0.5 at the SmA_1 transition temperature.

5.4.2 The SmA_1–SmÃ transition

According to a mean-field treatment of the frustrated smectics model, the SmA_1–SmÃ transition would be second order, but fluctuation effects of the Brazovskii type make this transition first order [18, 19, 20]. This is confirmed by the heat capacity measurements, which indicate a weakly first-order transition with a coexistence region of $\sim$ 85 mK [12]. No x-ray data were obtained close to the SmA_1–SmÃ transition temperature, but Fig. 5-5 suggests that very little change occurs in $\underline{a} = 2\pi/q_T^0$ on going from the SmA_1 to SmÃ phase, which is consistent with any first-order discontinuity being small.

5.4.3 Evolution of lateral modulations in the SmÃ phase

The highest temperature x-ray data in the SmÃ phase were obtained at 393.75 K. The nearly resolution-limited off-axis peaks shown in Fig. 5-4 indicate that lateral modulation extends a considerable distance at that temperature. Although there is no theory dealing with fluctuation behavior at the SmA_1–SmÃ transition, Fig. 5-12 shows that energy fluctuations are large and distinctly different above and below T_c=T_c(A_1– Ã). The ΔC_p^- data below T_c can be well described by

$$\Delta C_p^- = Aln(|\Delta T|/T_c) + B$$

with $A = -0.0224 JK^{-1}g^{-1}$ and $B = -0.096 JK^{-1}g^{-1}$, suggesting XY-like fluctuations.

In the middle of the SmÃ phase, say, 388–394 K, the lateral dimension of the SmÃ domains remains essentially unchanged. The mosaic spread of the off-axis peaks broadens significantly on cooling, but the intergrated intensity I_T remains nearly constant, in agreement with an almost constant C_p across this temperature range [12]. Throughout the entire SmÃ phase, q_T^0 evolves in a smooth systematic way, until the lateral period $\underline{a} = 2\pi/q_T^0$ reaches a maximum value of 315$\mathring{A}$, in reasonable agreement with the value 335$\mathring{A}$ given by Levelut [8] for DB_6CN and C_5 stilbene. Electron micrographs of a freeze-fractured DB_5CN + C_5 stilbene mixture with a mole fraction (X) of 0.63 show a very clear lateral periodicity of $400 - 500\mathring{A}$ [4]. This is consistent with our value since $\underline{a}$ appears to increase as X increases and the range of the SmÃ phase shifts to lower temperatures [4, 8]. The quadratic form

$$(q_T^0 - 0.02) = 0.01(T - 384.4)^{1/2}$$

found to represent the temperature dependence of q_T^0 is an empirical rather than a theoretically predicted result.

As the SmÃ phase is cooled toward the transition region where conversion into SmA_2 occurs, the integrated intensity I_T increases substantially. This qualitative

trend in I_T is parallel to that in the heat capacity shown in Fig. 5-12. These C_p data represent a truncated version of the inverted Landau Sm$\tilde{C}$-SmC_2 heat capacity peak observed in DB_8ONO_2 and $DB_{10}ONO_2$ mixtures of alkyloxyphenyl-nitrobenzoyloxy benzoates [21]. In the latter case, the first-order coexistence region is only 0.17 K wide, whereas the C_p data in Fig. 5-12 indicate a broad two-phase coexistence region of $\sim$ 2.2 K.

Note that the ratio $(q_0)/(2q_0)$ for the L component of the off-axis (q_T^0, 0, q_0) and on-axis (0, 0, $2q_0$) peaks equals 0.5 in the Sm$\tilde{A}$ phase. There is a systematic linear increase in $2q_0$ on cooling throughout the Sm$\tilde{A}$ phase followed by a very rapid decrease in $2q_0$ on the transition into the SmA_2 phase, as shown in Fig. 5-5.

5.4.4 The Sm$\tilde{A}$+SmA_2 coexistence region

For a mixture of DB_5CN and C_5 stilbene with $X \sim 0.5$, it was previously reported that another modulated smectic-A phase, denoted SmA_{cren}, which has the structure shown in Fig. 5-2, exists between the Sm$\tilde{A}$ and SmA_2 phases [8]. In contrast to this, we find that the 382–384.4 K range corresponds to a broad two-phase coexistence region. Levelut's key argument [8] for the existence of a SmA_{cren} phase instead of Sm$\tilde{A}$ + SmA_2 coexistence was the presence of the ($2q_T^0$, 0, q_0) harmonic of the off-axis (q_T^0, 0, q_0) fundamental since even harmonics are not allowed by symmetry for the Sm$\tilde{A}$ and SmA_2 phases separately. However, as shown by Fig. 5-11, we see no ($2q_T^0$, 0, q_0) peak although a weak ($3q_T^0$, 0 , q_0) peak was detected. Furthermore, the mosaic structure in Fig. 5-10, as discussed in Sec. 5.3, strongly supports the presence of two coexisting phases. It seems that the situation here is very similar to the recent demonstration that a proposed incommensurate smectic-A phase SmA_{inc}, existing between the SmA_d and SmA_2 phases, is in fact a broad coexistence of SmA_d+SmA_2 phases that interconvert very slowly [22]. As noted previously, the observation of weak ($\pm 2q_T^0$, 0, q_0) peaks could possibly be explained by double scattering between two domains in a Sm$\tilde{A}$+SmA_2 coexistence mixture. We should point out, however, that, according to Levelut [23], her photographically detected diffraction patterns are inconsistent with this explanation and the observed scattering in her experiment

necessitates the existence of an intrinsic SmA_{cren} phase. We can only state definitively that the SmA_{cren} phase was not observed in our experiment.

The existence of a first-order SmÃ-SmA_2 transition is consistent with the prediction of Prost's frustrated smectic model [11, 24], which does not yield a Sm$_A$*cren* phase for any set of model parameters. Sluggish two-phase coexistence is also compatible with the heat capacity results shown in Fig. 5-12. Indeed, Ref. (11) describes the C_p behavior between the two arrows as being "like a special type of two-phase coexistence," and the small phase shift anomaly $\Delta\phi$ reported in Ref. (11) for the T_{ac} signal could well be due to the motion of domain walls betwen SmÃ and SmA_2 regions rather than antiphase SmA_{cren} domain walls. Finally, the microscopic observation of transient textures in this region [4] can be as well explained by two-phase coexistence as by a SmA_{cren} phase [25].

5.4.5 The smectic-A_2 phase

In the SmA_2 phase there are only two on-axis peaks at q_0 and $2q_0$, both slightly mosaic broadened in the same way. At 376.3 K, which is $\sim$ 6.9 K below the midpoint of the SmÃ+SmA_2 coexistence range and $\sim$ 48 K below the N-SmA_1 transition, the ratio of intensities $I(2q_0)/I(q_0)$ is 0.3. This value can be compared with $I(2q_0)/I(q_0)$ ratios of 0.07 at $\Delta T = T - T_{NA_2} = -2$ K in 7APCBB and $\sim$ 0.2 at $\Delta T \approx -20$ K in DB_6CN [16, 17]. Since the DB_5CN and C_5 stilbene mixture forms a SmA_2 phase from already well-ordered SmÃ antiphase domains, one would expect temperature independent values $I(q_0)$ and $I(2q_0)$, as observed, and a $I(2q_0)/I(q_0)$ ratio which reflects a saturation value comparable to that deep in the SmA_2 phase for materials undergoing a N-SmA_2 transition.

Bibliography

[1] *Phase Transitions in Liquid Crystals*, Vol. 290 of NATO Advanced Study Institute, Ser. B: Physics, edited by S. Martellucci and A. N. Chester, Plenum, New York, 1992.

[2] F. Hardouin, A. M. Levelut, J. J. Benattar, and G. Sigaud, Solid State Commun. **33**, 337 (1980).

[3] G. Sigaud, F. Hardouin, M. F. Achard, and A. M. Levelut, J. Phys. (Paris) **42**, 107 (1981).

[4] G. Sigaud, F. Hardouin, and M. F. Achard, Phys. Rev. A **31**, 547 (1985).

[5] G. Sigaud, M. Mercier, H. Gasparoux, Phys. Rev. A **32**, 1282 (1985).

[6] C. W. Garland, in *Geometry and Thermodynamics*, Vol. 229 of *NATO Advanced Study Institue, Series B: Physics*, edited by J.-C. Toledano (Plenum, New York, 1990), pp. 221–254.

[7] M. J. Young, Lei Wu, G. Nounesis, C. W. Garland, and R. J. Birgeneau, Phys. Rev. E **50**, 368 (1994).

[8] A. M. Levelut, J. Phys. Lett. **45**, L603 (1984).

[9] C. R. Safinya, W. A. Varady, L. Y. Chiang, and P. Dimon, Phys. Rev. Lett. **57**, 432 (1986).

[10] B. I. Ostrovskii and M. A. Saidachmetov, Mol. Cryst. Liq. Cryst. **192**, 19 (1990).

[11] P. Barois, J. Pommier, and J. Prost, in *Solitons in Liquid Crystals*, edited by L. Lam and J. Prost (Springer-Verlag, New York, 1989), Chap. 6.

[12] K. Ema, C. W. Garland, G. Sigaud, and N. H. Tinh, Phys. Rev. A **39**, 1369 (1989).

[13] C. W. Garland, G. Nounesis, M. J. Young, and R. J. Birgeneau, Phys. Rev. E **47**, 1918 (1993), note that the value $2q_o = 0.2115\mathring{A}^{-1}$ cited therein is a typographical error; the correct value is $2q_o = 0.2481\mathring{A}^{-1}$.

[14] J. C. Chen and T. C. Lubensky, Phys. Rev. A **14**, 1202 (1976).

[15] L. J. Martínez-Miranda, A. R. Kortan, and R. J. Birgeneau, Phys. Rev. A **36**, 2372 (1987).

[16] K. K. Chan, P. S. Pershan, L. B. Sorensen, and F. Hardouin, Phys. Rev. A **34**, 1420 (1986).

[17] L. Wu, M. J. Young, Y. Shao, C. W. Garland, R. J. Birgeneau, and G. Heppke, Phys. Rev. Lett. **72**, 376 (1994).

[18] V. V. Lebedev and A. R. Muratov, J. Phys. II **1**, 135 (1991).

[19] J. Prost and P. Barois, J. Chim. Phys. **80**, 65 (1983).

[20] J. Wang and T. C. Lubensky, J. Phys. (France) **45**, 1653 (1984).

[21] K. Ema, G. Nounesis, C. W. Garland, and R. Shashidar, Phys. Rev. A **39**, 2599 (1989).

[22] S. Kumar, L. Chen, and V. Surendranath, Phys. Rev. Lett. **67**, 322 (1991).

[23] A. M. Levelut (private communication).

[24] P. Barois, C. Coulon, and J. Prost, J. Phys. (Paris) Lett. **42**, L107 (1981).

[25] G. Sigaud (private communication). See also G. Sigaud, M. F. Achard and F. Hardouin, J. Phys. (Paris) Lett. **46**, L825 (1985).

Appendix A

X-ray Scattering from a Vicinal Surface

X-ray scattering from the surface of an elemental crystal will be calculated following the formalism of Held and Brock [1]. Thus, starting with the first Born approximation for charge scattering: $d\sigma/d\Omega = r_0^2|A(\mathbf{Q})|^2$, where the scattering amplitude A($\mathbf{Q}$) is simply the Fourier transform of the charge density of the scatterers $\rho(\mathbf{r})$, and r_0 is the classical electron radius. Therefore,

$$A(\mathbf{Q}) = \int_{\text{vol}} d^3r \rho(\mathbf{r}) exp(-i\mathbf{Q}\cdot\mathbf{r}) \tag{A.1}$$

and

$$\rho(\mathbf{r}) = \sum_{\{\mathbf{R}\}} \sum_i \rho_i(\mathbf{r} - \mathbf{R} - \tau_i)\,, \tag{A.2}$$

where the integral is carried out over the volume of the crystal. Here the sum is performed over the basis set of the bulk lattice, $\{\mathbf{R}\}$, and over the i atoms in the unit cell. One can exploit the symmetry of the lattice and re-express the scattering amplitude A($\mathbf{Q}$) as a product $\mathrm{F}(\mathbf{Q})\sum_{\{\mathbf{R}\}} e^{(-i\mathbf{Q}\cdot\mathbf{r})}$, where

$$F(\mathbf{Q}) = \sum_i e^{(-i\mathbf{Q}\cdot\tau_i)} \int d^3r \rho_i(\mathbf{r}) e^{-i\mathbf{Q}\cdot\mathbf{r}} \tag{A.3}$$

The scattering of x-rays from a crystal with an exposed surface can be calculated from the above relations in the simple case of a semi-infinite crystal. The surface is introduced mathematically by restricting the sum over $\{\mathbf{R}\}$ via a Heavyside function which is a function of the surface height at a given lateral position on the surface. Hence,

$$A(\mathbf{Q}) = F(\mathbf{Q}) \sum_{\{\mathbf{R}\}} e^{-i\mathbf{Q}\cdot\mathbf{r}} \Theta[\mathbf{R}\cdot\mathbf{n} - (h(\mathbf{R}_\parallel) + r_0)] \tag{A.4}$$

The local surface height is represented by $h(\mathbf{R}_\parallel)$ and the local surface normal is $\hat{n}$. Vicinal (or miscut) surfaces are defined in terms of this local surface normal. The sum over real space lattice vectors can be replaced by a sum over reciprocal lattice vectors, giving

$$A(\mathbf{Q}) = F(\mathbf{Q}) \sum_{\{\mathbf{G}\}} \int d^3r e^{-i(\mathbf{Q}-\mathbf{G})\cdot\mathbf{r}} \Theta[\mathbf{r}\cdot\hat{n} - h(\mathbf{r}_\parallel) - r_0] \tag{A.5}$$

The integral over the direction normal to the surface ($\mathrm{r}_\perp$) can be carried out immediately, leaving us with

$$A(\mathbf{Q}) = \frac{F(\mathbf{Q})}{V_{\text{cell}}} \sum_{\{\mathbf{G}\}} \frac{e^{-i(\mathbf{Q}-\mathbf{G})\cdot\mathbf{r_0}}}{-i[(\mathbf{Q}-\mathbf{G})\cdot\hat{n}]} \int d^2r_\parallel e^{-i(\mathbf{Q}-\mathbf{G})\cdot(\mathbf{r}_\parallel + \mathbf{h}(\mathbf{r}_\parallel))} \tag{A.6}$$

In this equation $\mathbf{h}(\mathbf{r}_\parallel) \equiv h(r_\parallel)\hat{n}$, and $\mathbf{r_0} \equiv r_0\hat{n}$. The scattering cross-section $\mathrm{S}(\mathbf{Q})$ is proportional to $\mathrm{A}(\mathbf{Q})\mathrm{A}^*(\mathbf{Q})$. Taking the complex conjugate of $\mathrm{A}(\mathbf{Q})$ above and

carrying out the multiplication results in

$$S(\mathbf{Q}) = \frac{|F(\mathbf{Q})|^2}{V_{\text{cell}}^2} \sum_{\mathbf{G},\mathbf{G}'} \frac{e^{-i(\mathbf{Q}-\mathbf{G})\cdot\mathbf{r_0}} e^{+i(\mathbf{Q}-\mathbf{G}')\cdot\mathbf{r_0}}}{[(\mathbf{Q}-\mathbf{G})\cdot\hat{n}][(\mathbf{Q}-\mathbf{G}')\cdot\hat{n}]} \times \int d^2r_\parallel d^2r'_\parallel [e^{-i(\mathbf{Q}-\mathbf{G})\cdot(\mathbf{r}_\parallel+\mathbf{h}(\mathbf{r}_\parallel))}][e^{+i(\mathbf{Q}-\mathbf{G}')\cdot(\mathbf{r}'_\parallel+\mathbf{h}(\mathbf{r}'_\parallel))}] \quad \text{(A.7)}$$

Adding and subtracting terms to symmetrize the factor in the exponent and cancelling the terms $\mathbf{Q}\cdot\mathbf{r_0}$, the integral can be re-written as

$$S(\mathbf{Q}) \propto \sum_{\mathbf{G},\mathbf{G}'} \frac{e^{-i(\mathbf{G}'-\mathbf{G})\cdot\mathbf{r_0}}}{[(\mathbf{Q}-\mathbf{G})\cdot\hat{n}][(\mathbf{Q}-\mathbf{G}')\cdot\hat{n}]} \times \int d^2r_\parallel d^2r'_\parallel [e^{-i(\mathbf{G}'-\mathbf{G})\cdot(\mathbf{r}'_\parallel+\mathbf{h}(\mathbf{r}'_\parallel))}][e^{-i(\mathbf{Q}-\mathbf{G})\cdot(\mathbf{r}_\parallel-\mathbf{r}'_\parallel)} e^{-i(\mathbf{Q}-\mathbf{G})\cdot(\mathbf{h}(\mathbf{r}_\parallel)+\mathbf{h}(\mathbf{r}'_\parallel))}] \quad \text{(A.8)}$$

The first bracketed term in the integral is a double delta function, $\delta^{(2)}((\mathbf{G}'-\mathbf{G})\times\hat{n})$, where $\mathbf{G}'-\mathbf{G}$ is a vector connecting two reciprocal lattice points. One is free to choose the origin $\mathbf{r_0}$ such that the statistical averaged height, $<\mathbf{h}(\mathbf{r}_\parallel)>$, is exactly zero. Averaging over height fluctuations and defining $\rho_\parallel \equiv \mathbf{r}_\parallel - \mathbf{r}'_\parallel$, the structure factor becomes

$$S(\mathbf{Q}) = (2\pi)^2 \frac{F^2}{V_{\text{cell}}^2} \sum_{\mathbf{G},\mathbf{G}'} \frac{e^{-i(\mathbf{G}'-\mathbf{G})\cdot\mathbf{r_0}} \delta^{(2)}((\mathbf{G}'-\mathbf{G})\times\hat{n})}{[(\mathbf{Q}-\mathbf{G})\cdot\hat{n}][(\mathbf{Q}-\mathbf{G}')\cdot\hat{n}]} \times \int d^2\rho_\parallel e^{-i(\mathbf{Q}-\mathbf{G})\cdot\rho_\parallel} < e^{-i(\mathbf{Q}-\mathbf{G})\cdot(\mathbf{h}(\rho_\parallel)-\mathbf{h}(0))} > \quad \text{(A.9)}$$

The set of vectors $\{\mathbf{G}\}$ define the location of the bulk peaks in an x-ray scattering experiment. Thus, the delta function will be non-zero at the bulk peak positions, ie. when $\mathbf{G}' = \mathbf{G}$, or when the vector connecting two bulk peaks happens to lie on a line parallel to the surface normal $\hat{n}$, that is, when $(\mathbf{G}'-\mathbf{G})\times\hat{n} = \vec{0}$. This condition is satisfied by many vectors, all of which terminate on a special line in reciprocal space known as the *crystal truncation rod* or CTR. This is best illustrated by examining

Fig. 2-9 many truncation rods, each one passing through at least one bulk peak. In the case of a surface oriented slightly away from a high symmetry direction (a vicinal surface), each truncation rod will pass through exactly one bulk peak since the surface normal ($\hat{n}$) cannot be expressed in terms of an integral sum of reciprocal lattice vectors. That is, the condition $\mathbf{G}' = \mathbf{G}$ is only satisfied at single Bragg peaks, even though $(\mathbf{G}' - \mathbf{G}) \times \hat{n}$ is zero when $(\mathbf{G}' - \mathbf{G})$ lies parallel to the surface normal.

The term in the integral, $< e^{-i(\mathbf{Q}-\mathbf{G})\cdot(\mathbf{h}(\rho_{\|})-\mathbf{h}(\mathbf{0}))} >$, defines the height–height correlation function, $C_{\mathbf{Q}-\mathbf{G}}(\rho_{\|})$. Thus, x-ray scattering can probe directly the fluctuations in surface height if the experimental geometry is chosen such that the scattering due to this contribution is maximized with respect to scattering from the bulk.

[1] G. Held and J. Brock, Phys. Rev. B **51**, 7262 (1995).